Using remote sensing to track resilience of subtropical rainforests against fires and tropical cyclones

Chan Hei Yeung

Downing College

Forest Ecology and Conservation Group
Department of Plant Sciences
University of Cambridge

September 2023

This thesis is submitted for the degree of Doctor of Philosophy

Supervisors:
Prof David Coomes (Principal Supervisor)
Dr Andrew Tanentzap (Graduate Advisor)
Prof Howard Griffiths (GEC)

I declare that -

1. This thesis is the result of my own work and includes nothing which is the outcome of work done in collaboration except as declared in the preface and specified in the text.

2. It is not substantially the same as any work that has already been submitted before for any degree or other qualification except as declared in the preface and specified in the text.

3. It does not exceed the prescribed word limit of 60,000 for the Biology Degree Committee.

Abstract

Using remote sensing to track resilience of subtropical rainforests against fires and tropical cyclones

Chan Hei Yeung

The large-scale restoration of tropical and subtropical rainforests is crucial for mitigating climate change and biodiversity loss. Disturbances such as fire and wind potentially undermine efforts to restore degraded landscapes, interacting with the existing vegetation and background topography to produce complex patterns of damage. It is therefore crucial for us to understand these interactions and study the factors that contribute to disturbance resilience. Rapid developments in the field of remote sensing have provided new tools to study forest-disturbance dynamics across unprecedented spatiotemporal scales. In this thesis, a range of high-resolution remote sensing products, including aerial imagery, satellite multispectral imagery, and airborne LiDAR scans, were used to evaluate how fires and tropical cyclones have affected vegetation in wet subtropical Hong Kong. **Chapter 1** provides an overview of how forest disturbances interact with restoration ecology. It then describes the vegetation history of Hong Kong, highlighting how the region represents an interesting case study as a long-running restoration project over highly degraded landscapes in the wet tropics. **Chapter 2** reconstructs the fire history of Hong Kong using a 34-year Landsat imagery time series. Burn area detection in the wet tropics and subtropics is challenging due to high cloud cover and rapid revegetation of burn areas. A pipeline was developed to process hundreds of satellite multispectral images and accurately map out thousands of burnt areas. The pipeline additionally dated every detected burn area polygon and estimated burn severity for pixels in the burn area. The final product is the first of its kind in wet tropical Asia. **Chapter 3** proceeds to use this burn area and severity time series to study fire-vegetation feedbacks in Hong Kong. When early successional vegetation is more fire susceptible than late-successional closed-canopy forests, positive fire-vegetation feedbacks are created. These feedbacks can then form “fire traps” that undermine restoration of degraded landscapes. Here, fire occurrence and post-fire recovery in different vegetation types were investigated. The results provided compelling evidence for the presence of strong fire traps in Hong Kong. **Chapter 4** describes a pipeline to model long-term mean and typhoon maximum wind speeds across the rugged topography of Hong Kong, as a precursor for Chapter 6. Specifically, wind models based on computation fluid dynamics (CFD) modelling were validated by wind data collected from a dense network of weather stations and our own anemometers. **Chapter 5** analyses the resulting wind maps and a repeated LiDAR dataset (2010, 2017, 2020) to study forest resilience against strong tropical cyclones. The LiDAR dataset captured the forest damage incurred during Typhoon Mangkhut in 2018, which was the strongest tropical cyclone to affect Hong Kong in over 40 years. Plantations, tall forests, and normally wind-sheltered forests were found to be more susceptible to tropical cyclones. Effects of tropical cyclones and wind exposure cascaded through time to create strong wind-related

limits on local forest height. **Chapter 6** provides a holistic discussion of the findings of this thesis by summarising how the two studied disturbance processes (fires and wind) act alongside other disturbances to shape restored subtropical landscapes. The chapter also describes planned future work on (1) modelling and extrapolating the effects of fire on restoration and (2) exploring effects of wind on forest structure. Overall, this thesis provides a detailed account of the patterns of resilience against fire and tropical cyclones in the wet tropics. Such knowledge on resilience could help land managers better plan and restore degraded landscapes in the wet tropics under changing climate and disturbance regimes.

Acknowledgements

This PhD would not have been possible without the many people who supported me throughout the four-year journey.

First and foremost, I would like to thank my supervisor, Prof David Coomes, for the countless hours of academic discussions and informal chats. You have been an amazing supervisor and mentor. I cannot overstate how much I appreciated your support even when I get hopelessly stuck while diving into overly complex research ideas or traversing impossibly thick forests halfway across the globe.

I am incredibly grateful to my colleagues in the David Attenborough Building for all their help over the past four years. In particular, I would like to thank Toby Jackson as a colleague who offered the irreplaceable insights on wind modelling and as a friend who shared great times at the Wind and Trees Conference. Special thanks go to Kyaw Sein Win Tun (O'Neill) for being a great friend and helping me go through all the ups and downs throughout my PhD. Another special mention goes out to Ed Tanner, who served as a great mentor and organised exciting outdoor trips that helped us get through the worst times during lockdowns. I would like to thank E-Ping Rau, Michelle Kalamandeen, and Alejandro Guizar-Coutiño for their company, helpful advice, and co-authorship of the manuscripts derived from this work. I am grateful for all the support offered by Yi Zhang on the endless paperwork (and all the snacks from China). Thanks also goes out to Adam Pellegrini, Johanna Schoenecker, and Courney Currier, for their passion and expertise on fire ecology. Additionally, I would like to thank my colleagues around in the office who supported me through the highs and lows, including but not limited to James, Barbara, Amelia, Edgar, Liam, Tom, Boris, Sacha, Jon, and Cicely.

I am also grateful to those who helped me during my visits to Hong Kong despite the challenging situation with covid. To start with, I would like to thank Billy Hau for hosting me at the University of Hong Kong. Your passion in ecology and restoration in Hong Kong inspired a whole generation of local ecologists. I would also like to thank Jin Wu for helping with my remote sensing work. Special thanks also go out to Rocky, Jess, and Theodora for all your help in the field under (sometimes) very harsh conditions. I will meet you all back in the mountains! Finally, I would like to thank Maria for the generous equipment support, Fung for lending us the anemometer, and Laura for all the delicious cakes.

I also want to thank the those in the HSI Clustering and Classification group, including but not limited to Raymond Chan, Bob Plemmons, Jason Cui, Sam Polk, Ruoning Li, and Sylvia Huang, for the development of the vegetation classification maps.

I would like to thank Gates Cambridge Trust for funding this PhD project and making everything possible; Frank Smart Studentship for believing in this project; the staff in the Civil Engineering and Development Department of Hong Kong for spending hours out of your way to provide us with research data; The Fire Services Department and the Agricultural, Fisheries and Conservation Department for providing fire records; and the Hong Kong Observatory for helping us with the wind data.

I would like to thank my family for providing unwavering support throughout my PhD including. Special thanks go to my mom, who had to put up with my sloppiness in doing housework. I promise I will do more dishes after this document sees the light of day. I also deeply appreciate my aunt, my uncle, and my grandmother for hosting me during my trips to Hong Kong. I owe all of you so so much.

To all my table tennis friends and hiking mates, including but definitely not limited to Max, Samual, Anthony, Karl, Mathew, Chiu, Julian, Hampton, I thank you for keeping me sane over the past few years.

Finally, Kay, I know you will be the only one reading through till the end of this long list of acknowledgements, so I put you down last, but do not for one second think that you are the least important. You have been my emotional support animal and the special someone through this incredible journey, and I will forever be grateful. It is your turn to submit a PhD thesis next, so I wish you the best of luck. I promise to be by your side, high and low, just like how you have been by my side, high and low.

Table of Contents

List of Figures

List of Tables

Chapter 1: Introduction

1.1 Introduction to forest restoration

1.1.1 The decade of ecosystem restoration

Tropical and subtropical forests provide crucial ecosystem services and house enormous biodiversity (Delgado-Aguilar et al., 2017; Gentry, 1992; Silvério et al., 2019). These ecosystems are, however, threatened by land conversion and degradation. The need to feed the rising population has led to extensive conversion of forests to arable land or pastures. Globally, 314 Mha of forests were lost between 2001 and 2015 (Curtis et al., 2018). Forests that escape land conversion are often logged to meet the strong demand for timber and firewood. A total of 500-600 million hectares, or 30-40% of remaining tropical forests, are now degraded by anthropogenic activity (Budiharta et al., 2014; Pan et al., 2011). Deforestation, degradation, and fragmentation of tropical forests need to be reversed to avert a biodiversity crisis and a sixth mass extinction (Barnosky et al., 2011). The restoration of degraded forests represents a race against time. The fragmentation of tropical forests creates extinction debts – species residing in fragmented forest patches tend to go extinct in the long term if the patches are not reconnected (Kuussaari et al., 2009; Tilman et al., 1994). Additionally, the global community has increasingly recognised the ability for tropical forests to mitigate anthropogenic climate change by acting as carbon sinks (Bastin et al., 2019; Pan et al., 2011; Wheeler et al., 2016). As a result, international initiatives have repeatedly called for the large-scale restoration of previously deforested or degraded landscapes in the wider tropics. The Bonn Challenge pledges to restore 350 Mha of forests by 2030 (Verdone & Seidl, 2017); the One Trillion Tree initiative aims to conserve, restore, or grow a trillion trees in the same time frame (Brancalion & Holl, 2020); and the UN has subsequently marked the years 2021 to 2030 as the Decade of Ecosystem Restoration (Abhilash, 2021).

1.1.2 Types of restoration

Various strategies have been implemented to promote forest restoration in the tropics, each with its own advantages and drawbacks. The simplest restoration strategy is natural regeneration. Sites earmarked for restoration are left alone, allowing for the natural colonisation of shrubs and trees to push the site through various stages of succession. Across much of the wet tropics, natural regeneration has been hailed to be the most cost-effective restoration strategy that delivers the greatest benefits to both carbon sequestration and local biodiversity (Lamb et al., 2005; Lewis et al., 2019). Several interventions could potentially increase the effectiveness of natural regeneration. The control of disturbances, such as fires or herbivory pressure, can reduce the mortality of seedlings (Florens, 2013; Flores & Holmgren, 2021; Wheeler et al., 2016). The selective removal of early successional tree species has also been explored as a solution to speed up the rate of succession (Swinfield et al., 2016). Despite the benefits, several factors could potentially undermine the efficiency of natural regeneration as a restoration strategy. The soils on degraded landscapes can sometimes be heavily eroded and nutrient poor (Corlett, 1999; Davies et al., 2010; Jim, 2003). In some regions, this could lead to the formation of gullies and moon-like landscapes where trees do not naturally regenerate. Additionally, when landscapes are extensively deforested or degraded, much of the area may lack sufficient seed sources for effective regeneration (Herrmann et al., 2016; Levine & Murrell, 2003; Rogers et al., 2019). This could be further exacerbated by the dominance of early successional vegetation or invasive species, which could physically occlude the establishment of trees and lead to arrested succession (Florens, 2013; N. Liu et al., 2013; Pang et al., 2018; Rochimi et al., 2021). In such case, active restoration can sometimes provide an alternative to natural regeneration. Trees can be planted in the restoration site by either direct seeding or sapling plantation (Corlett, 1999; Lamb et al., 2005; Law et al., 2023; Scheper et al., 2021; Wheeler et al., 2016). This could be facilitated by the removal of grasses, ferns, or shrubs dominating the degraded site (Florens, 2013). There is also flexibility in how plantations are established. Due to its low cost and economic value, monocultures of fast-growing trees planted in neat rows currently represent the most popular restoration strategy (Lewis et al., 2019). The practice is, however, increasingly discouraged as mounting evidence shows that they fail to restore local biodiversity and have low resilience against disturbances (Jucker et al., 2014; Lewis et al., 2019; Tilman et al., 1994; Zhu et al., 2023). Alternatively, plantations formed by a mixture of different native species can deliver better biodiversity benefits but are often more costly to establish (Stephens & Wagner, 2007; Trauernicht et al., 2018). Agroforestry, the practice of planting economically valuable crops in restored forests, can offer a compromise in areas where the income generated by the crops are necessary to pay for the cost of restoration (Bhagwat et al., 2008). Previous studies have also explored the idea of changing the spatial arrangement of planted trees. Applied nucleation – planting trees in small clusters while leaving the rest of the landscape for natural regeneration – has been trialled in a number of sites (Corbin & Holl, 2012). This approach could accelerate the rate of natural regeneration by introducing seed sources into degraded landscapes, while still having the benefit of creating structurally and biologically diverse forests at lower costs than plantations (Corbin & Holl, 2012).

1.2 Forest disturbances in the tropics and subtropics

1.2.1 Introduction to forest disturbance and the ecosystem resilience

Disturbances are events that negatively affect forest growth and productivity. The term usually refers to natural events, but some studies also consider anthropogenic disturbances that directly result from human activity (e.g. logging and coppicing) (FAO, 2018). Common disturbances in the tropics and subtropics include fires, wind, droughts, landslides, and pathogens (Brando et al., 2019; Seidl et al., 2017). Disturbances create a dynamic equilibrium amongst forest systems (Mori, 2011). Most disturbances are discrete events manifested across short time scales, with return times ranging from years to centuries. When disturbance event occurs, it could cause retrogressions and push affected areas back to earlier stages of succession. In years without disturbances, vegetation tends to move along the successional gradient to later stages of succession. By stochastically occurring through time and space, disturbances create a mosaic of habitat patches with different disturbance-recovery profiles (Mori, 2011). Disturbances have a complicated relationship with biodiversity. The intermediate disturbance hypothesis (IDH), which states that sites subjected to moderate levels of disturbance supports the highest biodiversity, has received mixed support since its development in the 1970s. It is, however, generally accepted that recently disturbed sites support different species compositions compared to long undisturbed habitats (Fox, 1979; Grime, 1973; Moi et al., 2020; Sheil & Burslem, 2013).

The responses of forests in face of disturbances can be described in the framework of resistance, recovery, and resilience (D. Hodgson et al., 2015; Holling, 1973) (**Figure 1.1**). Forests with low resistance (or high susceptibility) respond more strongly to disturbance events (Derose & Long, 2014). Depending on the context of study, this could mean larger changes in canopy height, species diversity, or other vegetation metrics (Jactel et al., 2017). After disturbances, forests slowly recover to pre-disturbance conditions (D. Hodgson et al., 2015). Notably, different floral and faunal groups could have very different rates of recovery. For instance, the recovery time of epiphytes could be an order of magnitude longer than that of tree canopy height (Price et al., 2017). Realistically, it is not always possible to track forests through the entire recovery trajectory. In the context of forest restoration, an added complexity is the lack of a fixed pre-disturbance baseline for recovery rate estimations as the landscape is itself on a recovery trajectory without the disturbance (black dashed line, **Figure 1.1**). As such, there is no universal protocol for the estimation of recovery rates, and studies ought to set pre-defined, measurable thresholds appropriate for the research question being answered (green dotted line, **Figure 1.1**). Finally, forest resilience is defined as the product of both resistance and recovery (D. Hodgson et al., 2015). It represents the overall ability of forest ecosystems to counter disturbances. Resilience could be achieved by being resistant to disturbances, having short recovery times, or a combination of both (D. Hodgson et al., 2015).

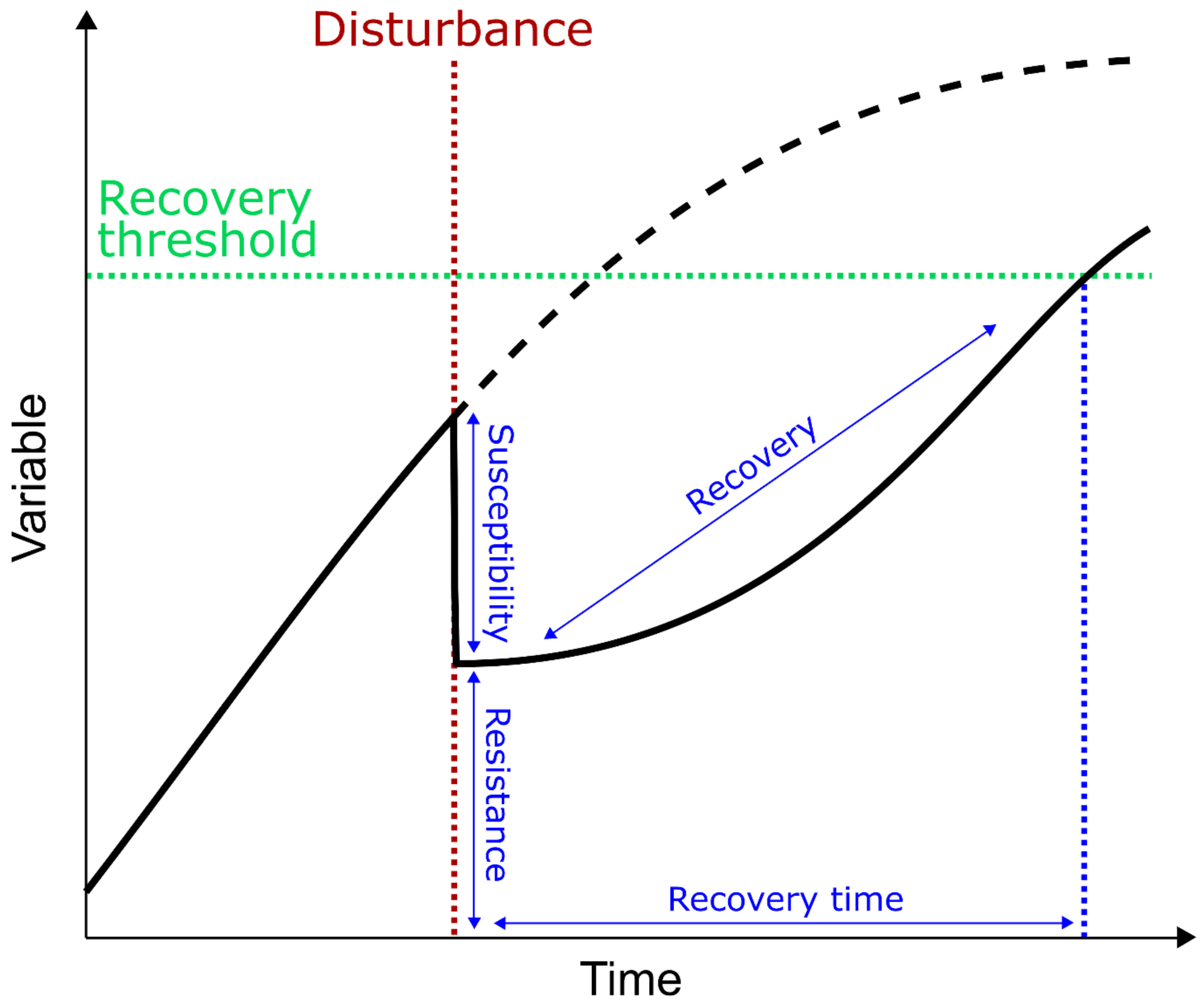

Figure 1.1: Diagram showing the different components that contribute to resilience against disturbances in a forest restoration context. The black dashed line represents the restoration trajectory without the disturbance and the black solid line represents the actual observed changes with the disturbance.

1.2.2 Considering disturbance and resilience in forest restoration

Forest restoration projects can potentially be undermined by disturbances. In some cases, disturbances could cause restoration targets to be missed. For instance, land managers could be expecting a certain amount of carbon being sequestered in restored forests, only to have a proportion of the stored carbon being removed by disturbances such as droughts or tropical cyclones. In other cases, disturbances could lead to outright failure in establishing forests on degraded landscapes (Abbas et al., 2016; Florens, 2013; Lamb et al., 2005; Zhuang & Corlett, 1997). Targeted studies on how disturbances affect forest restoration projects are necessary as degraded landscapes often have markedly different disturbance regimes compared to natural forests (Mark A. Cochrane, 2003; Ko & Lo, 2018; Mahood & Balch, 2019). For instance, these areas could have higher fire susceptibility due to the abundance of invasive grasses or have higher exposure to anthropogenic ignition sources due to its proximity to human settlements (Davies et al., 2010; Mahood & Balch, 2019; Tien Bui et al., 2016; Wheeler et al., 2016). These disturbance regimes are also expected to shift due to anthropogenic climate change (Seidl et al., 2017).

The rise in air temperatures is causing more intense droughts and higher fire occurrence due to the increase in vapor pressure deficit (Clarke et al., 2022). Similarly, increases in sea surface temperatures are leading to fewer but stronger tropical cyclones (Chand et al., 2022; Kossin et al., 2020) and poleward shifts in tropical cyclone hotspots (Murakami et al., 2020). Given these changes, there is a pressing need for us to better understand the factors that contribute to disturbance resilience within ecosystems undergoing restoration. Untangling these patterns is critical for setting appropriate restoration strategies and achievable restoration targets.

1.3 Hong Kong as a case study for restoration in the wet subtropics

1.3.1 Introduction to case studies in ecological research

Due to the spatial extent of the study systems, ecological research relies on case studies to achieve generality. Concentrating resources to study smaller areas allow researchers to better scrutinise ecological patterns of interest in greater detail. Once the area accumulates a collection of studies and large amounts of data, it would also enable researchers to better control for confounding factors. Well-known case studies include Cedar Creek for forest-prairie ecosystems (Pellegrini et al., 2021; Tilman et al., 2006), Barro Colorado Island for tropical rainforests in the Americas (Leigh, 1999), and Danum Valley for lowland dipterocarp forests in Southeast Asia (Reynolds et al., 2011). An ideal selection of case studies should produce results that could be generalisable and transferrable to cover the major biomes across the globe (Spake et al., 2022). In this section, we will present Hong Kong as a useful case study for forest restoration and disturbance ecology in the wet subtropics.

1.3.2 The climate and geography of Hong Kong

Hong Kong (22° 16’ 8’’ N, 113° 57’ 6’’E) is a Special Administrative Region located in south China. It borders the city of Shenzhen in the Guangdong province of China in the north and faces the South China Sea towards the south. The majority of the land area of Hong Kong (1114 km^2) consists of a peninsula that includes Kowloon (47 km^2) and mainland New Territories (747 km^2) (HK Lands Department, 2019). Additionally, there are over 200 islands disconnected from the mainland. The largest being Lantau Island (147 km^2) and Hong Kong Island (79 km^2) (HK Lands Department, 2019). Housing over 7 million inhabitants, Hong Kong has one of the highest population densities in the world. However, the rugged terrain largely prevented urban expansion into the countryside and instead squeezed much of the population into high-rise buildings. As a result, approximately 60% of the land area remains vegetated and undeveloped (Kwong et al., 2022). In total, the territory has over 300 steep sided hills >100 meters above sea level (m.a.s.l). The tallest mountain is Tai Mo Shan, located in central New Territories with a height of 957 m.a.s.l. Other notable peaks include Lantau Peak (934 m.a.s.l) and Sunset Peak (869 m.a.s.l.) on Lantau Island, Ma On Shan (702 m.a.s.l) in eastern New Territories, and Pat Sin Leng – Wong Leng ridgetop (489 to 639 m.a.s.l.) in the northeast.

The background geology of Hong Kong is diverse. The region is predominantly covered by igneous rocks (Fletcher, 1997). These rocks were mainly formed during repeated volcanic activity in the Mesozoic era. The tallest mountains of Hong Kong consist of extrusive igneous rocks, mainly tuff, expelled in violent volcanic eruptions (Fletcher, 1997). Much of these rocks originated from the now extinct High Island Supervolcano, which expelled an estimate of 1300 km^3 of acidic volcanic ash (>400 times that of the St. Helena eruption in 1980), representing a globally significant geological event (Sewell et al., 2012; Yan, 2018). The caldera of the volcano is still observable today, forming the various geological features in the Sai Kung district (Sewell et al., 2012). Apart from extrusive rocks expelled during eruptions, around a third of the land area is covered by intrusive igneous rocks, mainly granite (Fletcher, 1997). Finally, some sedimentary rocks, formed between the Devonian to late Cretaceous periods, are also found in Hong Kong. Overall, the rocks in Hong Kong weather into acidic (pH 4-5) soils with low cation exchange capacities (Jim, 2003; Luo et al., 2005). The red-yellow podzols found in many areas across Hong Kong are rich in iron and aluminium oxides, which trap anions and lead to low phosphate and nitrogen availability (K. C. Chau & Marafa, 1999; Luo et al., 2005). This lead to poor soils for plant growth even in well-developed soils in mature forests (Jim, 2003).

The climate of Hong Kong is wet subtropical. The average temperature over the last century is approximately 23 ^{o}C with an average rainfall of 2400 mm (Hong Kong Observatory, 2023). The climate is also characterised by clear seasonal changes. Summers in Hong Kong are hot and wet, while winters are cool and dry. Temperatures in Hong Kong rarely drop below freezing, but frosts occasionally affect areas of high elevation (Abbas et al., 2017; Hong Kong Observatory, 2023). Geographically and climatically, Hong Kong lies within the Indo-Burma biodiversity hotspot, which makes the region floristically diverse (>2100 native vascular plants recorded) (Hong Kong Herbarium, 2012). The temperature gradient on mountains produces a two-tiered vegetation structure, with lowland forests dominated by tropical species and montane forests hosting more temperate flora (Dudgeon & Corlett, 2004).

Comprehensive meteorological and geological records in Hong Kong provide useful information for ecological research. Hong Kong Island and the Kowloon Peninsula was ceded to Britain under the Treaty of Nanking in 1841 and Treaty of Peking in 1860, respectively (Tsang, 2003). The increase in commercial activity and shipping prompted the establishment of the Hong Kong Observatory in 1883. Barring the second world war, the observatory made continuous records of temperature, rainfall, and wind speed for >140 years (Hong Kong Observatory, 2023). The economic importance of Hong Kong and the proximity of urban areas to the countryside created a large local demand for accurate weather monitoring and geological mapping to mitigate the risks of natural disasters such as flooding and landslides (Ho et al., 2009; Ko & Lo, 2018). With over 50 automatic weather stations, each providing decades of meteorological data, the region is now home to one of the densest networks of weather stations in the tropics and subtropics (Hong Kong Observatory, 2023). These records are invaluable for understanding the ecology of forest disturbances.

1.3.3 The vegetation history of Hong Kong

Like many regions in the wet tropics, the vegetation history of Hong Kong is a story of degradation and restoration. Vegetation in the region has been profoundly transformed by the establishment of human settlements around 6000-7000 years ago (Cheung et al., 2022; Planning Department, 2001). Changes in vegetation structure were tightly linked to socioeconomic development of settlers. Before the arrival of humans, the landscape of Hong Kong was predominantly covered by subtropical rainforests (Dudgeon & Corlett, 2004). Pollen evidence from Ho Chung Valley identified large quantities of *Quercus* and *Castanopsis* pollen deposited during the Middle Neolithic period (Yang et al., 2018). This does not necessarily mean that the vegetation at the time were dominated by species in Fagaceae. Palynology tends to better represent wind-pollinated species and disadvantage insect-pollinated species (e.g. Lauraceae). However, it does suggest that even easily accessible lowland alluvial plains were covered by late-successional forests the Middle Neolithic period (Yang et al., 2018). There is considerable uncertainty in whether open habitats existed on mountaintops. However, given the relatively mild climate of Hong Kong, it is generally believed that open habitats would be rare in the region without human intervention (Dudgeon & Corlett, 2004; Zhuang & Corlett, 1997). In the first several thousand years after the arrival of humans, the population of Hong Kong is sparse and mostly confined to coastal areas (Planning Department, 2001). Archaeological excavations have shown that early settlers were mainly hunters, gatherers, and fishermen (H. W. Chau, 2003; Cheung et al., 2022). These settlers had limited impact on the local vegetation structure. The population in Hong Kong rose substantially during the Tang and Song dynasties (618 – 1276 AD). These new settlers brought more advanced agricultural practices and converted much of the lowland forests into rice paddies (F. Huang & Pei, 2001; Yang et al., 2018). Most of the settlements would be limited to fertile alluvial plains in the lowlands, but the demand for firewood might have led to increased logging activity on slopes. Additionally, the landscape was also impacted by two industries that developed over this period – salt and lime production. Shallow bays and inlets were converted to produce sea salt, while kilns were built to convert coral and shells to lime (Planning Department, 2001). Both industries required substantial fuelwood, which decimated much of the woodlands in the area (Corlett, 1997; Stokes, 1995). Between 1661 – 1683 AD in the Qing Dynasty, the government at the time ordered residents to move inland in an effort to combat rebel forces that controlled coastal areas in the region. When the order ended, the government actively encouraged the population to move back into the area, which led to a large spike in population density in Hong Kong (Planning Department, 2001). One group, the Hakka people, settled in previously unoccupied mountainous regions. Villagers at the time kept patches of forests behind villages for various economical and non-economical purposes (Fung Shui Woods), but otherwise cleared much of the landscape for agriculture (Zhuang & Corlett, 1997). Rice terraces covered the lowlands and tea plantations stretched to mountaintops. Slopes that were not used for agriculture were also logged to meet the demand for firewood. When the British arrived in 1842, the landscape of Hong Kong was mostly barren with patches of highly diverse forests in ravines and Fung Shui Woods (Dudgeon & Corlett, 2004). Under British rule, the government of Hong Kong led several reforestation campaigns. The new plantations mainly consisted of *Pinus massoniana*, a native conifer that survived in heavily eroded areas. These efforts were largely undone during the second world war. During the war, Hong Kong fell under Japanese rule in 1941, and the plantations were logged to provide fuelwood for the local populace both before and during the occupation. The end of the second world war in 1945 marks the start of a >70-year restoration period (Abbas et al., 2016). Over this period, Hong Kong experienced rapid economic development marked by industrialisation and later a transition to a financial hub (Tsang, 2003). These changes led to a sharp fall in rural population and widespread agricultural abandonment. With the cessation of rural land management practices, shrublands and secondary forests expanded on the barren landscape mostly through natural regeneration. This transition was facilitated by a change in government policy, which abandoned commercial forestry for a purely restoration-based framework mid-1960s (Corlett, 1999; Daley, 1965). *Pinus massoniana* plantations were gradually phased out, especially after the Pinewood Nematode *Bursaphelenchus xylophilus* decimated most *P. massoniana* stands in the late 1970s (Kishi & others, 1995). However, plantations of exotic species, notably *Acacia confusa*, *Lophostemon confertus*, and the nematode-resistant *Pinus elliottii*, remained significant features of the landscape (Corlett, 1999). By the early 1990s, forests were estimated to make up approximately 14% of the total land area, with a third being plantations (Ashworth et al., 1993). The increased emphasis on conservation also led to the designation of vegetated areas as strictly protected Country Parks since the 1970s, which now cover over 40% of the land area (HK Lands Department, 2019). The current vegetation in the countryside of Hong Kong consists of a mosaic of grassland (**Figure 1.2a**), shrubland (**Figure 1.2c**), secondary forests (**Figure 1.2d-e**), and plantations (**Figure 1.2f**).

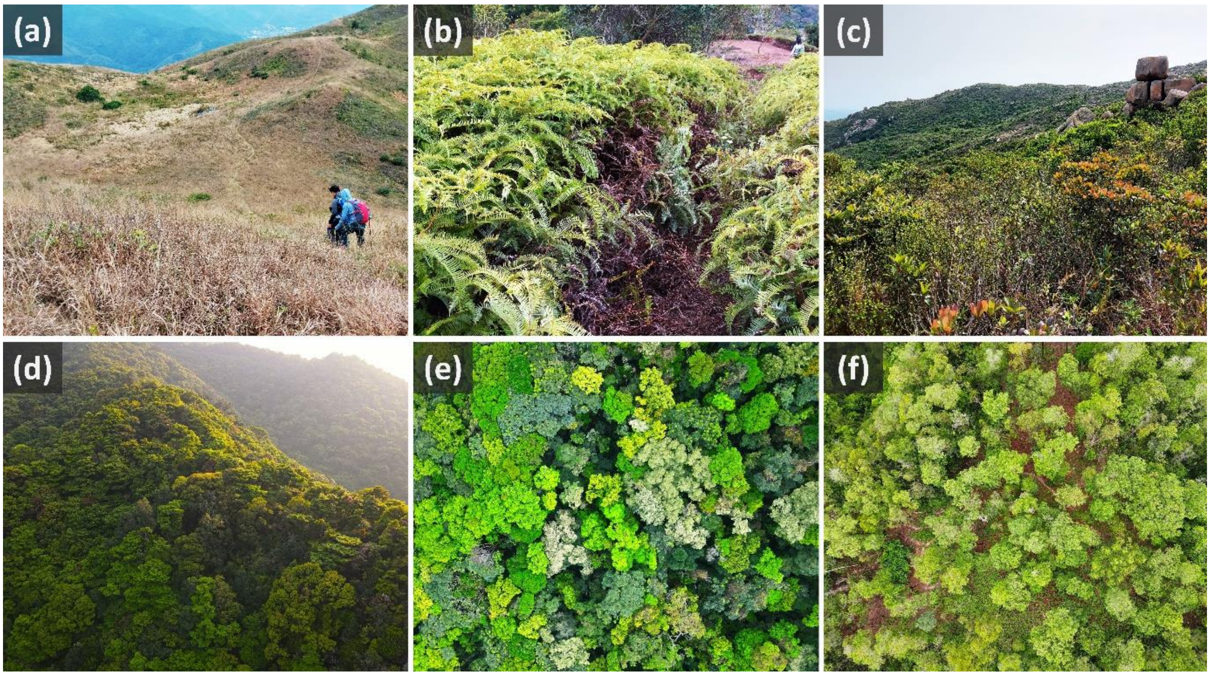

Figure 1.2: Different vegetation types found in Hong Kong: (a) Grasslands on Robin's Nest, (b) Fern (Dicranopteris pedata) mats near Sheung Wo Hang, (c) Mixed shrublands on Lamma Island, (d) Montane forests on Tai Mo Shan, (e) Lowland forests in Mau Ping, (f) Plantations in Pak Fu Au.

1.3.4 Disturbances in Hong Kong

Efforts to restore the degraded landscapes in Hong Kong are often met with challenges due to the range of disturbances that affect the region. Most notably, the vegetation in Hong Kong is affected by fires, wind, landslides, frosts, droughts, and pathogens. In this section, we briefly introduce the scale and impact of these events on local vegetation.

1.3.4.1 Fires

Fires represent the most prominent disturbance in the degraded landscape of Hong Kong. As with most wet tropical and subtropical regions across the globe, natural fires are rare (Mark A. Cochrane, 2003). Past research on fuel flammability in has suggested that fires could theoretically propagate through most habitats in Hong Kong after dry spells (K. L. Chau, 1994). However, natural ignition sources are rare. The most likely source of ignition, lightning strikes, occur mainly in the wet season and are usually accompanied by storms with heavy precipitation. Additionally, mature rainforests retain moisture well and are generally considered least flammable amongst the various types of vegetation in Hong Kong (K. L. Chau, 1994). Centuries of degradation and exposure to human activity has substantially changed the fire regime in Hong Kong due to two main factors. Firstly, wet biomes are characterised by positive fire-vegetation feedbacks – the phenomenon where early successional vegetation is more fire prone than late successional forests (Hoffmann et al., 2003; Hoffmann, Geiger, et al., 2012; A. D. Miller et al., 2019; Tepley et al., 2018; Uhl et al., 1988). Degraded landscapes in Hong Kong are commonly colonised by *Dicranopteris* fern mats (**Figure 1.2b**), *Miscanthus* grasslands, or *Baeckea* shrublands (Hau & Corlett, 2002). These vegetation types tend to accumulate dry biomass that do not readily decompose, making them susceptible to fires. Secondly, humans introduce sources of ignition. Fires are regarded by villagers as a convenient way to keep sites open and accessible. Residents in Hong Kong also widely observe the traditional ritual of mourning the deceased by burning incense and joss paper around graves (K. L. Chau, 1994; Zhuang & Corlett, 1997) (**Figure 1.3**). Since many graves are in the countryside, this leads to spillover wildland fires each year. The drop in rural population after the second world war and government campaigns have led to fewer ignition sources in the countryside. However, at the time of writing, the Fire Services Department continue to receive hundreds of wildland fires reports every year (Fire Services Department, 2021). Various authors have suggested that hillfires are the main factor that delays forest restoration and maintain open habitats in Hong Kong (Au et al., 2006; K. L. Chau, 1994; Corlett, 1999; Dudgeon & Corlett, 2004; Fung & Jim, 1993). However, other than several rough estimates of burnt areas in selected years (Fung & Jim, 1993; Marafa & Chau, 1999), a comprehensive burn area map for the region is currently lacking.

Figure 1.3: Villagers lighting fires near natural vegetation during local festivals. Photo taken from Starling Inlet, Hong Kong.

1.3.4.2 Wind

Strong winds represent another major disturbance in the forests of Hong Kong. Hong Kong sits within the Northwest Pacific tropical cyclone hotspot (Chand et al., 2022; Kossin et al., 2020). Between 1961 and 2020, an average of 6.08 typhoons occurs within 500 km of Hong Kong, predominantly between June and October (Hong Kong Observatory, 2023). Stronger typhoons that make landfall close to Hong Kong bring destructive winds and heavy rainfall to the territory. Even tropical cyclones of categories 1-2 on the five-point Saffir-Simpson scale bring sustained wind speeds of >125 km/h and could lead to defoliation, branch-breakage, bole-snapping, and uprooting of forest trees (Lin et al., 2020; Negrón-Juárez et al., 2014; Tanner et al., 1991). Tropical cyclones reportedly led to the removal of 34% and 23% of aboveground biomass in Mexican (Parker et al., 2018a) and Peurto Rican (J. Hall et al., 2020) forests, respectively. Large geographical discrepancies exist in forest resilience to tropical cyclones, with Taiwanese forests showing different patterns of damage in face of tropical cyclones of similar intensity (Lin et al., 2020; Mabry et al., 1998). Studies on the effects of typhoons on forests in Hong Kong and nearby Guangdong are scarce. The widespread destruction caused by Typhoon Mangkhut in 2018, the strongest tropical cyclone to affect Hong Kong in over 40 years, brought much needed attention to the issue (**Figure 1.4**). Abbas et al. (2020) provided a first quantification of forest damage after the event, finding that plantations and forests on south-facing slopes showed disproportionally large drops in Normalised Difference Vegetation Index (NDVI) between two relevant Landsat 8 scenes. In neighbouring Guangdong province, a field study conducted by Ni et al. (2021) found a higher susceptibility amongst old growth forests in Dinghushan Nature Reserve. Also using NDVI, Xu et al. (2021) found scattered urban trees to have suffered more damage during Typhoon Mangkhut and suggested that taller buildings partially protected trees from snapping and uprooting. The relationships between wind damage, background topography, and natural forests in forests restorations sites are, however, still poorly known.

Figure 1.4: Forests near Mui Tze Lam after Typhoon Mangkhut in 2018.

1.3.4.3 Landslides

Another disturbance that affects vegetation in Hong Kong is landslides. Landslides are failures of slopes along slip planes. The disturbance is estimated to affect 4% of the earth's terrestrial surface every century (Restrepo & Alvarez-Berríos, 2006). Landslides are highly destructive disturbances as they remove the topsoil layer along with the vegetation and arbuscular mycorrhizal network (**Figure 1.5**). In many cases, plants need to be reestablished through lengthy primary succession, especially on the crown of the landslide (L. Walker & Shiels, 2013). The rugged terrain of Hong Kong creates many opportunities for slope failures, usually after heavy rainfall (Ko & Lo, 2018; Lee et al., 2001) (**Figure 1.5**). Landslides receive much attention in the local research community due to the proximity of steep slopes to built-up areas. This includes the compilation of 110,000 landslides in the Enhanced Natural Terrain Landslide Inventory (ENTLI) by the Civil Engineering and Development Department (CEDD) of Hong Kong (Ho et al., 2009). Important factors that facilitate landslide occurrence include a >30° slope gradient, proximity to streams, and southern aspects (Dai et al., 2001; Ko & Lo, 2018; Haojie Wang et al., 2021). Historical deforestation and degradation of the natural vegetation also greatly increased landslide probability as forests tend to stabilise slopes (Dai et al., 2001; Haojie Wang et al., 2021). Several ongoing projects are investigating the recovery trajectory of landslides in Hong Kong (Pang et al., 2018) and potential solutions for targeted restoration (Law et al., 2023).

Figure 1.5: A landslide scar in Chek Keng, Hong Kong. Note the removal of topsoil with only small patches of remanent vegetation.

1.3.4.4 Droughts

Droughts represent another notable disturbance in wet tropical and subtropical forests. In wet biomes, low hydraulic safety margins of forest trees often mean that extended dry spells could cause widespread mortality either directly or due to secondary causes on weakened trees. Seasonal droughts are known affect forest restoration efforts in Hong Kong, especially on seedlings in degraded sites (Hau & Corlett, 2003). Notably, precipitation and typhoon landfall in Hong Kong are both correlated to El Niño Southern Oscillation (ENSO) cycle (Hong Kong Observatory, 2023; M. C. Wu et al., 2004; W. Zhou et al., 2012). Droughts related to ENSO cycles are known to impact many tropical forest ecosystems, inducing defoliation, branch shedding, and increased tree mortality (Holmgren et al., 2001; Miyamoto et al., 2021; Nunes et al., 2021). Some of these effects are presumably observable in Hong Kong but have not yet been systematically studied.

1.3.4.5 Low temperatures and frosts

Low temperatures and frosts also disturb vegetation in Hong Kong. Hong Kong lies on the boundary between subtropical and warm temperate biomes, with noticeable temperature gradients between the lowlands and mountaintops. In years with warmer winters, cold-sensitive tropical plants tend to move up the elevation gradient and invade montane forests. On the other hand, cold snaps caused by northernly winds in winter periodically cool mountaintops to freezing temperatures. These weather events were observed to selectively disturb tropical genera in the region (Abbas et al., 2017; Corlett, 1992; Dudgeon & Corlett, 2004). They also have a proportionately larger effect on exotic plantations. In particular, the cold snap in 2016 killed many *Acacia confusa* trees planted on the highest mountains in Hong Kong. The associated patterns of damage being dependent on elevation and forest type were clearly observable from satellite imagery (Abbas et al., 2017).

1.3.4.6 Pests and pathogens

Lastly, pests and pathogens also cause observable disturbances amongst forests in Hong Kong. While species-rich subtropical rainforests are resilient to large-scale diebacks caused by pests and pathogens, the same cannot be said for species-poor plantations. In Hong Kong, the Pinewood Nematode *Bursaphelenchus xylophilus*, which decimated widely planted *Pinus massoniana* in the late 1970s, represents the most prominent case of such disturbances (Corlett, 1999; Kishi & others, 1995). More recently, brown root rot caused by the fungus *Phellinus noxius* caused small-scale diebacks of a range of host tree species (Ribera et al., 2016) and the moth *Phauda flammans* induced dieback of *Ficus* trees (Lu et al., 2019).

1.3.5 Hong Kong as a case study for forest restoration and disturbances

Hong Kong provides a useful case study for forest restoration projects in the wet tropics and subtropics. Firstly, with the continuous deforestation and landscape degradation over thousands of years, Hong Kong acts as a benchmark for the “worst case scenario” in forest restoration (Abbas et al., 2016; Corlett, 1999; Zhuang & Corlett, 1997). If restoration strategies succeed in bringing forests back to Hong Kong, the same strategies are likely to work in regions with less severe environmental degradation (Hau et al., 2005). Secondly, compared to much of the wet tropics, Hong Kong has a long history of forest restoration. The British colonial government largely treated Hong Kong as a small trading port devoid of natural resources (Tsang, 2003). As a result, for over a century, land management has been centered around restoring forests for aesthetics, erosion control, water management, and biodiversity, with production only as a secondary objective (Corlett, 1999; Daley, 1965; Dunn, 1906). The >70 years of uninterrupted forest restoration since the second world war provides invaluable insights for land managers in other wet tropical or subtropical regions hoping to envision how restored forests would develop in the future (Abbas et al., 2016). Thirdly, restored vegetation in Hong Kong faces many commonly encountered disturbances across the wider tropics. The high population density of the city and the continued existence of rural villages mean that the area is an exemplar of a wildland-urban interface, with many of the associated patterns of disturbances (Curran et al., 2017; van Butsic et al., 2015). The presence of different vegetation types, topographical complexity, and its location in a typhoon hotspot provides opportunities to study how disturbances interact with various biophysical factors. Lastly, as a developed economy, there is sufficient demand and resources to justify the collection of environmental data. This includes long-running meteorological records, detailed geological maps, LiDAR scans, and full-territory aerial imagery periodically collected since 1963 (HK Lands Department, 2020). While not all of these resources are used in this thesis, these datasets could potentially answer a large number of research questions that would be difficult to investigate elsewhere.

1.4 New opportunities offered by remote sensing

Developments in remote sensing provide new opportunities for studying forest disturbances across previously unthinkable spatiotemporal scales. Early studies in disturbance ecology depend on field surveys across a limited number of designated plots (K. C. Chau & Marafa, 1999; Cremer et al., 1982; Dalling & Tanner, 1995; Guariguata, 1990; Morrison et al., 1995; Tanner et al., 1991; Uhl et al., 1988; L. R. Walker, 1994). Increased availability of remote sensing data created new possibilities for monitoring various aspects of disturbed vegetation. Firstly, many disturbances operate on very large spatial scales. For instance, the largest recorded tropical cyclone (Typhoon Tip) spans a diameter of 2200 km (Dunnavan & Diercks, 1980). To capture spatial patterns of resilience against disturbances, it is important to study these disturbances at large spatial scales. Many remote sensing technologies allow for large areas to be surveyed at relatively affordable costs (Franklin, 2013; Frolking et al., 2009; Sinha et al., 2015; Szpakowski & Jensen, 2019). Secondly, understanding disturbances requires measurements to be made at various times. For instance, estimating the burn severity of a fire requires measurements to be made before and after fires occur (Parks et al., 2014), and post-fire recovery requires long term monitoring after the actual fire event (Kurbanov et al., 2022; Szpakowski & Jensen, 2019). Many types of remote sensing data can be repeatedly collected at reasonable costs to capture changes over time. Even with certain caveats such as changes in atmospheric conditions, these datasets are generally comparable and could provide the necessary temporal depth for the study of long-term processes (J. D. Miller & Safford, 2012; Pérez-Cabello et al., 2021). A summary of the major types of remote sensing data used in forest ecology can be found in **Table 1.1**.

Carrier	Sensor	Resolution	Vegetation properties detected
Satellite (Frolking et al., 2009)	Multispectral imagery	Down to 0.5m	• Calculate vegetative indices (VIs) (e.g. NDVI) to quantify properties such as canopy greenness, chlorophyll content, and water content • Monitor temporal changes in the vegetation • Obtaining soil information
	Synthetic aperture radar (SAR)	L-band: 40m P-band: 200m X-band: 1m to 16m C-band: 5m x 20m	• Calculating average canopy height • Measuring average vegetative structure
	Light detection and ranging (LiDAR)	25 m (Dubayah et al., 2020)	• Canopy height • Full waveform data for canopy structure
	Hyperspectral imagery	30m	• Phenology and biochemical properties of vegetation
Aircraft or drones	Multispectral imagery	<10cm achievable (Tang & Shao, 2015)	• Calculate vegetative indices (VIs) (e.g. NDVI) to quantify properties (e.g. canopy greenness, chlorophyll content, and water content) • Monitoring temporal changes • Soil information
	Hyperspectral imagery	<0.5m achievable (Gonzalez-Dugo et al., 2015)	• Species classification and distribution • Phenology • Leaf traits and biochemistry
	Light detection and ranging (LiDAR)	Down to 1m (Dechesne et al., 2017)	• Canopy height (Individual tree crown) • Mapping canopy and understory structure
	Digital aerial photogrammetry	<0.5m achievable (Bohlin et al., 2012)	• Low-cost alternative to LiDAR in mapping canopy height

Table 1.1: Common remote sensing techniques used in forest ecology.

1.5 Thesis structure

In this PhD thesis, we aim to utilise remote sensing data to track forest resilience against fires and tropical cyclones. Specifically, we explored how these disturbances interacted with the wet subtropical restored vegetation in Hong Kong.

In **Chapter 2**, we reconstruct the fire history of Hong Kong using a 34-year Landsat imagery time series. We developed a pipeline to process hundreds of satellite multispectral imagery to allow for accurate burn area detection in areas with high cloud cover and rapid post-fire revegetation. The chapter aims to produce dated burn area polygons at 30 m ground resolution and estimate associated burn severity. These maps provide the background for studying fire dynamics in our study area. The chapter was submitted twice to *Remote Sensing of Environment*, but was rejected for the lack of cross-continental validation. The revised manuscript after addressing three rounds of reviewer comments has been published on *Remote Sensing* (A. H. Y. Chan et al., 2023).

In **Chapter 3**, we investigated into fire traps in degraded wet subtropical landscapes. In many wet biomes, early successional vegetation is more fire-prone than closed canopy forests. These positive fire-vegetation feedbacks can hinder forest restoration and trap landscapes in a degraded state. In the chapter, we leveraged the burn area maps produced in **Chapter 1** and a set of Landsat-based vegetation map time series to quantify different components of the fire trap in Hong Kong. Specifically, we investigated how vegetation type, ignition sources, and other factors contributed to variations in fire occurrence. We also identified the environmental and biophysical factors that determined the rate of post-fire recovery. The manuscript produced from this work has been submitted to the *Journal of Applied Ecology* and has received generally favourable reviewer comments. This thesis chapter is derived from the manuscript after addressing reviewer comments.

In **Chapter 4**, we describe a pipeline based on open-source computational fluid dynamics (CFD) software to model local near-surface wind speeds across the complex topography of Hong Kong. The modelled wind speeds were validated by anemometer measurements at 27 non-urban weather stations in the territory. We additionally set up our own anemometer to validate the modelled wind speeds on slopes. The chapter serves as a precursor to **Chapter 5**.

In **Chapter 5**, we studied the factors that affected forest resilience against tropical cyclones using a repeated LiDAR dataset and the wind maps produced by the pipeline detailed in **Chapter 4**. Specifically, we investigated into the patterns of damage casted by Typhoon Mangkhut in 2018, the strongest tropical cyclone to affect Hong Kong in over 40 years. The answered three research questions – (1) whether plantations were more susceptible to tropical cyclones than natural forests, (2) what were the factors that contribute to wind resilience amongst natural forest patches, and (3) how important strong winds and tropical cyclones were in defining long-term forest structure. We plan to submit the manuscript derived from the chapter for publication, with *Global Change Biology* as the target journal.

In **Chapter 6**, we provide a holistic discussion of the findings in this thesis. We also outline future plans on modelling changes in vegetation structure using the results from **Chapter 3** and further analyses of relationships between wind and forest structure based on results from **Chapter 5**.

1.6 Co-author contributions

The contents of this thesis represent my own work except for that described here or explicitly stated in the text. In **Chapter 2**, Alejandro Guizar-Coutiño and Michelle Kalamandeen assisted with the code in Google Earth Engine and reviewed the manuscript. In **Chapter 4 and 5**, Toby Jackson and E-Ping Rau provided supervision and guidance through the development of the CFD model and the subsequent analysis of the data. In **Chapter 4**, Ying Ki Law helped digitise the vegetation map developed by Ashworth et al., (1993), drafted **Table 4.1** of the chapter, and helped organising fieldwork in Hong Kong. Also in **Chapter 4**, Rocky Leung and Jess Chung participated in several field trips and helped setting up the anemometer on steep slopes.

Chapter 2: Reconstructing 34 Years of Fire History in the Wet, Subtropical Vegetation of Hong Kong Using Landsat

2.1 Abstract

Burn-area products from remote sensing provide the backbone for research in fire ecology, management, and modelling. Landsat imagery could be used to create an accurate burn-area map time series at ecologically relevant spatial resolutions. However, the low temporal resolution of Landsat has limited its development in wet tropical and subtropical regions due to high cloud cover and rapid burn-area revegetation. Here, we describe a 34-year Landsat-based burn-area product for wet, subtropical Hong Kong. We overcame technical obstacles by adopting a new LTS fire burn-area detection pipeline that (1) Automatically uniformized Landsat scenes by weighted histogram matching; (2) Estimated pixel resemblance to burn areas based on a random forest model trained on the number of days between the fire event and the date of burn-area detection; (3) Iteratively merged features created by thresholding burn-area resemblance to generate burn-area polygons with detection dates; and (4) Estimated the burn severity of burn-area pixels using a time-series compatible approach. When validated with government fire records, we found that the LTS fire product carried a low area of omission (11%) compared with existing burn-area products, such as GABAM (49%), MCD64A1 (72%), and FireCCI51 (96%) while effectively controlling commission errors. Temporally, the LTS fire pipeline dated 76.9% of burn-area polygons within two months of the actual fire event. The product represents the first Landsat-based burn-area product in wet tropical and subtropical Asia that covers the entire time series. We believe that burn-area products generated from algorithms like LTS fire will effectively bridge the gap between remote sensing and field-based studies on wet tropical and subtropical fire ecology.

2.2 Introduction

Fire regimes in natural ecosystems have changed drastically over the past half century. The fragmentation of vegetation, as well as anthropogenic fire suppression, has reduced fire occurrence in some regions (Marlon et al., 2012), while land clearance by fire, and the associated degradation of fire-resistant vegetation types, has increased fire frequency in other regions where natural fires were rare (Fernandes et al., 2011). In recent years, the feedback between fires and climate change has attracted much attention, with fires being recognized as a significant source of carbon emissions (Aragão et al., 2018; Silva et al., 2020), while changes in temperature, precipitation, and wind patterns under climate change in turn exacerbate extreme fire events (Abatzoglou et al., 2019). Given the importance of fires as disturbance agents, both locally and globally, various aspects in the vegetation-fire feedback, including fire susceptibility (K. L. Chau, 1994; Tien Bui et al., 2016), post-fire recovery trajectory (Johnstone et al., 2010; Kemp et al., 2016), and feedback direction/strength (Tepley et al., 2018), have been closely scrutinized. Understanding the influences of historical fire events on current vegetation composition and structure is essential for predicting how vegetation might respond to future fire regime shifts and managing existing landscapes in preparation for these changes.

Accurate burn-area (BA) maps are critical to research on fire regime shifts and fire-vegetation feedback. The groundwork for large-scale BA maps was laid down by products based on SPOT and ASTER optical imagery, such as L3JRC (Kevin Tansey et al., 2008) and GLOBSCAR (Simon et al., 2004). These products were largely superseded by products based on MODIS, which provided longer-running multispectral imagery with a high temporal resolution (1–2 days) (Chuvieco et al., 2019). In particular, MCD64A, developed by NASA (Giglio et al., 2018), and FireCCI51, developed by the ESA, (Lizundia-Loiola, Otón, et al., 2020) have been widely used in recent years. MCD64A1 has mapped burn areas over a 22-year period (2000–2022) at 500 m ground resolution by detecting the thermal signature of active fires and changes in surface reflectance each day. Temporal composites were built from multiple overlapping MODIS scenes. The spatiotemporal distribution of pixels experiencing large changes in surface temperature was then used to estimate burn probabilities. The probabilities were subsequently masked and refined to daily BA maps (Giglio et al., 2018). Similarly, FireCCI51 also combines thermal anomalies and surface reflectance detected by MODIS to create daily BA maps over a similar time frame. However, FireCCI51 differs from MCD64A1 in focusing specifically on growing active fire "seeds" using the NIR band, which produces BA maps with a finer 250 m ground resolution (Lizundia-Loiola, Otón, et al., 2020).

Several studies have used MODIS-based global BA products to analyze fire patterns on global-to-regional scales (Archibald et al., 2010; Chuvieco et al., 2020; Lizundia-Loiola, Pettinari, et al., 2020; Zheng et al., 2021), but the uptake of these products in the ecological community has been relatively slow. The commission and omission errors of existing global BA products typically exceeded 40% and 65%, respectively, with a significant discrepancy between different products (Luigi Boschetti et al., 2019; Franquesa et al., 2022; Humber et al., 2019; Padilla et al., 2015; Szpakowski & Jensen, 2019). For studies concerning total burn area or carbon emissions, these errors can be estimated and corrected, but for many ecological applications, these errors make it difficult for researchers to reconstruct the fire history of their areas of interest within a reasonable degree of certainty. The issue is further compounded by the low ground resolution (250–1000 m) of MODIS products, which does not relate well to field survey plots at sub-hectare spatial scales. As a result, the research on fire ecology continues to focus on single-fire events or a small handful of local fire scars, seldom combining field data with MODIS-based fire maps (Busby et al., 2020; Fernández-García et al., 2018; Kibler et al., 2019; Polychronaki et al., 2013).

In recent years, efforts in burn-area mapping have increasingly shifted to processing imagery of higher-resolution imagery provided by the Landsat and Sentinel satellite programmes. Successive Landsat satellites have provided nearly uninterrupted global multispectral imagery at ≤ 30 m ground resolution since 1984 for six wavebands, namely blue, green, red, near-infrared (NIR), and two shortwave infrared (SWIR) bands. The long mission time and high spatial resolution compared to MODIS allows for the fire history of landscapes to be comprehensively reconstructed. Several regional Landsat-based fire datasets have emerged in the past few years, mostly in dry Mediterranean and temperate biomes, with burn-area maps constructed in the US (Hawbaker et al., 2017; Vanderhoof et al., 2017), Australia (Goodwin & Collett, 2014), and Greece (Tompoulidou et al., 2016). The high spatial resolution and accuracy of Landsat-based BA maps have enabled a large body of fire-related research (Chuvieco et al., 2020), such as studies on fire frequency and severity trends (Abatzoglou et al., 2021; Daldegan et al., 2019; Gibson et al., 2020; Hagmann et al., 2021; Mallek et al., 2013; Wimberly & Reilly, 2007), fire-risk modelling (M. A. Cochrane et al., 2012), post-fire vegetation recovery (Bright et al., 2019; Fernández-García et al., 2018; Frazier et al., 2018), and post-fire community ecology (Mahood & Balch, 2019).

Despite these successes, there is a paucity of comprehensive Landsat-based BA maps in the wet tropics. The temporal resolution of Landsat satellites (16 days) is an order of magnitude lower than MODIS (1–2 days), making it impractical to grow burnt areas from active fires picked up by thermal bands of the Landsat sensor (Luigi Boschetti et al., 2016). Thus, Landsat-based algorithms rely exclusively on changes in pixel reflectance or texture for BA detection. In some biomes, this does not greatly affect fire scar detectability. For instance, with relatively slow revegetation, BAs in temperate and arid/Mediterranean biomes are often distinguishable for years after a fire (Luigi Boschetti et al., 2016; Bright et al., 2019). As such, Landsat BA mapping has become routine in these ecoregions (Bastarrika et al., 2011; Goodwin & Collett, 2014; C. Huang et al., 2009; Mallinis & Koutsias, 2012; Mitri & Gitas, 2004; Nelson et al., 2013). In tropical savannas, grasses readily resprout, but low cloud cover means that BAs are still easily mappable across a number of post-fire Landsat scenes (Bowman et al., 2003; Hudak & Brockett, 2010; J. Liu et al., 2018). However, in the wet tropics/subtropics, a high cloud cover (> 50%) often occludes Landsat imagery for months on end, leaving no more than a dozen of partially cloudless scenes each year (Brun et al., 2022). Coupled with rapid revegetation that obscures burnt patches within months (**Figure 2.3**), the task eludes many existing BA mapping approaches (Nelson et al., 2013). Several studies have attempted BA mapping in the wet tropics/subtropics using Landsat imagery, but these focus on pairs of pre-selected cloudless pre-fire and post-fire scenes (**Supp. Table A.1**). These single-scene algorithms are difficult to scale up as the effort to pre-select scenes increases markedly with the spatial and temporal breadth of the study. Additionally, in many regions of the tropics, it is not uncommon for all scenes in a year to be partially (> 30%) clouded, especially for years prior to the launch of Landsat 7 in 1999 (Asner, 2001). As a result, none of the single-scene studies have managed to create wet tropical BA databases at temporal scales comparable to those in temperate or Mediterranean biomes (**Supp. Table A.1**). An alternative to the single-scene approach is to include all partially cloudless scenes and perform pairwise change detection across all unmasked pixels across every time step. Using this approach, Roteta et al. (2019) successfully generated a single year (2016) BA product for Sub-Saharan Africa with Sentinel 2 data but have not, as yet, produced a time series (E. Roteta et al., 2019). A compromise between using single scenes and the full-time series is to create multiple seasonal or yearly composites to reduce the size of the dataset while being temporally scalable. To date, the two main studies published long-term Landsat BA products in the wet tropics, and both are based on yearly composites (Daldegan et al., 2019; Long et al., 2019). Daldegan et al. (2019) created yearly medoid composites from Landsat 5/7/8 data in the Cerrado–Amazon transitionary zone in Brazil (Daldegan et al., 2019). Spectral mixture analyses were then performed on the composites to separate burnt and unburnt pixels. The final product resulted in 32 yearly BA maps (1985–2017) of the study area. Long et al. (2019) estimated the burnt probabilities from Landsat 5/7/8 imagery and created yearly burn-probability composites (Long et al., 2019). A seed-growing algorithm was then used to create a global Landsat-based BA product. At the time of writing, the dataset covers 26 years (1989, 1992, 1995, 1996, 1998, and all years between 2000 and 2020) and is freely accessible through an FTP server. Despite these current advances in Landsat BA mapping in the tropics, neither study has estimated the time of fire, but instead provided annual maps of BA locations. Approximating the fire date through the date of detection provides crucial information for evaluating the relationship between weather patterns and fire susceptibility/post-fire recovery. Additionally, ecologists are often not only interested in the extent, but also the severity of the burnt patch. Common remotely sensed indices used to estimate severity, such as dNBR, RdNBR, and RBR (reviewed in (Szpakowski & Jensen, 2019)), are mainly based on single pairs of pre- and post-fire Landsat scenes. The modification and incorporation of burn severity into wet tropical BA maps would be invaluable to the ecological community.

In this study, we generated a Landsat-based BA time series based on a new pipeline—LTSfire (**Figure 2.2**). Specifically, we —

(1) Developed a preprocessing pipeline that is robust in regions affected by high cloud cover and haze.

(2) Minimized both commission and omission errors in burn-area detection and allowed small features to be accurately detected.

(3) Approximated the fire dates of detected burnt patches by preserving the dates of detection throughout the pipeline.

(4) Estimated burnt severity across pixels in the detected burnt patches.

The resulting product represents the first Landsat-based BA map in wet tropical/subtropical Asia that covers the entire Landsat 5/7/8 time series. It is also the first long-term Landsat BA map in the wet tropics/subtropics that estimated both BA detection dates and burn severity.

2.3 Materials and methods

2.3.1 Study area

The study was conducted in Hong Kong (22°16′8″N, 113°57′6″E) over an area of 1110 km^2. Despite its reputation as a densely populated city, Hong Kong has an extensive countryside with over 40% of the area protected as Country Parks (**Figure 2.1**). The climate is wet subtropical, with pronounced seasons and high cloudiness (68% average cloud cover) (Hong Kong Observatory, 2023). The region was historically covered by broad-leaved evergreen rainforest, but most of the natural vegetation was deforested and degraded after centuries of human settlement and agricultural activity (Dudgeon & Corlett, 2004). Under better protection following the second world war, the landscape gradually recovered into the mixture of grasslands, shrublands, and secondary forests seen today (Dudgeon & Corlett, 2004). Fires are common in Hong Kong, with the Fire Services Department (FSD) reporting over 1000 outdoor fires in 2018 alone, and these fires maintain grasslands and return forests to earlier stages of succession (Dudgeon & Corlett, 2004). Since natural fires are very rare under the wet subtropical climate of Hong Kong (1400–3000 mm rainfall per year), such fires are almost exclusively anthropogenic. Fire records are kept by the FSD and the Agricultural, Fisheries, and Conservation Department (AFCD), but detailed maps of fire extents have not been compiled.

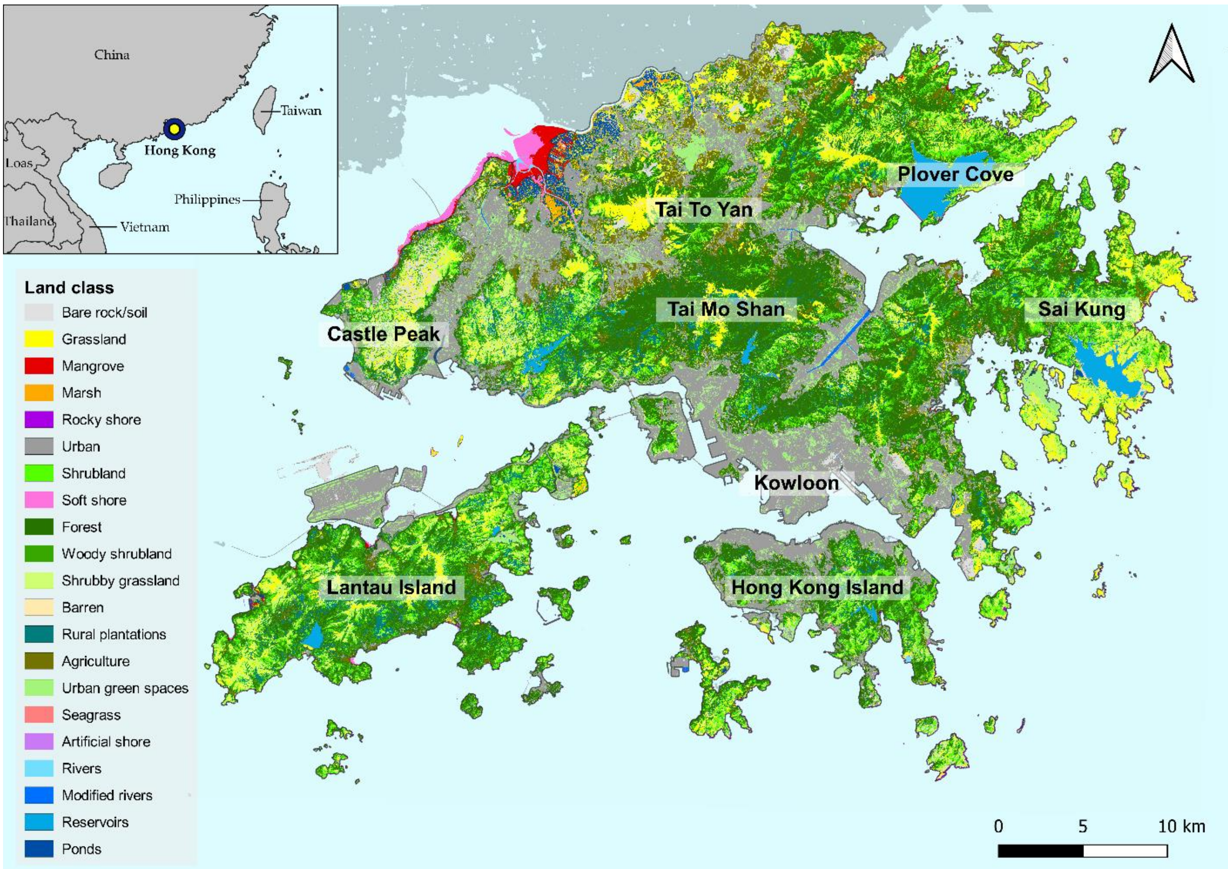

Figure 2.1: Map showing the study area of Hong Kong. The top left panel indicates the geographical position of Hong Kong overlayed on country boundaries from Natural Earth. The land classification raster is derived from Kwong et al. (2022).

2.3.2 Overview of the LTSfire pipeline

The LTS fire pipeline is composed of five main sections to create BA maps with dates of detection and burn severity (**Figure 2.2**). We first collated input data, including relevant Landsat imagery and training/validation datasets (**Section** Input data**2.3.3**). Then, the Landsat scenes were preprocessed into seasonal date-traceable composites (**Section 2.3.4**). Training data were extracted from the composites to build random forest Δτ regression models (**Section 2.3.5**). The models were later used to identify potential areas that resembled BAs, which were polygonised and iteratively merged (**Section 2.3.6**). Finally, burn severity of detected BA pixels was estimated by time series-relativized burn ratio (ts-RBR) (**Section 2.3.7**).

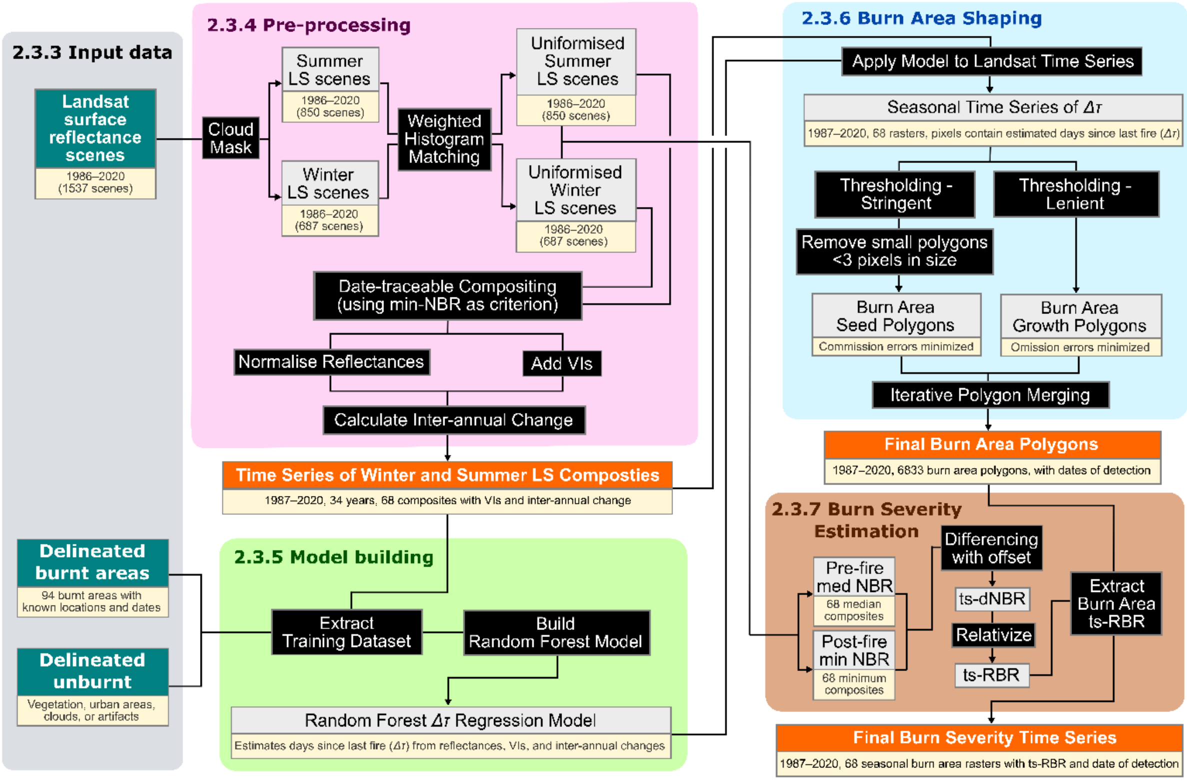

Figure 2.2: Flow chart visualizing the LTS fire pipeline. The green boxes indicate input datasets; black boxes represent actions taken; grey boxes signify intermediate products; and orange boxes show end products. Numbering corresponds to the relevant section in the methods.

2.3.3 Input data

2.3.3.1 Known burnt and unburnt area

A total of 94 known burn areas dating from 1988 to 2018 were used to train a regression model and validate BA maps. The Fire Services Department (FSD) provided a list of all 2036 reported fire events of 2017 and 2018. The database included the area burnt (in m^2), date the fire was reported, and the approximate location in Universal Transverse Mercator (UTM) coordinates or nearest lamp post. Most of these fires were small, so we mainly focused on features > 4000 m^2 (covering at least 4–5 Landsat pixels). In addition to the FSD records, we obtained a list of years and UTM coordinates for all major (>100 ha) fires between 2010 and 2017 from the Agricultural, Fisheries, and Conservation Department (AFCD). No exact fire dates were provided for this database, but the fires were significant enough so that fire dates could typically be found in local newspaper articles. Based on both the FSD and AFCD records, we manually delineated 75 burnt patches on high-resolution (<3 m) satellite images provided by Google Earth and Planet (**Figure 2.3**). When delineating the patches, we followed Stage 2 protocol outlined by the CEOS Land Product Validation (LPV) subgroup (L Boschetti et al., 2009; Franquesa et al., 2022). In particular, we checked images before and after the fire to ensure that the patch was not caused by earlier fire events. As fire dates were provided by FSD and AFCD, each polygon was associated with the exact fire data instead of temporal ranges between two images. Patches that were not clearly visible on the high-resolution satellite imagery were excluded. Since one of the aims of the pipeline is to create BA time series that spans the entire Landsat dataset, we additionally included 19 older burnt patches between 1988 and 2003 for training and validation. The UTM coordinates and fire dates of these patches were described in two local fire studies (W.-W. E. Chan, 2005; K. L. Chau, 1994). Neither Google Earth nor Planet data was available for these patches, so manual delineation was carried out on Landsat scenes. We recognize that CEOS LPV recommends having higher-resolution imagery when creating validation datasets, but we believe that it is still valuable to include validation data from the Landsat 5 era to test pipeline applicability across imagery collected by different Landsat sensors.

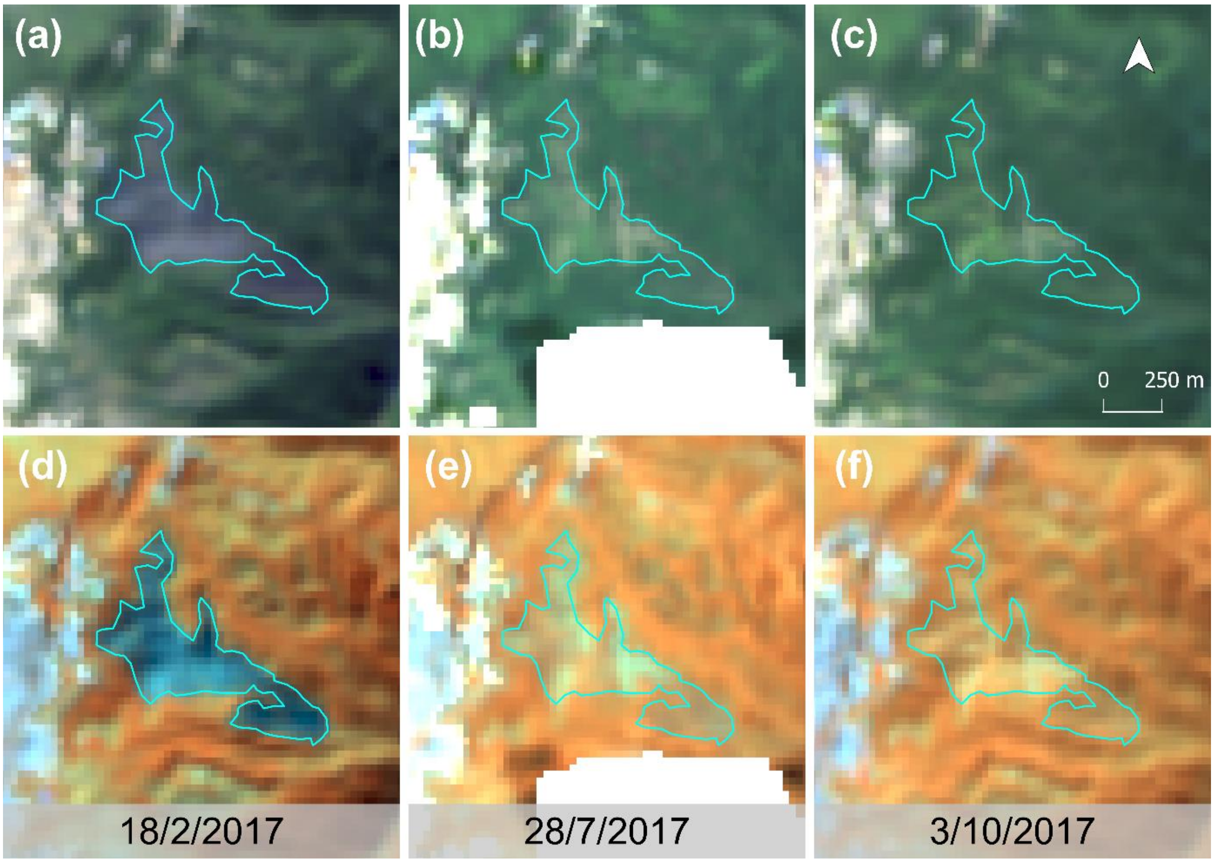

Figure 2.3: A burnt patch in degraded shrublands near Tai To Yan, Hong Kong (22°27′15.51″N, 114°6′12.55″E) demonstrating the transient nature of local BAs. The fire broke out on 14/2/2017, according to Fire Service Department records, and was manually delineated on high-resolution Google Earth satellite imagery (light blue polygon). The patch was clearly visible on the Landsat scene captured shortly after the fire (18 February 2017) but rapidly revegetated and became undistinguishable after a few months (28 July 2017 and 3 October 2017). Panels (a–c) shows true colour RGB imagery recreated from the Landsat scenes, while panels (d–f) show NIR band as red, SWIR1 band as green, and SWIR2 band as blue. Note the importance of SWIR bands, which is used to calculate the normalized burn ratio (NBR), in enhancing the contrast of burnt patches.

An additional 173 polygons were drawn to delineate unburnt pixels. Based on the premise that repeated burns within a year is rare, 94 of these polygons were derived from the same locations as the known burnt patches, but one season before the fire occurred. The remaining 79 polygons were urban areas and dense forests along with clouds and artifacts on the Landsat min-NBR composites. Together, these polygons cover a wide range of unburnt features, which is critical for accurate burn-area mapping (Franquesa et al., 2020).

2.3.3.2 Landsat 5, 7, 8 Surface Reflectance (SR) Scenes

Landsat 5 ETM SR, Landsat 7 ETM+ SR, and Landsat 8 OLI/TIRS SR scenes between 1986 and 2020 covering the study area were obtained through Google Earth Engine (GEE). Wavebands that were not shared between Landsat missions (e.g., the ultra-blue band in Landsat 8) were removed. The scenes already underwent basic radiometric/atmospheric correction.

2.3.4 Pre-Processing

2.3.4.1 Cloud Masking and Sorting by Season

Pixels affected by clouds in the Landsat SR scenes were masked using the cloud and cloud shadow bitmasks provided by GEE. As a fail-safe, we additionally applied a brightness threshold based on the red, green, and blue (RGB) bands to remove remaining clouds. The bands were chosen since visible light is less likely to penetrate clouds. Pixels were masked out if any one of the three bands had a reflectance > 0.2. A total of 1297 scenes with no clear pixels were removed. The remaining scenes were then sorted by season. A total of 850 summer scenes (March–October) and 685 winter scenes (November–February) from the 1986–2020 period—each covering an area of 2952 km^2—were analyzed separately to maximize the probability of detecting rapidly revegetating burnt patches under pronounced seasonal effects.

2.3.4.2 Weighted Histogram Matching to Uniformize Landsat SR Scenes

The Landsat SR scenes were uniformized by a novel weighted histogram matching approach to minimize inter-scene differences caused by haze and changing incident sunlight (weighted histogram matching, **Figure 2.2**). We first grouped the cloudless Landsat SR scenes into five seven-year image collections (1986–1992, 1993–1999, 2000–2006, 2007–2013, 2014–2020) and created a median composite for each collection on GEE. These composites were then used as “references” to uniformize individual Landsat SR scenes. Multiple references were used to avoid uniformizing recent Landsat scenes with references from another era. We specifically chose this time interval (seven years per composites) as it provided enough cloudless scenes to create stable composites of Hong Kong while still being able to reflect decadal changes in vegetation structure. Since Hong Kong has a high cloud cover (68%) (Hong Kong Observatory, 2023) and has recently experienced relatively drastic changes in vegetation structure (Abbas et al., 2016), we believe that the seven-year benchmark should generally be robust enough for other wet tropical or subtropical regions. Each Landsat SR scene was paired with two reference composites according to the date of capture. For instance, a scene taken on 24 July 2013 was paired with the 2007–2013 and 2014–2020 summer reference composites. We then performed histogram matching using the *histMatch* function in the *RStoolbox* package (version 0.2.6)(Leutner et al., 2019) in R-4.1.0 (R core team, 2021) to match each scene with the two paired references to create two matched rasters. The *histMatch* function compares the distributions of pixel brightness (histograms) of the source raster with the reference. It then makes adjustments to the brightness of the source raster such that the histogram matches that of the reference. The six bands were matched separately to correct systematic differences in reflectance ratios between different bands. Since urban areas and water bodies were often highly variable from scene to scene, non-vegetated pixels were masked out before matching. A weighted average was then taken between the two histogram-matched rasters based on time difference between the scene and the median date of the two references. This created a uniformized Landsat SR scene that was more inter-comparable with other uniformized scenes. Weighted histogram matching was repeated across all scenes to create 1535 uniformized Landsat SR scenes (865 summer and 685 winter).

2.3.4.3 Date-Traceable Compositing (Using Min-NBR as Criterion)

The uniformized Landsat SR scenes were distilled into 35 summer and 35 winter composites over the 35-year study period by date-traceable min-NBR compositing (date-traceable compositing, **Figure 2.2**). We generated seasonal composites to increase the signal-to-noise ratio and reduce data volume by selecting the pixel in the season that most resembles burn areas. We used minimum normalized burn ratio (min-NBR), based on the NIR (0.77–0.9μm) and SWIR2 (2.08–2.35μm) bands, as the compositing criterion. The index is chosen for its ability to identify pixels that resemble burnt patches (Szpakowski & Jensen, 2019).

$$\text{NBR} = (\text{NIR} - \text{SWIR2})/(\text{NIR} + \text{SWIR2}) \tag{1}$$

For each pixel, we identified the scene in the season with the lowest NBR. We then transferred the reflectance of the six Landsat bands to the seasonal composite. We kept the date of capture and stored it as an extra seventh band. This allowed us to build regression models on burnt-area age using our training dataset and predict fire dates within seasonal composites in later stages of the pipeline (Sections 2.3.5 and 2.3.6 in **Figure 2.2**).

2.3.4.4 Vegetation Indices (VIs), Normalization, and Inter-Annual Changes

Several additional steps were taken to preprocess the seasonal composites to suppress both commission and omission errors in BA detection. Seven vegetation indices (VIs), namely the Burned Area Index (BAI), Mid-Infrared Burn Index (MIRBI), Normalized Burn Ratio (NBR), Enhanced Vegetation Index (EVI), Normalized Difference Vegetation Index (NDVI), Simple Ratio (SR), and Soil Adjusted Vegetation Index (SAVI) were added to the seasonal composites. These VIs utilize NIR and/or SWIR bands to highlight fire-affected regions (**Figure 2.3**) and have been shown to improve separability of burnt patches in the wet tropics (Penha et al., 2020). Additionally, the six Landsat wavebands were normalized by dividing them with the average reflectance of the same pixel as suggested by Wu (2004) and Chan et al. (2021) (A. H. Y. Chan et al., 2021; C. Wu, 2004). Finally, a distinctive feature of burn areas is the sudden change in spectral features from pre-fire vegetation and post-fire patches (Chuvieco et al., 2019; Gaveau et al., 2021). Hence, in addition to current-year data, inter-annual changes were calculated by subtracting the reflectance and VIs of the previous year from that of the current year.

2.3.5 Model Building

We built random forest (RF) regression models to detect burn area from remotely sensed data (model building, **Figure 2.2**). The RF regression models were built using the *randomForest* package (version 4.6-14) (Breiman et al., 2018) in *R-4.1.0* (R core team, 2021) with ntree = 500 and mtry = 5. The explanatory variables of the models were normalized reflectance, VIs, and associated interannual changes. The response variable was the estimated number of days since the last fire ($\Delta\tau$), ranging from 0 to 365 days. The model took the form:

Days since fire ($\Delta\tau$) ~ reflectances (6 bands) + VIs (7 indices) + changes (6 bands, 7 VIs)

We chose the number of days between the date of detection and the known fire date ($\Delta\tau$) as the response variable, since it carries more information than a simple binary fire/non-fire variable: the long return time of Landsat and high cloud cover means that many known burnt areas were only detected from space months after the fire event, by which time they were partially revegetated. $\Delta\tau$ served as a useful proxy for pixel resemblance to burnt areas. A smaller $\Delta\tau$ indicated higher pixel resemblance to burnt areas, while a larger $\Delta\tau$ indicated resemblance to fully revegetated or unburnt pixels. For pixels in the 94 known burn areas, we calculated $\Delta\tau$ and extracted the 26 explanatory variables from the date-traceable Landsat composites. For pixels in the 173 unburnt polygons, we extracted the 26 explanatory variables and assigned pixels with a $\Delta\tau$ of 365 days, which is the largest value of $\Delta\tau$ a known BA pixel could take (i.e., a fire broke out in the first day of a season but was only detected in the last day of the next season) and an interval long enough for optical properties of BAs to recover (**Figure 2.3**).

To estimate the accuracy of the LTS fire product the extracted data were randomly split into 10 folds for cross validation. Since there were way more unburnt than burnt pixels, we performed stratified random sampling in each fold to ensure that the ratio between unburnt and burnt pixels was capped at 1.5. This prevented extreme class imbalances from biasing the model predictions (Khoshgoftaar et al., 2007). In each of the 10 iterations, 9 out of the 10 folds were used to train an RF model. The remaining fold was kept unseen throughout the pipeline and was only used to validate the final burn-area map produced after shaping burn-area polygons (burn-area shaping, **Figure 2.2**). When creating the 10-folds, pixels extracted from the same polygon were always grouped into the same fold. This ensured that the cross-validation was always carried out across sites. In other words, if pixels from a BA polygon were used to build the fire map, we would avoid using other pixels from the same polygon to validate the results. We trained 10 RF models from the 10-folds, which were passed onto the next stage of the pipeline. Finally, to assess whether the preprocessing pipeline improved accuracies in burn-area detection, we repeated the 10-fold cross validation exercise and trained RF models using non-uniformized/normalized Landsat SR bands and VIs as inputs (referred as no-preprocessing, or NPP below).

2.3.6 Burn Area Shaping

2.3.6.1 Applying Models to Landsat Time Series and Thresholding Δτ Rasters

The RF models were then used to predict $\Delta\tau$ from the time series of seasonal LS composites. Each model generated a seasonal time series of 68 $\Delta\tau$ rasters with pixel values ranging from 0 to 365 (**Figure 2.4**).

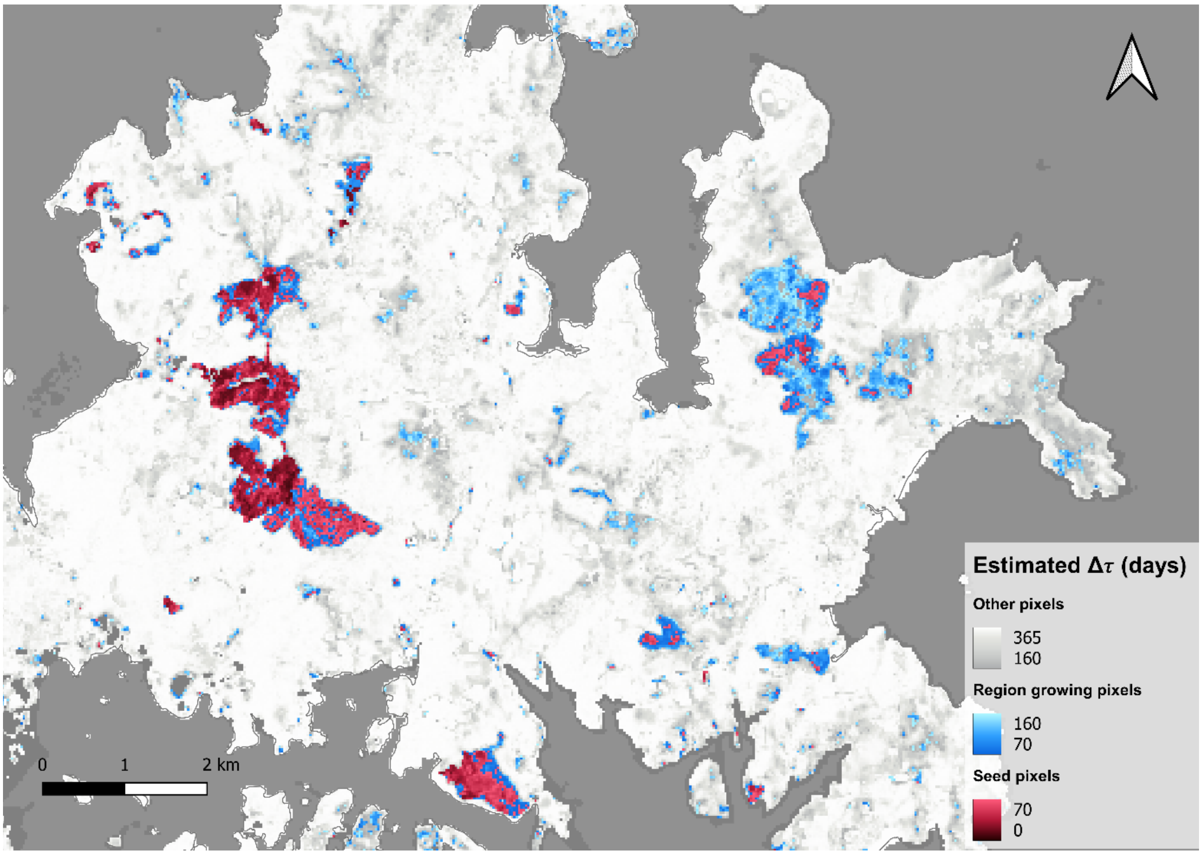

Figure 2.4: Raster showing estimated $\Delta\tau$ of Sai Kung Peninsula, Hong Kong (22°25′14.4″N, 114°19′51.4″E) for the summer of 1996. We trained a Random Forest model that estimated $\Delta\tau$ from bands in the seasonal min-NBR composites. $\Delta\tau$ is a proxy for burn area resemblance. A lower $\Delta\tau$ indicates closer resemblance to burn-area pixels, while a higher $\Delta\tau$ indicates closer resemblance to unburn pixels. Red and blue areas indicate the seed and growth pixels after thresholding.

Burnt and unburnt pixels were not easily separable by a single threshold on $\Delta\tau$, so burn-area polygons were created by twice thresholding the $\Delta\tau$ rasters followed by seed-growing (thresholding, **Figure 2.2**). As shown in **Figure 2.4**, some unburnt pixels often had lower $\Delta\tau$ than some of the less severely burnt pixels in BAs. Using a single threshold would either omit a substantial number of BA pixels or mistake many unburnt pixels as burnt (**Figure 2.5**). Hence, a two-phase region-growing algorithm, similar to that described in Bastarrika et al. (2011), was adopted (Bastarrika et al., 2011). In the first phase, two thresholdswere applied — one stringent and one lenient — on the estimated $\Delta\tau$ rasters. This created two sets of polygons: the seed polygons minimized commission errors by keeping only the most severely burnt pixels (red, **Figure 2.5**); the growth polygons minimized omission errors by including pixels that resembled burnt patches (blue, **Figure 2.5**). In the second phase, we removed small-seed polygons (less than three pixels in size), which often represented artifacts (Long et al., 2019), then overlaid the two sets of polygons and grew the seeds with intersecting growth polygons. Since most burnt patches would at least contain a few severely burnt-seed polygons that unburnt patches were unlikely to possess, and less severely burnt pixels would be captured by the growth polygons, the algorithm boosts both specificity and sensitivity in BA detection (Bastarrika et al., 2011). The two thresholds adopted in this study were derived from the training datasets. For each iteration in the 10-fold cross validation, we performed a smaller nine-fold cross validation within the training dataset, creating nine RF models that estimated $\Delta\tau$ from the holdout. We then applied thresholds ranging from 0 days to 365 days on the estimated $\Delta\tau$ and plotted the error-threshold curves for (1) pixel-omission error, (2) patch-omission error, and (3) pixel-commission error (**Figure 2.5**). The stringent threshold was set after the sharp drop in site-omission errors, while the lenient threshold was set after the drop in pixel-omission errors. We observed that the error-threshold curves were similar across different folds, so for simplicity, we set a single set of stringent (70 days for summer; 60 days for winter) and lenient (160 days) thresholds across all 10 folds (**Figure 2.5**). Thresholds were chosen by qualitative assessment of the error-threshold curves in this study, but these thresholds could potentially be derived mathematically in the future.

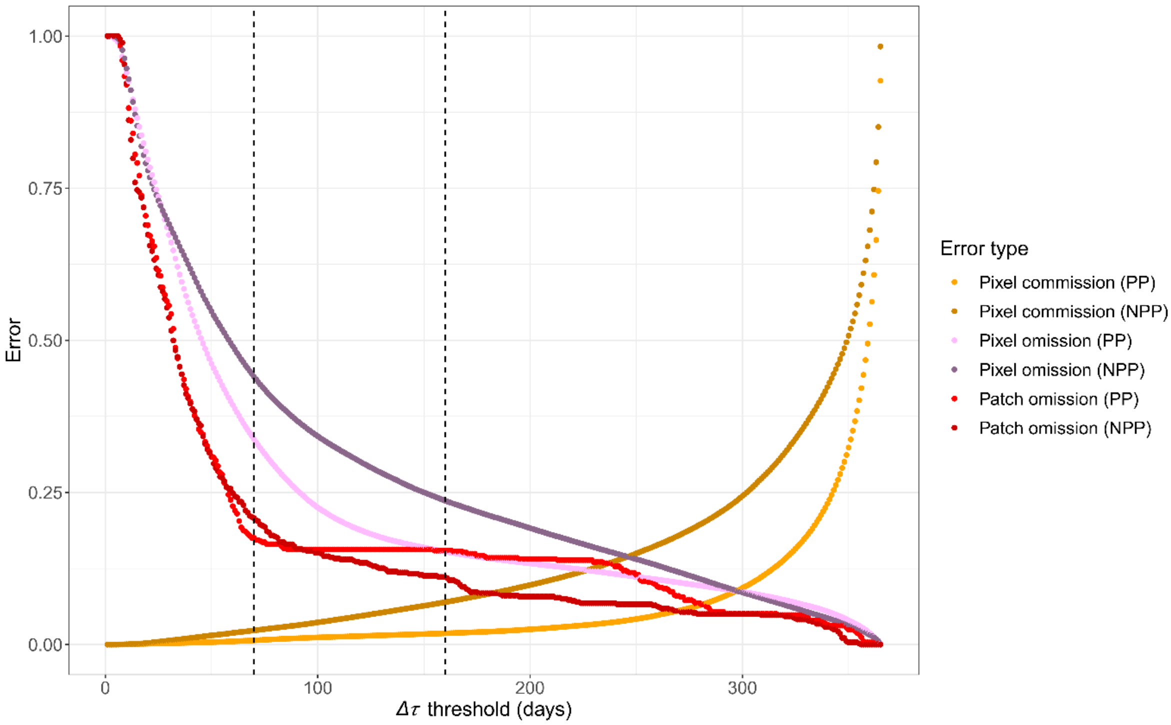

Figure 2.5: Effects of varying the $\Delta\tau$ threshold of summer pixels. $\Delta\tau$ is the predicted time interval between a fire and date of detection from Landsat, which acts as a proxy variable for burn-area resemblance. A lower $\Delta\tau$ indicates closer resemblance to burn-area pixels, while a higher $\Delta\tau$ indicates closer resemblance to unburn pixels. We trained random forest (RF) models that predicted $\Delta\tau$ from either (1) Landsat data that went through the entire preprocessing pipeline (PP) or (2) reflectance/VIs that had not underwent uniformization by weighted histogram matching (NPP). Different thresholds were applied to convert the continuous $\Delta\tau$ to binary fire/non-fire predictions. Errors of commission (unburnt pixels misclassified as burnt), pixel omission (proportion of burnt pixels missed), and patch omission (proportion of known burnt patches that had < 6 correctly classified pixels) were calculated. The vertical dash lines represent the thresholds (70/160) we adopted to seed and grow fire scars in LTS fire.

2.3.6.2 Iterative Polygon Merging

BA polygons over the 34-year study period were iteratively merged to create a single shapefile with a single dated polygon per BA. Despite quick vegetative recovery in the wet tropics/subtropics, it is not uncommon for the same burnt patch to be detected across multiple seasons, with complex overlapping of polygons. To prevent repeated observations from erroneously inflated estimated burn area, polygons needed to be appropriately dated and merged. **Figure 2.6** shows the decision tree used to handle seed and growth polygons based on two criteria: seed detection date (T) and seed area (A). We used attributes from seed polygons rather than growth polygons as merging criteria, since seed polygons represent areas with high confidence in detection and were less affected by artifacts. The seed-detection date (T) was calculated by taking the earliest date of detection amongst encapsulated pixels; the seed area (A) was the area of the entire seed polygon (**Figure 2.6**). For each growth polygon, we first checked whether it contained seed polygons from the same season. If it did not, we checked whether it intersected with polygons from the previous season. Growth polygons that do not intersect with seed polygons of the same season or merged polygons from last season were discarded (rightmost branch, **Figure 2.6**). Growth polygons that only intersected with merged polygons from last season often represented genuine burnt patches, though many were not fully detected last season due to cloud occlusion or gaps between Landsat 7 scan lines. Hence, we merged these polygons together and adopted the seed date and seed area of polygons from last season (second branch from the right, **Figure 2.6**). For growth polygons that contained seed polygons from the same season, we first merged the growth polygons with the seed polygons. The resulting polygon took the date and area from the seed polygon. If the growth polygon contained more than one seed polygons, we took the date from the largest seed polygon and the area by summing areas of all intersecting seed polygons (black box after first split, **Figure 2.6**). We then checked whether the polygon overlaps with polygons from last season. If it did not, the feature likely resulted from a new fire this season, so we kept it as a separate polygon (third branch from the left, **Figure 2.6**). If it did, the polygon either resulted from two fires at close proximity or was part of a burnt patch from last season. We did not have enough information to separate the two scenarios, so we opted for an area-based approach to ensure that the dates of large patches would not be unduly dragged behind by small fires or artifacts. If the polygon from this season carried a significantly (> 50%) larger seed area, we merged the polygons and adopted the new seed date and area (leftmost branch, **Figure 2.6**). Otherwise, we still merged the polygons but adopted the date from the largest overlapping polygon from the last season and the seed area from all overlapping polygons from last season (second branch from the left, **Figure 2.6**). Once all polygons from a particular season were sorted and merged following the criteria set out by **Figure 2.6**, we moved on to the next season. By iteratively adding polygons from all 68 seasons, we condensed all features into a single vector layer with overlapping features ± 1 season apart merged, and fire date estimated for each feature. In our validation exercise, iterative polygon merging was repeated 10 times for both the preprocessed and no-preprocessing datasets, creating 20

LTS fire maps. All steps were carried out in *R-4.1.0* with polygons merged using the *sf* package (version 1.0-1) (Pebesma, 2018; R core team, 2021).

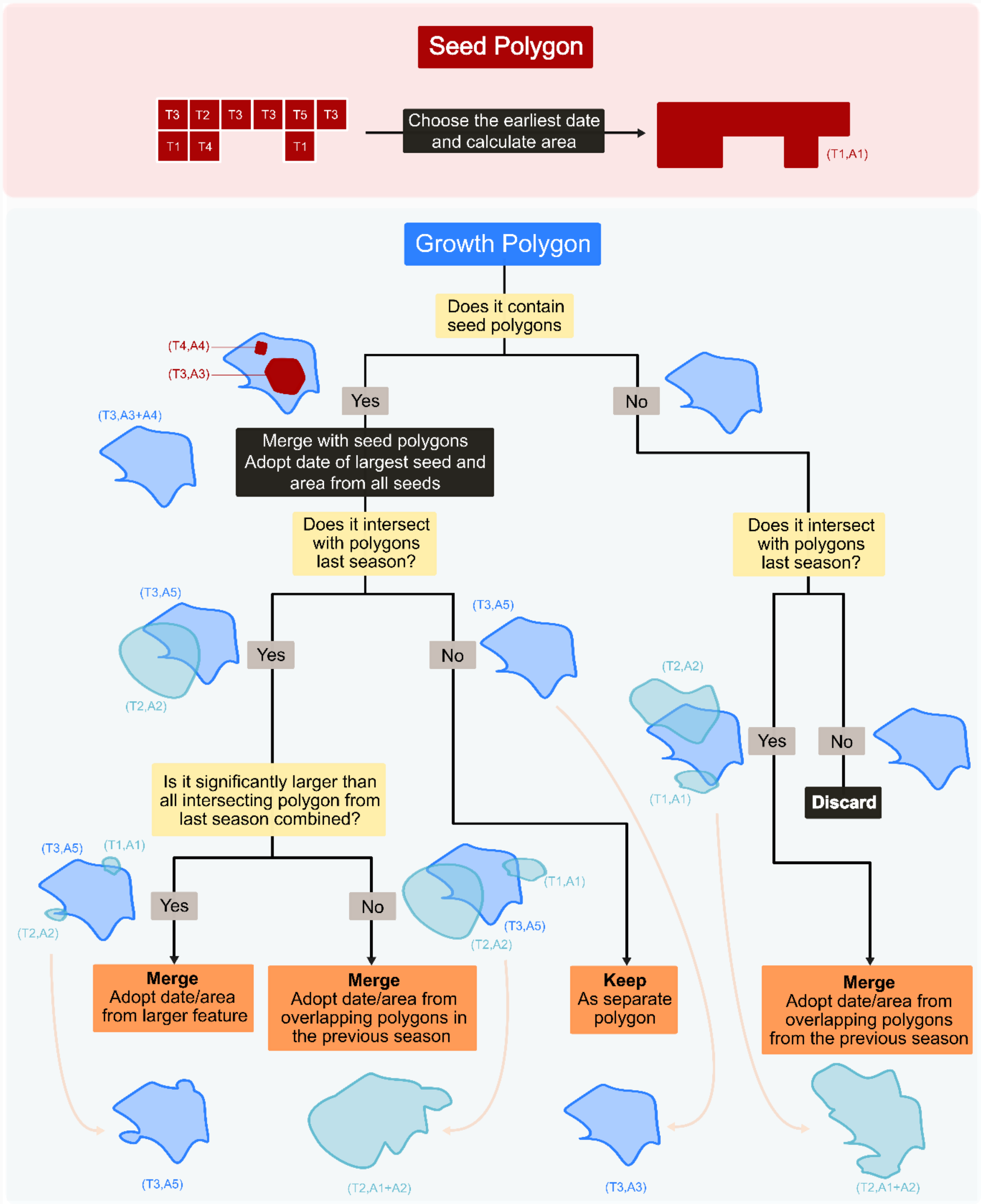

Figure 2.6: Decision tree for iterative polygon merging based on the date (T) and area (A) of seed polygons.

2.3.7 Burn Severity Estimation

The burn severity of pixels in the burn-area polygons were estimated by a modified version of Relativized Burn Ratio (RBR) described in Parks et al. (2014) (Burn severity estimation, **Figure 2.2**).

The existing RBR described by Parks et al. (2014) is calculated in three steps based on a pair of Landsat scenes captured before and after the fire.

$$NBR = (NIR - SWIR2)/(NIR + SWIR2) \quad (1)$$

$$dNBR = (NBR_{prefire} - NBR_{postfire}) \times 1000 - dNBR_{offset} \quad (2)$$

$$RBR = dNBR/(NBR_{prefire} + 1.001) \quad (3)$$

The $dNBR_{offset}$ term represents the change in NBR unrelated to fire and is usually estimated from pixels outside the burn area. Other terms are self-explanatory. In this study, we kept the general structure of the equations but replaced the terms in (2) and (3) to create the time series Relative Burn Ratio (ts-RBR), a new variant of RBR derived from multiple, instead of single, pre- and post-fire scenes. This is critical in our wet subtropical study area as cloudless scenes capturing the entire landscape pre- and post-fires were often unavailable. An approach that calculates burn severity by combining information from multiple overlapping scenes is, therefore, needed.

$$ts\text{-}dNBR = (NBR_{med\ prefire} - NBR_{min}\ postfire) \times 1000 - dNBR_{med\ min\ offset} \quad (4)$$

$$ts\text{-}RBR = ts\text{-}dNBR/(NBR_{med\ prefire} + 1.001) \quad (5)$$

For pre-fire conditions, we replaced the $NBR_{prefire}$ term with the median pre-fire NBR ($NBR_{med\ prefire}$) calculated across all uniformized Landsat scenes (Section 2.3.4, **Figure 2.2**) in the season before the fire. We then replaced the $NBR_{postfire}$ term with the minimum NBR ($NBR_{min\ prefire}$) across all uniformized Landsat scenes in the two seasons after the date of detection. The minimum was taken to prioritize the pixels showing the highest burn severity over those recorded after the patch starts to revegetate. An issue with differencing $NBR_{med\ prefire}$ and $NBR_{min\ postfire}$ is that the pre-fire median is expected to be larger than the post-fire minimum, resulting in overestimated burn severity. This was accounted for by adjusting the $dNBR_{offset}$ term, which now represents the mean difference between NBR_{median} and $NBR_{minimum}$ amongst unburnt pixels. Different $dNBR_{offset}$ values were used for the three vegetation types (grasslands, shrublands, forests) based on a Landsat-based vegetation map time series of the area (**Appendix B:**). A comparison was made between the ts-RBR across grasslands, shrublands, and forests to assess whether the approach properly relativized burn severity across various vegetation types. We did not conduct field surveys to validate the burn severity estimated by ts-RBR, but mathematically, ts-RBR is near-equivalent to RBR and is expected to perform similarly as RBR.

2.3.8 Comparison with Other Burn Area Products

The accuracy of the LTS fire map and three global BA products (MCD64A1 version 6, FireCCI51, and GABAM) were assessed by comparing detected BAs with known fire/non-fire polygons (see **Section 2.3.3**). We polygonised and downloaded all three datasets from Google Earth Engine and the GABAM FTP server. The attributes of polygon contained estimated fire date (for MCD64A1 and FireCCI51) or year (GABAM). We overlaid the detected BA polygons onto the known fire/non-fire polygons delineated based on government fire records (**Section 2.3.3**) and analyzed the degree of overlap. For LTS fire, since all the known fire/non-fire polygons were used to train the final product, we instead carried out 10-fold cross-validation using LTS fire maps built from different subsets of the training data (see **Section 2.3.5**). In other words, we overlaid the set of validation polygons on the version of the LTS fire map built from an RF model that was not trained by pixels in the validation polygons. Since estimated fire dates were not always accurate, especially for the temporally coarse GABAM dataset, we matched features that were ± 1 year apart. We then calculated site omission (proportion of known BA polygons completely omitted), area omission (proportion of burnt area omitted), area commission (proportion of unburnt area mistaken as burnt patches), and overall accuracy (proportion of correctly classified area) from the confusion matrix. Additionally, we investigated into how accurately the iterative polygon merging algorithm dated the LTS fire polygons by plotting a histogram showing the difference between LTS fire estimated date of detection and actual fire date.

Apart from comparing burn-area products with a small number of manually delineated fire/non-fire polygons, we also evaluated the LTS fire dataset through a full intercomparison with established global burn-area products. We followed the protocol of matching features dated ± 1 year from each other. For GABAM, no fire dates were estimated, so we dated the features to the middle of the year and matched LTSfire features dated ± 365 days from the 1st of July. Additionally, at the time of writing, GABAM only included several scattered years before 2000, making it difficult to accurately match features with LTS fire. Hence, we focused our comparison on years after 2001. For each pairwise comparison between LTS fire and existing burn-area maps, we tallied the number of overlapping and non-overlapping features to obtain feature agreement. We also calculated the overlapping and non-overlapping area to get area agreement.

Finally, we used videos, figures, and graphs derived from the LTS fire map to visualize the seasonal-to-decadal trends in fire occurrence across Hong Kong. We created a time-lapse video that plots LTS fire polygons against yearly Landsat median composites at the estimated date of detection. The Temporal Controller functionality in QGIS 3.18 (QGIS Development Team, 2021) was used to date vector and raster datasets, with the output converted to .mp4 format with FFmpeg (Tomar, 2006). The LTS fire map was also used to provide a holistic overview of the fire regime of the study area. We investigated the change in burn area between 1987 and 2020, analysed seasonal fire prevalence, and tallied the number of times each pixel burnt throughout the study period.

2.4 Results

2.4.1 Validation with Known Burnt Patches

LTS fire with the full pre-processing pipeline had the highest overall accuracy and lowest omission errors amongst the burn-area products compared (**Table 2.1**). The full LTS fire map detected 96.8% of all validation burn-area polygons and 88.8% of the known burnt area. The Landsat sensor type does not seem to significantly affect burn-area detection. Lower-area omission errors were observed before the launch of Landsat 8 in 2013 (5.6%) or before the launch of Landsat 6 in 1999 (6.3%). The algorithm misclassified 2.42% of the unburnt pixels. It is important to note that out of the 173 non-fire polygons, 94 were created by encircling pixels a few months before fires broke out (pre-fire). These polygons could easily be misclassified if the fire events were misdated during iterative polygon merging. If these polygons were excluded, errors of commission were very low (0.5% by area). If we adopted a less rigorous preprocessing pipeline and skipped weighted histogram matching (no pre-processing, **Section 2.3.4**), commission errors slightly increased and omission errors approximately doubled (**Table 1.1**). GABAM, a Landsat-based global burn-area product, detected 43.5% of the known burnt patches, or 50.7% of the burnt area in the validation dataset. A higher site omission than area omission indicates that the dataset disproportionally omitted smaller patches. The errors of commission were low overall (1.2% by area) but higher than the two LTS fire datasets if we excluded pre-fire polygons prone to misdating (1.18%). The two MODIS-based burn-area products generally had very high omission errors (**Table 1.1**), likely due to the low spatial resolution of the source data, while commission errors were negligible (0%) for both datasets.

Table 2.1: Accuracies of LTS fire and existing global burn-area products. The burn-area maps were compared with 94 known burn-area polygons and 173 unburnt polygons. Site omission errors refer to the proportion of undetected burn-area polygons (no overlap at all); area omission errors refer to the proportion of burnt area omitted; commission errors refer to the proportion of unburnt area misclassified as burnt; and the overall accuracy refers to the overall proportion of correctly classified area. Numbers representing the highest accuracy or lowest error are bolded.

Dataset	Overall Accuracy	Site Omission Error	Area Omission Error	Commission Error
LTSfire	**0.952**	**0.0319**	**0.112**	0.0242
LTSfire no pre-processing	0.935	0.0851	0.175	0.025
GABAM	0.860	0.565	0.493	0.012
FireCCI51	0.720	0.987	0.960	**0**
MCD64A1	0.799	0.949	0.720	**0**

The date of BA detection derived from iterative polygon merging was moderately successful in estimating the actual fire date. Some 62.6% of the estimated date of BA detection was within one month (± 30 days) of the actual fire date, and some 76.9% of the dates were within two months (± 61 days) of the actual fire event (**Figure 2.7**). Given the low (16-day) temporal resolution of the input Landsat data, the dates of BA detection were usually later than the actual fire date. However, a small number of BA polygons were misdated to dates earlier than the actual fire, possibly due to erroneously adopting the wrong date of detection from nearby fires or artifacts (**Figure 2.7**).

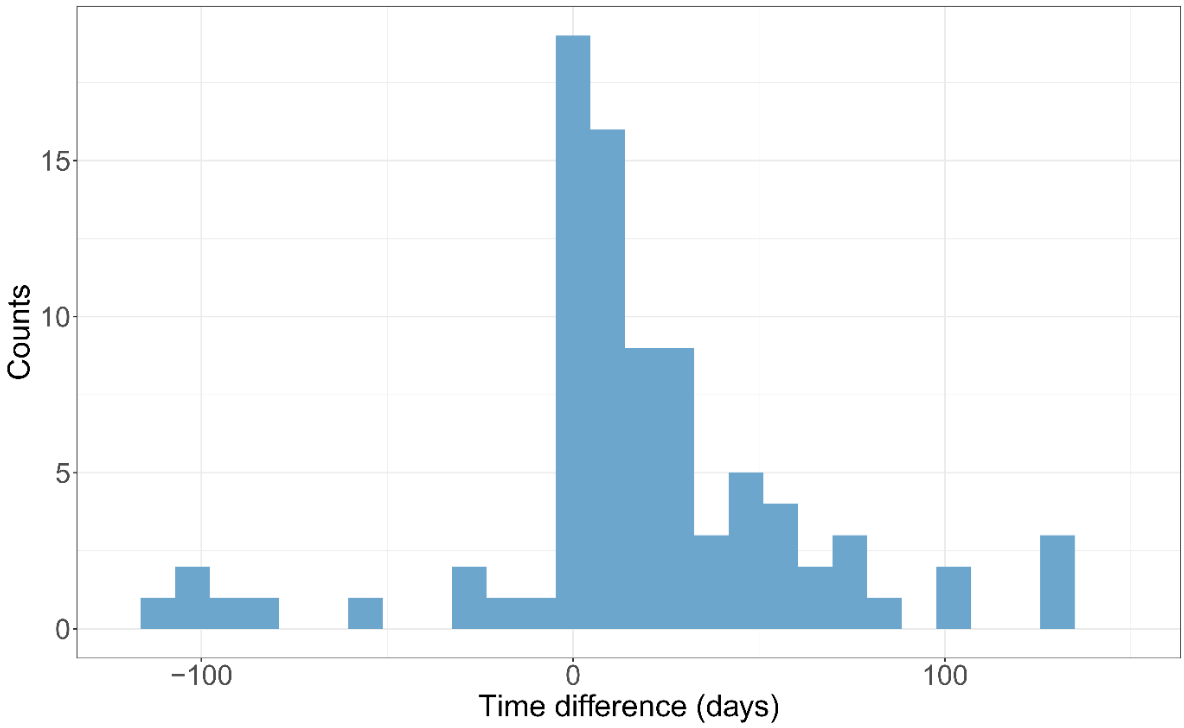

Figure 2.7: Accuracy of estimated fire dates amongst LTS fire polygons. The time difference is the time (in days) between the estimated fire date in LTS fire and the date of the fire event in the governmet (FSD/AFCD) fire records.

2.4.2 Evaluating the LTSfire Map against the MCD64A1, FireCCI51, and GABAM

Comparisons with existing burn-area products highlighted the ability of LTS fire in accurately identifying smaller BA features. MODIS-based MCD64A1 and FireCCI51 only detected 3% and 3.6% of LTSfire features, respectively (**Supp. Figure A.1**). The datasets did manage to detect several of the largest fires (**Figure 2.8a-b**), but even by area, the omitted patches accounted for > 80% of the total burnt area detected by LTS fire (**Supp. Figure A.1**). In comparison, LTS fire detected a majority of features in both MCD64A1 (73.1%) and FireCCI51 (57.7%), and most features undetected by LTSfire were not fires but artifacts associated with the airport, urban fringes, and fishponds (**Figure 2.8a-b**). A relatively higher agreement was observed between LTS fire and GABAM. The two datasets agreed on 40.7% of the burnt patches and had a Sørensen–Dice coefficient of 0.521 (**Supp. Figure A.1**). However, the dataset, still omitted most of the smaller local fires (**Figure 2.8c**). Several large Landsat 7 scan lines were mistaken as burnt patches in GABAM (**Figure 2.8c**), while LTSfire commission errors were mainly smaller features at fringes of urban areas and water bodies (**Figure 2.8c**).

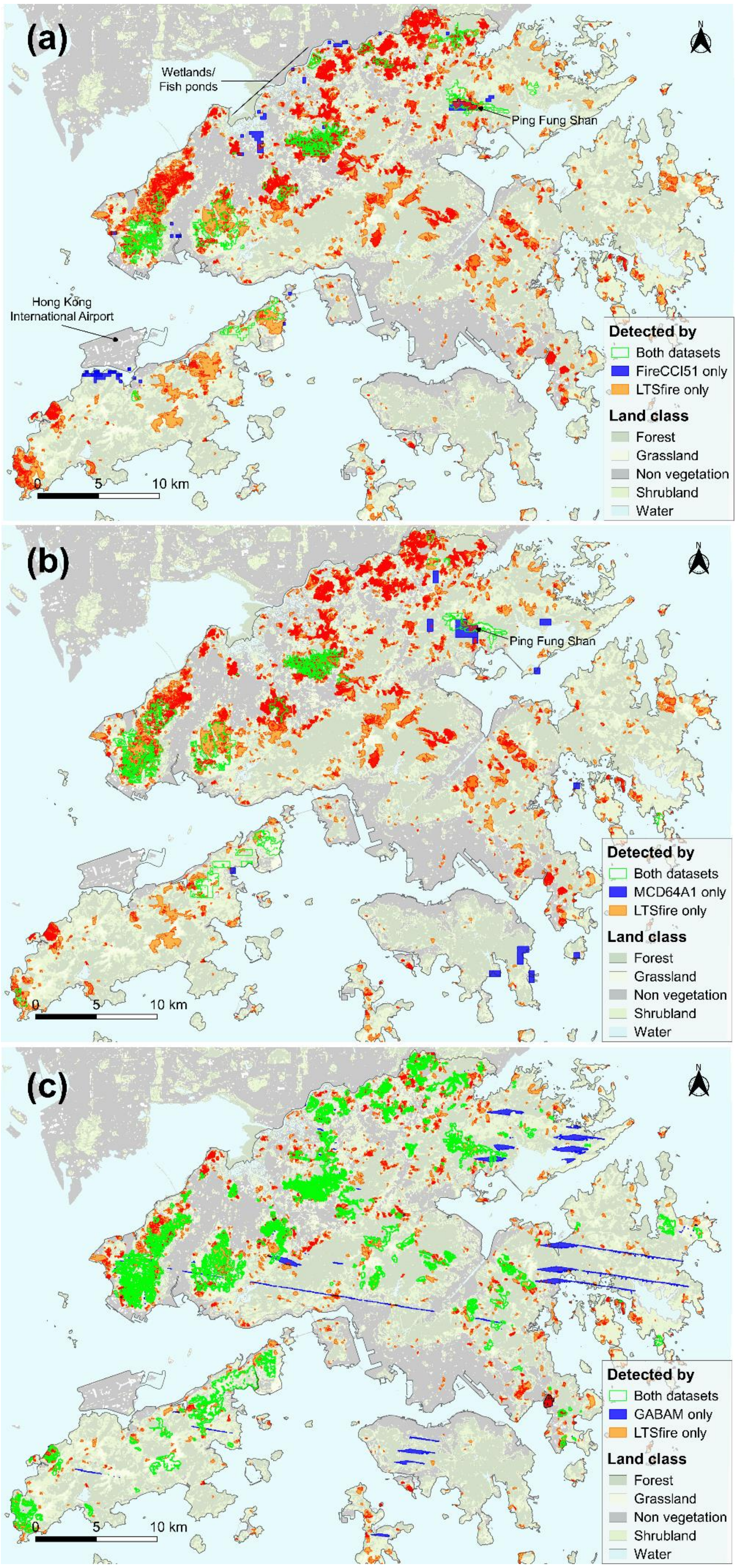

(a)
Wetlands/
Fish ponds
Ping Fung Shan
Hong Kong
International Airport
Detected by
Both datasets
FireCCI51 only
LTSfire only
Land class
Forest
Grassland
Non vegetation
Shrubland
Water
0
5
10 km
(b)
Ping Fung Shan
Detected by
Both datasets
MCD64A1 only
LTSfire only
Land class
Forest
Grassland
Non vegetation
Shrubland
Water
0
5
10 km
(c)
Detected by
Both datasets
GABAM only
LTSfire only
Land class
Forest
Grassland
Non vegetation
Shrubland
Water
0
5
10 km

Figure 2.8: Comparing the burn area map produced in this study (LTSfire) with three existing global BA products, (a) FireCCI51, (b) MCD64A1, and (c) GABAM. Areas delineated by the green polygons corresponds to the areas where LTSfire agrees with the existing dataset (Denoted by Ai ∩ Bi, or grey shading, in **Supp. Figure A.1**). Polygons with blue or orange fill represent burnt patches only detected by the existing (Bd in **Supp. Figure A.1**) or LTSfire (Ad in **Supp. Figure A.1**) map, respectively. Darker shades of orange represent repeated fires in the same area omitted by the existing dataset. A 2013–2014 land classification map of Hong Kong (22°16′8″N, 113°57′6″E) derived from the Landsat data is shown in the background.

2.4.3 Overview of the Fire Regime in Hong Kong

The 34-year Landsat burn-area time series was visualized by a time-lapse video (A. H. Y. Chan et al., 2023), a fire-frequency map (**Figure 2.9**), and summary graphs (**Figure 2.10**), which together revealed spatial and temporal patterns of fires in Hong Kong. The total detected burnt area was 909.9 km^2, against a total vegetated area of 728.4 km^2, which would amount to 125% of land if fires never occurred at the same location twice. In reality, repeated fires often occur. In fact, most (60.6%, or 441.1 km^2) of the vegetated pixels were unburnt throughout the study period (**Figure 2.9**), while a majority of burnt pixels (65.4%) burnt more than once, suggesting strongly positive fire-vegetation feedback dynamics. Spatially, the forested vegetation on the highly urbanized Hong Kong Island appeared to be better protected and was the least-burnt region in the study area. Grasslands and shrublands on the Sai Kung Peninsula and near Plover Cove burnt frequently before 2000 but has since seen reduced fire occurrence, likely due to a drop in rural population and associated land-management practices. Vegetation in the Northern District, along with the mountains near Kai Kung Leng and Castle Peak, burnt frequently across the entire study period, with many of the grassy slopes burning ≥ 6 times in the last 34 years (**Figure 2.9**).

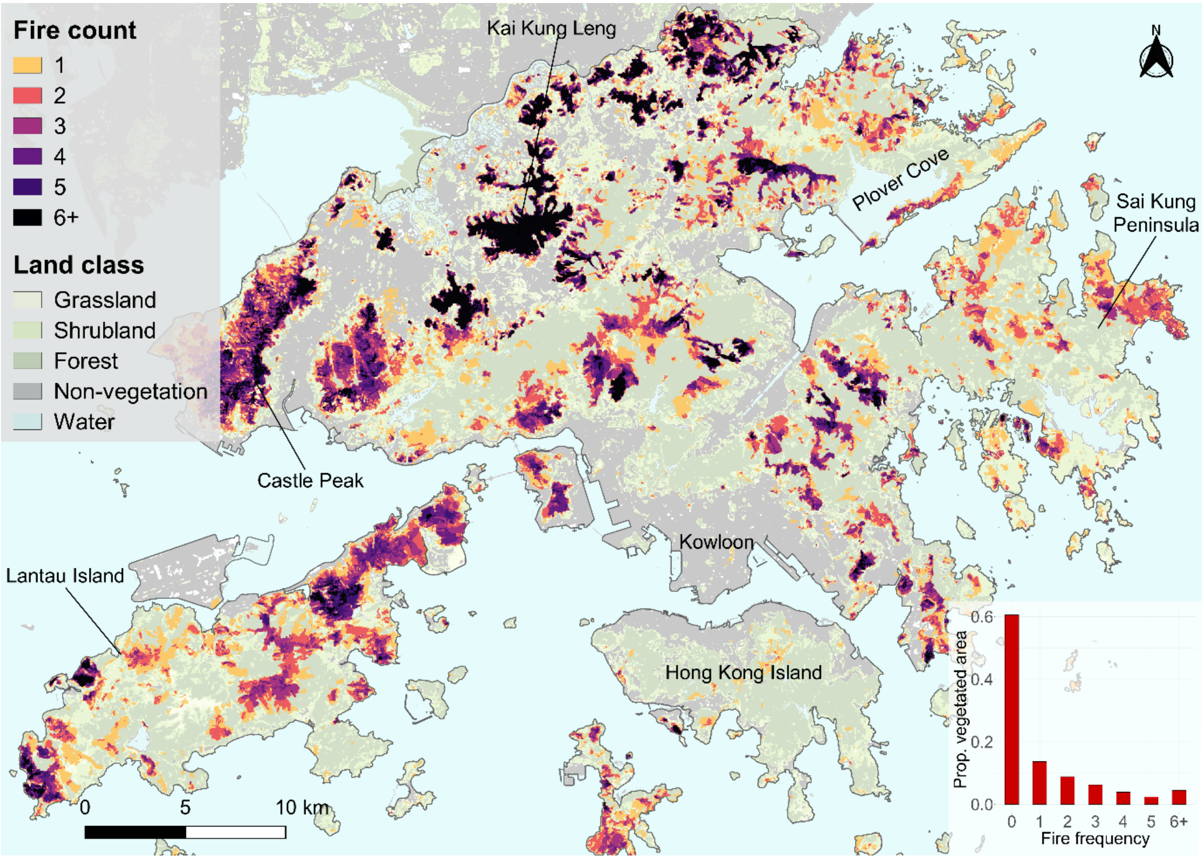

Figure 2.9: Frequency of fires over different regions of Hong Kong (22°16′8″N, 113°57′6″E). Pixels were coloured according to the number of times it burnt over the 34-year study period (1987–2020). The proportions of vegetated area being burnt 0–6+ times were tallied and plotted on the bottom right panel. The background is a 2013–2014 land classification map derived from Landsat data.

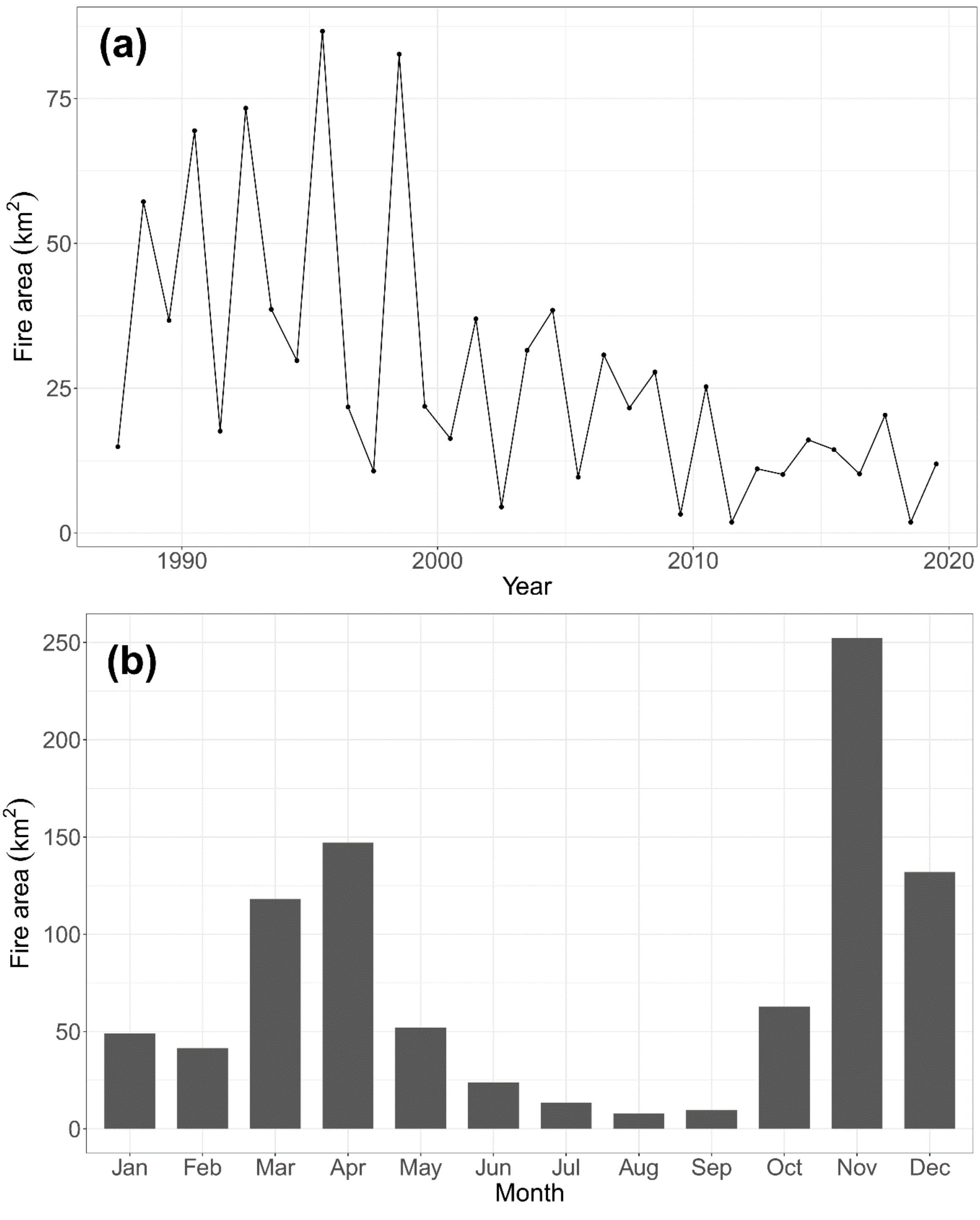

Figure 2.10: Fire prevalence in Hong Kong over time. (a) The burnt area detected by LTS fire in 33 fire seasons (15th July–15th July of the next calendar year). (b) The burnt area detected by LTS fire in each calendar month over the entire study period. Note that there might be a delay between the fire and patch detection.

Fires have become less prevalent over time. Fire-affected area dropped from 20–50 km^2 per fire season before 2000 to 5–25 km^2 per fire season in 2008–2020 (**Figure 2.10a**). The trend highlights an overall success in fire suppression in Hong Kong. Fire prevalence oscillated strongly, usually in 2–3-year cycles, possibly due to fuel accumulation entrained by weather patterns. Despite cool ambient temperatures, most fires broke out in the drier autumn and winter months (October–January). Notably, albeit with the delay in detection (**Figure 2.9**), the peaks in fire occurrence could be attributed to the traditional Ching Ming (early April) and Chung Yeung (October) Festivals (**Figure 2.10b**). During these festivals, locals clear vegetation around graves, light candles, and burn joss paper to pay respect to their ancestors, which often led to spillover fires if weather conditions are dry (W.-W. E. Chan, 2005; K. L. Chau, 1994).

2.4.4 Burn Severity Estimation

Burn severity estimated by ts-RBR was effectively relativized across different types of vegetation. Figure 11 demonstrates burn severity estimated by ts-RBR over a burnt patch near Discovery Bay, Lantau Island in 2004. No field surveys were carried out to verify ts-RBR patterns observed, but we generally found lower burn severity near the edge and patchy distribution of severity across the rest of the burn area. ts-RBR values typically ranged between 50–500. With a large sample size (n = 179,713), the vegetation type was found to significantly affect ts-RBR ($F = 300$, $p < 0.001$, ANOVA). However, the effect sizes were very small (**Supp. Figure A.2**). Ω^2 of the model shows that the vegetation type only accounts for 0.3% of the variance in ts-RBR, indicating that the metric was effectively relativized and ts-RBR values were comparable across different types of vegetation.

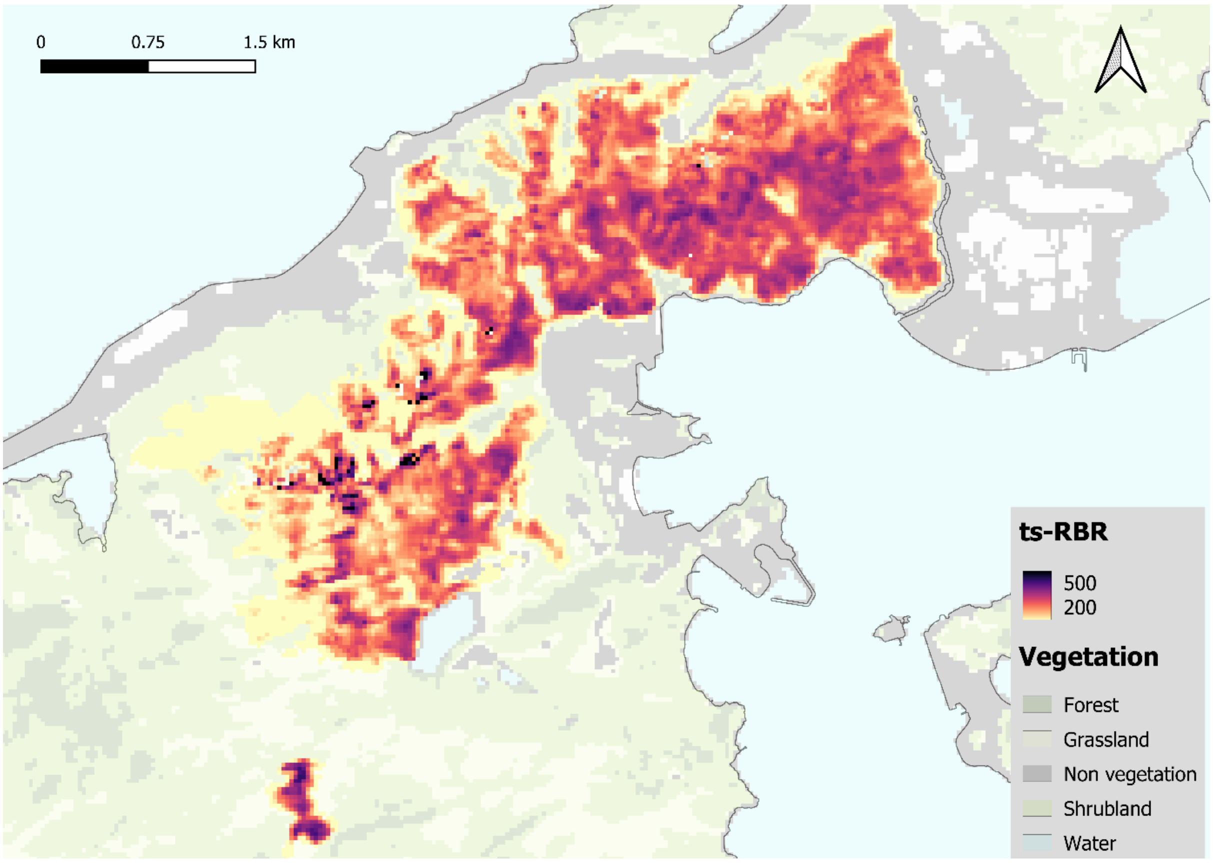

Figure 2.11: Burn severity estimated by time series relativized burn ratio (ts-RBR) of two fires near Discovery Bay, Lantau Island (22°18′35.19″N, 114°0′25.95″E) in 2004. The background map is a Landsat-based vegetation map of the area in the same year.

2.5 Discussion

Our LTS fire map of Hong Kong represents the first regional Landsat BA map in wet tropical/subtropical Asia that covers the full Landsat 5/7/8 time series (**Supp. Table A.1**). It is also the first long-term Landsat BA map in the wet tropics/subtropics that incorporated estimated date of BA detection and burn severity (**Supp. Table A.1**). When validated with government fire records, the LTS fire map was found to carry very low omission errors, omitting only 11.2% of the burnt area compared with MCD64A1 (72%) and FireCCI51 (96%). The high omission errors of MODIS-based BA maps were partially due to the low spatial resolution MODIS, as 4.1% and 18.1% of the burnt area in the ancillary dataset were found in patches that were smaller than the pixel size of FireCCI51 (250 m) and MCD64A1 (500 m), respectively. However, most of the pixels omitted (74.9% of MCD64A1 omissions and 95.7% of FireCCI51 omissions) were attributable to larger patches. Many of these fires were probably still too scattered to be readily detectable or were extinguished before the MODIS satellite returned. The results revealed the limitations of algorithms that grow BAs based on MODIS active fire data. It is also worth noting that the mean area of burnt patches detected by LTS fire (13.3 ha) was significantly smaller than the patches delineated for validation (31.1 ha) (**Supp. Figure A.3**). Had we sampled the true size distribution of burnt patches, the omission errors of the two MODIS BA products would be even higher. While burnt patches in Hong Kong tend to be smaller than other tropical/subtropical regions due to habitat fragmentation and government fire suppression (**Supp. Figure A.3**) (Hantson, Pueyo, et al., 2016; Morton et al., 2011), the results nonetheless highlighted the importance of incorporating higher-resolution datasets if fire histories of landscapes were to be accurately reconstructed.

LTS fire also performed well compared to Landsat-based GABAM, omitting 11.2% rather than 49.3% of burnt area while keeping commission errors low (**Table 1.1**). We do acknowledge that direct comparisons between locally trained BA maps with global datasets may lead to biases, even with independent cross-validation. However, we believe that the stark differences in accuracies could at least be partially attributed to methodological differences in preprocessing. Most existing BA mapping algorithms, including GABAM, do not directly classify pixels into binary burnt/unburnt maps. Rather, continuous proxies of BA resemblance, such as VIs, predicted burnt probabilities, or, in this study, the equivalent number of days after fire ($\Delta\tau$), which are thresholded into BA products. Thresholding makes BA mapping more flexible. For instance, our study adopted the two-phase seed-growing approach proposed by Bastarrika et al. (2011) (Bastarrika et al., 2011). The approach elegantly incorporates spatial information into feature selection by overlaying polygons created by two thresholds, reducing both omission and commission errors (**Figure 2.5**). GABAM additionally incorporated a number of additional thresholds that could vary according to land cover (Long et al., 2019). However, existing approaches rarely explicitly address the issue of temporal stability. When a single set of thresholds is applied across multiple scenes in the time series, the balance between omission and commission errors can change drastically. Depending on incident sunlight and haze, some scenes have lower baseline NIR:SWIR ratios across all pixels, leading to bursts in commission errors (**Figure 2.8c** and **Supp. Figure A.4**). Similarly, burnt pixels in a particular season can be omitted if the scenes had a high baseline of NIR:SWIR ratios. At smaller spatial-temporal scales, this issue could be avoided by preselecting Landsat scenes that are unaffected by atypical incident sunlight or atmospheric effects. In fact, most existing Landsat BA maps in the wet tropics and subtropics operate on preselected scenes (**Supp. Table A.1**). However, we believe that scene preselection makes algorithms difficult to generalize. Moreover, the high cloud cover in the wet tropics and subtropics means that it is not uncommon for seasons to be only covered by a single atypical scene. GABAM addressed this by adding more thresholds and adopting relatively conservative thresholds (Long et al., 2019). Even so, atypical Landsat 7 scenes still caused bursts in commission errors in the GABAM time series (**Figure 2.8c**). In LTS fire, we developed a new weighted histogram matching approach to address this issue (**Section 2.3.4**, **Figure 2.2**). By uniformizing Landsat scenes, we effectively minimized these sudden bursts in commission errors (**Supp. Figure A.4**). The preprocessing also ensured that the model performance was comparable across imagery collected by different sensors in Landsat 5, 7, and 8. LTS fire did not perform significantly worse for known burnt patches in the Landsat 5 era, even when most training pixels were derived from Landsat 7/8 years. We also did not observe any significant changes in size distribution of detected patches across time, indicating that LTS fire was equally sensitive to smaller features when applied to Landsat 5 data (**Supp. Figure A.5**). This temporal stability allowed us to adopt less conservative thresholds when mapping BAs, which in turn significantly suppressed omission errors without the expense in commission errors (**Table 1.1**). One potential concern of weighted histogram matching is the possibility of the process smoothing out BA features when burnt pixels are adjusted to match the histogram of the unburnt reference composite, increasing omission errors. Since burnt pixels are scarce relative to unburnt pixels, we found this to be a relatively minor issue in our study site. The benefits of temporal stability, which suppressed omission errors by allowing for less conservative thresholds, significantly outweighed the potential increase in omissions caused by smoothing (**Table 1.1**). Nevertheless, minor changes to the algorithm would probably be needed if burn patches are large enough to span significant portions of Landsat scenes. In this case, the function to adjust pixel brightness could be derived from vegetated pixels only, then applied to both vegetated areas and potential burnt patches. This would uniformize the scenes without forcing output Landsat scenes with large burnt patches to have the exact histogram of the unburnt reference composite.

Another important addition to the pipeline is the coupling of date-traceable compositing with iterative polygon merging to estimate dates of detection of BA polygons. Date stamps facilitate temporal analyses on fire occurrence (**Figure 2.10**) to be carried out at a level of detail previously only available in MODIS-based datasets or after cross-validation with government fire records (Hawbaker et al., 2017; K. C. Ryan & Opperman, 2013; Szpakowski & Jensen, 2019). Considering the low temporal resolution of Landsat (16 days), the fact that the algorithm dated most polygons within a month and 76.9% of polygons within two months of the actual fire exceeded expectations (**Figure 2.7**). This is achieved by incorporating the full time series, including many heavily clouded or hazy scenes, when creating the date-traceable composites (**Section 2.3.4**, **Figure 2.2**). These min-NBR composites preserved the dates of pixels once they were captured by Landsat, even when many BAs were at the time only partially visible through cloud gaps or amongst Landsat 7 scan lines. Creating a set of criteria to decide how these dated BA polygons should be merged was by far the most challenging part in fire date estimation. Specifically, two separate issues were in play. Firstly, pixels burn repeatedly (**Figure 2.9**). The minimum interval between two separate fires depends mainly on landcover type and the rate of fuel accumulation. In Hong Kong, grassy slopes could occasionally burn repeatedly within a year, but apart from rare exceptions, repeated fires were usually more than a year apart. Hence, we designed the iterative polygon merging process such that overlapping polygons were merged if seed-polygon dates were ± 1 season apart. We are aware that the rate of revegetation and fuel accumulation can be vastly different in other biomes. In regions with rapid revegetation, quick fuel accumulation, and frequent repeated fires, the definitions of seasons would have to be shortened, while in regions with sluggish revegetation, slow fuel accumulation, and infrequent repeated fires, polygons dated more than one season apart ought to be merged. The second issue concerns neighboring burnt areas. Even if pixels do not burn repeatedly, two separate burnt patches ± 1 season apart could intersect at the border. It is challenging to determine whether intersecting patches with different dates of detection were (1) Caused by the same fire but were scattered across more than one Landsat scenes; or (2) Caused by two different fires. In this study, we did not make this distinction, and, occasionally, BA polygons were dated earlier than the actual fire (negative time differences in **Figure 2.7**). However, we did adopt an area-based algorithm such that if two separate polygons were wrongfully merged, at least the fire dates of large patches would not be dragged by much smaller ones. A solution to this issue is to extract additional data from the Landsat scenes before they were made into seasonal min-NBR composites, but that would likely come at the expense of computational time. Finally, it is worth noting that the accuracy of estimated dates depends on the temporal resolution of the input Landsat time series. In earlier years with only Landsat 5 data, or in cloudy seasons, the estimated dates of detection would unavoidably be less accurate. Nevertheless, the estimated dates of BA detection at its current form should be robust enough for a large range of ecological applications, such as how seasonal weather patterns affect fire susceptibility or post-fire recovery in the wet tropics and subtropics.

The LTS fire pipeline also incorporated the time series relativized burn ratio (ts-RBR) as a burn severity metric. The index was developed as a variant of relativized burn ratio (RBR) (Parks et al., 2014) but made robust against poor data quality by considering multiple pre- and post-fire scenes in the Landsat time series simultaneously (**Section 2.3.7** and **Figure 2.11**). The search for appropriate remotely sensed indices to represent burn severity has received much attention in recent years. Earlier studies often directly used NBR (Equation (1)) or its difference pre- and post-fire, dNBR (Equation (2)), to estimate burn severity (Cocke et al., 2005; Escuin et al., 2007; Key & Benson, 2006; Soverel et al., 2010). However, these metrics do not address the issue of shifting NBR baselines across different vegetation types. Grasslands or short shrublands often have lower absolute NBR and, hence, smaller dNBR values compared to forests, regardless of relative severity (Parks et al., 2014; Szpakowski & Jensen, 2019). Recognizing these issues, many studies started adopting relativized dNBR, or RdNBR, to estimate burn severity (Busby et al., 2020; Chu & Guo, 2013; Kemp et al., 2016; Mallek et al., 2013; J. D. Miller & Thode, 2007). In recent years, the robustness of RdNBR in accurately quantifying burn severity has come into question (Parks et al., 2014; Soverel et al., 2010). In particular, Parks et al. (2014) pointed out that RdNBR is mathematically unstable and introduced RBR (Equation (3)) as a more reliable alternative that better echoed field-measured severity (Parks et al., 2014). In this study, we hope to contribute to this discussion by proposing the use of ts-RBR in areas where single cloudless pre- and post-fire scenes are not readily available. By consulting multiple pre- and post-fire scenes, the approach maximizes the chance of reconstructing burn severity patterns that would otherwise be partially occluded by clouds and artifacts. We are aware that more sophisticated methods have been developed to better match remotely sensed fire severity with a field-measured composite burn index (CBI). However, many are contingent upon calibrations to local climate regimes (Parks et al., 2018; Szpakowski & Jensen, 2019). This makes such approaches less generalizable, especially in the tropics/subtropics where data needed to calibrate the burn severity models are not readily available. Therefore, we decided to make less assumptions and adopt ts-RBR in the pipeline instead. Finally, it is important to note that RBR was mainly validated in the US (Parks et al., 2014). The caveats of applying the metric outside its validation window would also apply to ts-RBR. Moreover, ts-RBR should be viewed as a method to obtain RBR from time series data, not as a new and fully validated severity metric. Nevertheless, we believe that the severity data provided here could act as a rough baseline for future ecological studies, and we hope that this could elicit further discussions to find the best practice in estimating burn severity across wet tropical and subtropical BAs.

Looking into the future, we believe that the LTS fire pipeline can be adopted more widely to provide ecologically relevant BA maps for researchers. Our results demonstrated how over three decades of fire history could be accurately reconstructed using Landsat data in a wet subtropical landscape with a highly diverse vegetation structure (**Figure 2.9** and **Figure 2.10**). The seasonal, decadal, and spatial trends that we observed, such as the overall changes in fire abundance and seasonal peaks near local festivals, closely echoes what was reported by local ecological studies in Hong Kong (W.-W. E. Chan, 2005; K. L. Chau, 1994; Marafa & Chau, 1999). Compared with most previous studies on Landsat/Sentinel BA mapping the wet tropics and subtropics, LTS fire is comparatively close to being data agnostic as it does not require preselection of Landsat scenes (**Supp. Table A.1**). We do, nonetheless, recognize five areas where the LTS fire pipeline needs further modification before it could be applied more widely. Firstly, as mentioned above, the weighted histogram matching approach might need slight adjustments if the area of interest contains very large BAs. Secondly, we adopted $\Delta\tau$, the equivalent number of days after fire, as the proxy for pixel resemblance to BAs. While $\Delta\tau$ is a more information-rich proxy and should be adopted, if possible, it cannot be derived from training datasets without exact fire dates. An alternative that trains RF models from binary burnt/unburnt pixels may be useful. Thirdly, the two thresholds used to create seed and growth polygons are currently chosen by eyeballing the threshold-error curves (**Figure 2.5**). A mathematical expression to derive the threshold from the curves will make the pipeline more automatable. Fourthly, as briefly discussed above, the rate of revegetation and fuel accumulation affects the minimum temporal interval between fires. In this study, the Landsat scenes were grouped by seasons, and resulting BA polygons are merged accordingly. An option to change seasonal boundaries and merging criteria based on the rate of revegetation would make the pipeline more generalizable. Finally, the current pipeline was mainly written in R and implemented in a local cluster. While R provides ample flexibility for pipeline development, a translation that allows the pipeline to be implemented on cloud computing platforms such as GEE would greatly lift limitations in computational capacity. Overall, these five areas of future work are not insurmountable. In addition to the compilation of BA training data, such as the newly developed Burned Area Reference Database (BARD) (Franquesa et al., 2020), we believe that the LTS fire pipeline can be a step toward creating a new generation of Landsat-based BA maps in the wet tropics and subtropics. By providing relevant and specific information on thousands of BAs across decadal time scales, these maps will bridge the missing link between remotely sensed and field data, providing a new bedrock for tropical fire ecology.

2.6 Conclusions

A 34-year Landsat-based BA time series was created to reconstruct the fire history of Hong Kong by recording the location, date, and severity of burnt patches. To generate the product, a new BA detection pipeline was developed and tested on the challenging wet subtropical landscape where high cloud cover, diverse habitat types, and rapid revegetation commonly obscures BAs. The map successfully captured the fire regime of the area at a level of detail unmatched by existing global satellite-based burn-area maps. A wider availability of such long-term fire-severity maps with fine temporal and spatial resolution will greatly benefit studies in fire ecology, global climate modelling, and fire management.

Chapter 3: Fire traps in the wet subtropics: a perspective from Hong Kong

3.1 Abstract

1. Fires undermine efforts to restore degraded forests in the wet tropics and subtropics. Grasslands and shrublands established after fires are more fire-susceptible than forests and tend to be set alight more often, creating a feedback loop that curbs succession. Understanding the factors that underpin the strength of these fire traps could transform restoration programmes by identifying the steps needed to escape them.

2. Fire traps are notoriously challenging to quantify because multiple factors influence fire occurrence and vegetation recovery. Here we used multi-decadal satellite imagery from Landsat to create a 34-year time series of burn areas and vegetation dynamics in wet subtropical Hong Kong. These dynamic maps were then used to characterise (1) the influence of successional stage on fire occurrence, having accounted for topographical and ignition source imbalances using neighbourhood analyses and entropy balancing (EBAL) weights, and (2) recovery time to the next successional stage by survival analysis with EBAL weights.

3. Our analyses revealed that fire regimes in the wet subtropics are defined by strong fire-vegetation feedbacks. Grasslands and shrublands were 20 and 9 times more susceptible to fires than forests in similar topographic positions. Human activities compounded these differences by disproportionally introducing more ignition sources to grasslands (2.3 times) and shrublands (2.0 times) than to forests.

4. Burnt shrublands recovered to forests faster (19 years) than grasslands (40 years). Proximity to forest patches had strong positive effects on recovery rates, highlighting the importance of seed sources. Post-fire recovery was faster on wetter northwest-facing sites and valleys. Overall, topography strongly influenced recovery processes but hardly affected fires occurrence.

5. Synthesis and applications. Our study provides the first quantification of fire-trap processes in the wet subtropics, which provides new opportunities for evidence-based fire suppression and post-fire restoration. Our results suggest that (1) fire traps could be mitigated by fire-supression programmes as they are currently exacerbated by ignition source imbalance; (2) establishing green fire breaks represent an effective fire suppression measure in the wet subtropics; and (3) active restoration could target areas where models predict sluggish post-fire natural regeneration.

3.2 Introduction

Humans have fundamentally changed fire regimes in the wet tropics and subtropics. Naturally, pristine rainforests retain moisture well. Barring extreme droughts, these forests are naturally fire-resistant with fire return intervals of 100-1000 years (Mark A. Cochrane, 2003; J. G. Goldammer & Seibert, 1989; Johann Georg Goldammer, 1990). However, up to 30-40% of all tropical forests are now degraded by logging and agricultural activities (Budiharta et al., 2014). Dominated by C4 grasses, *Dicranopteris* fern mats, short bamboos, and shrublands, degraded wet tropical landscapes retains moisture poorly and are much more likely to burn during dry spells (Haberle et al., 2010; Hoffmann, Geiger, et al., 2012; Hoffmann, Jaconis, et al., 2012; Matos et al., 2002). Fires, in turn, disproportionately kill saplings of fire-sensitive late-successional tree species. Meanwhile, grasses, forbs and shrubs tend to have basal meristems, lignotubers, or other forms of underground energy stores (De Moraes et al., 2016; Paula et al., 2016; Simpson et al., 2016). These features help plants survive by exploiting the steep temperature gradients created by soil insulation (Beadle, 1940). By resprouting and dispersing into burnt patches, grasses and shrubs reinforce its dominance in fire-disturbed habitats (Paula et al., 2016; Simpson et al., 2016). In many degraded landscapes, this lead to positive fire-vegetation feedbacks, which could create "fire traps" that perpetuate early-successional vegetation in areas where the climate supports closed-canopy forests (Bell, 1984; Flores et al., 2016; Hoffmann, Geiger, et al., 2012; Mata et al., 2022; Staal et al., 2018; Van Nes et al., 2018). These effects are further compounded by the abundance of anthropogenic ignition sources (Mark A. Cochrane, 2003; Tien Bui et al., 2016) and stronger droughts under climate change (Clarke et al., 2022; Hoffmann et al., 2003; Lizundia-Loiola, Pettinari, et al., 2020; Seidl et al., 2017).

Properly describing and quantifying fire-trap dynamics in the wet tropics is crucial for the management and restoration of degraded wet tropical landscapes. International initiatives, such as the Bonn Challenge, UN Decade of Ecosystem Restoration, and the One Trillion Tree initiative, have repeatedly called for large-scale restoration in the wet tropics (Lamb et al., 2005; Secretariat, 2010; Verdone & Seidl, 2017). Understanding fire-trap dynamics in degraded wet tropical and subtropical sites is critical for developing viable, cost-effective, and climate-resilient local restoration strategies (Scheper et al., 2021). Assessing the relative importance of vegetation structure, anthropogenic ignition source distribution, and local topography on fire occurrence is the first step towards targeted fire suppression (Carmo et al., 2011). Similarly, evaluating how post-fire recovery rate is affected by pre-fire vegetation structure, burn severity, and topographical factors helps land managers decide where and when intervention is needed (Souza-Alonso et al., 2022).

Fire susceptibility and post-fire recovery in the wet tropics and subtropics are currently understudied. Despite evidence showing that degraded sites in the wet tropics are reasonably fire-prone (Flores et al., 2016; Mata et al., 2022; Uhl et al., 1988), there is still a prevailing perception of these bioregions being "too wet to burn". Existing studies on fire dynamics continue to focus on naturally fire-adapted Mediterranean, boreal, and savanna ecosystems (Kibler et al., 2019; Kurbanov et al., 2022; Mallek et al., 2013; Qiu et al., 2021; van Butsic et al., 2015). Since wet tropical landscapes are rarely fuel-limited and have distinctive fire-vegetation dynamics (Tepley et al., 2018), it is questionable whether patterns observed in other ecosystems hold true in wet tropical and subtropical biomes. Existing studies also does not fully address the issue of covariate imbalance when evaluating fire susceptibility amongst different vegetation types. For instance, it is reasonable to expect forests to disproportionally occupy wetter valleys, while grasslands dominate the drier ridgetops. This is further complicated by the non-random distribution of ignition sources (Oliveira et al., 2012; Tien Bui et al., 2016). Grasslands and shrublands could be more exposed to ignition sources as they are closer to settlements and more accessible to humans. To accurately quantify fire traps, these relationships need to be carefully untangled. Similarly, post-fire recovery trajectories in the wet tropics are worth re-evaluating as they determine whether sites could escape the fire trap. Previous studies have identified fire frequency, distance from forest patches, burn severity, soil type, species composition, and several topographical variables as factors that affect rate of post-fire recovery (Araújo et al., 2017; Bright et al., 2019; Goosem et al., 2016; Ireland & Petropoulos, 2015; Kurbanov et al., 2022; Marsh, Crockett, et al., 2022; Rochimi et al., 2021), but a systematic evaluation of the importance of these variables in the wet tropics is currently lacking~~. Most existing studies~~ Crucially, many existing studies quantified post-fire recovery by tracking the rebound of remotely-sensed indices, such as the normalized difference vegetation index (NDVI) or normalized burn ratio (NBR), to pre-disturbance values (Bright et al., 2019; Fernández-García et al., 2018; Gouveia et al., 2010; Ireland & Petropoulos, 2015; Kurbanov et al., 2022; Pérez-Cabello et al., 2021). In the degraded wet tropics, however, the background landscape is itself on a succession trajectory. Burnt areas rapidly revegetate and return to pre-fire conditions quickly (A. H. Y. Chan et al., 2023; Idris et al., 2004; Melchiorre & Boschetti, 2018), but returning the system to the pre-fire degraded condition is often not the goal of land managers. Instead, it is more appropriate to study recovery time to forests after fire, yet none of the existing studies have adopted such an approach to analyse post-fire recovery over large scales (Kurbanov et al., 2022).

Methodological advances in remote sensing and biostatistics have made it increasingly manageable to track fire susceptibility and post-fire recovery across large spatiotemporal scales. Accurate burn area mapping in the wet tropics and subtropics is technically challenging (A. A. C. Alencar et al., 2022; A. H. Y. Chan et al., 2023). High cloud cover and rapid burn area revegetation have largely limited full burn area mapping across decadal time scales to satellites with short return times (e.g. MODIS), which led to tradeoffs in accuracy and ground resolution (A. H. Y. Chan et al., 2023; Franquesa et al., 2022; Humber et al., 2019; Szpakowski & Jensen, 2019). Advances in imagery processing have, however, lifted many of these restrictions. Long-term Landsat-based burn area products, which have 30 m ground resolutions and are better at detecting small burnt patches than MODIS-based maps, are now available for parts of the wet tropics and subtropics (A. A. C. Alencar et al., 2022; A. H. Y. Chan et al., 2023). Additionally, new statistical tools have also made it easier to handle data extracted from burn area and vegetation time series. There are now standardised workflows to handle covariate imbalance, such as the tendency for forests to be found in wetter valleys, by matching or reweighting (Cannas & Arpino, 2019; Markoulidakis et al., 2022). Survival analysis, which is used to model fire-vegetation feedbacks (Reed et al., 1998; Tepley et al., 2018) and vegetation succession (Longpre & Morris, 2012), has also developed rapidly. The integration with machine learning to create random survival forests now make it possible to easily visualise variable importance and make survival time predictions, especially for large datasets with non-linear or covarying predictors of survival (Ishwaran et al., 2008).

In this study, we utilised these remote sensing and statistical approaches to (1) quantify the strength of fire-vegetation feedbacks relative to other predictors of fire occurrence and (2) describe how different factors affect post-fire recovery rates. We conducted the study in the extensive wet subtropical landscapes of Hong Kong, which was heavily degraded in the past and experiences a large number of anthropogenic fires despite restoration efforts. The objective is to use the results to identify effective approaches for fire suppression and active restoration of burnt areas.

3.3 Methods

3.3.1 Study area

The study was conducted in the wet subtropical countryside of Hong Kong (22^{o} 16’ 8’’ N, 113^{o} 57’ 6’’E) (**Figure 3.1**). On average, the region receives over 2400 mm of rainfall per year and would have historically been covered by evergreen broadleaved subtropical rainforests (Abbas et al., 2016; Dudgeon & Corlett, 2004; Yang et al., 2018). However, centuries of human settlement and agricultural activity had decimated >90% of the natural forests, creating a barren landscape of grasslands and short shrublands (Dudgeon & Corlett, 2004; Zhuang & Corlett, 1997). After the second world war, an economic transition led to a sharp fall in the rural population and associated land management practices (Hau et al., 2005). Widespread agricultural abandonment, along with the designation of strictly protected Country Parks over 40% of the land area, led to over 70 years of natural and assisted regeneration (Abbas et al., 2016). The current vegetation of Hong Kong consists of a mosaic of grasslands, shrublands, secondary forests, and plantations (Kwong et al., 2022).

Natural fires are rare in Hong Kong as the main natural ignition source (lightning) is usually accompanied by torrential rain, but anthropogenic fires are frequent (A. H. Y. Chan et al., 2023; Dudgeon & Corlett, 2004; Fung & Jim, 1993). Common anthropogenic ignition sources include joss paper burnt around graves in local festivals, cigarette butts, and campfires (W.-W. E. Chan, 2005; K. L. Chau, 1994). The Fire Services Department received 4561 reports of vegetation fires between 2016 and 2020. Overall, 287 km^2 (39%) of the 728 km^2 of vegetated area burnt at least once between 1986 and

2020, with 65% of the affected area burning more than once (A. H. Y. Chan et al., 2023). The diverse vegetation structure coupled with notable fire occurrence creates a convenient setting to study fire traps.

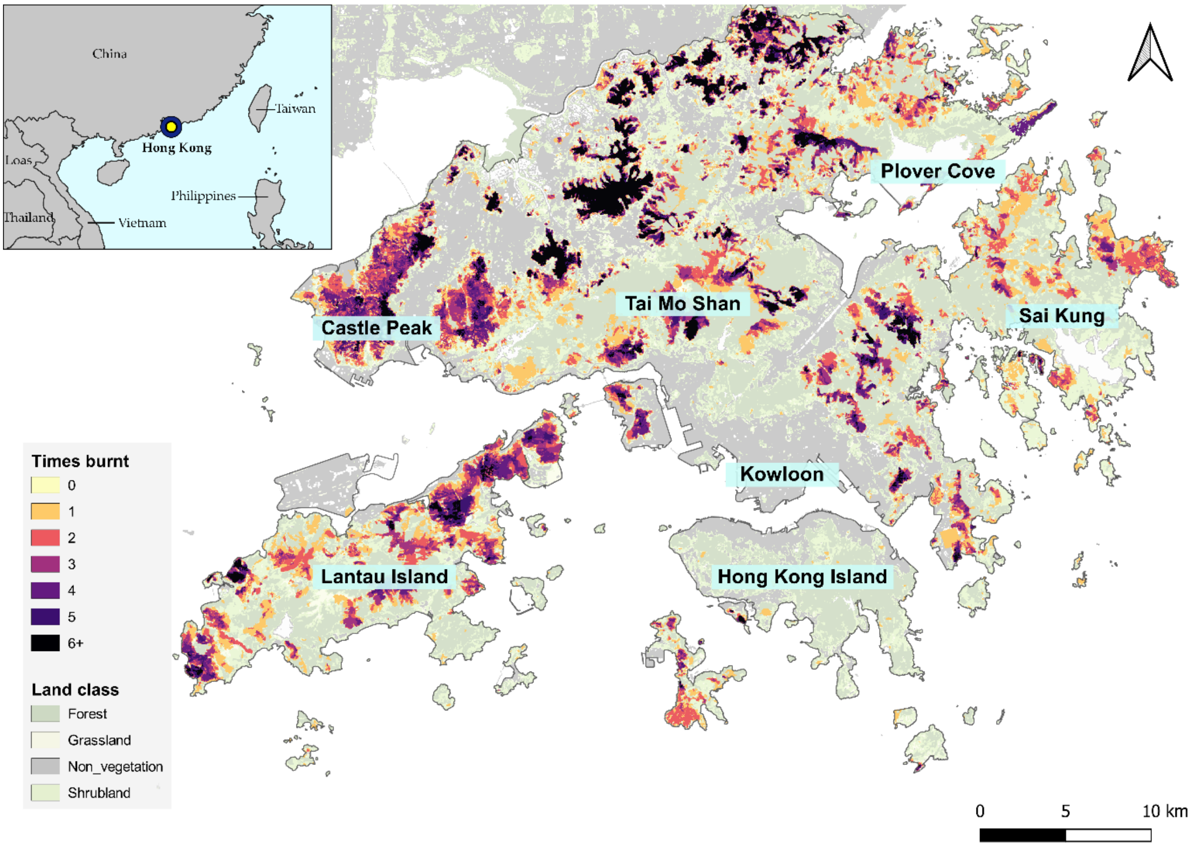

Figure 3.1: The study area of Hong Kong. Burnt areas detected by the LTSfire pipeline between 1986 and 2020 are overlaid on a Landsat based land cover map of 2013-2014 (A. H. Y. Chan et al., 2023).

3.3.2 Overview of methods

Overall, we used (1) Landsat imagery to create burn area and vegetation maps for the study period (1986 – 2020) and (2) LiDAR data to calculate topographical variables. We then used these products to study how different factors affected fire occurrence, fire susceptibility, and post-fire recovery rates. **Figure 3.2** provides a methodological flow chart with numbers serving as a guide to the relevant sections where the detailed methodologies are described.

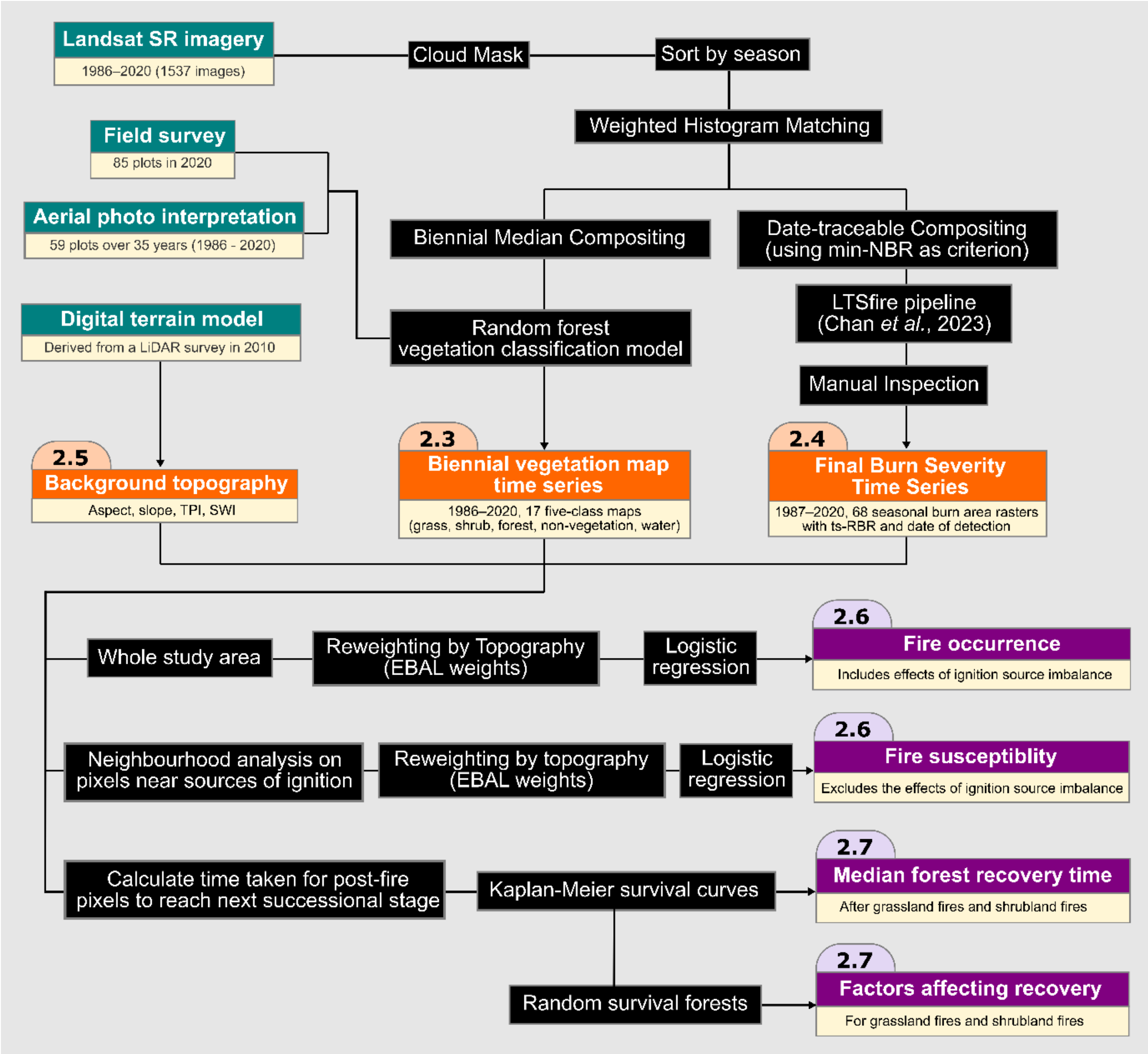

Figure 3.2: Methodology flow chart showing how fire trap processes were evaluated by remote sensing data. Numbers indicate the relevant section in the main text. Green boxes are input data; black boxes represent steps taken; orange boxes indicate intermediate products; and purple boxes are the fire trap processes quantified.

3.3.3 Vegetation map time series

A Landsat-based vegetation map time series was produced to track changes in vegetation structure over the 35-year study period (1986-2020). We distilled 1537 relevant Landsat surface reflectance scenes into 17 biennial (every two years) composites. Weighted histogram matching, band normalisation and vegetation indices were adopted to make the scenes and composites intercomparable (A. H. Y. Chan et al., 2021, 2023; C. Wu, 2004). We then built random forest (RF) classification models based on pixels with known vegetation cover. For every biennial composite, the RF model classified the landscape into five classes (forest, shrubland, grassland, non-vegetation, and water). Detailed methodology can be found in the **Appendix B:**, with RF model accuracies listed in **Supp. Table B.1**. Finally, we hypothesised that distance to nearest forest patch may affect post-fire recovery trajectories. Hence, we calculated this distance for all grassland and shrubland pixels using the *distance* function in the *raster* package. Unless otherwise specified, all geospatial analyses were carried out in *R-4.1.0* (R core team, 2021).

3.3.4 Burn area and burn severity time series

Burn areas (BAs) in Hong Kong were mapped across a 35-year Landsat multispectral time series (1986-2020) using the LTSfire pipeline (A. H. Y. Chan et al., 2023). The pipeline was designed to accurately detect small BAs in regions with high cloud cover and rapid burn area revegetation. The product of LTSfire includes two components – (1) a shapefile of BA polygons with dates of detection and (2) rasters containing estimates of burn severity, time series relativized burn ratio (ts-RBR), for all burnt pixels. We refer readers to Chan et al. (2023) for details on the LTSfire pipeline, but an overview of the pipeline and accuracies can be found in the **Appendix B:** and **Supp. Table B.2**. We further manually inspected the dataset and removed 1179 dubious features that were potential artifacts and modified the shape of 137 polygons. The final dataset contained 5654 burnt patches.

3.3.5 LiDAR background topography

To investigate how background topography affected vegetation fire susceptibility and post-fire recovery, we built rasters for four topographical variables – slope, aspect, topographic position index (TPI), and SAGA wetness index (SWI). The rasters were generated from a digital terrain model (DTM) based on an airborne LiDAR dataset collected in 2010. Slope and aspect were calculated using the terrain function in the raster package; TPI was generated by the gdaldem function in GDAL; while SWI was calculated by calling the rsaga.wetness.index function through the RSAGA package in R-4.1.0. Since many of these topographical variables were resolution-dependent, we selectively downsampled the DTM before generating the topographical layers. Aspect was calculated from a DTM downsampled to 30 m resolution. We then tested how different DTM resolutions affected the TPI and SWI to ensure that the indices (1) did not focus exclusively on highly local topographical features such as boulders or rocks, while (2) not smoothing out the effects of valleys and ridges in the mountainous terrain (**Supp. Figure B.1**). From the analysis, DTMs of 20m and 15m ground resolutions were used to generate TPI and SWI, respectively. Since local steepness has been reported to affect fire propagation (Viegas & Viegas, 2004), we used the original 1m DTM when calculating slope. After generation, all topographical variables were eventually tidied to 30m ground resolutions to match that of Landsat images. Finally, as the effect of aspect is cyclical, we linearized the variable by calculating cos_aspect with the local optimum aspect of 5.795 in radians (Stage, 1976). The optimum aspect was identified by analysing forest growth rates as measured by photogrammetry- and lidar-based digital surface models (Hong Kong Observatory, 2023) (**Supp. Figure B.2**).

$$\text{Cos\_aspect} = \cos(\text{Aspect} - 5.795)$$

3.3.6 Fire susceptibility, ignition source distribution, and fire occurrence

3.3.6.1 Overview

Pixel values were extracted from the vegetation, burnt area, and topographical rasters to analyse how different factors shaped the fire regime of the study area. We defined fire susceptibility as the likelihood for pixels to burn given the same exposure to ignition sources. It is an inherent property of the site defined by the vegetation type and background topography. This differs from fire occurrence, which represents the actual proportion of burnt pixels after considering the non-random distribution of ignition sources. We conducted two separate analyses to estimate the differences in (1) fire occurrence and (2) fire susceptibility amongst different vegetation types. By comparing the two estimates, we quantified the contribution of ignition source imbalance on fire patterns. For instance, if grasslands and forests are equally fire prone, but villagers only set fire to easily accessible grasslands not dense forests, we would see a large difference between grassland and forest fire occurrence, while observing no difference in fire susceptibility. The approach avoids the use of indirect proxies, such as distance to roads, to model ignition source distribution. This makes the analysis more robust and generalisable as the relationship between distance to roads and ignition source density is region-specific and dependent on socio-economic factors. Lastly, we also investigated into how topography interacted with vegetation type in determining fire susceptibility on a site level. All analyses below were carried out in *R-4.1.0* (R core team, 2021).

3.3.6.2 Fire occurrence

For each of the 17 biennial vegetation maps in the time series, we filtered out grassland, shrubland, and forest pixels, then tracked whether the pixels experienced a fire within the two-year window. We also took note of the TPI, TWI, cosine aspect, and slope of the pixels. The *WeightIt* package was used to assign entropy balancing (EBAL) weights to tackle topographical covariate imbalance amongst the four vegetation types (Greifer, 2019). The reweighting process is akin to matching grasslands, shrubland, and forest pixels with comparable background topography, but without discarding or synthetically creating data. We then used the reweighted data to build a logistic regression model that predicted fire occurrence from vegetation type and background topography. Odds ratios were calculated to estimate how fire occurrence differed between different vegetation types as result of both fire susceptibility and ignition source imbalance.

3.3.6.3 Fire susceptibility

Neighbourhood analysis was performed to estimate how vegetation type and background topography affected fire susceptibility when pixels were exposed to the same ignition source. To achieve this, we focused on the vicinity of detected burn areas where ignition sources were known to have existed. For each burn area polygon, we first located the centroid using the *st_centroid* function in the *sf* package.

We then drew the longest line between the centroid and the edge of the polygon. Using the line as the radius, we created a circle representing the theoretical maximum fire extent (orange circle, **Supp. Figure B.3**). The circle was modified by removing regions that were cut off by non-vegetated areas such as roads or other fire breaks. Pixels within the modified circle would have been exposed to the ignition source, with the vegetation fire susceptibility determining whether it actually burnt. We recognise that pixel fire susceptibility is affected by variables other than vegetation type, and the exposure of the encircled pixels to the ignition source may still vary (directed acyclic graph, or DAG, in **Supp. Figure B.4**). We addressed these measured and unmeasured confounding variables using *do*-calculus logic (Pearl, 1995, 2009; Shrier & Platt, 2008; Suttorp et al., 2015) (see **Appendix B:** for details). EBAL weights were assigned to the pixels to ensure that pixels of the four different vegetation classes were comparable with respect to the four topographical covariates and distance to fire centroid (Greifer, 2019; Markoulidakis et al., 2022; Matschinger et al., 2020). Using the weighted data, we built a logistic regression model that predicted fire susceptibility from vegetation type, topographical variables, and distance from burn area centroid. All continuous variables were scaled such that the coefficients reflected the effect sizes and variable importance. A forest plot was generated to evaluate variable importance using odds ratios calculated from the model coefficients. The detailed structure of models can be found in **Supp. Table B.3**.

3.3.7 Survival analysis on post-fire recovery

Post-fire vegetation recovery rates were quantified by running survival analysis on the times it took for burnt pixels to reach the next successional stage. We chose survival analysis as the data is temporal and right censored (Muenchow, 1986; Tepley et al., 2018; Therneau, 2019). Two types of right censorship were observed – pixels might have not reached the next successional stage by 2020 or might have experienced another fire. The latter type of censorship was problematic as repeated fires would disproportionally censor pixels that failed to recover. This violated the assumption of non-informative censorship in survival analysis (Therneau, 2019). Hence, we focused our study on the recovery trajectory after the last observed fire between 1986 and 2020. Another assumption made was the unidirectional vegetative succession without retrogressions. The assumption was largely met, with 97.1% of the pixels either staying in the same vegetation class or transitioning to a later successional stage over time (grasslands to shrublands to forests), so we proceeded after filtering out retrogressed pixels.

Median post-fire recovery times after grassland and shrubland fires were estimated by constructing Kaplan-Meier survival curves using the *survival* package (Therneau, 2019). The curves were built from: (1) survival time – the number of years the pixel "survived" as grassland or shrubland before transitioning into forest and (2) censorship – binary variable that records whether a pixel ever became forest in the observed period. The approach worked well for shrubland fires, but for grasslands, it was complicated by the median post-fire recovery time being longer than the 34-year study period. This was problematic as Kaplan-Meier curves are non-parametric and could not be easily extrapolated (Therneau, 2019). To tackle this, we estimated the grassland > young shrubland and young shrubland > forest recovery times separately. "Young shrubland" represented pixels that just transitioned from grassland to shrubland in our vegetation maps. While these pixels have not necessarily experienced a fire in the study period, it is likely that these pixels burnt in the past given the historical fire frequency in Hong Kong (A. H. Y. Chan et al., 2023). To ensure that the young shrubland pixels have the same topographical profile as the grassland burnt in our study period, we used the *WeightIt* package to generate EBAL weights based on cosine aspect, slope, TPI, and SWI (Greifer, 2019). Finally, we estimated the median grassland to forest recovery time by adding the survival times obtained from the two sets of Kaplan-Meier curves.

To investigate the relative importance of different factors in determining post-fire recovery rates, we used the *randomForestSRC* package to build a random survival forest (RSF) model (Ishwaran et al., 2023). The RSF model predicted recovery time from pre-fire vegetation type, burn severity (ts-RBR), distance to the nearest forest patch, cosine-aspect, slope, topographical position (TPI), and wetness (SWI). We used RSF as the non-parametric machine learning approach was more robust against multicollinear and non-linear relationships while still being able to handle right-censored temporal data (Ishwaran et al., 2008). Variable importance was estimated from the RSF model with subsampling inference and the delete-d jackknife estimator.

To visualise the partial effects of biophysical and topographical variables on post-fire recovery, we constructed 240 Kaplan-Meier curves based on stratified and reweighted datasets. Hypothesising that biophysical and topographical variables may have different effects on grassland and shrubland fires, we analysed grassland to shrubland and shrubland to forest transitions separately. We then stratified the two datasets by ts-RBR, forest distance, TPI, SWI, slope, and aspect, with 20 groups per variable. To isolate the effect of the variable in question, we reweighted the groups to tackle the imbalance of potentially confounding variables. For instance, it is reasonable to expect pixels with low TPI (valleys) being closer to forests and have lower burn severity (ts-RBR), so we assigned EBAL weights to pixels in the 20 TPI groups such that weighted pixels would have the same ts-RBR and forest distance distribution across the groups. Finally, we constructed 20 Kaplan-Meier curves per variable and quantified how changes in the variable affected median post-fire succession time. Further details regarding the Kaplan-Meier curves and EBAL weights can be found in **Supp. Table B.3**.

3.4 Results

3.4.1 Fire susceptibility, ignition source distribution, and fire occurrence

Our results support the existence of strong fire-vegetation feedbacks (fire traps) in the wet subtropics that were exacerbated by anthropogenic ignition source imbalance. From the neighbourhood analysis, it is estimated that the fire susceptibility of grasslands and shrublands were 19.5 and 8.5 times higher than that of forests, respectively, given the same exposure to ignition sources (**Figure 3.3**). Ignition sources were not randomly distributed. Grasslands and shrublands were 2.3 and 2.0 times more likely to be exposed to ignition sources compared to forests, respectively. The compounding effects of high fire susceptibility and increased exposure to anthropogenic ignition sources led to much larger differences in actual fire occurrence across vegetation types. Fire occurrence was 44.5 and 16.9 times higher amongst grassland and shrubland pixels, respectively, compared with forest pixels with similar background topographies. Background topography had relatively minor effects on vegetation fire susceptibility. Slope and topographical position had nearly no effect on fire susceptibility (**Figure 3.3**). Wetter (high SWI) pixels were less fire susceptible (**Figure 3.4a**) and aspect had vegetation-specific effects on fire susceptibility (**Figure 3.4b**), but their effect sizes were small compared to that of vegetation type and ignition source abundance (**Figure 3.3**). Overall, our results show that local fire regimes in the wet subtropics are defined by fire-vegetation feedbacks (fire traps) interacting with ignition source distribution, not background topography.

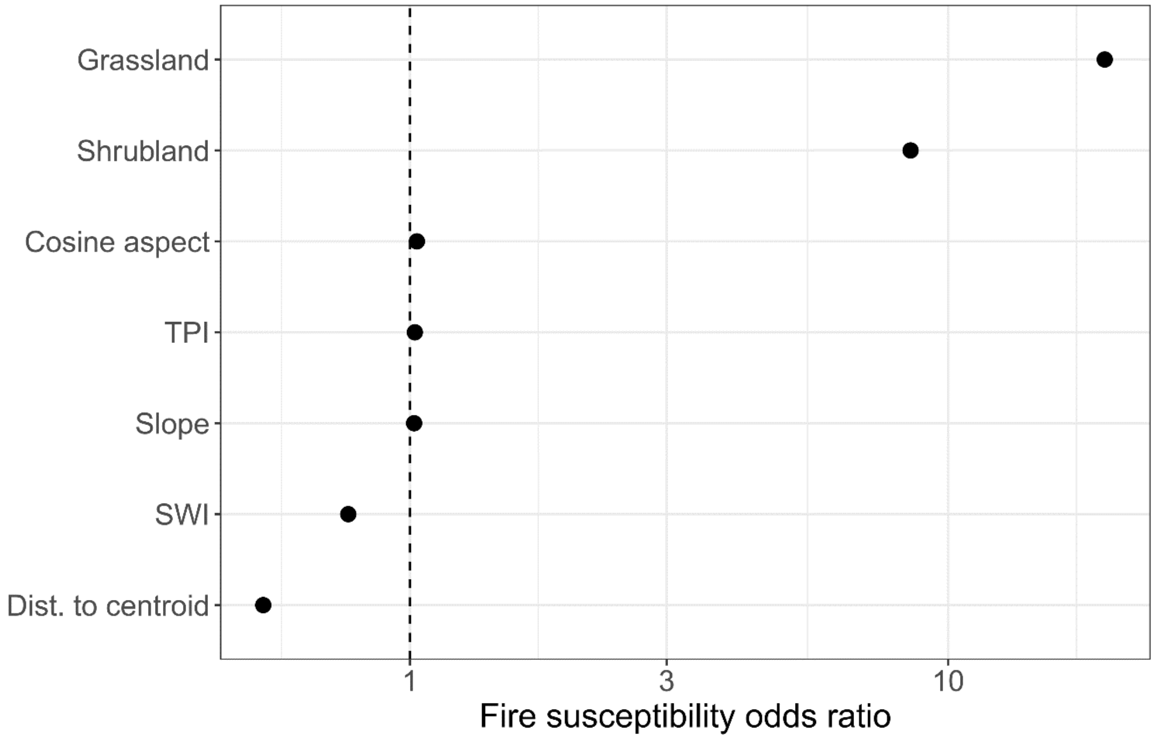

Figure 3.3: Effects of vegetation type and topographical variables on fire susceptibility in wet subtropical Hong Kong. Odds ratios represent how the variables change the likelihood of a pixel burning, given a fixed exposure to ignition sources. The odds ratios of the two categorical variables (grassland and shrubland) refers to the fire susceptibility compared to that of forests. "TPI" represents topographical position index. "SWI" represents SAGA wetness index. "Dist. to centroid" refers to the distance between the pixel and centroid of the burnt area in the neighbourhood analysis. All pixels in the neighbourhood analysis would have been close to known ignition sources, but a longer distance to centroid would indicate lower exposure at a local level. The 95% confidence intervals were too small to be visible.

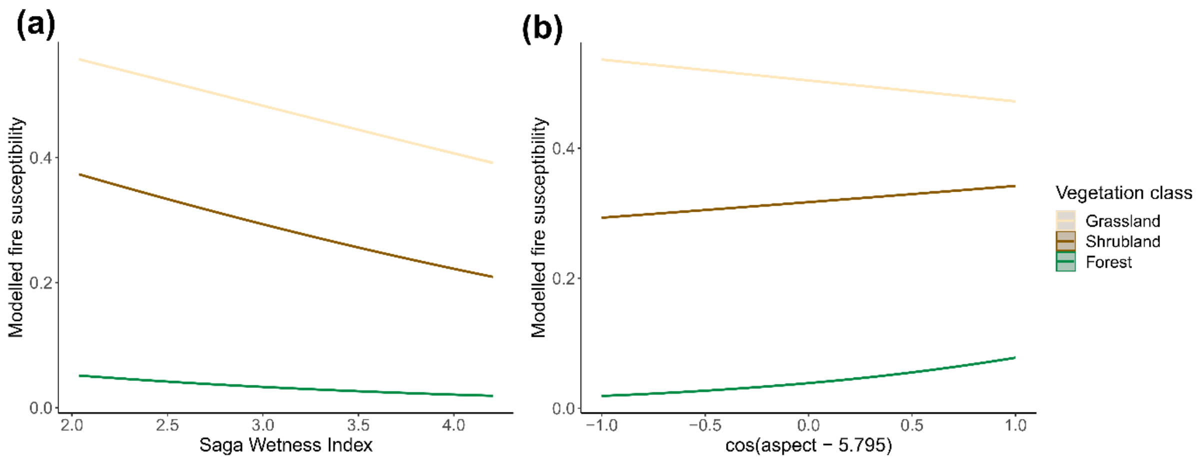

Figure 3.4: The effects of SAGA wetness index (SWI) and linearised aspect on fire susceptibility modelled by logistic regression. The shaded area (barely visible due to the large sample size) represents the 95% confidence interval.

3.4.2 Post-fire recovery

Pre-fire vegetation type significantly affected post-fire recovery rates, indicating strong legacy effects. The proportion of pixels in each vegetation class before and after detected fires were tallied in **Figure 3.5**, which shows how pixels moved through the stages of succession over time. Note that while some shrubland pixels retrogressed to grasslands after fires, most tended to stay in the same class. The median time required for grasslands to recover back to forests after fires was 40 years, while shrublands on similar topographies recovered in 19.2 years.

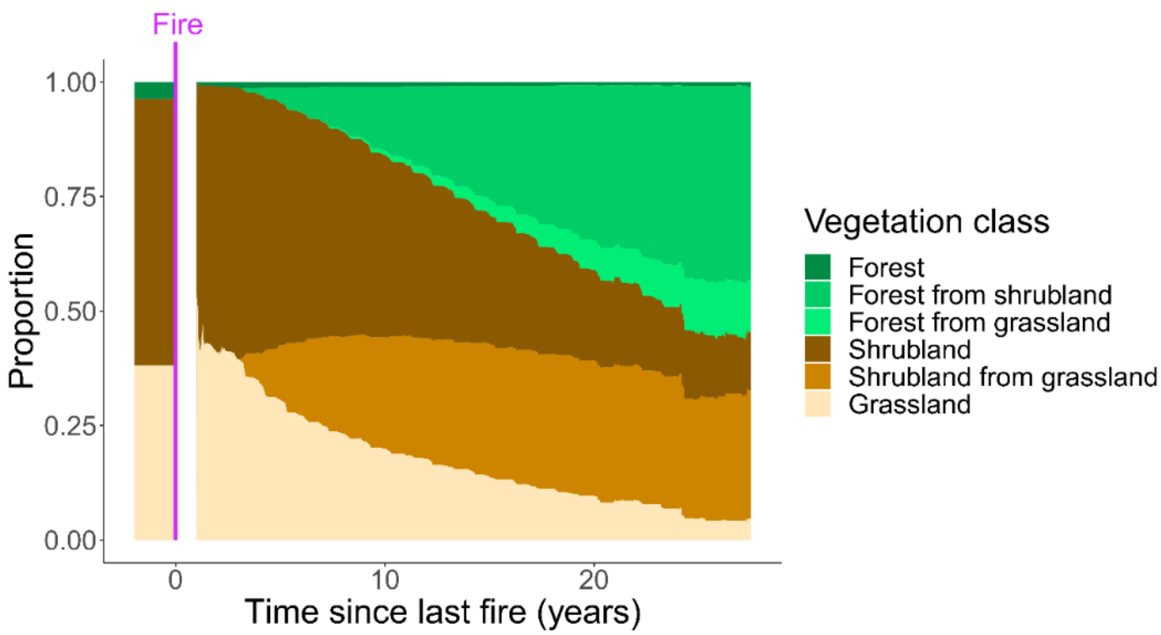

Figure 3.5: Area plot to visualise post-fire recovery trajectories in wet subtropical Hong Kong. The y-axis represents the proportion of pixels in each vegetation class before (left of the magenta line) and after (right of the magenta line) the fire.

Post-fire recovery rates were highly variable and correlated with a range of vegetative, biophysical, and topographical factors (**Figure 3.6**). Post-fire distance to the nearest forest patch strongly affected rate of recovery (**Figure 3.6 and Figure 3.7**). Sites closer to forest patches recovered significantly faster than those further away from forest patches (**Supp. Figure B.5a-b and Figure 3.7**). The effects were strongest for pixels between 0-250 m from forest patch, but levelled off after 250 m. Aspect had a significant cyclical effect on post-fire recovery rates (**Figure 3.7**). For both grassland to shrubland and shrubland to forest transitions, sites facing the northwest recovered the quickest (**Figure 3.7**). Interestingly, burn severity was found to have significant but opposite effects on post-fire recovery rates in grasslands and shrublands. Severe fires (high ts-RBR) promoted recovery to shrubland after grassland fires, but inhibited recovery to forests after shrubland fires (**Figure 3.7**). These effects persisted through the Kaplan-Meier curves (**Supp. Figure B.5c-d**). Finally, pixels in valleys (low TPI) recovered quicker than those on ridges (high TPI), and, given the same topographical position, wetter pixels (high SWI) recovered quicker than drier ones (low SWI). The variable importances of both TPI and SWI were smaller than other variables assessed (**Figure 3.6**), but both factors seem to be proportionally more important for the transition to shrublands after grassland fires (**Figure 3.7**). Slope was found to be a non-significant predictor in the RSF model (**Figure 3.6**), with the slope-stratified dataset generating broadly negative but messy relationships between slope and median recovery times (**Figure 3.7**). The multitude of factors influencing recovery contrast with the analyses of fire susceptibility, in which a single factor – vegetation type – stood out as the predominant driver.

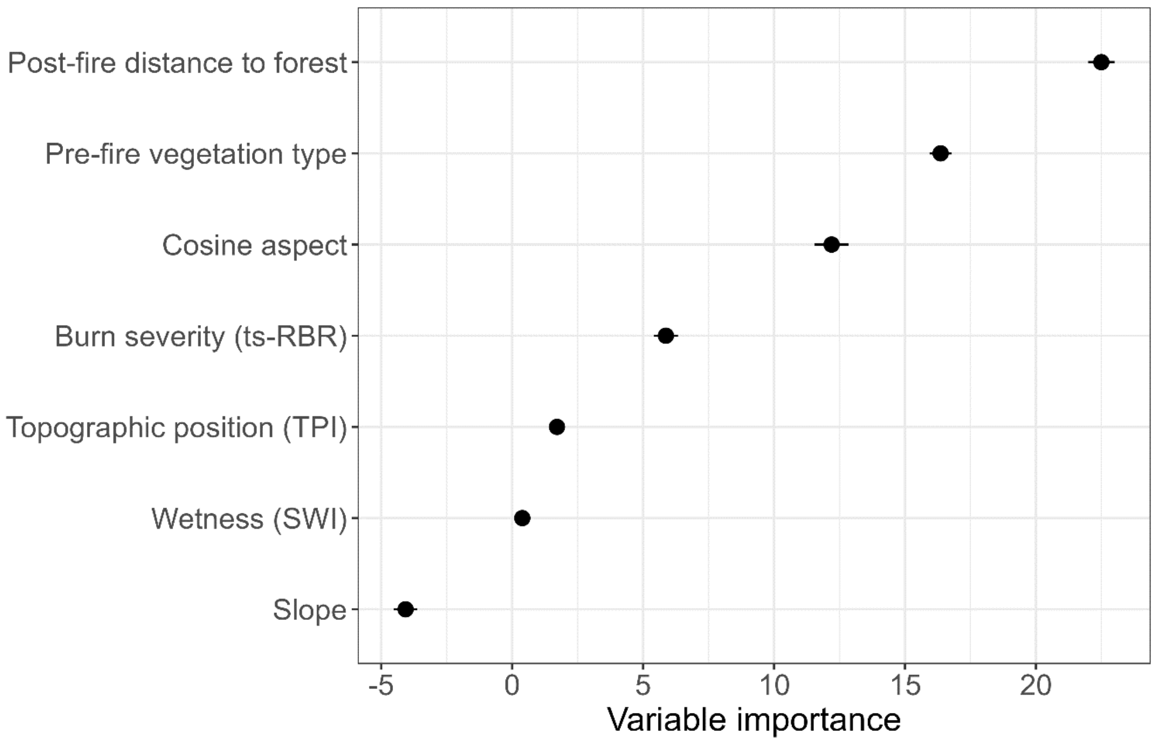

Figure 3.6: Variable importance derived from a random survival forest (RSF) model that predicts median post-fire recovery times back to forests. All variables were statistically significant ($p < 0.05$) except for slope. Confidence intervals for variable importances were calculated by subsampling the dataset and using the delete-d jackknife estimator.

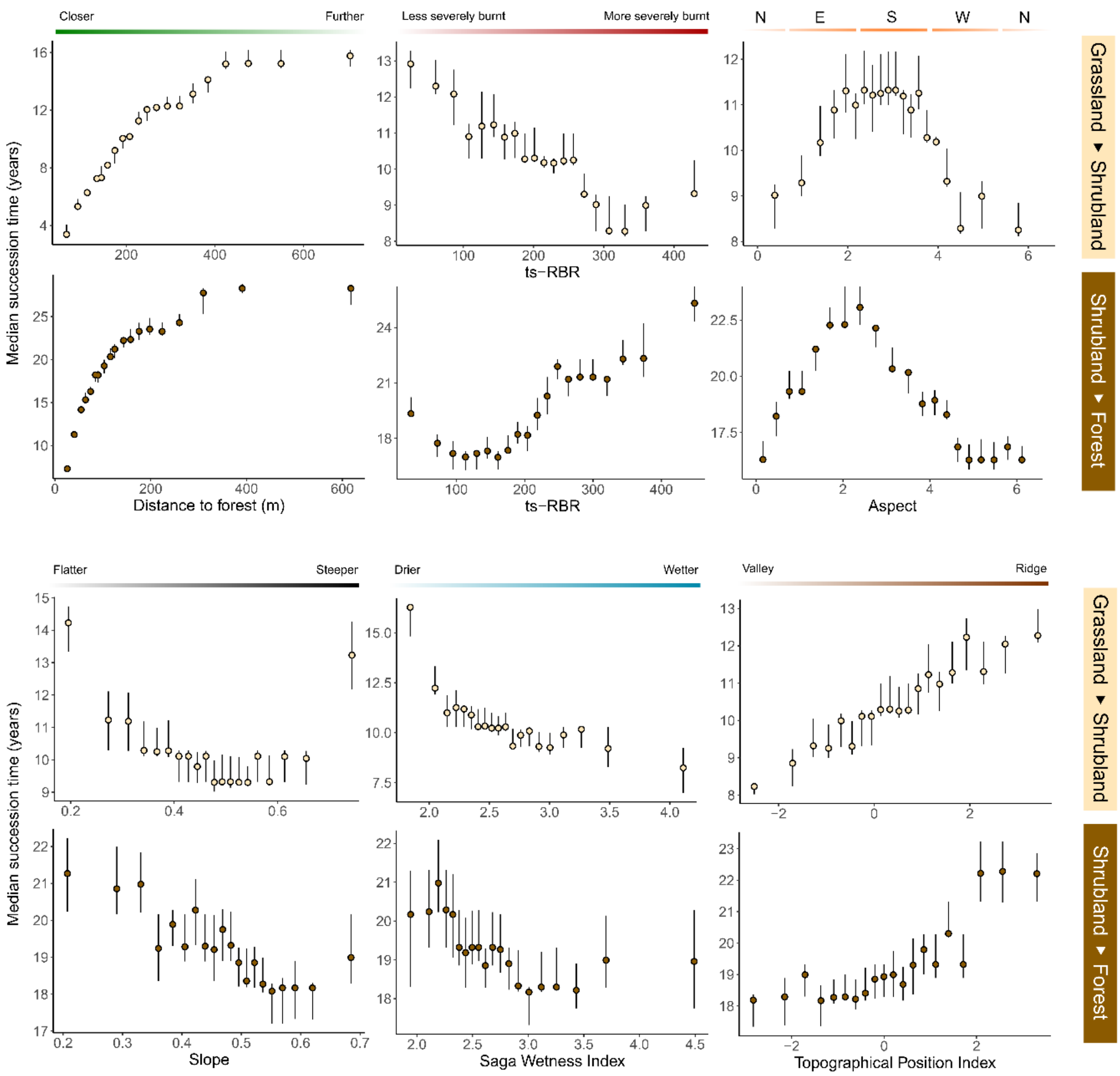

Figure 3.7: Plots showing how different variables affect median recovery times for the transition from burnt grassland to shrubland and burnt shrubland to forest. The median recovery times were estimated by stratifying the dataset by the variable in question and building Kaplan-Meier curves for each stratified group. Pixels in the groups were assigned entropy balancing (EBAL) weights to tackle the imbalance of relevant covariates to isolate the effect of the variable in question (see **Supp. Table B.3**). The error bars represent 95% confidence intervals.

3.5 Discussion

3.5.1 Quantifying the strength of the fire trap

This study demonstrates the existence of strong fire-vegetation feedbacks in the wet subtropics. Degraded grasslands and shrublands were 20 and 9 times more fire-susceptible than forests. Previous research showed that grassy fuels have three times lower bulk densities compared to litter fuels (Prior et al., 2017), and shrubs produce finer litter fuels than forest trees (Plucinski et al., 2010). Given that wet subtropical vegetation is not generally fuel limiting, the lower fuel bulk densities in grasslands and shrublands lead to high ignitability and rapid rate of fire spread (Hoffmann, Jaconis, et al., 2012; Iván et al., 2023; Prior et al., 2017; Uhl et al., 1988). Additionally, as more open habitats, grasslands and shrublands tend to retain moisture poorly (Hoffmann, Jaconis, et al., 2012; Iván et al., 2023). In particular, *Dicranopteris* fern mats and C4 grasses are commonly found in open habitats in Hong Kong. These vegetation types accumulate dead biomass that decompose slowly and desiccate easily, making them particularly fire-prone (Hoffmann, Jaconis, et al., 2012; Matos et al., 2002). Th high fire susceptibility of early successional vegetation creates fire traps that make degraded wet tropical and subtropical landscapes inherently difficult to restore.

Anthropogenic ignition source imbalance – the tendency for humans to set fire to open grassland and shrubland habitats – greatly exacerbated natural fire traps. In our study area, humans introduced 2.3 and 2 times more ignition sources to grasslands and shrublands, leading to the actual fire occurrences of the two early successional vegetation types being 45 and 17 times higher than in forest patches of comparable background topography. Using distance to roads and settlements as proxies, previous studies also reported the importance of anthropogenic ignition sources in affecting fire occurrence (Oliveira et al., 2012; Tien Bui et al., 2016). Our results further demonstrates that these ignition sources are not evenly distributed across different vegetation types. Grasslands and shrublands receive more sources of ignition either because they are more accessible to humans or, alternatively, sites closer to settlements tend to be more degraded and less forested.

Surprisingly, background topography hardly affected fire susceptibility. The effect size of the strongest topographical predictor, wetness (SWI), was an order of magnitude smaller than vegetation type and ignition source exposure. This echoes other studies in the region (Tien Bui et al., 2016) but is in stark contrast with results from Mediterranean Europe, where several studies reported clear effects of slope or aspect on fire susceptibility, with effect sizes in the same order of magnitude as that of background vegetation type (Barros & Pereira, 2014; Carmo et al., 2011; Oliveira et al., 2013). These differences highlight how fire regimes in the wet tropics and subtropics fundamentally differ from that in other biomes.

3.5.2 Factors influencing post-fire recovery rates

Pre-fire vegetation type was the strongest predictor of post-fire recovery rate, with shrublands recovering much quicker than grasslands after experiencing a fire (median recovery time 19 years vs 40 years). Many shrubs and pioneer trees tend to survive the fires and resprout, even in the ecoregions where fires are naturally scarce (K. L. Chau, 1994; Teixeira et al., 2020; Van Nieuwstadt et al., 2001). The ability to re-establish itself using basal or epicormic regrowth might partly have evolved against rare natural fires, but it is more likely to be a general trait that helps these species recovery from other disturbances posed by large herbivores or windstorms (K. L. Chau, 1994; Teixeira et al., 2020).

Other than pre-fire vegetation type, the distance from the nearest forest patch after fires had an equally strong effect on post-fire recovery rates. The relationship between forest distance and recovery time was found to be non-linear and flattens out over distances >250m. This resembles the inverse of seed dispersal kernels, which indicates limitations in seed availability (Flores & Holmgren, 2021; Herrmann et al., 2016; Levine & Murrell, 2003; Rogers et al., 2019). Unlike regions were serotiny is the norm, burnt patches in the wet tropics and subtropics rely heavily on external seed sources to move along the recovery trajectory (Flores & Holmgren, 2021; Van Nieuwstadt et al., 2001). Au et al. (2006) quantified the seed rain in degraded grasslands and shrublands in the study area and found large variations in the number of seeds per m^2 per year, ranging from 47 in open grasslands to >6000 under female shrubs on grasslands. While one might argue that 47 seeds per m^2 per year might be sufficient to push the landscape through succession, many seeds would fail to penetrate the dense mats of early successional grasses or ferns to reach the mineral soils, and established seedlings can get smothered under the thick vegetation (Pang et al., 2018; Rochimi et al., 2021). Many seeds may also belong to shorter shrub species that may not necessarily help the site recover back to forests. Most species in the four dominant tree families in Hong Kong (Lauraceae, Moraceae, Fagaceae, Euphorbiaceae) rely on animals for seed dispersal (Dudgeon & Corlett, 2004). The lack of perch sites for birds and suitable habitats for scatter-hoarding mammals could prevent the seed dispersal kernels from extending into large burnt areas far from forest patches (Au et al., 2006; Levine & Murrell, 2003; Rogers et al., 2019).

Interestingly, high burn severities promoted post-fire recovery in burnt grasslands but inhibited recovery in burnt shrublands (**Supp. Figure B.5c-d, and Figure 3.7**). Past studies have generally found post-fire recovery times to be longer for more severely burnt sites, even if recovery rates were higher (Bartels et al., 2016; Bright et al., 2019; Ireland & Petropoulos, 2015). Severe fires tend to cause higher plant mortality, especially for fire-sensitive late successional tree saplings (Bright et al., 2019; Hoffmann et al., 2003). This corroborates with the patterns observed in shrublands in our study (**Supp. Figure B.5d and Figure 3.7**). The opposite relationship observed in grasslands was, however, unexpected. One possible explanation is that dense grasslands might have arrested succession (Rochimi et al., 2021). More severe fires could open the habitat for shrub or tree encroachment, though targeted field surveys would be needed to test this hypothesis.

Background topography also had strong influences on post-fire recovery rates. Echoing previous studies conducted in the northern hemisphere (Ireland & Petropoulos, 2015; Pausas & Vallejo, 1999; Wittenberg et al., 2007), we found post-fire recovery to be faster on north-facing slopes. This could be attributable to more sheltering on north-facing slopes, which dampen local fluctuations in temperature and humidity (Ireland & Petropoulos, 2015; Stage, 1976; Stage & Salas, 2007). We would also expect such sheltering to benefit east-facing slopes, as it warms up quicker in the morning but avoids overheating during the day (Stage, 1976). The optimal aspect for post-fire recovery was, however, skewed to the northwest in Hong Kong (**Figure 3.7**). This might be due to the prevailing wind direction in Hong Kong from the southeast, which leaves westward slopes better sheltered (Hong Kong Observatory, 2023). We also found that sites in valleys (low TPI) and wetter areas (high SWI) had quicker post-fire recovery. Research have demonstrated that DTM-based position and wetness indices serve as effective proxies of variations of microclimates (Jucker et al., 2018; Man et al., 2022; Marsh, Crockett, et al., 2022; Marsh, Krofcheck, et al., 2022). A recent study by Marsh, Crockett, et al. (2022) found DTM-based topographical variables to be almost as accurate as direct microclimatic measurements in predicting post-fire seedling survival in New Mexico. The study reported high seedling survival in areas with high topographical wetness and low TPI, which corroborates with patterns in post-fire recovery observed in Hong Kong. Our results further suggest that TPI and SWI may be affecting post-fire recovery in slightly different ways despite the two variables being correlated with each other. TPI did not fully capture the variation in wetness. Even after reweighting by TPI, SWI was still negatively correlated with recovery times (**Figure 3.7**). SWI may have captured edaphic factors better (e.g. soils in slopes at the foot of mountains may be wetter than valleys near mountaintops) (Böhner & Selige, 2006). On the other hand, TPI was a more important variable for predicting recovery times in the RSF model (**Figure 3.6**), indicating that it might have captured information other than wetness, such as sheltering from wind or direct sunlight (Dobrowski, 2011; Jucker et al., 2018). Interestingly, wetness seems to have a stronger effect on the grassland to shrubland transition than in the shrubland to forest transition (**Figure 3.7**). Research in nearby Guangdong suggests that shrubs act as both facilitators and competitors to tree saplings in wet subtropical environments (N. Liu et al., 2013). In drier sites, shrubs moderate post-disturbance microclimates by reducing irradiance and ameliorate temperature fluctuations (Crockett & Hurteau, 2022; N. Liu et al., 2013; Urza et al., 2019). In wetter sites, shrubs compete with tree saplings and undermine the topographical benefits (N. Liu et al., 2013). Our results indicate that these biotic buffering effects of shrubs may have overridden topographical determinants of post-fire recovery rates, which, over a landscape scale, might smooth out spatial variations in rates of forest establishment after shrubland fires.

3.5.3 Escaping the fire trap

Fire traps make it inherently difficult for land managers to suppress fires on degraded wet subtropical landscapes, but several policy actions could help overcome these traps. While our results supported the existence of strong natural fire-vegetation feedbacks, it also revealed the observed difference in fire occurrence to be partly anthropogenic due to ignition source imbalance. In other words, fire suppression campaigns would not only reduce fire occurrence across all habitats but would also disproportionally reduce fire occurrence in early successional vegetation. Hong Kong also provides a valuable case study for how fire suppression should be carried out in the wet tropics and subtropics. Over the past 70 years, the government set up a Fire Danger Warning System based on weather and fuel conditions (Hong Kong Observatory, 2023). Public education campaigns were launched to prompt citizens to properly handle potential ignition sources and heed any fire warnings. The government then established a network of 11 fire lookouts on mountaintops such that fires are quickly detected and tackled. The results of these efforts were substantial, with yearly fire occurrence more than halved over the last three decades (A. H. Y. Chan et al., 2023). While the approach would be costly to implement over larger areas in developing countries, it nevertheless provides a viable pathway towards effective fire-suppression. Fires could also be managed by controlling their spread. Fire breaks can stop ignition sources in other areas from spilling over to sites designated for restoration (Scheper et al., 2021). A common approach to establish fire breaks is to remove vegetation across a strip of land to create "fuel breaks" (Shinneman et al., 2019). Our results, however, suggest that this might be ineffective in the wet subtropics. Vegetative regrowth on fuel breaks is fast in wet ecoregions, which makes them difficult to maintain (A. H. Y. Chan et al., 2023; Rochimi et al., 2021; Scheper et al., 2021). If not properly maintained, grasses and shrubs would be highly susceptible to fires regardless of the background topography of the fuel break (**Figure 3.4**). Green fire breaks may provide a viable alternative in the wet tropics. These fire breaks are created by planting strips of secondary forest or connecting fragmented forest patches (Curran et al., 2017). This could be effective in the wet subtropics by levying the fire-vegetation feedback and the fire-resistance of close-canopied forests to stop fire spread, although the ideal width of these breaks would need to be determined by further investigation and experimentation.

Results from this study also have direct implications on vegetation management after fires. Firstly, rather than using the rebound time of vegetation indices such as NDVI, we quantified post-fire recovery rates by estimating recovery time back to the next successional stage or close-canopied forests. This is much more relevant for land managers hoping to restore the landscape past its pre-fire degraded condition. Unlike fire-susceptibility, post-fire recovery in the wet subtropics is significantly affected by a range of vegetation, biophysical, and topographical factors. Land managers may consider using the results to perform direct seeding in regions where natural seed sources are rare. Resources could be redirected to replant burnt sites that would not have naturally recovered within a reasonable time frame (Law et al., 2023; Rurangwa et al., 2021). Alternatively, under budget limitations, managers could also consider using the model to identify areas that could readily undergo natural regeneration. These areas could be prioritised and protected from further disturbances before attempting to restore areas that require active interventions.

Chapter 4: Modelling wind speeds across complex topographies using open-source computational fluid dynamics (CFD) software

4.1 Abstract

Modelling near-surface wind speeds across complex topographies is technically challenging and expensive. The development of free and open-source computational fluid dynamics (CFD) modelling software provides new opportunities to model wind speeds, but validated wind maps remain scarce. We used WindNinja, a free CFD solver based on open-source programmes, to build wind models for different wind scenarios across the rugged subtropical landscape of Hong Kong. We estimated near-surface wind speeds by averaging multiple CFD-modelled scenarios based on actual wind data collected from 27 weather stations in Hong Kong. The estimated wind speeds were cross validated by wind data from weather stations and our own anemometers. Compared to a null model that used elevation and wind speeds in nearby stations as predictors, the CFD-based models were better at estimating near-surface wind speeds (RMSE of 4.22 km/h vs 3.77 km/h). The advantage of the CFD models were especially apparent when the study area was affected by strong winds from typhoons or monsoons. We highlighted several areas in the wind modelling pipeline that could be improved in future work, such as better inclusion of surface roughness into the modelling pipeline and subdividing the study area to improve local wind speed estimations. Despite the shortfalls, the study demonstrated how open-sourced software could generate reasonable validated wind maps across complex topographies at affordable computational and monetary costs.

4.2 Introduction

Near-surface wind speed is an important environmental factor for research on forest ecosystems, fire management, renewable energy, and hydrology. Our understanding of wind begins with direct measurements of surface wind speeds using anemometers in weather stations or mounted on masts. However, the limitations of these measurements are apparent. Even with the rapid development of doppler wind LiDAR systems that remotely measure wind speeds (Z. Liu et al., 2019), measurements still have limited spatial coverage and does not provide wall to wall surface wind estimations required in many use cases. We thus rely on wind modelling to expand our understanding of wind regimes across the landscape.

Wind modelling requires an understanding and approximation of how wind flows through the landscape, including the speed and direction at different heights. In flat terrains with low roughness, wind follows a power law or logarithmic wind profile, with higher wind speeds at higher heights above ground

(Wieringa, 1986). These profiles are shifted or stretched when objects like houses or tall vegetation increases the roughness length of the landscape (Wieringa, 1986). Wind profiles are quickly complicated under complex background terrains in mountainous areas. Wind speeds increase significantly on windward slopes but are sheltered on leeward slopes (Belcher et al., 2011; Finnigan et al., 2020; Lemelin et al., 1988; C. A. Miller & Davenport, 1998). Mountains cast wind shadows based on incoming wind direction. The size of these wind shadows depends on wind speed and the associated deflection of wind (Belcher et al., 2011; Finnigan et al., 2020). On steeper hills, separation bubbles could form on leeward slopes, which cause wind near the boundary layer to reverse direction (Belcher et al., 2011; Finnigan et al., 2020; Kaimal & Finnigan, 1994). In narrow valleys, the Venturi effect is known to speed up incoming wind (Mikkola et al., 2023). To create useful estimations of surface winds, these processes need to be considered and approximated in computational fluid dynamics (CFD) modelling.

Several numerical models to model surface wind have been developed and made available to researchers, but the adoption of these products remain challenging for several reasons. Firstly, computational fluid dynamics (CFD) modelling is very computationally expensive. Many use cases, such as the mapping of microclimates of forest habitats, require sub-hectare level spatial resolutions of wind models. Modelling wind at fine scales could easily overwhelm even the most powerful computers available. Secondly, due to the complexity of CFD modelling, the task could be technically formidable for non-experts. Most CFD programmes are not free or open-source. The cost of acquiring CFD solver software or even commissioning experts to produce wind models could be prohibitive for non-commercial applications (Clifton et al., 2022; Jasak, 2009). Thirdly, the use of CFD surface wind models is often hindered by the difficulty in validation. Existing software is often only validated in the areas where the software has been developed before being published. For instance, the Wind Analysis and Application Program (WAsP) was mainly validated in Denmark and later several locations in continental Europe (Berge et al., 2006; Lange & Højstrup, 2001; Mortensen et al., 1993); WindSim is validated in two sites of undisclosed location (Wallbank, 2008); and WindNinja is developed and validated with wind measurements from three sites in the US (Wagenbrenner et al., 2019). The accuracy of these models far from its validation window (e.g. in mountainous regions covered by tropical vegetation) needs to be better investigated. Validation data in sites of interests could, however, be scarce and expensive to collect (Clifton et al., 2022). In particular, a recent review on the use of CFD modelling to study effects of tropical cyclones have found a general lack to sufficient model validation (Shah et al., 2023).

This chapter aims at exploring the use of free and open-source software to generate reasonable surface wind models for sites with complex topographies. We experimented with the use of WindNinja, a free surface wind solver built upon an open-sourced CFD software (OpenFOAM), on building surface wind maps for the rugged subtropical countryside of Hong Kong. The resulting wind models were validated using an extensive collection of anemometer data. The wind models developed in this Chapter are used in Chapter 6 to understand the impacts of wind on forest dynamics.

4.3 Methods

4.3.1 Study area

We conducted the study in the complex topography of Hong Kong (22° 16’ 8’’ N, 113° 57’ 6’’E). The 2755 km^2 special administrative region boarders the city of Shenzhen in the north, faces the South China Sea in the south, and faces the Pearl River estuary to the west (**Figure 4.1**). The sea accounts for 60% of the total area of the territory, with the land area mainly comprised of islands and peninsulas. The land area has a diverse set of different land cover types. As a financial centre, urban areas in Hong Kong are exceptionally dense and is filled with high rises. The territory is, however, very rugged so much of the territory (ca. 60%) remains vegetated. Most of the vegetated area is protected as country parks and is covered by subtropical rainforests, shrublands, or grasslands. Dotted across the countryside are the >300 steep sided hills of heights >100 meters above sea level (m.a.s.l.), with the tallest (Tai Mo Shan) rising to 957 m.a.s.l.. Compared to many subtropical regions of similar latitude (e.g. Hawaii), the wind regime in Hong Kong is complex and shows strong seasonality. Prevailing winds sweep through Hong Kong from the east, but as the territory is sandwiched between a large landmass towards the north and the ocean towards the south, strong monsoons bring substantial variation to local winds. Summer monsoons bring wind from the southwest, while winter monsoons bring northeasterly winds. Located within the Northwest Pacific tropical cyclone hotspot, typhoons are a common occurrence in Hong Kong, with several of these storm systems bringing very high wind speeds to the territory each year. Together, these features make Hong Kong a challenging yet interesting landscape for wind modelling.

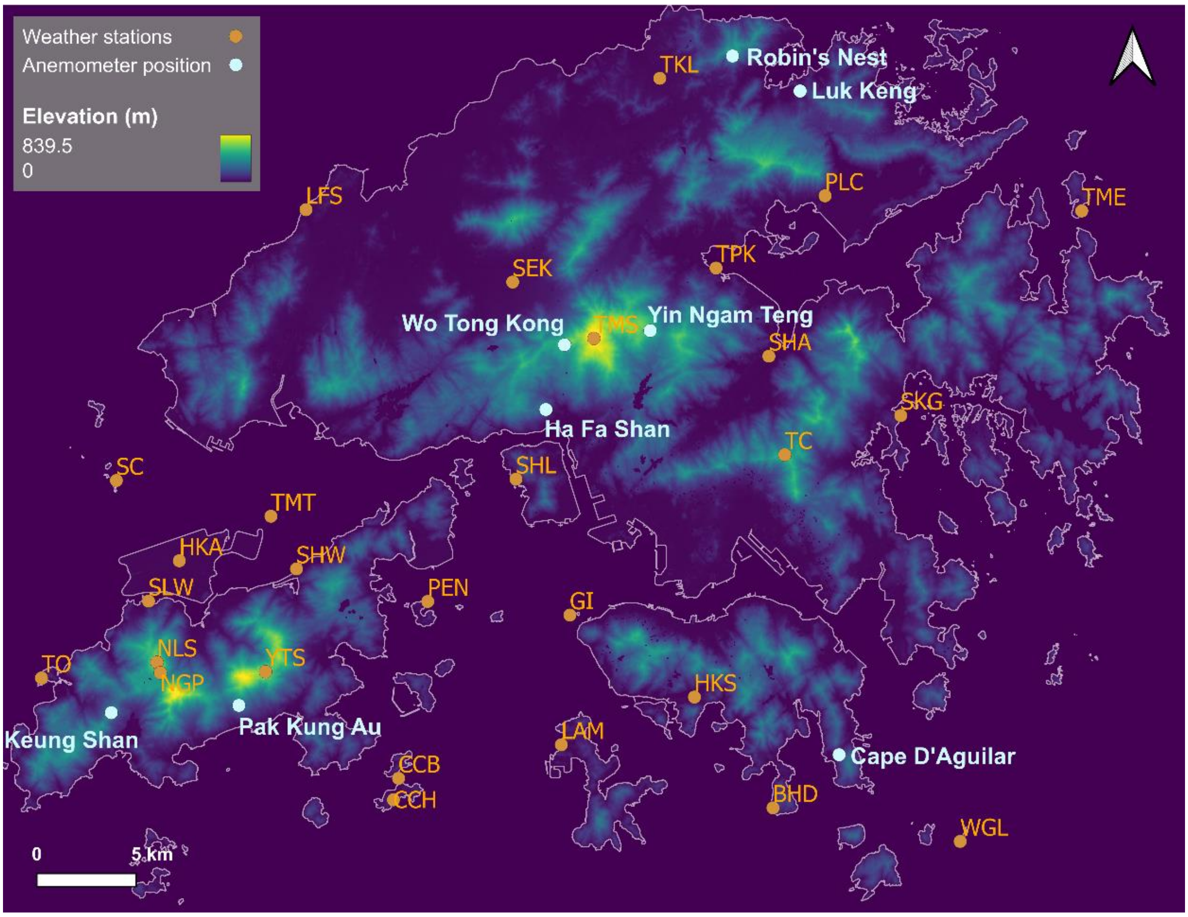

Figure 4.1: The network of non-urban weather stations (n = 28) and our own anemometers (n = 8) across the complex topography of Hong Kong. The code names of the weather stations refers to that used by the Hong Kong Observatory (Hong Kong Observatory, 2023). The background shows the LiDAR-derived digital terrain model of Hong Kong with the land area being outlined in white.

4.3.2 Background topography

The background topography of Hong Kong was mapped using a LiDAR-derived digital surface model (DSM). The LiDAR dataset was collected by a manned aircraft commissioned by the Civil Engineering and Development Department of the Hong Kong government in early 2020. The LiDAR point cloud (point density = 54.5 points/m^2) was processed using *LAStools* (Isenburg, 2020). In particular, we used the *las2dem* function to create spike-free DSMs from all LiDAR returns. The detailed principles of the approach can be found in Khosravipour et al. (2016). Since mountains located outside Hong Kong could affect wind speeds in the territory, we further expanded the 2020 LiDAR-based DSM using SRTM Digital Elevation Data Version 4 (Jarvis et al., 2008). Specifically, we added a 15 km buffer to the existing DSM to include parts of Shenzhen, including Wutong Mountain (943.7 m.a.s.l.) and Dapeng Peninsula.

4.3.3 Wind data

Local wind data for model validation were obtained from two sources: (1) the local observatory and (2) our own anemometers. The dataset collected by the Hong Kong Observatory was obtained from

38 automatic weather stations and spans over 37 years (1984-2022). For each of the 38 stations, the wind speed, direction, and gust were continuously measured at 10 m aboveground averaged across hourly time steps. We removed 10 urban stations that were within 500 m of high-rising buildings, leaving anemometer data collected from 28 non-urban weather stations. While the 28 stations represent one of the densest local anemometer networks in TC-prone regions, they are mainly located on mountaintops, rooftops of man-made structures, or near the coast. To ensure that our wind models accurately estimate wind speeds on slopes, we additionally placed a temporary cup anemometer linked to a HOBO U30 data logger on eight hillslope sites. The sites were chosen such that the surrounding area was devoid of tall vegetation to avoid local wind shadows cast by trees. The anemometer was secured on a plastic pipe mounted on a tripod at a height of 2.4 m aboveground and measures wind speed and gusts every 30 seconds. The locations where wind data was collected are shown in **Figure 4.1**.

4.3.4 Wind modelling

We modelled surface winds in Hong Kong by combining outputs of the "conservation of mass and momentum solver" in WindNinja. WindNinja (available on https://weather.firelab.org/windninja/) is a free CFD modelling software developed by the Missoula Fire Sciences Laboratory (Forthofer et al., 2014). The programme provides solvers to estimate wind speeds across the landscape at user-specified heights above ground based on two inputs – (1) a digital surface model (DSM) of the area and (2) a set of initial conditions (domain average wind speed and direction). Two separate solvers are available in WindNinja – the "conservation of mass" and the "conservation of mass and momentum" solver. While the former is designed to maximise computational speed for wildfire behaviour modelling, we would focus on the latter as previous validation efforts have found it to provide more realistic approximations of surface winds, especially on leeward slopes in complex terrains (Wagenbrenner et al., 2019). The "conservation of mass and momentum" solver is a numerical model based on Reynolds-Averaged Navier-Stokes (RANS) equations, assuming steady, incompressible, turbulent, and neutrally-stratified wind flows. Its mesh creation and CFD calculations are built upon OpenFOAM, a free and open-sourced CFD modelling software (Jasak, 2009; Wagenbrenner et al., 2019).

Using WindNinja, we modelled wind speeds for 128 domain average wind scenarios. Specifically, we generated wind speed and direction rasters from the products of 8 compass directions (0°, 45°, 90°, 135°, 180°, 225°, 270°, 315°) and 16 wind speeds in km/h (1, 8, 13, 17, 21, 24, 28, 32, 37, 44, 50, 70, 100, 150, 200, 250). The mesh resolution was set to 60 m; background vegetation type was set to "-brush"; and both the input and output wind height was set to 10 m aboveground to match that of the anemometer data. The modelling was carried out in a Windows workstation with 48 cores and 1TB RAM.

We then used combinations of the 128 domain average wind scenarios to estimate time-resolved surface wind speeds. In order to cross-validate the results, we first split the wind data collected from the 28 weather stations into 10 folds. In each of the 10 iterations, we took the wind measurements from 9 folds as training and used the remaining fold for validation. During every hour in the 37 years for which we have data, we identified the four scenarios where wind directions and speeds most closely matched that of the training data. We then took a weighted average of the four scenarios to obtain a time-specific estimation of surface wind direction and speed. We then applied a roughness correction on these estimations as WindNinja currently does not incorporate variations in surface roughness in its CFD model, which makes it prone to overestimating wind from rough urban areas and underestimating wind from smoother oceans. Following Wieringa (1986), we assigned roughness lengths to pixels based on its land cover class. For each pixel, we then estimated directional roughness by calculating distance-weighted roughness of the eight compass directions. We then corrected the estimated wind speeds using a simple linear regression model (prediction error ~ roughness + roughness:predicted wind speed). The accuracy of the roughness-corrected wind speed estimates were validated using the holdout validation dataset.

Alternatively, we built a null model where we used (1) the mean wind speed across all stations and (2) elevation to predict location-specific wind speeds. We compared the performance of the CFD-based model and the null model in predicting (1) overall mean wind speeds of weather stations and (2) wind speeds during typhoons or monsoons. The accuracies of the wind models were evaluated by calculating the absolute root mean square error (RMSE) and percentage root mean square error (%RMSE) between the actual and predicted wind speed.

Finally, apart from cross validating the wind models using the weather station data, we also validated the models with our own anemometer measurements on slopes. We used the weather station data to produce time-resolved hourly estimates of surface wind speeds at the locations where we set up our own anemometer. The estimated surface wind speed, both by the CFD model and the null model, were compared to the wind speeds we observed at the site. It is important to note that our anemometers were measuring wind speed at approximately 2.4 m above ground. Although wind speeds 2.4 m above ground (observed) would be correlated with speeds at 10 m above ground (model prediction), local surface roughness caused by vegetation could easily introduce location-specific, systematic biases. Hence, RMSE and %RMSE is not a good measurement of model accuracy. We therefore used an alternative way to validate the models and relied on the R^2 of linear regression models through the data (actual ~ predicted wind speeds) instead.

4.4 Results

4.4.1 Validation with weather station data – mean wind speed

Results from the 10-fold cross validation using the weather station anemometer data showed that the the computational fluid dynamics (CFD) model performed better than the null model in estimating long-term mean wind speeds. The root mean square error (RMSE) of the CFD model was 3.77 km/h, representing a percentage RMSE (%RMSE) of 30%. Meanwhile, the null model had a higher RMSE of 4.22 km/h, representing a %RMSE of 41%. The results are summarised in **Figure 4.2**, where the vertices of each polygon represent the predicted and actual mean wind speeds for wind blowing from the eight compass directions. An ideal wind model should produce points close to blue line, with edges of polygons parallel to the blue line. While elevation does capture some variation of wind speed, the null model was making predictions at the 10-15 km/h range for most weather stations at low elevations. The CFD model, being able to capture the effects of wind shadows, produce more reasonable estimates that line up better with the blue 1:1 line.

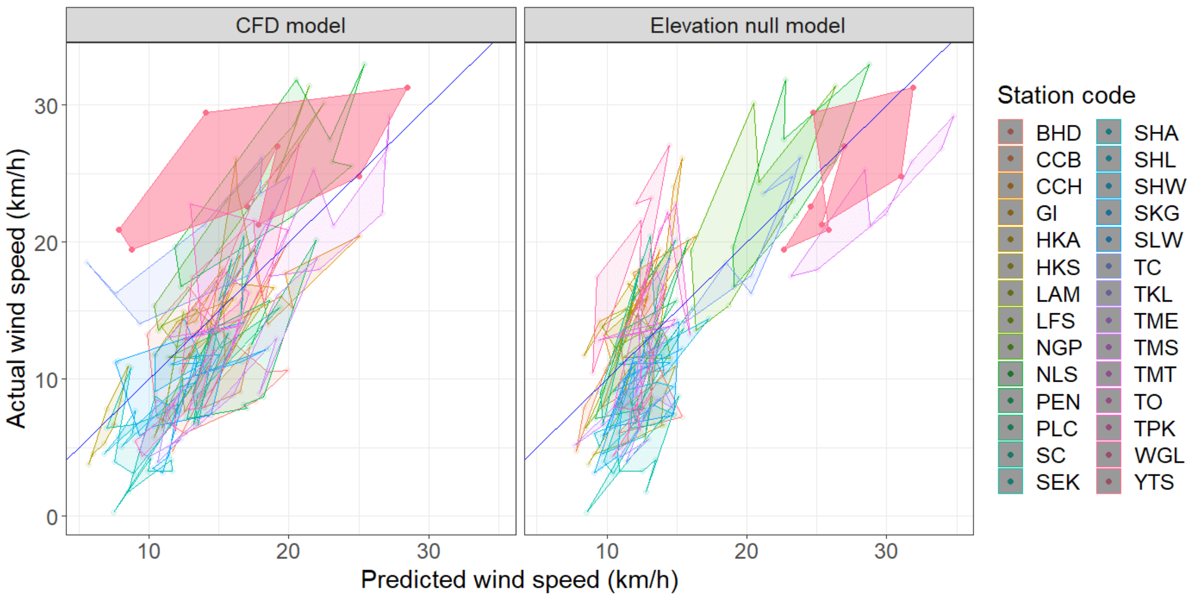

Figure 4.2: Predicted and actual long-term mean wind speeds of 28 non-urban weather stations. Each point represents wind approaching from one of the eight compass directions. The blue line indicates perfect prediction.

4.4.2 Validation with weather station data – during typhoons

The CFD model also performed better during periods when a typhoon or strong monsoon warning was issued by the Hong Kong Observatory (**Figure 4.3**). With higher wind speeds, the RMSE was slightly higher (4.22 km/h), but the %RMSE dropped to 22%. Under these scenarios, the advantages of the

CFD model over the null model were also more apparent. The null model generated many near-vertical polygons far from parallel with the 1:1 line (**Figure 4.3**).

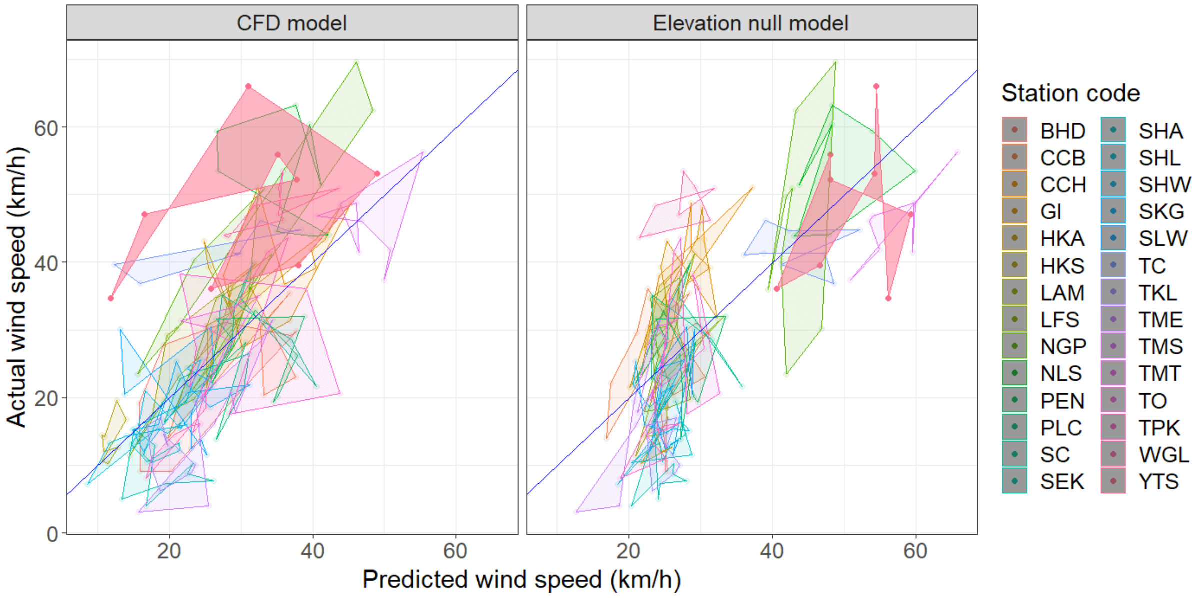

Figure 4.3: Predicted and actual mean wind speeds when typhoon or strong monsoon warnings were issued. The coloured polygons represent 38 non-urban weather stations. Each point represents wind approaching from one of the eight compass directions. The blue line indicates perfect prediction.

4.4.3 Validation with data from our own anemometers

Lastly, we validated the wind models using our own anemometers placed on eight slope locations. Overall, the performance of the CFD model was similar to the null model that used mean wind speed and elevation as predictors. The CFD model performed better at four locations (Wo Tong Kong, Keung Shan, Cape D'Aguilar, and Yin Ngam Teng), while the null model better predicted wind speeds at Robin's Nest, Pak Kung Au, Ha Fa Shan, and Luk Keng (**Table 4.1**). While the sample size was small for statistical analysis, there was a trend of the CFD model performing better when the wind speeds were strong at the times of measurement (**Table 4.1**). Finally, it is also important to note that we only had four hours of data from Robin's Nest, and the Luk Keng site was partially occluded by trees, but we still included the data here for completeness.

Table 4.1: Validating the wind models with our own anemometer measurements. We built linear models for actual wind speed against predicted wind speed. Higher R2 values indicates better agreement between model predictions and actual wind speed. Mean wind represents mean wind speed across all measurements from that anemometer. Duration represents how long the anemometer had been place out.

Location	Duration (h)	Mean wind (km/h)	CFD model R^2	Null model R^2
Wo Tong Kong	73	13.7	**0.23**	0.17
Keung Shan	116	11.6	**0.45**	0.40
Cape D'Aguilar	77	9.0	**0.80**	0.75
Robin's Nest	4	7.5	-0.47	**0.94**
Pak Kung Au	30	7.1	0.06	**0.13**

Ha Fa Shan	23	7.0	0.81	**0.85**
Yin Ngam Teng	21	5.8	**0.70**	0.30
Luk Keng	28	0.7	0.08	**0.10**

4.5 Discussion

Our study showed the possibility to use free and open-source CFD programmes to estimate surface wind speeds over complex topographies. The validation exercise showed that, for predicting both long-term mean wind speeds and winds during monsoons or typhoons, these models outperformed a null model that used elevation and overall mean wind speed in other weather stations as predictors. Our results indicate that explicitly modelling wind flows, even using a coarse and highly simplified model, has advantages over indirect proxies of wind speed and exposure. We did, however, found the RMSE (3.77 km/h) and %RMSE (30%) of the CFD model to be higher than that reported from other validation studies for WindNinja and WAsP (Berge et al., 2006; Wagenbrenner et al., 2019). This likely stems from the complexity of the landscape in Hong Kong. Extensive seas, steep hills, sophisticated vegetation structure, and the >600 skyscrapers in urban areas makes Hong Kong one of the most challenging landscapes for wind modelling.

The CFD model was found to excel in high wind scenarios. Its advantage against the null model was more apparent when the typhoon or monsoon warning signal was hoisted by the local observatory (**Figure 4.2**). Similarly, when validating the wind models using our own anemometer data, the CFD model performed better if wind speeds were strong at the times of measurement (**Table 4.1**). In calm days, local wind regimes are likely dominated by diurnal winds caused by the differences in heating or cooling across different types of terrain. Since the conservation of mass and momentum solver in WindNinja assumes neutrally stratified wind flows and does not model for diurnal winds, it is not designed to model these flows. Rather, the CFD solver stands out when the landscape is exposed to stronger unidirectional winds driven by larger low- or high-pressure systems.

We identified four factors could have contributed to errors in the CFD model. Firstly, variations in roughness of the landscape were not considered in WindNinja. Although the post-hoc roughness correction partially addressed these effects, including roughness into the CFD model would create more realistic estimations of wind flows (Finnigan et al., 2020). Secondly, due to limitations in computational capacity, we only modelled wind from eight compass directions in our study. In reality, wind could approach from any direction. We simulated this by taking the weighted average of wind flows from two of the eight compass directions, but modelling wind from more compass directions could have improved accuracies of the model (Berge et al., 2006). Thirdly, many weather stations in Hong Kong are located at mountaintops or ridges. This means that they lie at the border between the windward slope and the wind shadow on the lee side. Where this border was placed heavily affects the modelled wind speeds at these weather stations. In several cases, weather stations were placed in the wind shadows by the CFD model but received strong winds sweeping up from the windward slopes. This does not affect the accuracy and utility of the CFD model, but could inflate the RMSE figures in validation. Finally, our approach involved taking weighted averages between different incoming wind speed and direction scenarios. Although a total of 128 different scenarios were produced, they all implicitly assumed a single dominant wind speed and direction affecting the entire study area. Despite the relatively modest size of Hong Kong as a study area, this assumption does not necessarily hold. This is less of an issue when predicting long-term wind speeds – regional differences would be cancelled out when wind data were to be averaged across long periods of time. However, it could be an issue when the model is used to generate time-resolved wind speed predictions for specific events or time periods. This likely affected the accuracy of the CFD model when we validated it using our own anemometer data as the validation exercise was carried out at specific locations over short time periods. WindNinja does provide a "point-initialization" functionality that models wind flows based on a set of anemometer measurements taken from known locations across the landscape. However, the functionality is yet to be compatible with the "conservation of mass and momentum" CFD solver. Additionally, to build a wind flow model for every time step is extremely computationally expensive, which makes it impractical for most use cases. Another approach would be to keep the current pipeline (i.e. averaging relevant "wind scenarios" to estimate wind speed), but choose different representative "scenarios" for different subregions of the study area. The issue with such an approach is the difficulty in spatially interpolating the results from different subregions (for both wind direction and speed) to create one single wall-to-wall wind map, though the idea could very much be further explored in future work.

Chapter 5: Tall, wind-sheltered forests and plantations suffered more damage during Typhoon Mangkhut

5.1 Abstract

In many regions across the globe, forests are periodically damaged by tropical cyclones (TCs). Due to the difficulty in monitoring forest damage and modelling wind flows, we know very little about the factors contributing to forest resilience to TCs, especially on rugged landscapes with localised wind regimes. In 2018, rainforests in subtropical Hong Kong were hit by Typhoon Mangkhut, the strongest TC to affect the region in >40 years. Remarkably, its effect was captured by repeated LiDAR surveys in 2010, 2017, and 2020. The region is also home to one of the densest networks of anemometers in the tropics for wind modelling. We differenced the LiDAR-based digital surface models to quantify changes in canopy heights across >400000 30m-by-30m pixels. We then estimated both long-term mean wind speed and maximum wind speed during Typhoon Mangkhut for every pixel by building computation fluid dynamics (CFD) models. Our results show that plantations were more heavily damaged than natural forests of comparable stature and on similar topographical position (0.86 m vs 0.39 m average height loss). Amongst natural forests, height was by far the strongest predictor of damage, with taller forests being less resistant to typhoons. Interestingly, wind-exposed forests subjected to relatively high long-term mean wind speeds suffered less damage during the typhoon, consistent with acclimation to wind. Over the decade studied, growth in years without strong TCs largely offset damage incurred during extreme typhoons, except for the tallest forests. This placed strong limits on local forest height, with the tallest trees in sheltered sites ~50% taller than those in exposed sites. The limits were stronger than that posed by any other environmental factor considered. Our study highlights that forest resilience to TCs is highly dependent on local wind-topography-forest interactions, which needs to be considered if we were to predict how changing TC regimes might affect the structure of forest ecosystems.

5.2 Introduction

Tropical cyclones (TCs), also known as typhoons or hurricanes, are rotating storm systems that bring strong winds and heavy rainfall, often causing substantial damage to natural ecosystems. Even TCs graded 1-2 on the five-point Saffir-Simpson scale bring sustained wind speeds of >125 km/h, leading to defoliation, branch-breakage, bole-snapping, and uprooting of forest trees (Everham & Brokaw, 1996; Lin et al., 2020; Negrón-Juárez et al., 2014; Tanner et al., 1991). TCs caused substantial loss of aboveground forest biomass, with losses after Category 3-4 TCs estimated at 34% in a west Mexican study (Parker et al., 2018a) and 23% in a Puerto Rican study (J. Hall et al., 2020). TCs have long-term impacts on forest structure, not only by damaging trees but also by triggering changes in architecture amongst survivors (Bonnesoeur et al., 2016). Regions that frequently experience strong TCs were reported to have shorter forests with higher stem densities (De Gouvenain & Silander, 2003; Ibanez et al., 2019; Lin et al., 2020). Trees exposed to TCs may additionally invest into larger basal areas relative to their heights (Ibanez et al., 2019). The structural changes could, in turn, increase the resilience of forests to future TC events (Lin et al., 2020; Mabry et al., 1998). Under climate change, TCs have become less frequent but more intense in recent decades (Chand et al., 2022; Kossin et al., 2020) and have shifted towards higher latitudes (Chand et al., 2022; Murakami et al., 2020). To predict how these changes might affect forests in the future, it is critical that we have a comprehensive understanding of wind-forest dynamics at various spatiotemporal scales (Lin et al., 2020).

We currently have limited knowledge on how wind, topography, and forest structure affect TC-resistance at a landscape scale. Previous studies have shown that canopy height, soil type, stock density, and management action (e.g. thinning) could all affect forest resistance against strong winds (Cremer et al., 1982; Gardiner, 2021; Martin & Ogden, 2006). However, most of these studies were carried out in coniferous monocultures on flat terrain. We now know that the most valuable forests from the biodiversity, carbon, and ecosystem services stand points are those with complex canopy structure. Given that many of these forests grow on rugged landscapes, where sites a mere few hundred meters apart could have vastly different wind profiles, there is a pressing need to re-assess wind resistance in these forest systems. Only a handful of studies have investigated into the factors affecting TC-resistance in these complex forests (Boucher, 1990; Lin et al., 2020; Martin & Ogden, 2006; Ni et al., 2021; Tanner et al., 1991). While these studies have identified a few variables that affect resistance, such as forest stature and prior wind exposure, most are based on field observations with small sample sizes and none have explicitly modelled wind (both long-term or during TCs) across the landscape. Thus, the relationship between site-level exposure to wind and the patterns of damage remains poorly resolved. We also have very little understanding of how these patterns of forest damage affect forest structure through longer time scales. At a regional level, Eric B. Gorgens et al. (2021) found that wind determines the distribution of giant trees in the Amazon basin. Chi et al. (2015) suggested that typhoons reversed the elevation-tree height gradient in Taiwan by disproportionally impacting lowland vegetation. However, to our knowledge, no studies have explored whether effects of TCs on long-term forest height operate on finer spatial scales. It is also unclear whether these wind-effects are more important than other environmental variables, such as wetness or aspect, in shaping local forest structures.

The paucity of studies investigating the landscape-level effects of TCs is partly down to two technical challenges: measuring damage to forests in the immediate aftermath of storms and mapping wind exposure on complex terrain. Monitoring forest damage after TCs is no trivial task. Many existing studies are based on field measurements in established forest inventory plots, which provide detailed measurements of tree damage and mortality but only over limited spatial scales (Everham & Brokaw, 1996; Tanner et al., 1991). A few recent studies have turned to analysing changes in satellite multispectral imagery, but changes in vegetation indices such as NDVI and EVI reflect defoliation and are only indirectly linked to structural damage (Abbas et al., 2020; J. Hall et al., 2020; Rossi et al., 2013; Xu et al., 2021). The development of repeated airborne laser scanning provides a solution to this. By generating point clouds from millions of returns, LiDAR datasets can produce detailed maps of both canopy structure and background topography across large spatial scales. Comparing repeated LiDAR scans can provide unparalleled information on forest structural responses against wind. The main constraint of LiDAR is that we cannot predict the arrival of extreme TCs. Hence, datasets that capture forest condition both before and after devastating TCs are rare.

Similarly, wind modelling across a forested, mountainous site is notoriously difficult (Finnigan et al., 2020). Fundamental models of wind flow across flat terrain assume that wind speeds exhibit a logarithmic height profile, depending on the roughness of the surface (Wieringa, 1986), but these models fail to capture how wind interacts with complex terrain. Wind speeds increase significantly on windward slopes but are sheltered on leeward slopes (Belcher et al., 2011; Finnigan et al., 2020; Lemelin et al., 1988; C. A. Miller & Davenport, 1998). The position of wind shadows casted by mountains is dependent on incoming wind direction, while the size of the shadows depends on wind speed and associated deflection of wind (Belcher et al., 2011; Finnigan et al., 2020). On steeper hills, separation bubbles could form on leeward slopes, which cause wind near the boundary layer to reverse direction (Belcher et al., 2011; Finnigan et al., 2020; Kaimal & Finnigan, 1994). In narrow valleys, the Venturi effect is known to speed up incoming wind (Mikkola et al., 2023). Modelling these effects is difficult, and actual wind data for training and validation are often unavailable (Shah et al., 2023). As a result, most studies on TCs avoid modelling local wind speeds and rather resort to simple proxies of wind exposure, such as aspect, elevation, or topographical exposure (TOPEX) (Albrecht et al., 2019; Gardiner, 2021; Wilson, 1984). To our knowledge, no study has combined modelling of local wind speeds with repeated LiDAR surveys of wind damage to assess impacts of TCs on forest.

New datasets available for the mountainous countryside around the city of Hong Kong provide a unique opportunity to model local wind speeds during TCs and measure their impacts on native and planted forests of different ages. In September of 2018, subtropical rainforests on the rugged landscape of Hong Kong were hit by Typhoon Mangkhut. The typhoon was the strongest TC to affect Hong Kong in over four decades, bringing 10-min average wind speeds of >190 km/h in exposed areas (category 3 on the Saffir-Simpson scale) (Hong Kong Observatory, 2023). Remarkably, the whole area was surveyed by airborne LiDAR scans in 2010, 2017, and 2020. These LiDAR scans captured changes in the vertical structure of forests through time and provide a rare opportunity to study pre-typhoon growth and post-typhoon damage across large areas. Furthermore, hourly wind data is available from 28 non-urban automatic weather stations distributed across the mountains (Hong Kong Observatory, 2023). This allowed us to properly validate wind maps generated by computational fluid dynamics (CFD) modelling software, which estimates near-surface wind speeds from a given digital terrain model. In this study, we utilise the rare availability of repeated LiDAR and wind data to advance our understanding of how TCs affect forests on rugged terrains. In particular, we address four research questions:

(1) Were natural forests more resistant to Typhoon Mangkhut than plantations?
(2) How did forest height, local wind profile, and background topography affect forest resistance against Typhoon Mangkhut?
(3) Did the effect of strong TCs produce long-term limits in local forest height?
(4) How important was wind compared to other environmental variables in limiting local forest height?

5.3 Methods

5.3.1 Study area and Typhoon Mangkhut

Hong Kong (22^{o} 16' 8'' N, 113^{o} 57' 6''E) has a wet subtropical climate, receiving over 2400 mm of rainfall per year with an average temperature of 23.3 ^{o}C (1961-2022). Despite its reputation as a densely populated city, over 60% of the total land area (1110 km^2) is covered with natural vegetation, with another 4% covered by tree plantations. The landscape was almost devoid of forests by the close of the Second World War, but forests have subsequently recovered following widespread agricultural abandonment and better protection of the countryside for nature and the ecosystem services it provides. As of 2020, the vegetated countryside was composed of a mosaic of broadleaved-evergreen rainforests (53%), shrublands (41%) and grasslands (6%) based on the vegetation classification system in Abbas et al. (2016). With a median slope of 0.47, the countryside of Hong Kong is rugged. Dotted across the territory are the over 300 steep-sided hills of heights >100 meters above sea level (m.a.s.l.), with the tallest, Tai Mo Shan, rising to 957 m.a.s.l.. Hong Kong lies within the west Pacific TC hotspot, experiencing multiple TCs each year. Typhoon Mangkhut on the 16th September, 2018 represents the strongest typhoon that affected the territory in decades (**Figure 5.1**). Anemometers in exposed areas recorded hourly average wind speeds of >150 km/h, 10-min average wind speeds of >190 km/h, and gusts >250 km/h (category 3 on the Saffir-Simpson scale) (Hong Kong Observatory, 2023).

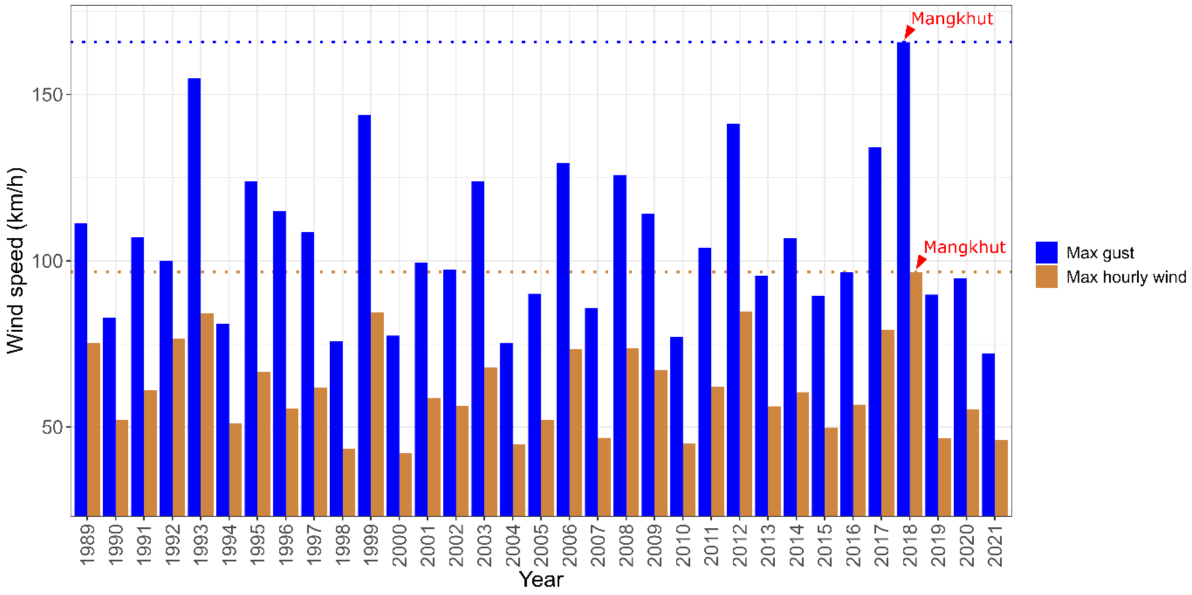

Figure 5.1: Typhoon Mangkhut is the strongest TC that affected Hong Kong in decades. Wind data was derived from 28 automatic weather stations. Hourly wind speeds and gusts were averaged across stations to produce two numbers per hour. The maximum averaged hourly wind speed and gust each year were then plotted out.

5.3.2 Repeated LiDAR surveys of canopy heights and topography

Three repeated LiDAR scans were used to reconstruct background topography and changes in forest structure. The first scan was conducted in late 2010, covering the entire territory of Hong Kong. The second scan was carried out in late 2017 and covers approximately half of the territory. The third scan was a repeat of the first scan and was conducted in early 2020, 1.5 years after Typhoon Mangkhut. Technical specifications of the LiDAR surveys are listed in **Table 5.1**.

Table 5.1: Technical specifications of the three LiDAR datasets.

Dataset	2010	2017	2020
Date Acquired	Dec 2010 – Jan 2011	Nov 2017	Dec 2019 – Feb 2020
Coverage	Whole territory	500 km^2	Whole territory
Carrier	Manned aircraft	Manned aircraft	Helicopter
Scanner	Optech Gimini ALTM	RIEGL LMS-Q780	N/A
Flight height	1000 – 1200 m	2147 – 2893 m	600 m
Point density	5.3 points/m^2	5.9 points/m^2	54.5 points/m^2
Returns per pulse	4 returns	Up to 7 returns	8 returns

LiDAR point clouds were processed using *LAStools* (Isenburg, 2020). Digital terrain models (DTMs) were created by ground-classifying LiDAR returns with *lasground_new* and triangulating ground returns with *blast2dem*. Canopy height models (CHMs) were created by triangulating the point cloud layer by layer to avoid empty pits due to the lack of returns following the methodology of Khosravipour et al. (2014). Finally, digital surface models (DSMs) were built using the -spike_free option in *las2dem*, which identifies relevant returns amongst all returns to generate smooth 3D surfaces based on Khosravipour et al. (2016). Canopy height changes between 2010, 2017, and 2020 were calculated by differencing the relevant DSMs. We specifically chose to difference DSMs (absolute heights) instead of CHMs (heights relative to ground elevation) since it avoids errors in ground classification. However, DSMs are more sensitive to errors in absolute height, so we differenced the DTMs to check whether there were significant biases in absolute heights. One region of the 2017 dataset was found to have a systematic but consistent bias in absolute heights, so we isolated the flightline and corrected the bias using geodetic control points of known elevations (HK Lands Department, 2019).

We also addressed two minor issues with the LiDAR data before analysis. Firstly, variations in point densities could undermine comparability of DSMs as point clouds with a higher density are more likely to include treetops or valley bottoms. Hence, we carried out a sensitivity analysis to investigate how point densities affected the DTMs, DSMs, and CHMs (**Section C.1**; **Supp. Figure C.1; Supp. Figure C.2; Supp. Figure C.3**). Following the results, we thinned the dense 2020 point cloud to 5.4 points per m^2 before generating the three LiDAR products. In contrast, edges of the 2017 dataset had exceptionally low point densities, so we masked out areas with <1.5 points per m^2 to ensure that errors of DSM differencing were <1m. The second issue was urban features, especially power lines that encroach into the countryside. We therefore excluded areas classified as urban in the zoning map of Hong Kong (Town Planning Board, 2020) or areas within 40 m of power lines mapped on OpenStreetMap (OpenStreetMap contributors, 2022).

We also generated rasters for four topographical variables: slope, aspect, topographic position index (TPI), and SAGA wetness index (SWI). Aspect, which is a cyclical variable, was linearised by subtracting the reported local optimal aspect for forests (5.795 radians) and taking the cosine (cos_aspect = cos(aspect – 5.795)) (**Chapter 3:**). TPI is a variable calculated from the DTM that refers to whether the site sits in valleys (low TPI) or on ridges (high TPI). SWI, also calculated from the DTM, refers to the catchment area of a pixel in question (i.e. how much water flows to the pixel). Compared to other wetness indices, SWI does not treat flow as a thin film and hence gives more realistic wetness estimates for pixels close to, but not exactly at, valley bottoms (Mattivi et al., 2019). The technical details regarding the calculation of topographical variables could be found in (**Chapter 3:**). The resulting rasters have different resolutions – (elevation (1m), slope (1m), aspect (30 m), TPI (15 m), SWI (15 m) – but were all tidied and down-sampled to 30 m resolution before subsequent analyses.

5.3.3 Wind modelling

The aim of wind modelling was to obtain two maps, one showing the mean long-term wind speed across Hong Kong and one showing maximum wind speeds during Typhoon Mangkhut. To build the wind maps, we followed the pipeline described and validated in **Chapter 4:**. Specifically, based on the

SRTM-expanded DTM of Hong Kong, we used the Conservation of Mass and Momentum solver in WindNinja (Forthofer et al., 2014; Wagenbrenner et al., 2019) to estimate near-surface wind speeds across every 60 m x 60 m pixel across the study area (**Chapter 4:**). We did this for 128 wind scenarios that correspond to 8 compass directions and 16 domain average wind speeds (**Chapter 4:**). We then compared the scenarios with actual wind data collected from the 28 anemometers at non-urban weather stations. For each hour across the last 37 years, we identified the four scenarios that best matched the observed wind direction and speed. From the predicted and actual wind speeds at the weather stations, we additionally built a simple roughness correction model to adjust wind speed predictions based on terrain roughness in the upwind direction (**Chapter 4:**). To create a long-term mean wind speed map for Hong Kong, we applied the roughness correction model on the 128 modelled wind speed scenarios. We then took the weighted average across the scenarios based on the frequency of those wind scenarios occurring throughout the 37-year study period. To create the map showing maximum wind speed during Typhoon Mangkhut, we first went through the wind data collected by the 28 non-urban weather stations and took note of the times between 2017 and 2020 with the strongest observed wind speed (24 hourly time steps identified per station). As one might expect, these time steps were overwhelmingly from 16th September 2018 when Typhoon Mangkhut hit Hong Kong. For every hourly time step, we built wind maps by taking a weighted average across the relevant roughness-corrected wind scenarios. We then overlaid these hourly wind maps and calculated the maximum. The final raster represents the maximum hourly wind speed during Typhoon Mangkhut for every 60 m x 60 m pixel across Hong Kong. Both wind maps (long-term mean and Mangkhut maximum) were subsequently resampled to 30 m resolution to match that of the topographical rasters.

5.3.4 Vegetation and plantation maps

We gathered a vegetation map time series of the study area to focus our investigation on forests. The maps were generated by classifying Landsat composites into five classes (forest, shrubland, grassland, water, and non-vegetation) using a supervised random forest (RF) model. Technical details of the vegetation maps can be found in **Chapter 3:** and **Appendix B:**. The full dataset contains 17 biennial vegetation maps spanning 34 years (1986-2020), but in this study we only used the maps of relevant years (2009-2020, 2017-2018, and 2019-2020). Non-forest pixels were excluded from the analysis.

To evaluate differences in the response of plantations and natural forests to typhoons, we created a plantation database by manual delineation. Most plantations in Hong Kong are monospecific stands of exotic species such as *Acacia confusa*, *Lophostemon confertus*, *Melaleuca quinquenervia*, and *Pinus elliottii*, though mixtures of native species have been increasingly planted in recent years. These plantations were used for afforestation and to combat erosion, so they were not harvested for timber. We identified plantations by visually inspecting aerial photos collected in 2014(0.3 m ground resolution) (HK Lands Department, 2019) and the LiDAR-derived CHMs. Google Satellite, Streetview, and photospheres were also widely available across the countryside of Hong Kong and provided additional ways to check the species composition of various forest stands. We also consulted an older vegetation map produced by Ashworth et al. (1993). The map only existed in paper format as the digital maps were lost, so we scanned, georeferenced, classified, and polygonised the document. Most of the 566 polygons were redrawn, but the dataset nevertheless provided a point of reference for older plantations now partially encroached by native trees. The final plantation map contains 3442 polygons covering an area of 42.3 km^2.

5.3.5 Comparing TC-resistance of natural forests and plantations

To test whether natural forests were more resilient to extreme TCs than plantations, we started by simply calculating the 2017-2020 height change and comparing the results between natural forests and plantations. This gave a holistic overview of typhoon-related damage amongst the two forest types. The problem with this approach is that the results could be confounded by covariate imbalances. For instance, it is reasonable to expect plantations to suffer more damage simply because they are taller or disproportionally planted on exposed ridges for erosion control. To investigate whether the structure of natural forests was inherently more wind resilient than plantations after accounting for these differences, we repeated our analysis after reweighting.

Reweighting is a statistical technique akin to pixel matching and commonly used in medical research (Markoulidakis et al., 2022; Matschinger et al., 2020). It tackles covariate imbalance by assigning weights to each datapoint such that the weighted dataset has comparable covariate distributions across categories of interest. In our case, the goal is to assign weights to pixels such that weighted natural forest pixels are comparable to plantations in terms of (1) height, (2) TPI, (3) SWI, (4) mean wind speed, and (5) maximum wind speed during the typhoon. By doing so, we could isolate the effect of forest type on typhoon-resistance. We followed the protocol outlined in Markoulidakis et al. (2022) in assigning weights. Firstly, we removed parts of the dataset for which there was too little overlap (e.g. tall plantations >23 m that had insufficient analogous natural forest pixels for meaningful comparison). Secondly, entropy balancing (EBAL) weights were assigned to the data using the *WeightIt* package in *R* (Greifer, 2019) based on the five covariates. Thirdly, the weights were trimmed at the 99.9th percentile such that results were not overwhelmed by several heavily weighted pixels. Fourthly, the *cobalt* package was used to confirm that, after weighting, plantation and natural forest pixels had comparable distributions of covariates (mean differences <0.05 and variance ratios <2) (Greifer, 2020). Lastly, we used the weighted heights to conduct a like-for-like comparison of typhoon-resistance between natural and planted forests.

5.3.6 Factors affecting natural forest resistance against typhoons

We investigated the factors that affected forest resilience against extreme TCs using a multiple regression model. We first removed plantations and focused on natural forests as the two forest types have different height and structural profiles. We then built a multiple regression model that predicted forest damage during Typhoon Mangkhut, measured as the canopy height change between 2017 and 2020, using different environmental variables. Recognising that multicollinearity could undermine the results by inflating or even flipping the signs of coefficients, we transformed and removed several predictor variables. Firstly, maximum wind speed during Typhoon Mangkhut correlated with long-term mean wind speed ($R^2 = 0.9$, **Supp. Figure C.4**), so we normalised the variable by subtracting the maximum wind speed by that predicted by mean wind speed. After the transformation, the variable represented whether the site was disproportionately exposed to Typhoon Mangkhut and was less correlated with mean wind speed ($R^2 = 0.32$, **Supp. Figure C.4**). Secondly, SWI, TPI, and slope were moderately correlated (**Supp. Figure C.4**). We dropped TPI as a predictor as the variable had a small effect size by itself but significantly affected the coefficients of SWI and slope when included (**Supp. Figure C.4**). The final model contained five predictor variables, namely (1) 2017 canopy height, (2) long-term mean wind speed, (3) normalised maximum wind during Mangkhut, (4) wetness (SWI), and (5) slope. Last but not least, to better understand how the two wind variables and forest height interacted and shaped patterns of forest damage, we included the two-way interaction terms between (1), (2), and (3). All predictor variables were scaled by subtracting the values by the mean and dividing them by the standard deviation. This ensured that the model produced comparable coefficients that accurately represented the effect sizes of the variables.

5.3.7 Long-term implications of strong typhoons

We explored how differences in TC-resistance amongst natural forests cascaded into the long term. We started by visualising the short-term destruction of Typhoon Mangkhut across pixels with different height and wind profiles. To do so, we binned the pixels by (a) maximum wind speed experienced during Typhoon Mangkhut and (b) tree height in 2017 prior to the typhoon (n =191744, 816 bins). For all bins with >10 pixels, we calculated the average change in canopy height between 2017 and 2020 and plotted the results in a heatmap. We then used a similar approach to visualise how these effects were relayed into the long term. We again binned the pixels, but this time by (a) tree height in 2010 and (b) long-term mean wind speed (n = 406482, 816 bins). For all bins with >10 pixels, we calculated the average change in canopy height across the decade-long study period (2010 – 2020) to create another heatmap. A comparison between the two heatmaps revealed the balance between short-term TC damage and long-term growth. Finally, the 97.5th percentiles of forest heights were overlaid on the heatmaps to reveal limits on local forest stature.

5.3.8 The importance of wind on local forest height limits

We used quantile regression to evaluate whether these wind-dependant limits on local forest heights were important compared to limits posed by other environmental variables. Regression through the top quantiles is a powerful tool to study limiting factors in ecology due to its robustness against other measurable or unmeasurable confounding factors (Cade et al., 1999; Cade & Noon, 2003; Coomes & Allen, 2007). For example, in our case forest height in a particular location could be constrained by one of many environmental variables (e.g. soil nutrients, forest age, disturbance history, etc.). Even if wind strongly constrains forest height, the heights of many forest stands may have been constrained by other variables before the wind constraint takes effect. If we perform ordinary least squares regression, these stands would confound the results and produce a very weak effect size regardless of whether the wind poses a hard limit on forest height. Quantile regression through the top percentiles avoids this by focusing only on the tallest trees. Forest stands that have reached these heights would be those that are least constrained by other environmental variables, thus allowing us to better isolate the effects of the variable of interest. In this study, we performed quantile regression through the 97.5th percentile of 2010 canopy heights using six environmental variables as predictors, namely (1) mean wind speed, (2) elevation, (3) cosine aspect, (4) slope, (5) wetness (SWI), and (6) topographical position (TPI). Second-order polynomials were fitted through the data as several factors had non-linear effects on maximum canopy height. We used the results to evaluate the importance of wind limits on local forest heights compared to the other variables. The analysis was also repeated with canopy heights from 2020 to ensure that the patterns observed were robust across different years.

5.3.9 Local effects of wind and topography on typhoon damage

To further uncover how different variables shaped local patterns of wind damage after Typhoon Mangkhut, we built a multiple regression model on canopy height change between 2017 and 2020. The model included five predictors, namely (1) 2017 canopy height, (2) long-term mean wind speed, (3) normalised maximum wind during Mangkhut, (4) wetness (SWI), and (5) slope. Several steps were taken to minimise the effects of multicollinearity. Firstly, maximum wind speed during Typhoon Mangkhut correlated with long-term mean wind speed ($R^2 = 0.9$, **Supp. Figure C.4**), so we normalised the variable by subtracting the maximum wind speed by that predicted by mean wind speed. After the transformation, the variable represented whether the site was disproportionately exposed to Typhoon Mangkhut and was less correlated with mean wind speed ($R^2 = 0.32$, **Supp. Figure C.4**). Secondly, SWI, TPI, and slope were moderately correlated (**Supp. Figure C.4**). We dropped TPI as a predictor as the variable had a small effect size on itself but significantly affected the coefficients of SWI and slope when included. Finally, to better understand how the two wind variables and forest height interacted to produce the patterns of forest damage observed, we included the two-way interaction terms between (1), (2), and (3).

5.4 Results

5.4.1 Mean and maximum wind maps

The rugged topography of Hong Kong created variable wind profiles across the landscape. Both the modelled long-term mean wind speed and 2017-2020 maximum wind speed (Typhoon Mangkhut) showed over three-fold differences across pixels. Overall, exposed sites such as ridges and mountaintops with higher long-term mean wind speed also experienced higher wind speeds during

Typhoon Mangkhut (**Figure 5.2**). However, the typhoon brought disproportionally strong winds from the east and created prominent wind shadows towards the western slopes of mountains (**Figure 5.2b**). Therefore, there was considerable variation in maximum wind speed even amongst pixels with similar long-term wind regimes, which can be visualised by normalising the maximum Typhoon Mangkhut wind speed raster by the long-term mean wind speed raster (**Figure 5.2c**).

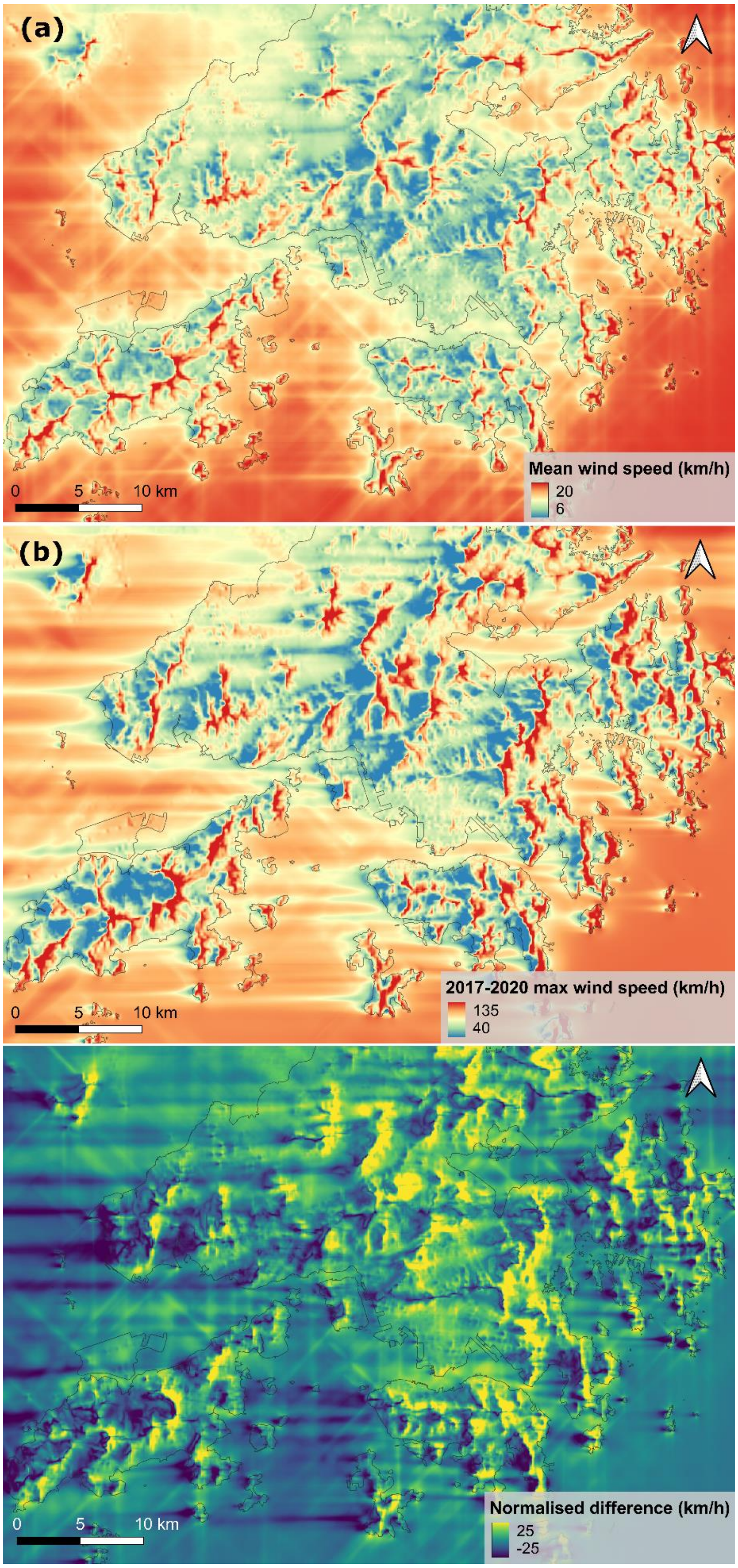

Figure 5.2: Modelled (a) long-term mean wind speed, (b) maximum wind speed during Typhoon Mangkhut, and (c) the normalised difference between the two. The grey lines represent the outline of the terrestrial areas of Hong Kong.

5.4.2 Natural forests were more wind-resilient than plantations

Compared to natural forests, plantations were more heavily hit by Typhoon Mangkhut. On average, plantations lost 0.86 m in height between 2017 and 2020, equivalent to 45% of the growth in the previous seven years. In contrast, natural forests only lost 0.1 m in height between 2017 and 2020, or 10% of the growth between 2010 and 2017. Part of these differences could be attributed to the imbalance of covariates, such as plantations being taller and being disproportionally planted on ridges. Nevertheless, after accounting for these differences by reweighting, we found that plantations were still more than twice as susceptible to typhoons (-0.86 m) compared to natural forests of similar heights and topographical positions (-0.39 m) (**Figure 5.3a**). In particular, a larger proportion of trees were either snapped or uprooted in plantations, creating a fat tail in violin plot of 2017-2020 height change (**Figure 5.3a**). Visually assessing the relevant rasters revealed how entire stands of planted trees were wiped out by the typhoon (**Figure 5.3b-c**). The scale of damage seen in these sites was not observed in natural forests in the same region (**Figure 5.3b-c**).

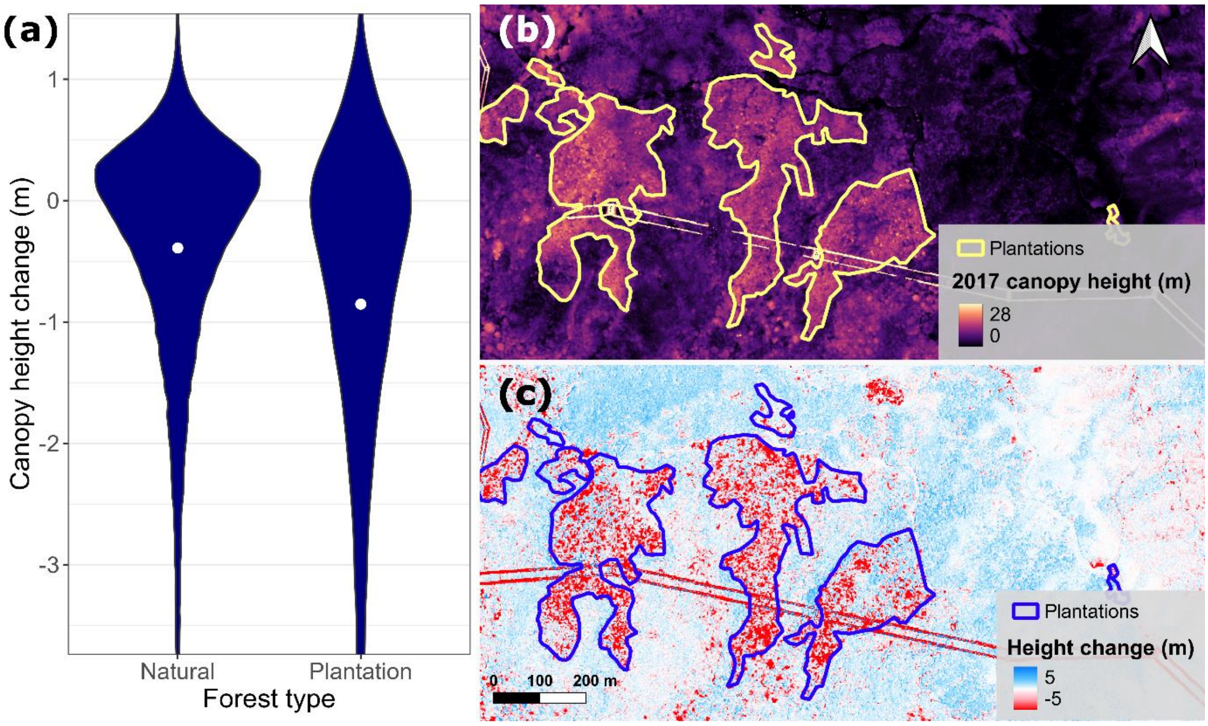

Figure 5.3: Plantations suffered heavier losses during Typhoon Mangkhut. Panel (a) contains a violin plot of height changes between 2017 and 2020. The pixels were reweighted such that the natural forests had comparable height, TPI, SWI, and wind distribution as the plantations. Effective sample sizes (ESS) were 114838 for natural forests and 16381 for plantations. Panel (b) shows the canopy heights of forests near Tate's Cairn, Hong Kong in 2017. Panel (c) shows the height changes of the same region between 2017 and 2020. The linear features in panels (b) and (c) are power lines, which were masked out before data analysis.

5.4.3 Taller and wind-sheltered forests were more susceptible to Typhoon Mangkhut

Coefficients of the multiple regression model built on 2017 – 2020 canopy height change revealed how forest stature, wind, and topography shaped the resistance of natural forests to wind damage during Typhoon Mangkhut. Among the variables investigated, canopy height had by far the strongest effect on forest resistance against wind. Taller forests were much more heavily damaged during Typhoon Mangkhut (**Figure 5.4**).

Wind-sheltered forests with low long-term mean wind speeds suffered more damage during the typhoon, while forests on exposed sites were relatively unscathed, presumably due to better acclimation to wind (mean wind, **Figure 5.4**). This acclimation effect was especially pronounced in taller, more mature forests (height : mean wind, **Figure 5.4**). On the other hand, sites that experienced stronger than expected maximum wind speeds during Typhoon Mangkhut suffered more damage during the storm (norm. max, **Figure 5.4**). Interestingly, forests appeared to over-acclimate to their long-term wind regime. Sites with higher long-term mean wind speeds were less sensitive to disproportionally strong maximum wind speeds during Mangkhut (mean: norm. max, **Figure 5.4**). Finally, we identified two topographical factors that were largely orthogonal to the wind variables (**Supp. Figure C.4**) and had substantial effects on forest typhoon resistance – wetter sites were more susceptible to typhoons (SWI, **Figure 5.4**), while steeper sites were more resistant to damage (slope, **Figure 5.4**)

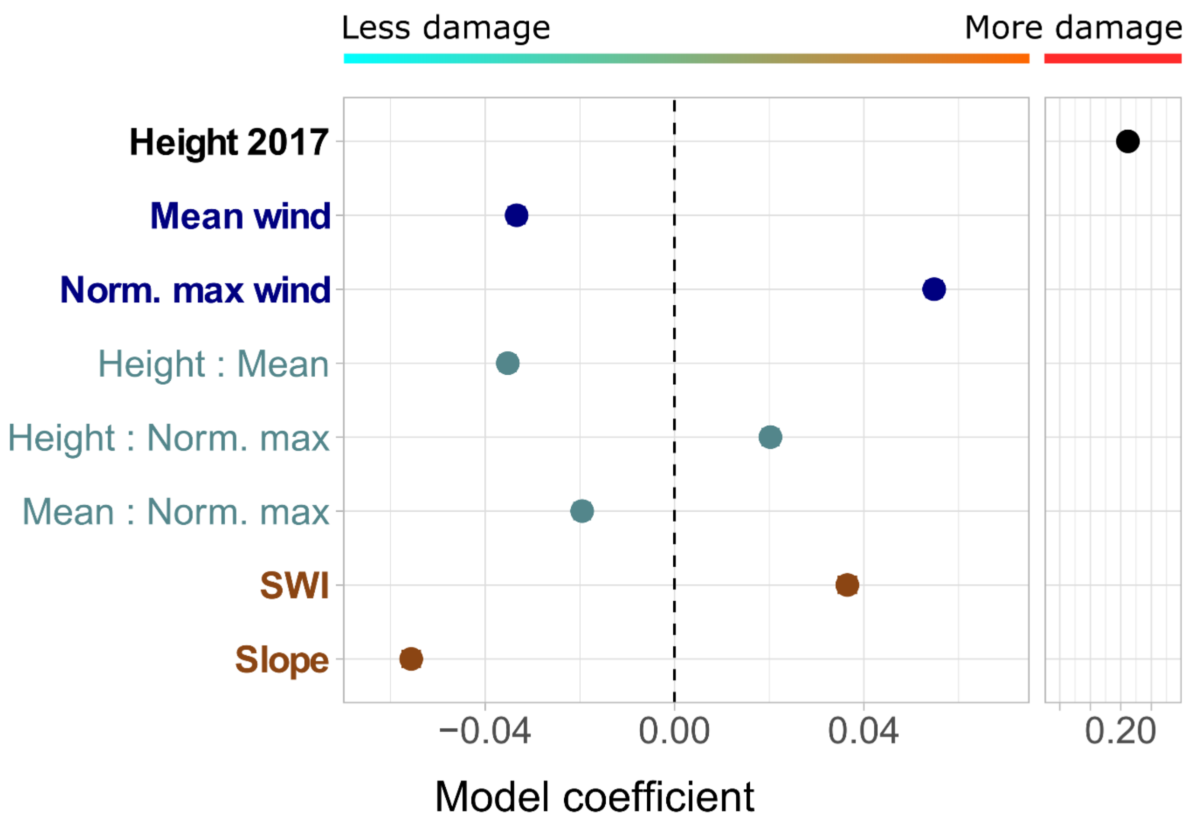

Figure 5.4: Coefficients of multiple regression model predicting damage after Typhoon Mangkhut (measured as drop in canopy height between 2017 and 2020). Norm. max wind is a variable created by normalising the maximum modelled wind speed during Typhoon Mangkhut with the long-term mean wind speed and reflects whether the site was disproportionally affected by the event. SWI represents Saga Wetness Index. The variables were scaled such that effect sizes and directions are comparable. Error bars (barely visible) are the standard errors of the coefficient estimate.

5.4.4 Low typhoon resistance of tall forests created long-term height limits

The effects of high TC-susceptibility amongst taller forests cascade into the long term to limit local forest height. Amongst the variables studied, forest height was identified as the most important in defining resistance against TCs (**Figure 5.4**). **Figure 5.5** provides a visualisation of the interplay between forest stature, wind, and change in canopy height. Taller forests (over 15 m) lost height (-27.9 cm/year) between 2017-2020, while shorter forests under 7 m in height maintained growth (+3.1 cm/year) over the same period (**Figure 5.5a**). The positive growth of shorter forests also demonstrates that the differences in resilience were not due to taller forests having more height to lose during Typhoon Mangkhut. The trend of taller forests being more wind-susceptible was robust across a range of different maximum wind speeds (**Figure 5.5a**).

In the long term, natural forests acclimate to local wind conditions by adjusting both height and structure (**Figure 5.5b**). Sites with higher mean wind speeds tend to have a lower maximum height measured as the 97.5th quantile (black line, **Figure 5.5b**). These height limits were at least partly produced by tropical cyclones. In forests below these height limit, Typhoon Mangkhut did cause losses in canopy height (**Figure 5.5a**), but the losses were more than offset by growth in years without strong TCs (**Figure 5.5b**). However, in forests close to or exceeding these height limits (above black line, **Figure 5.5b**), growth could no longer offset the disproportionate damage incurred during Typhoon Mangkhut, leading to a stall or even drop in long-term canopy height (**Figure 5.5b**). Lastly, these figures also provide further support for structural wind-acclimation affecting forest resistance to typhoons. Amongst forests of similar heights, those on more exposed sites suffered relatively little damage during Typhoon Mangkhut compared to forests in more sheltered sites (**Figure 5.5a**). The trend is even more apparent if we replot the typhoon damage data in **Figure 5.5a** with long-term mean wind speed on the x-axis (**Supp. Figure C.5**).

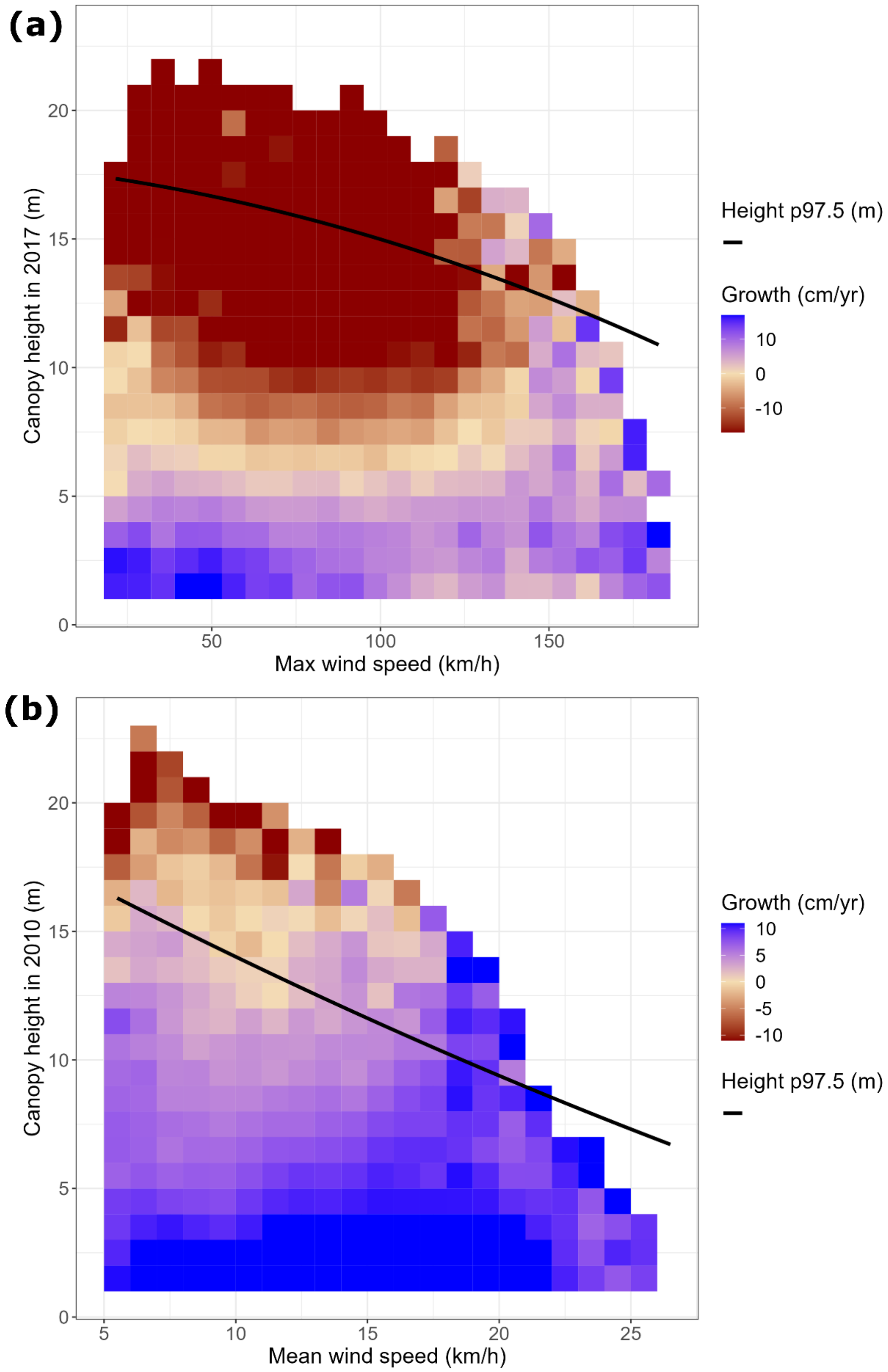

Figure 5.5: The change in canopy height (a) during the period affected by Typhoon Mangkhut (2017-2020, n=191744) and (b) over the entire study period (2010-2020, n = 406482). The max wind speed represents the strongest hourly mean wind speed between 2017-2020, mostly reflecting the effects of Typhoon Mangkhut. The mean wind speed represents modelled long-term wind speeds over more than three decades. The black lines represent the maximum canopy height (97.5th percentile) estimated by second order quantile regression.

5.4.5 Local wind regimes more strongly limited forest height than other environmental variables

Quantile regression analysis on the 2010 dataset revealed that the 97.5th quantile of forest height strongly and unidirectionally correlated with mean wind speed. The tallest forests in the least windy sites were ~50% taller than those in the windiest sites (**Figure 5.6**). Topographical position (TPI) was the second most important variable limiting forest height, with forests in valleys (low TPI) having a higher height limit than ridges (high TPI). These patterns were not driven by collinearities with the other variables studied. Wetness (SWI), aspect, and slope all had relatively weak effects on maximum height. Elevation and temperature regimes were also not responsible for the wind-height relationship. Forests at higher elevations reached greater maximum heights despite having higher wind speeds and cooler temperatures (**Figure 5.6**). We repeated the quantile regression analysis on the 2020 canopy heights (**Supp. Figure C.6**), and the same patterns emerged. Overall, our results suggest that forests tend to adjust their heights in response to local wind conditions, more so than to other environmental variables

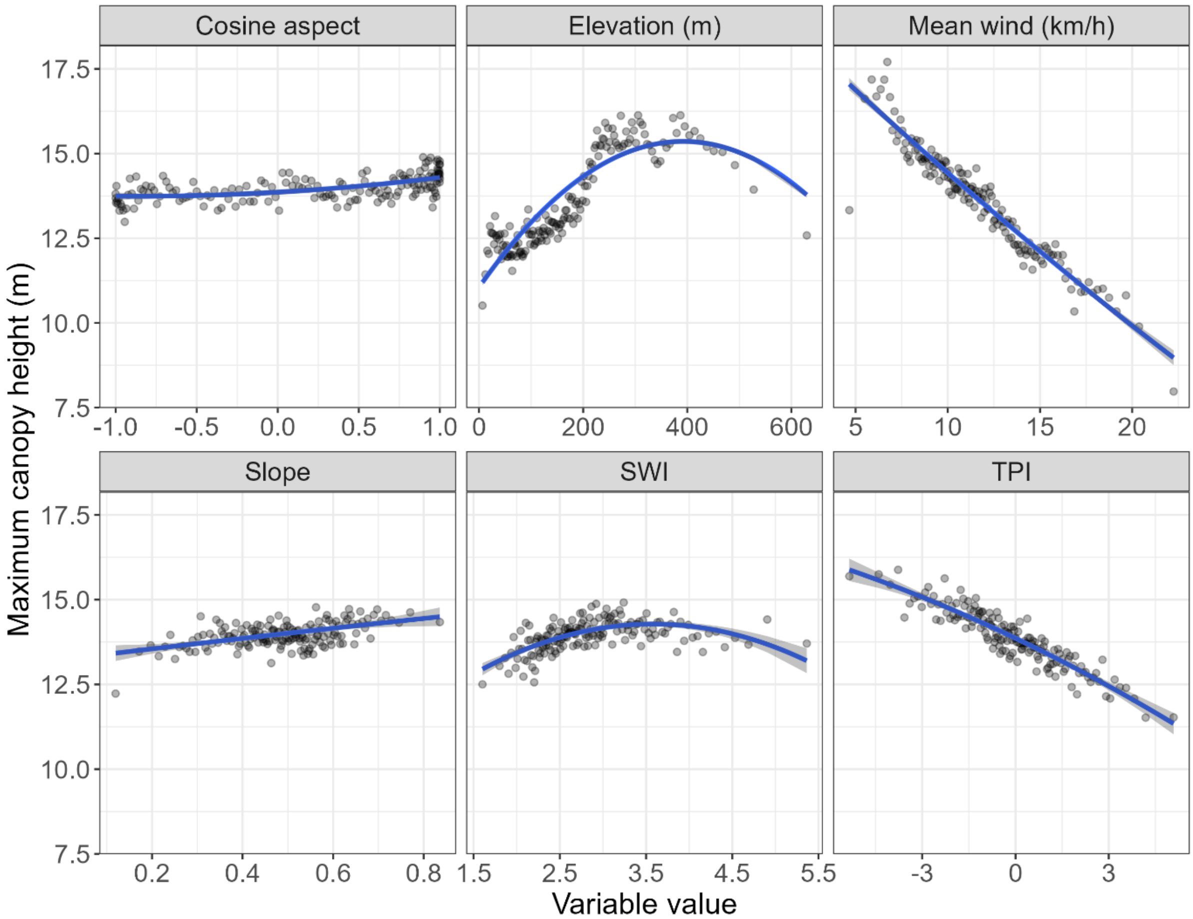

Figure 5.6: Wind strongly limits local canopy height. Each point represents the maximum average canopy height (97.5thpercentile) amongst 2000 pixels in 2010 (n = 324186, each pixel 30 x 30 m in size). The blue lines were second order 97.5th quantile regression lines through the entire dataset. SWI = SAGA wetness index; TPI = topographical position index.

5.5 Discussion

5.5.1 Plantations were more susceptible to wind damage than natural forests during Typhoon Mangkhut

Natural forests in Hong Kong were surprisingly resistant to Typhoon Mangkhut. Even the tallest (>15 m), most wind susceptible faction of natural forests lost <5% of its height between 2017 and 2020. This comes in contrast with reports of forests losing 23-33.7% of aboveground biomass in Mexico and Puerto Rico in face of category 2-4 hurricanes (J. Hall et al., 2020; Parker et al., 2018a). Our findings are more in line with Mabry et al. (1998), who reported a 1.4% forest mortality in Fu-Shan Experimental Forest, Taiwan after a category 3 typhoon. Lin et al. (2020) suggested that this may be attributable to the higher TC frequency and therefore better wind acclimation of forests in the west Pacific typhoon hotspot.

Plantations were much more susceptible to strong TCs, losing 0.86 m height between 2017 and 2020. Our results compliment those of two recent studies in the region, both based on satellite multispectral data, which reported larger reductions of greenness in plantations after typhoons compared to natural forests (Abbas et al., 2020; Stas et al., 2023).

The high susceptibility of plantations to wind damage is likely due to differences in tree architecture (Jackson et al., 2019; Tanner et al., 1991). Under higher stocking densities , trees tend to maintain height growth in the expense of diameter growth, leading to slender allometries (Cremer et al., 1982). Furthermore, trees in dense canopies are sheltered and therefore don’t acclimate by increasing their diameter growth rates (Bonnesoeur et al., 2016; Cremer et al., 1982). This sheltering protects trees from wind damage in most conditions, but when a strong TC creates gaps in the canopy, this exposes the previously sheltered trees to the full force of the wind. Several studies have found that wind damage can propagate quickly in even-aged monocultures where trees have similar critical wind speeds (Dupont et al., 2015; Gardiner, 2021; Kamimura et al., 2019). When Typhoon Mangkhut hit Hong Kong, wind damage propagated through several planted stands and led to stand-replacing level of damage in some sites (**Figure 5.4**). The same patterns of damage propagation were not observed in mixed species broadleaved rainforest, probably due to large variations in critical wind speeds (i.e. the wind speed that causes bole snapping or uprooting) across trees of different species and age classes (Jackson et al., 2019).

Finally, it is important to recognise that not all plantations are the same. In recent years, Hong Kong gradually pivoted towards using native trees to create mixed-species plantations. The shift was mainly biodiversity-motivated, but mixed species stands with more complex vertical structures were also found to be more stable under strong winds (Gardiner, 2021; Gardiner et al., 2005; Jactel et al., 2017; but also see Tanner & Bellingham, 2006). Overall, plantations are less wind-resistant compared to natural forests due to structural weaknesses. Monocultures suffered much more damage during Typhoon Mankhut despite the use of wind-resistant species (e.g. *Lophostemon confertus*), but mixed species native plantations could potentially fortify planted stands against future TCs.

5.5.2 Taller forests suffered more damage during Typhoon Mangkhut

Within natural forests, canopy height prior to Typhoon Manghkut was the strongest predictor of wind damage. Taller trees have been reported to be more susceptible to wind in the past. Foresters have long recognised that taller monoculture stands had lower critical wind speeds compared to shorter ones (Cremer et al., 1982; Gardiner, 2021). Similar patterns have also been reported in natural forests affected by TCs or storms (Halder et al., 2021; Martin & Ogden, 2006; Ni et al., 2021; Sánchez Sánchez & Islebe, 1999; Tanner et al., 1991). The evidence is, however, far less conclusive as these studies often lack direct measurements of height. Halder et al. (2021) focused on DBH measurements in the study on typhoon-resistance of mangrove trees in the Sundarbans. Sánchez Sánchez & Islebe (1999) also reported heavy damage amongst small understory trees. Ni et al. (2021) studied the effects of Typhoon Mangkhut in neighboring Dinghushan and concluded that mature forests suffered heavily compared to younger secondary forests. The patterns were likely related to forest stature, but the study made no explicit measurements of tree height. By summarising results derived from >190000 plots (30 m by 30 m in size), our study provided clear evidence supporting taller natural forests being more susceptible to TCs, with effect size over twice that of the next more important variable studied.

5.5.3 Wind-sheltered forests were less resistant to wind damage during Typhoon Mangkhut

Interestingly, wind-sheltered forests with lower long-term mean wind speeds suffered less damage during Typhoon Mangkhut. Previous studies have reported contrasting evidence on whether forests in wind-exposed locations were more resistant to TCs. In New Zealand, forests on leeward slopes were found to suffer more wind damage than their windward counterparts (Martin & Ogden, 2006). Similarly, both Weaver (1986) and Scatena & Lugo (1995) reported more windthrow in valleys and lowlands in hurricane-prone forests in Puerto Rico. On the other hand, Bellingham (1991) observed heavy damage amongst forests on ridges in Jamaica after Hurricane Gilbert, while Ostertag et al. (2005) found forests on ridges and valleys to suffer more heavily than those on slopes when Hurricane Georges hit Puerto Rico. These seemingly conflicting results from previous studies likely stems from the tangled effects of several confounding factors. Estimating wind exposure by aspect, elevation, or topographical position tends to mix up the effects of forest height, long-term mean wind speed, and exposure to the TC in question. The sample sizes of field-based studies were also insufficient to resolve the effects of all these factors with confidence. Our study overcame many of these limitations by analysing a large repeated LiDAR datasets. Our results demonstrate that, given the same height, forests in sheltered locations were indeed more susceptible to typhoons (**Figure 5.4 and Figure 5.5**). Sites that experienced higher wind speeds during Typhoon Mangkhut than expected were still more heavily damaged, but prior wind exposure substantially alleviates the damage suffered (**Figure 5.4**). We speculate that this is due to wind acclimation of forest trees. Forests exposed to strong winds tended to change their species composition, canopy structure and tree architectures over time, which facilitated resistance to extreme typhoon events (Bonnesoeur et al., 2016; Coomes et al., 2018; Jackson et al., 2019; Telewski & Jaffe, 1986).

5.5.4 Typhoon damage cascades through time to limit local forest height

Strong TCs such as Typhoon Mangkhut cause long-term effects on local forest structure. In Hong Kong, much of the landscape is still covered by secondary forests moving through the successional stages (Abbas et al., 2016). Hence, when averaged across longer periods of time, the growth of forests largely offset damage incurred during strong typhoons. This was, however, not the case for the tallest forests that were reaching the height limits of their respective local wind regimes (**Figure 5.5b**). The failure for growth to offset wind-damage created a strong height limit on local forest height (**Figure 5.5b and Figure 5.6**). These height limits are most likely strengthened by the known pattern of slower height growth with respect to radial growth in sites with very strong winds (Coomes et al., 2018; Telewski & Jaffe, 1986; Thomas et al., 2015; Wadsworth, 1959; Haoyu Wang et al., 2022). Putting the effects of wind into context, we found that mean wind speed more strongly limited tree height than the five other environmental variables studied. The effects of wind were not driven by collinearities with temperature and elevation gradients as the forests in higher elevations had taller maximum heights (**Figure 5.6**). Interestingly, topographical position (TPI) also had clear unidirectional, albeit smaller, effects on maximum canopy height. Since topographical wetness (SWI), which better represents nutrient and water availability, had relatively minor effects on maximum canopy height, we speculate that the effects of TPI might also be wind-related. Our wind models were based on a relatively coarse (60 m ground resolution) DSM, so it is possible that some localised wind sheltering effects might be better captured by TPI in the highly rugged landscape of Hong Kong.

Our results suggest that wind regimes are more important than other recognised limitations on tree height in TC-prone areas. Growth in years without TCs stopped balancing out wind damage before canopy heights even reached 30 m (**Figure 5.5b and Figure 5.6**). Forests in Hong Kong would rarely reach heights where hydraulic (Fernández-de-Uña et al., 2023; Eric Bastos Gorgens et al., 2019; M. G. Ryan & Yoder, 1997), temperature (Chi et al., 2015; Saremi et al., 2014), or nutrient (Gower et al., 1996) limits are significant. Wind regimes therefore largely displaced other factors in defining forest height limits. Given the localised wind regimes in rugged landscapes (**Figure 5.2**) and the varied TC-resilience across different forest patches (**Figure 5.4**), we further speculate that wind would be a main driver of forest structural diversity in TC-prone regions, a notion worth further exploring in future research.

5.5.5 The implications of climate change

Our results shed light on how changes of TC regimes under climate change might affect forest structure in the future. The frequency of TCs in the west Pacific typhoon hotspot is currently on a downward trajectory and is projected to further decrease in the future (Chand et al., 2022; Knutson et al., 2010), while intensity of TCs is expected to increase (Knutson et al., 2010; Kossin et al., 2020). These changes imply that forests would have fewer opportunities to wind-acclimate during weaker TCs before being affected by extreme TCs. Overall, forests are expected to grow taller but suffer from more damage during individual TC events. Nevertheless, our study demonstrates that local topography creates very diverse wind patterns across the landscape (**Figure 5.2**), so the associated local variations in forest stature will persist. Noteworthily, plantations are relatively ill-adapted to extreme TCs (**Figure 5.3**). This is concerning as fast-growing plantations are widely used to meet carbon sequestration targets (Lewis et al., 2019). Their higher susceptibility to wind needs to be properly considered, especially in TC-prone areas, to ensure that restoration objectives are not undermined by wind disturbance under a changing climate.

Chapter 6: General Discussion

6.1 Summary of findings

In this thesis, we demonstrated how we could utilise remote sensing to track resilience of wet subtropical vegetation against disturbances, with a focus on wildland fires and tropical cyclones. The lack of comprehensive burnt area maps represents a major stumbling block in studying wet tropical and subtropical fire ecology. In **Chapter 2:**, we tackled the issue by developing the LTSfire pipeline to reconstruct 34 years of fire history in Hong Kong using Landsat satellite imagery time series. Despite the high cloud cover and quick revegetation of burnt patches, we detected over 5500 burn areas with estimated burn severity and date of detection. The dataset represents the first comprehensive burn area time series in wet tropical and subtropical Asia. In **Chapter 3:**, we carried out a time series analysis on both the burn area and vegetation maps in Hong Kong. We found strong evidence supporting the existence of fire traps in the wet subtropics. Grasslands and shrublands were 20 and 9 times more susceptible to fires than closed canopy forests, respectively (**Figure 3.3**). Grasslands also took significantly longer to recover back to forests after fire events compared to shrublands (40 years vs 19 years) (**Figure 3.7**). These positive fire-vegetation feedbacks represent significant challenges in the restoration as the fires trap the degraded vegetation in an early state of succession. The chapter represents the first study to quantify fire-vegetation feedbacks in the wet tropics and subtropics, which provides land managers with clear and robust numbers to plan restoration projects. In **Chapter 4:**, we demonstrated how open-source computation fluid dynamics (CFD) modelling software could be used to estimate near-surface wind speeds in complex topographies. Validation with anemometer measurements at weather stations revealed that explicit CFD modelling of wind flows are more realistic than that predicted by elevation and nearby wind measurements alone (**Figure 4.2**). The approach was particularly useful for studying wind disturbances as it performed better under strong winds (**Figure 4.2**; **Figure 4.3**). In **Chapter 5:**, the wind maps produced were coupled with a repeated LiDAR dataset to study the forest resilience against Typhoon Mangkhut – the strongest typhoon to affect Hong Kong in over 40 years. By studying canopy height changes across >400000 30m x 30m pixels, the study revealed many hidden patterns in forest resilience against strong winds. Tall forests in wind-sheltered locations were found to be significantly less resistant to strong typhoons (**Figure 5.4**). Plantations also suffered more damage than natural forests of similar stature (-0.86 m vs -0.39 m) (**Figure 5.3**). Over longer periods of time, the wind speed of the site, as determined by the wind flows through the complex topography, posed strong limits on local canopy heights, more so than the other environmental variables studied (**Figure 5.5**). In this chapter, we aim to provide a holistic discussion of our findings, with an emphasis on the implications on disturbance and restoration ecology. Additionally, we will outline potential work that could be carried out in the future.

6.2 Opportunities provided by remote sensing time series

The rapid development of remote sensing over the past few decades is expanding the possibilities in the fields of disturbance and restoration ecology (Chuvieco et al., 2020; Kurbanov et al., 2022; Stone & Mohammed, 2017; Szpakowski & Jensen, 2019). In particular, results from this thesis highlight the potential of analysing remote sensing time series data to unveil patterns that are otherwise difficult to describe (Kuenzer et al., 2015). Due to the lack of data and limitations in computational capacity, the first generation of remote sensing studies on disturbance ecology focused on single or a handful of pre-selected images (**Supp. Table A.1**). In recent years, more and more multidecadal remote sensing data archives, such as AVHRR, MODIS, and Landsat satellite multispectral imagery time series, are being opened up for public use (Chuvieco et al., 2020; Gorelick et al., 2017; Kuenzer et al., 2015; Wulder et al., 2019). Coupled with the increase in computational speeds and the development of cloud computing (Gorelick et al., 2017), remote sensing time series analysis is becoming increasingly accessible to ecologists. The application of these time series in disturbance ecology could be mainly classified into two use cases. Firstly, these time series could be used to identify disturbances by change detection across thousands of temporally continuous time steps (A. A. C. Alencar et al., 2022; A. H. Y. Chan et al., 2023; Long et al., 2019; Ekhi Roteta et al., 2021). This is exemplified by the LTSfire pipeline described in **Chapter 2:**, which allowed us to fully reconstruct the fire history of Hong Kong over long time scales (1986-2020) with low omission (0.11) and commission (0.02) errors (**Table 2.1**). Having these databases of where and when disturbances occurred is tremendously important in ecological research (Bastarrika et al., 2011; Goodwin & Collett, 2014; Ho et al., 2009; C. Huang et al., 2010; Mitri & Gitas, 2004; Nelson et al., 2013; Stone & Mohammed, 2017). It not only allows us to understand risks and susceptibility (**Chapter 3:**; **Figure 3.3**) (Ko & Lo, 2018; Oliveira et al., 2013; Haojie Wang et al., 2021), but also enables ecologists to correlate measurements of vegetation structure, biomass, biodiversity, species composition, or other environmental variables with past disturbance history (**Chapter 3:**; **Figure 3.6**; **Figure 3.7**) (Bright et al., 2019; Fernández-García et al., 2018; Mahood & Balch, 2019). Secondly, remote sensing time series could be used to track post-disturbance recovery trajectories (Bright et al., 2019; Kennedy et al., 2010, 2012). While disturbances are mostly transient events, the effect of disturbances could be long-lasting, spanning into decadal or even centennial time scales (Crausbay & Martin, 2016; Price et al., 2017; L. Walker & Shiels, 2013). For instance, in our study system of Hong Kong, post-fire recovery back to forest was estimated to take 19 years after shrubland fires and 40 years after grassland fires (**Chapter 3:**; **Figure 3.5**), with rates depending on a suite of environmental and biophysical factors (**Figure 3.7**). The quantification of these processes would not have been possible without the Landsat time series, which provided continuous five-band multispectral imagery at 30 m ground resolution since the launch of Landsat 5 in 1984 (Wulder et al., 2019).

The types of remote sensing time series data available goes beyond optical multispectral imagery. Satellite Synthetic Aperture Radar (SAR) systems, such as SRTM, Tandem-X, and Sentinel 1, have now been continuously collecting data for decades (Paek et al., 2020). Similarly, spaceborne LiDAR systems, such as ICESat, ICESat-2, and GEDI, have also accumulated considerable amount of information on canopy height and structure (Dubayah et al., 2020; Simard et al., 2011). While none of these datasets currently provide easily interpretable data with high spatial resolution for our use case of studying forest resilience against typhoons (**Chapter 5:**), our analysis demonstrated the importance of having repeated measurements of forest structure in studying disturbances, and it is possible that future developments in remote sensing could provide the temporal depth and resolution to investigate the patterns observed in greater detail.

Analysing time series data for disturbance ecology requires a rethink of established statistical methodologies (Kennedy et al., 2010; Kuenzer et al., 2015; J. Zhou et al., 2016). The added temporal dimension in the data structure creates unique challenges in the data analysis and interpretation. For instance, the post-fire successional trajectories (grassland to shrubland to forest) observed in **Chapter 3:** were heavily right-censored. When estimating recovery times, one might be tempted to discard pixels that have not reached the next stage of succession and average the succession times of pixels that did. However, this intuitive approach leads to an underestimation of recovery times as the pixels that have not recovered by the end of the study period might do so in the future and should be considered. The analysis of these datasets requires statistical approaches that explicitly consider time (Kennedy et al., 2010, 2012; Kuenzer et al., 2015; Muenchow, 1986). In our analysis of largely unidirectional recovery trajectories, we used a suite of tools based on survival analysis to obtain unbiased survival times and variable importances (Muenchow, 1986; Therneau, 2019). More complex data structures where pixels transition between multiple vegetation classes might require alternative approaches such as those based on Markov Chains and Queuing Theory (Keshav, 2012). The integration of these techniques into disturbance and restoration ecology merits further exploration.

6.3 Disturbances and forest restoration under a changing climate

Fires and landslides pose challenges in the early stages of forest restoration in the wet subtropics, while wind and pathogens disproportionately affect the later stages of restoration projects. Early successional grasses and shrublands are highly susceptible to fires over dry spells (**Figure 3.3**). As a result, fires represent one of the main disturbances that prevent the establishment of forest trees at the early stages of restoration (Mark A. Cochrane, 2003; Scheper et al., 2021; Souza-Alonso et al., 2022; Wheeler et al., 2016). Similarly, landscapes devoid of trees are particularly prone to landslides and erosion (Dai et al., 2001; Haojie Wang et al., 2021). Landslides affect approximately 4% of the terrestrial surface of the earth every century (Restrepo & Alvarez-Berríos, 2006) and could leave scars on degraded landscapes if the topography is rugged (**Figure 1.5**). Disturbance regimes shift as we enter the later stages of forest restoration projects. Closed canopy rainforests have high resilience against fires by retaining moisture over dry spells (**Figure 3.3**). By intercepting precipitation and producing a tangled mat of roots, forests also stabilise slopes and prevent landslides (L. Walker & Shiels, 2013). On the other hand, forests of taller stature tend to suffer heavier damage during typhoons and storms (**Figure 5.4**; **Figure 5.5**). Forests also tend to be more susceptible to pests and pathogens, especially if restored forests are monocultures or have low tree diversity. To ensure that restoration objectives are met, land managers ought to be aware of these shifts in the relative importance of different disturbances throughout the life cycle of a restoration project.

Importantly, past experiences regarding the impacts of disturbances on forest restoration might not be applicable in the future. Disturbance regimes are rapidly changing under climate change (Seidl et al., 2017). The rise in air temperatures is leading to higher vapour pressure deficits, which increases fire and drought occurrence (Clarke et al., 2022; Koch & Kaplan, 2022; Nolan et al., 2021). Warmer sea surface temperatures are modifying tropical cyclone (TC) regimes, leading to poleward shifts in TC trajectories, overall drop TC frequency, and intensification of TC events (Chand et al., 2022; Kossin et al., 2020; Murakami et al., 2020). The global trade of forest products causes more accidental introductions of pests and pathogens, which benefit from the warming climate (Gandhi & Herms, 2010; R. J. Hall et al., 2016; Seidl et al., 2017). The shortening of the return periods of disturbances demand a reevaluation of disturbance ecology in a forest restoration context.

6.4 Concluding remarks: a shift towards evidence-based restoration

Results from this thesis demonstrate that, with the development of remote sensing, we now have cost effective ways to estimate forest resilience against fire (**Chapter 3:**) and wind (**Chapter 5:**) at a landscape scale. The hope is that these advances could contribute towards the development of evidence-based forest restoration (Sutherland et al., 2004). The forest restoration community is now entering the era where disturbances can be quantitatively described with large empirical datasets. Looking into the future, we expect more studies that estimate risks posed by disturbances on forest restoration projects by parameterising models based on remotely-sensed data. These models can be adjusted to achieve various research objectives. For instance, typhoons lead to substantial losses in aboveground biomass (J. Hall et al., 2020; Parker et al., 2018b), but the same event might enhance biodiversity by allowing native trees to establish in more heavily damaged exotic plantations (**Figure 5.3**) (Zhu et al., 2023). Different objectives of restoration (e.g. carbon and biodiversity) can be modelled separately using different sets of remote sensing data. Models can also be adjusted to account for the effects of climate change on disturbance regimes. Overall, we are hopeful that an improved quantitative understanding of forest resilience against disturbances could bring more certainty towards future forest restoration projects in the wet tropics and subtropics.

6.5 Future work

6.5.1 Towards a general theory on fire-vegetation feedbacks

It has long been known that the direction and strength of fire-vegetation feedbacks varies across different biomes (Tepley et al., 2018). The wet subtropical climate in our study area created strongly positive fire-vegetation feedbacks, but in some fuel limited systems, negative fire-vegetation feedbacks prevail as the accumulation of fuels in later stages of succession increases vegetation fire susceptibility (Héon et al., 2014; Kelly et al., 2013). In **Chapter 3:**, we outlined a methodology to estimate the differences in fire susceptibility between various types of vegetation. The approach, which is based on neighbourhood analysis and reweighting, isolated and quantified the effects of fire-vegetation feedbacks by minimising the imbalance of covariates (e.g. ignition sources). It would be valuable to repeat the analysis in other biomes and investigate how these feedbacks correlate with local climatic variables, such as temperature, precipitation, and seasonality. Additionally, it is noteworthy that the burnt areas in Hong Kong are relatively small due to the fragmentation of the countryside and active fire suppression (**Supp. Figure A.3**). In other ecosystems, large fires could sometimes lead to very different fire-vegetation interactions. For instance, in many temperate coniferous forests, smaller fires tend to be confined to open habitats and the understory, while larger events develop into crown fires with the presence of ladder fuels and cause much more damage on forest trees (Agee & Skinner, 2005; McKelvey et al., 1996). The relationship between the size distribution of burnt patches and the fire-vegetation feedback strength could be a topic worth investigating in the future. By untangling these relationships, we can move towards a general theory to quantitatively describe fire-vegetation feedbacks across different climates and biomes.

6.5.2 Escaping fire traps under climate change

In **Chapter 3**, we saw how positive fire-vegetation feedbacks create fire traps that arrest the landscape at early stages of succession. Land managers in the wet tropics and subtropics are generally aware that fires represent a stumbling block towards forest restoration and need to be controlled (Mark A. Cochrane, 2003; Scheper et al., 2021; Souza-Alonso et al., 2022; Wheeler et al., 2016). However, there is currently little information on (1) how much fire suppression or active restoration is necessary to bring forests back in these fire-ridden landscapes and (2) how long does it take for the landscape to reach forest cover targets under a given level of fire suppression. The current literature on the issue mainly surrounds the development of fire-enabled dynamic global vegetation models (DGVMs) (Hantson, Arneth, et al., 2016). However, existing models have a broad focus and are based on coarse MODIS-based burnt area maps that omit the vast majority of small fires (72% - 96% burnt area omitted in Hong Kong; **Table 2.1**). These models are therefore not particularly suitable to guide local forest restoration projects. Alternatively, Tepley et al. (2018) proposed a theoretical model that estimates equilibrium forest cover in a landscape based on three variables – (1) fire occurrence in forests (λ_1), (2) strength and direction of fire-vegetation feedbacks (λ_1), and (3) post-fire recovery time (r). The study also provided a mathematical framework to model how forest cover varies over time after a change in fire occurrence. Our results on fire occurrence (**Figure 2.10**), strength of fire-vegetation feedbacks (**Figure 3.3**), and post-fire recovery rate (**Figure 3.7**) in Hong Kong provide an exciting opportunity to parameterise the theoretical models and test whether the models could accurately capture forest restoration trajectories in the wet subtropics. The models could also be adjusted to predict our ability to meet restoration targets under changing fire regimes. By providing tangible suppression targets for land managers to operate on (e.g. restoring 75% of the landscape back to forest would require a 50% suppression of fires over three decades), land managers could reallocate resources to better meet forest restoration objects.

6.5.3 Further evaluating typhoon damage using different sources of data

In **Chapter 5**, we analysed changes in canopy height measured by repeated LiDAR scans to evaluate damage incurred during Typhoon Mangkhut. While the airborne LiDAR scans provided datasets of unparalleled scale and accuracy, there remain several questions in wind disturbance that could be better answered by combining multiple data sources. Firstly, forests are increasingly recognised as important carbon stores, and accurately estimating carbon losses over tropical cyclone (TC) events is of great importance to land managers (Bastin et al., 2019; Hernandez et al., 2020; Pan et al., 2011; Wheeler et al., 2016). Existing studies on the topic are mainly based on measurements from a handful of forest inventory plots extrapolated by optical remote sensing data (J. Hall et al., 2020; Hernandez et al., 2020; Parker et al., 2018b). This approach is not ideal as the vegetation indices derived from optical remote sensing imagery often correlates poorly with biomass (Patenaude et al., 2005). LiDAR-derived canopy heights could theoretically provide much more robust estimates of biomass loss. However, the relationship between the loss of canopy height observed in the LiDAR dataset and the loss of biomass is currently not well described. Existing allometric equations on the height-biomass relationship does not consider the potential changes in tree allometries after TCs (Coomes et al., 2017; Jucker et al., 2017). For instance, branch breakage could cause very large drops in canopy height, but may not indicate a corresponding drop in biomass if the stems remain intact. Comparisons between field estimates of biomass loss and changes in LiDAR-derived canopy height represent a notable knowledge gap that needs to be filled in the future.

6.5.4 Wind and forest structure

In this thesis, we demonstrated that local wind regimes created by complex topographies strongly limit maximum canopy height (**Figure 5.6**). With reference to findings from previous studies (Coomes et al., 2018; Ibanez et al., 2019; Telewski & Jaffe, 1986; Thomas et al., 2015; Haoyu Wang et al., 2022), it is reasonable to hypothesise that these effects might extend to other forest structural characteristics, such as the standard deviation in height and tree allometries. Forest structure, in turn, affects biodiversity and species composition (Bohn & Huth, 2016; Cleary et al., 2005). The importance of wind-topography-forest interactions in shaping habitat diversity merits further investigation.

Appendix A: Supplemental Information for Chapter 2

Supp. Table A.1: Major studies that mapped burn areas using medium to high resolution satellite imagery in the wet tropics and subtropics.

Sensor	Location	Biome	Years	Product	Reference
Landsat 5	Brazil	Tropical rainforest and pastures	'85	Burnt pixels	Pereira and Setzer (1993)
Landsat 8	Indonesia	Tropical peatlands	3 years ('15, '16, '18)	Burnt area (single scenes)	Sofan et al. (2019)
Sentinel 1 Sentinel 2	Pakistan	Subtropical dry forest	6 years ('15-'20)	Burnt area (single scenes), severity	Tariq et al. (2021)
Landsat 8	Madagascar	Tropical dry forest	1 year ('13)	Burnt area (single scenes)	Axel (2018)
Sentinel 1	Indonesia	Tropical rainforest, peat swamp forest, shrubland	1 year ('15-'16)	Burnt area (single scenes)	Carreiras et al. (2020)
Landsat 8 Sentinel 1	Indonesia	Tropical rainforest	1 year ('19)	Burnt area (single scenes)	Prasasti et al. (2020)
Landsat 7 Landsat 8	Brazil, Guinea Bissau, DR Congo	Tropical rainforest	3 years ('02, '13, '15)	Burnt area (single scenes)	Cabral et al. (2018)
Sentinel 1 Sentinel 2	Tropical Africa	Tropical forests, shrubland, grassland, savannas	1 year ('15-'16)	Burnt area (time series)	Tanase et al. (2020)
Landsat 7	Brazil	Tropical rainforest	1 year ('02)	Burnt area (single scenes)	Shimabukuro et al. (2014)
Landsat 5	Brazil	Tropical rainforest, savanna, wetland	1 year ('10)	Burnt area (single scenes)	Shimabukuro et al. (2015)

Landsat 8 MODIS	Ghana	Tropical rainforest, dry forest	1 year ('16)	Burnt area (single scenes)	Dwomoh et al. (2019)
Landsat 8 Planet	Africa	Tropical and subtropical forest, shrubland, savanna	1 year ('14-'15)	Burnt area (single scenes)	Martins et al. (2022)
Sentinel 2 MODIS	Sub-Saharan Africa	Tropical, subtropical, and temperate forest, savanna, grassland	1 year ('16)	Burn area (time series), Fire date	Roteta et al. (2019)
Disaster monitoring constellation DMC Landsat 5	Indonesia	Tropical peat swamp forest	3 years ('02, '04, '05)	Burn area (single scenes and 20-day composites)	Tansey et al. (2008)
Sentinel 2	Indonesia	Tropical rainforest, peat swamp forest	1 year ('19)	Burn area, burn severity (single composites)	Gaveau et al., (2021)
Sentinel 1	Indonesia	Tropical rainforest, peat swamp forest	1 year ('15)	Burn area (single scenes)	Lohberger et al. (2018)
Landsat 5 Landsat 7 MODIS	Brazil	Tropical rainforest	9 years ('97-'05)	Burn area (yearly single scenes)	Morton et al. (2011)
Landsat 5 Landsat 7	Brazil	Tropical rainforest	13 years ('92-'04)	Burn area (yearly single scenes)	Matricardi et al. (2010)
Landsat 5 Landsat 7 EO-1	Brazil	Tropical rainforest	13 years ('90-'02)	Burn area, severity (yearly single scenes)	Numata et al. (2011)

Landsat 5 Landsat 7	Brazil	Tropical rainforest	23 years ('83-'06)	Burn area (yearly single scenes)	Alencar et al. (2011)
Landsat 5 Landsat 7 Landsat 8	Brazil	Tropical savannas, grassland, rainforest	32 years ('85-'17)	Burnt area (yearly medoid composites)	Daldegan et al. (2019)
Landsat 5 Landsat 7 Landsat 8	Global	Global	26 years ('89, '92, '95, '96, '98, '00-'20)	Burnt area (yearly)	Long et al. (2019)
Landsat 5 Landsat 7 Landsat 8	Hong Kong	Subtropical rainforest, shrubland, grassland	34 years ('87-'20)	Burnt area (seasonal min-NBR composites), detection date, severity	This study

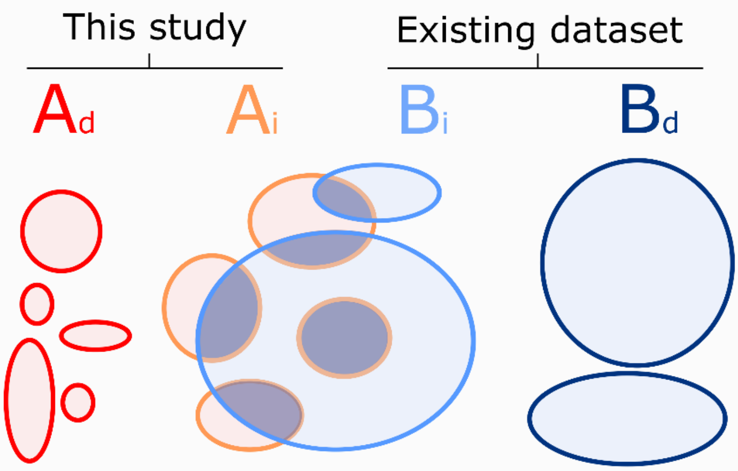

	Measure	Notation in diagram	GABAM	FireCCI51	MCD64A1
Feature count	LTSfire only	A_d	2288	2550	2566
	LTSfire intersect with existing	A_i	488	96	80
	Proportion LTSfire intersecting	$A_i / (A_d + A_i)$	0.176	0.0363	0.0302
	Existing only	B_d	291	44	14
	Existing intersect with LTSfire	B_i	1279	60	38
	Proportion existing intersecting	$B_i / (B_d + B_i)$	0.815	0.577	0.731
	Proportion feature agreement	$(A_i + B_i) / (A_d + A_i + B_d + B_i)$	0.407	0.0567	0.0437
Area (km^2)	LTSfire only	$A_d \cup (A_i \setminus B_i)$ [pink]	211	282	270
	Existing only	$B_d \cup (B_i \setminus A_i)$ [light blue]	37	49	51
	Intersecting	$A_i \cap B_i$ [grey]	135	51	62
	Proportion LTSfire intersecting	$(A_i \cap B_i) / (A_d \cup A_i)$ [grey / (pink + grey)]	0.389	0.153	0.186
	Proportion existing intersecting	$(A_i \cap B_i) / (B_d \cup B_i)$ [grey / (light blue + grey)]	0.787	0.508	0.547
	Sørensen–Dice coefficient	$(A_i \cap B_i) / (A + B)$ [2*grey / (2*grey + pink + light blue)]	0.521	0.235	0.278

Supp. Figure A.1: Table comparing the burn area map produced in this study (LTSfire) with three global burn area products – GABAM, FireCCI51, and MCD64A1. A hypothetical diagram is included to better visualise the metrics used. The circles represent hypothetical burnt patches. Patches could be detected in the LTSfire map and do not intersect with the features in the existing dataset (A_d); detected in the LTSfire map and intersects with features in the existing dataset (A_i); detected in the existing dataset and do not intersect with features in LTSfire (B_d); or detected in the existing dataset and intersect with features in LTSfire (B_i)

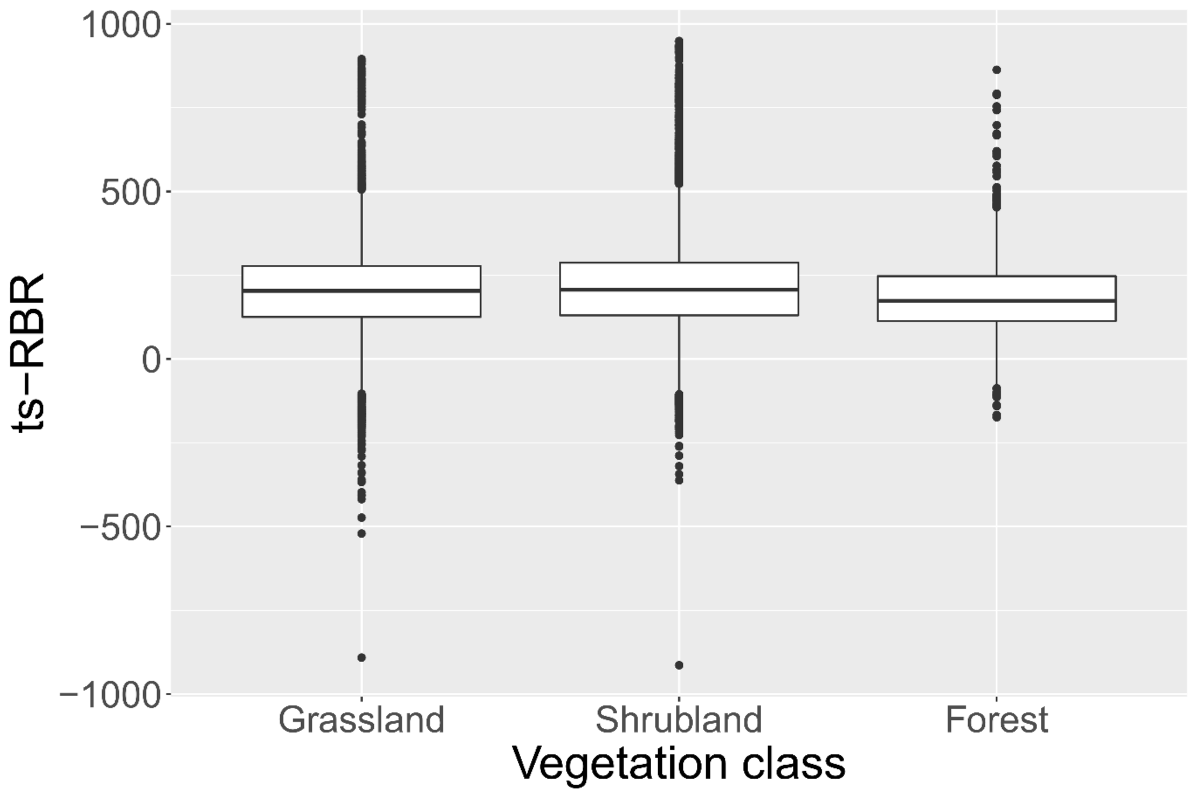

Supp. Figure A.2: Comparing ts-RBR values across three different vegetation classes. The vegetation classes were obtained from 1986-2020 land classification maps derived from Landsat data (**Chapter 3:**).

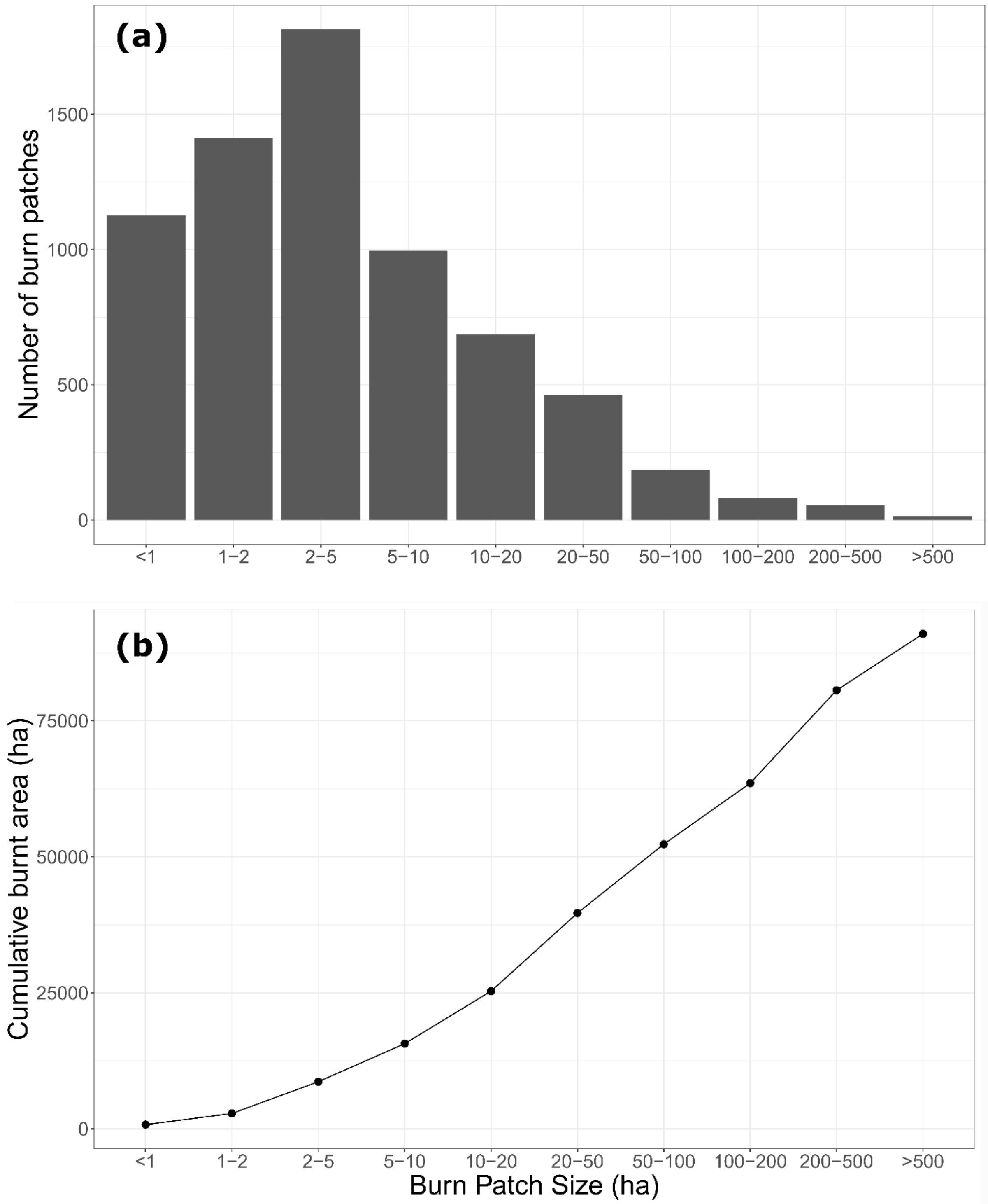

Supp. Figure A.3: Size distribution of burnt patches in Hong Kong detected by LTSfire by (a) patch size category and (b) cumulative burnt area.

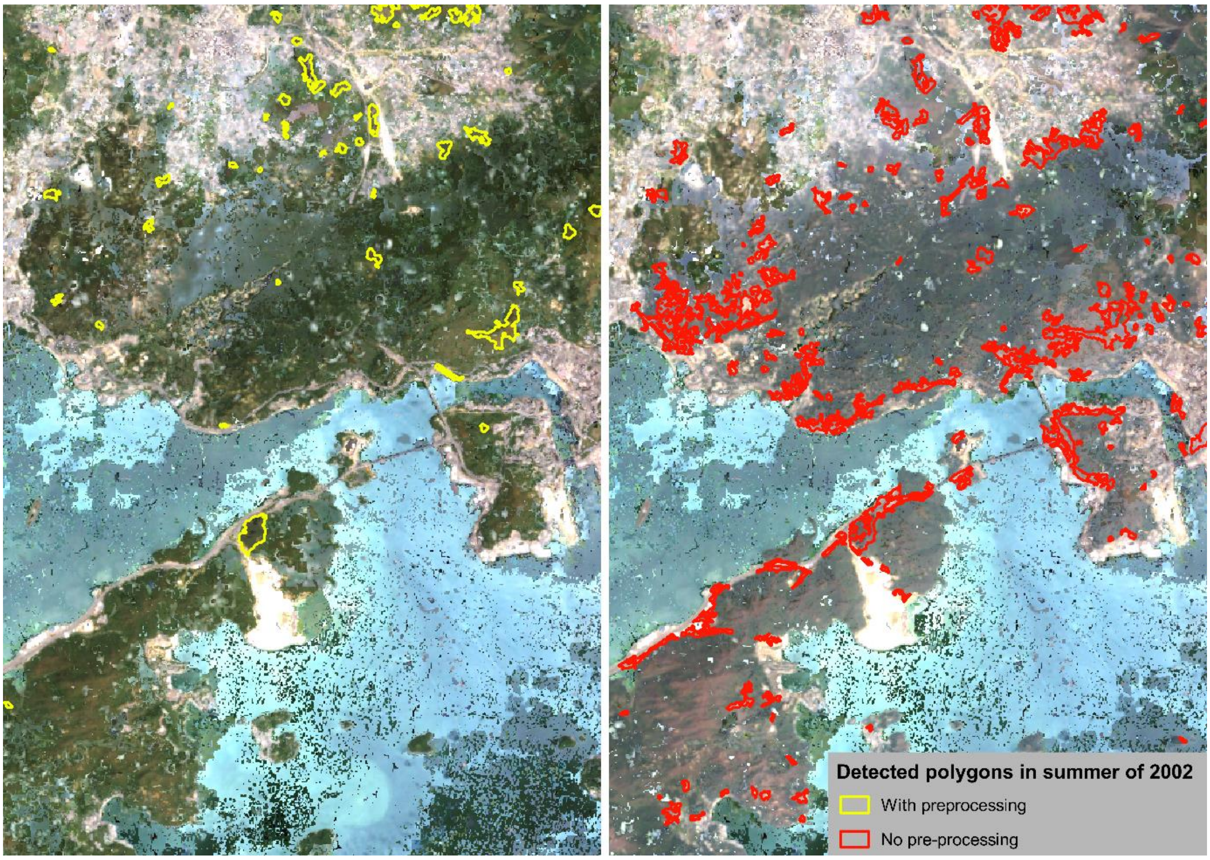

Supp. Figure A.4: Examples of sudden bursts in commission errors in the burn area time series if Landsat scenes were not uniformised in preprocessing. The panel on the left shows the burn areas detected by the full LTSfire pipeline in the summer of 2002 in the Tai Lam and North Lantau region (background shows the seasonal min-NBR composite from scenes uniformised by weighted histogram matching). The panel on the right shows the burn areas detected in the same region by an alternative LTSfire pipeline without weighted histogram matching (background shows the seasonal min-NBR composite of non-uniformised scenes). This particular burst in commission errors in the no pre-processing dataset was mainly caused by a single poorly radiometrically corrected scene on the 4/3/2002.

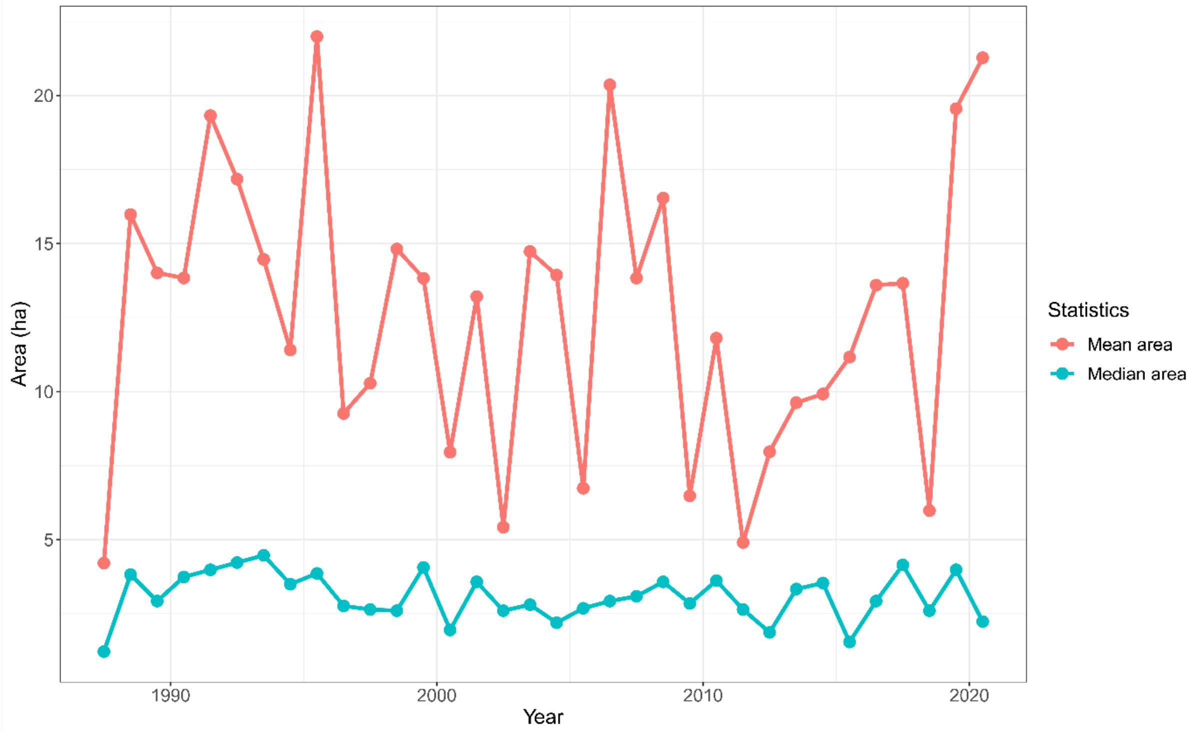

Supp. Figure A.5: Mean and median sizes of burnt patches detected by the LTSfire pipeline over time.

Appendix B: Supplemental Information for Chapter 3

B.1 Methods to create the Landsat-based vegetation map time series

The five-class vegetation map time-series underpinning the study was created from a total of 1537 Landsat 5, 7, and 8 surface reflectance (SR) scenes captured between 1986 and 2020. The scenes were downloaded through Google Earth Engine (Gorelick et al., 2017). Clouds were masked out using the in-built cloud bitmask and by removing pixels with mean RGB reflectances >0.2. We carried out weighted histogram matching to make the scenes more intercomparable to one another (A. H. Y. Chan et al., 2023). The scenes were then distilled into 17 biennial (every two years) median composites. We created separate composites for winter (November – February) and summer (March – October) as winter browning is locally important for distinguishing grasslands from other vegetation types. To minimise the effects of pixel brightness on classification accuracy, two vegetation indices (VIs), the normalised difference vegetation index (NDVI) and enhanced vegetation index (EVI), were added as extra bands to the raster. Additionally, the reflectances of the six Landsat bands were normalised by dividing the reflectance of each band by the mean reflectance of all the bands for any given pixel (A. H. Y. Chan et al., 2021; C. Wu, 2004).

A training dataset was created by extracting the reflectances and VIs from sites with known vegetation and landcover types. The vegetation and land cover of these sites were determined by a combination of field data and historical aerial photo interpretation. Field data consisted of 85 plots, each 10x10 m in size, selected from a vegetation survey conducted in 2020. The plots were grouped into forest, shrubland, or grassland classes based on species composition. A canopy height model (CHM) derived from LiDAR data collected by the Civil Engineering and Development Department (CEDD) was used to ensure that all forest plots had median heights >3m, following Abbas et al. (2016). We are aware that some studies adopt a higher 5m threshold for forests (Di Gregorio, 2005), but forests in Hong Kong tends to be of lower statue due to frequent typhoons, and forests would have grown significantly between the LiDAR survey in 2010 and vegetation survey in 2020. An additional 59 points were collected by interpretating historical aerial imagery. The images used were collected by the Lands Department to periodically cover the entire territory of Hong Kong over a 59-year period (1963–2021). Accessible images were mostly not orthorectified, but the high spatial resolution (up to 10 cm) made it possible to locate patches of grasslands, shrublands, or forest by matching local geological features. The final training dataset consisted of data extracted from 144 (85 field plots + 59 historical points) pixels.

Based on the training dataset, we then built a supervised random forest (RF) model that classified pixels into the five vegetation and landcover classes, namely forest, shrubland, grassland, water, and non-vegetation. The accuracy of the model was assessed by 17-fold cross validation. Validation was carried out across years (i.e. training and validation data were never from the same set of Landsat composites).

The results of the cross-validation exercise could be found in **Supp. Table B.1**. Finally, we built an RF model based on the entire training dataset. This model was applied to all 17 biennial LS composite to produce the five-class vegetation map time series (1986-2020).

B.2 A note on Plantations

Plantations were not analysed as a separate vegetation class in this study. Plantations in Hong Kong are not commercial and were mainly established in Hong Kong to accelerate restoration of degraded landscapes. Many older plantations consist of monocultures of *Lophostemon confertus*, *Acacia confusa*, and *Pinus elliottii*. In recent years, however, native trees are increasingly used to create mixed-species forests. We recognise that plantations could have different fire properties as native forests. However, these properties are dependent on the species composition, and relevant records do not currently exist. In practice, plantations are difficult to distinguish from native forests or shrublands based on Landsat imagery (Kwong et al., 2022). Since plantations only accounts for a small proportion of the landscape (Kwong et al., 2022), we decided against analysing them separately.

B.3 Accuracy of the LTSfire product

LTSfire is a burn area (BA) detection algorithm designed to map BAs in challenging wet tropical and subtropical regions with high cloud cover and rapid post-fire revegetation (A. H. Y. Chan et al., 2023). In the pipeline, we first uniformised the 1537 Landsat 5, 7, 8 surface reflectance scenes by weighted histogram matching (Section 2.2.1). We then produced a total of 68 seasonal composites from the scenes. Minimum normalised burn ratio (min-NBR) was used as the criterion for compositing to highlight burnt areas. The scenes were also composited in a date-traceable manner, with dates of capture carried forward from scenes to composites. Random forest (RF) models were then trained to predict pixel resemblance to BAs based on 94 known BAs. The RF model predictions were later thresholded twice to get seed polygons and growth polygons, which were iteratively merged into a final BA product. Burn severity of pixels encircled by the BA polygons were estimated by the time series relativized burn ratio (ts-RBR), a modified version of the relativized burn ratio (RBR) (Parks et al., 2014) for time series data.

The accuracy of the LTSfire product was estimated through a 10-fold cross validation with reference to known burn areas (BAs) cataloged in government databases. We specifically ensured that the training and validation dataset consisted of pixels from different fire events, not from different parts of the same BA. We also used these known BAs to evaluate global MODIS- and Landsat-based BA products, including MCD64A1 released by NASA, MCD64A1 produced by ESA, and GABAM by Long et al. (2019). Overall, the omission error of LTSfire was low (11%) compared with global BA products such as GABAM (49%), MCD64A1 (72%), and FireCCI51 (96%). Commission errors were also low, accounting for 0.5-2.4% of total area. Temporally, most estimated fire dates were accurate to within a month of the actual fire, and 76.9% of dates were accurate to ±2 months of the actual fire. Further details on the LTSfire pipeline and product validation could be found in Chan et al. (2023).

Supp. Table B.1: Confusion matrix showing the accuracy of the random forest (RF) vegetation classification model. Accuracies were assessed by 17-fold cross validation of training data from different years. The overall accuracy was 0.87 with a Kappa of 0.84.

		Reference					**User's accuracy**
		Forests	Grasslands	Non-vegetation	Shrublands	Water	
Prediction	Forests	38	1	0	3	0	0.91
	Grasslands	0	26	0	1	0	0.96
	Non-vegetation	0	0	26	0	0	1
	Shrublands	3	14	0	36	0	0.68
	Water	0	0	1	0	27	0.96
Producer's accuracy		0.93	0.63	0.96	0.9	1	

Supp. Table B.2: Accuracy of the LTSfire burn area (BA) product compared to that of other BA products (adapted from Chan et al. (2023)). The accuracies were estimated by 10-fold cross validation or direct comparison with manually delineated BA polygons in government fire records. Site omission error refers to the proportion of BA polygons omitted. Area omission error refers to the proportion of omitted BA pixels. Commission error refers to the proportion of unburnt pixels being misclassified as burnt. Numbers in bold represents the highest accuracy or lowest error. More details on the training and validation of the BA datasets can be found in Chan et al. (2023).

Dataset	**Overall Accuracy**	**Site Omission Error**	**Area Omission Error**	**Commission Error**
LTSfire	**0.952**	**0.0319**	**0.112**	0.0242
GABAM	0.860	0.565	0.493	0.012
FireCCI51	0.720	0.987	0.960	**0**
MCD64A1	0.799	0.949	0.720	**0**

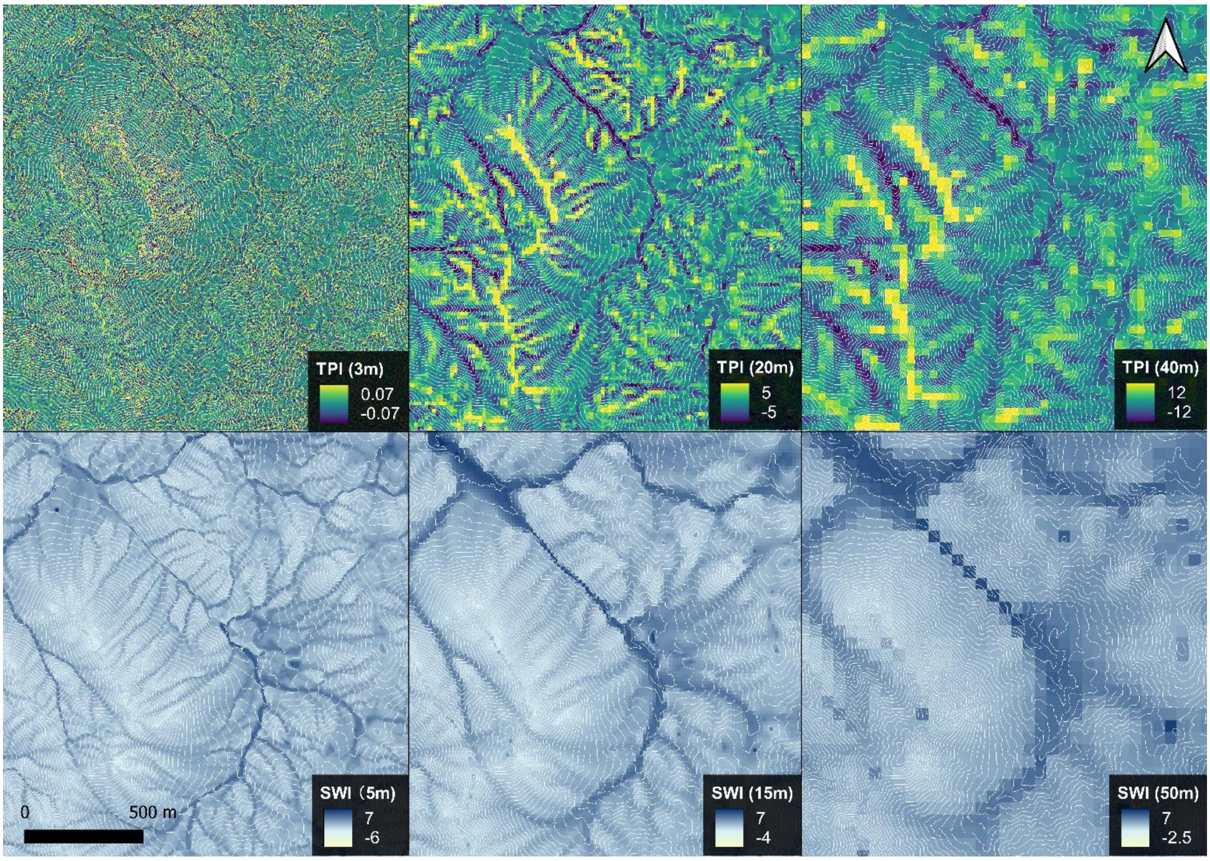

Supp. Figure B.1: The effect of resolution on TPI and SWI.

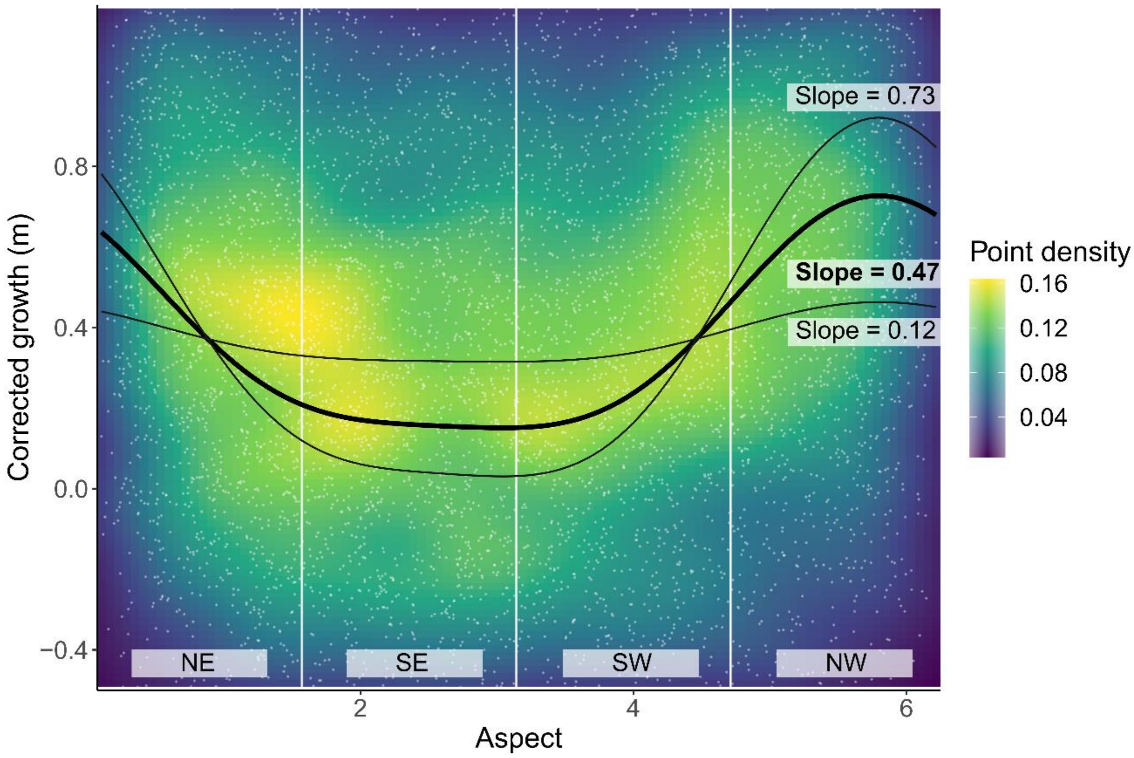

Supp. Figure B.2: The effect of resolution on TPI and SWI.

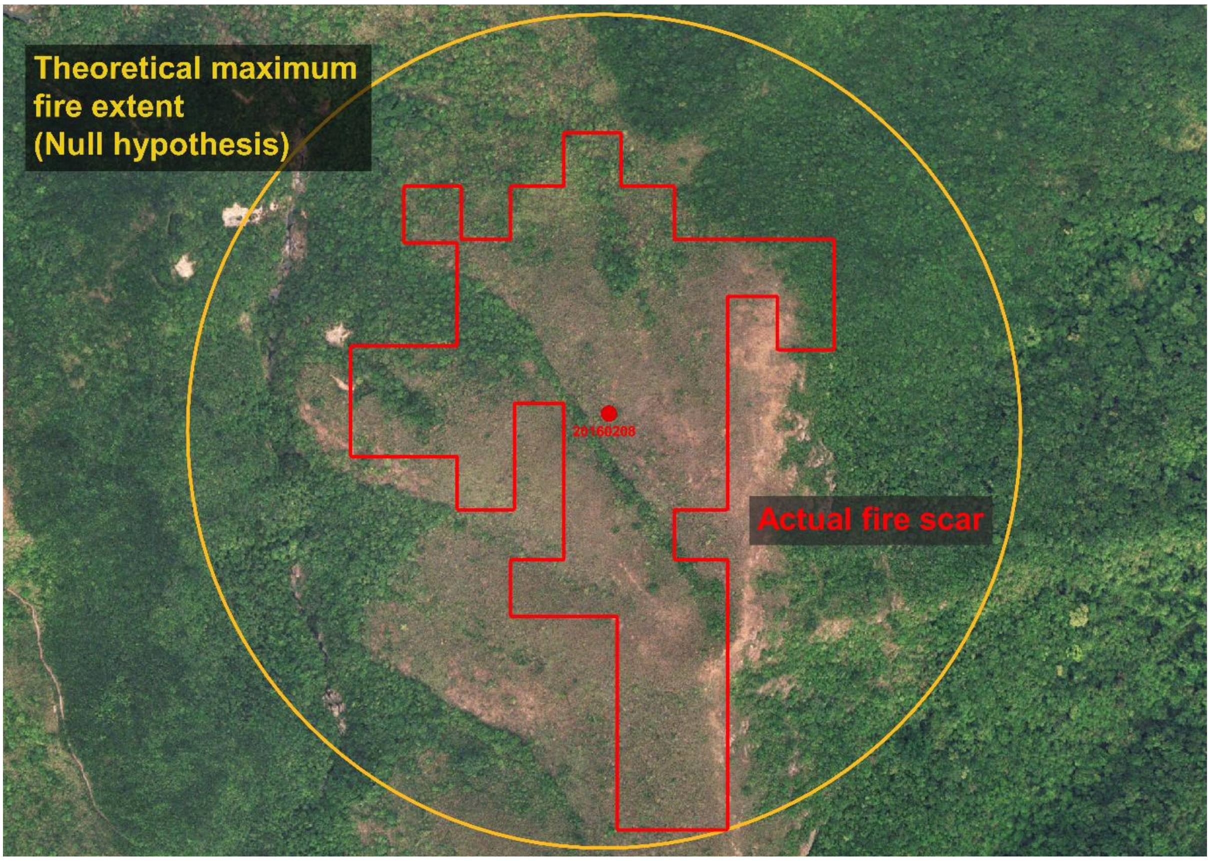

Supp. Figure B.3: Neighbourbood analysis to estimate fire susceptibility.

B.4 A note on covariate imbalance and *do*-calculus

When attempting to estimate the difference in fire susceptibility amongst different vegetation types (grasslands, shrublands, and forests), covariate imbalance could affect the interpretation of the results. For instance, forests could disproportionately occupy wetter valleys, and its low fire susceptibility may be due to topography not vegetation type. Another covariate that remained was the difference in exposure to ignition sources. Although we selected pixels in the neighbourhood of existing burnt areas, which ensured that all pixels have some level of exposure to the source of ignition, the different vegetation types could still have some residual differences in ignition source exposure. It is reasonable to speculate that forests could be further away from the source of ignition amongst all pixels in the circle (**Supp. Figure B.3**). A fair comparison of fire susceptibility between the different vegetation types could be achieved by reweighting pixels such that the reweighted pixels have the same statistical distribution of covariate values across vegetation types.

When a large number of variables are present, it is often difficult to keep track of which variables need to be addressed or controlled. Pearl (1995) pointed out that it is often unnecessary to control for all variables that could potentially confound our inference. Rather, we could use a graphical approach with a set of logical steps (*do*-calculus) to identify the correct variables to address before testing how the exposure variable (independent variable) affects the response variable (dependant variable). The approach involves first drawing a directed acyclic graph (DAG) that includes the exposure variable, response variable, and all other relevant measured or unmeasured variables. We connect the variables by how they relate to each other. The goal is to identify the paths that connect the exposure variable to the response variable (also known as "back doors"). These paths need to be addressed and blocked by approaches such as matching or reweighting. Each of these paths only has to be blocked once, which would be necessary and sufficient to make reliable causal inference between the two variables of interest (Pearl, 2009; Shrier & Platt, 2008; Suttorp et al., 2015).

Supp. Figure B.4 shows the DAG for the study of fire susceptibility amongst different vegetation types and how variables are controlled to minimise the bias when making the causal inference.

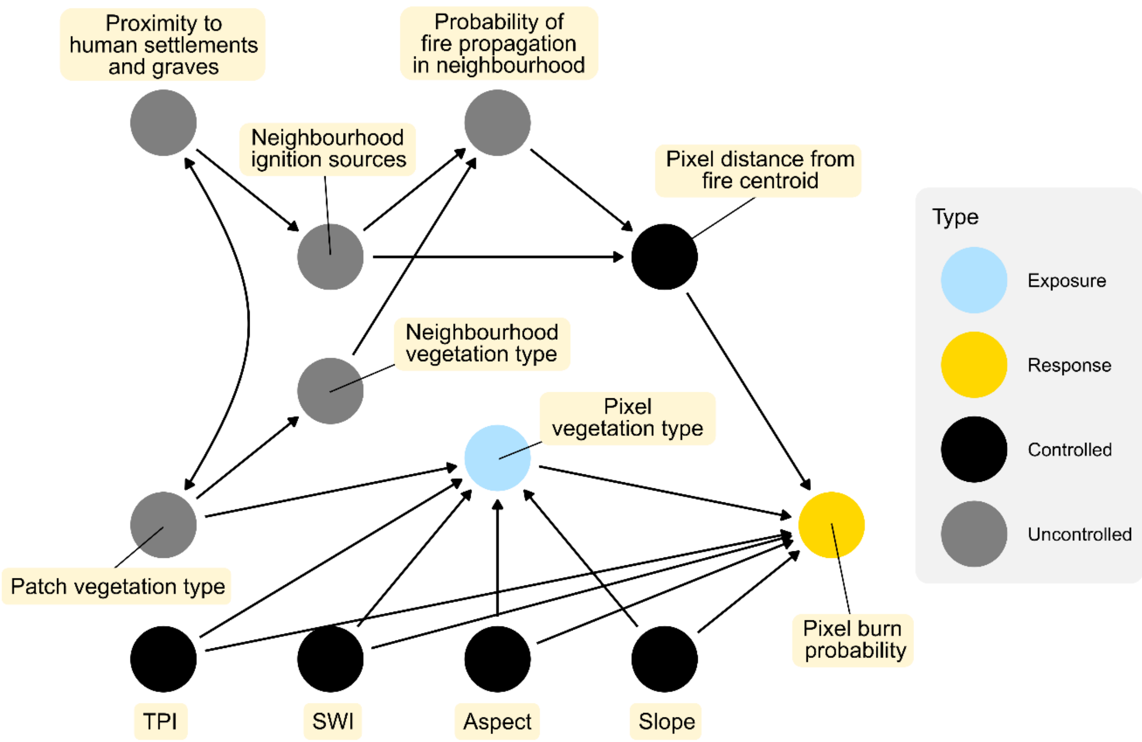

Supp. Figure B.4: Directed acyclic graph (DAG) of the study on fire susceptibility amongst different vegetation types

Supp. Table B.3: Structure of models built. The section number corresponds to where the model was described. TPI refers to topographical position index; SWI refers to SAGA wetness index; cos_aspect refers to aspect linearised by a cosine function; EBAL refers to entropy balancing weights.

Section	Model	Predictor variables	Outcome variable	Notes
2.5.2	Logistic regression	Vegetation type (Forest, shrubland, grassland), TPI, SWI, cos_aspect, slope	Probability of the pixel experiencing a fire	For estimating how fire occurrence differs between different vegetation types (no correction for ignition source imbalance). Training pixels was assigned EBAL weights to minimise covariate imbalance between different vegetation types.
2.5.3	Logistic regression	Vegetation type (Forest, shrubland, grassland), distance from burn area centroid, TPI, SWI, cos_aspect, slope	Probability of pixel burning given fire source in neighbourhood	For estimating how different variables affect fire susceptibility after correcting ignition source imbalance (**Figure 3.3**). Training pixels was assigned EBAL weights to minimise covariate imbalance between different vegetation types. Interaction terms were not included here for better visualisation.
2.5.3	Logistic regression	Vegetation type (Forest, shrubland, grassland), distance from burn area centroid, TPI, SWI, cos_aspect, slope, interaction terms between vegetation type and other variables	Probability of pixel burning given fire source in neighbourhood	For estimating how different variables affect fire susceptibility (**Figure 3.4**). Training pixels was assigned EBAL weights to minimise covariate imbalance between different vegetation types.

2.6	Kaplan-Meier survival function	NA	Burnt shrubland recovery rate (years to 50% forest)	For estimating median recovery time after shrubland fires
2.6	Kaplan-Meier survival function	NA	Burnt grassland recovery rate to young shrubland (years to 50% young shrubland)	For estimating median recovery time after grassland fires
2.6	Kaplan-Meier survival function	NA	Young shrubland recovery rate (years to 50% forest)	For estimating median recovery time after grassland fires
2.6	Kaplan-Meier survival function	Stratified TPI	Burnt grassland to young shrubland succession rate Burnt shrubland to forest succession rate	Stratified into 20 TPI groups for **Figure 3.7**. Pixels were assigned EBAL weights such that each TPI stratum had the same distribution of ts-RBR and distance from nearest forest patch
2.6	Kaplan-Meier survival function	Stratified SWI	Burnt grassland to young shrubland succession rate Burnt shrubland to forest succession rate	Stratified into 20 SWI groups for **Figure 3.7**. Pixels were assigned EBAL weights such that each SWI stratum had the same distribution of TPI, slope, ts-RBR and distance from nearest forest patch
2.6	Kaplan-Meier survival function	Stratified slope	Burnt grassland to young shrubland succession rate Burnt shrubland to forest succession rate	Stratified into 20 slope groups for **Figure 3.7**. Pixels were assigned EBAL weights such that each slope stratum had the same distribution of SWI, ts-RBR

				and distance from nearest forest patch
2.6	Kaplan-Meier survival function	Stratified aspect	Burnt grassland to young shrubland succession rate Burnt shrubland to forest succession rate	Stratified into 20 aspect groups for **Figure 3.7**. Pixels were assigned EBAL weights such that each aspect stratum had the same distribution of ts-RBR and distance from nearest forest patch
2.6	Kaplan-Meier survival function	Stratified ts-RBR	Burnt grassland to young shrubland succession rate Burnt shrubland to forest succession rate	Stratified into five ts-RBR groups for **Supp. Figure B.5c-d** and 20 ts-RBR groups for **Figure 3.7**. Pixels were assigned EBAL weights such that each ts-RBR stratum had the same distribution of TPI, SWI, slope, cos_aspect, and distance from nearest forest patch
2.6	Kaplan-Meier survival function	Stratified distance from nearest forest patch	Burnt grassland to young shrubland succession rate Burnt shrubland to forest succession rate	Stratified into five distance groups for **Supp. Figure B.5a-b** and 20 distance groups for **Figure 3.7**. Pixels were assigned EBAL weights such that each ts-distance stratum had the same distribution of TPI, SWI, slope, cos_aspect, and ts-RBR
2.6	Random survival forest	Prefire vegetation type, post-fire distance to nearest forest patch, ts-RBR,	Expected time it takes (years) for burnt pixels to recover to forests	For assessing the importance of different variables in predicting post-fire recovery

	TPI, SWI, cos_aspect, slope	rate. Results were plotted in **Figure 3.6**

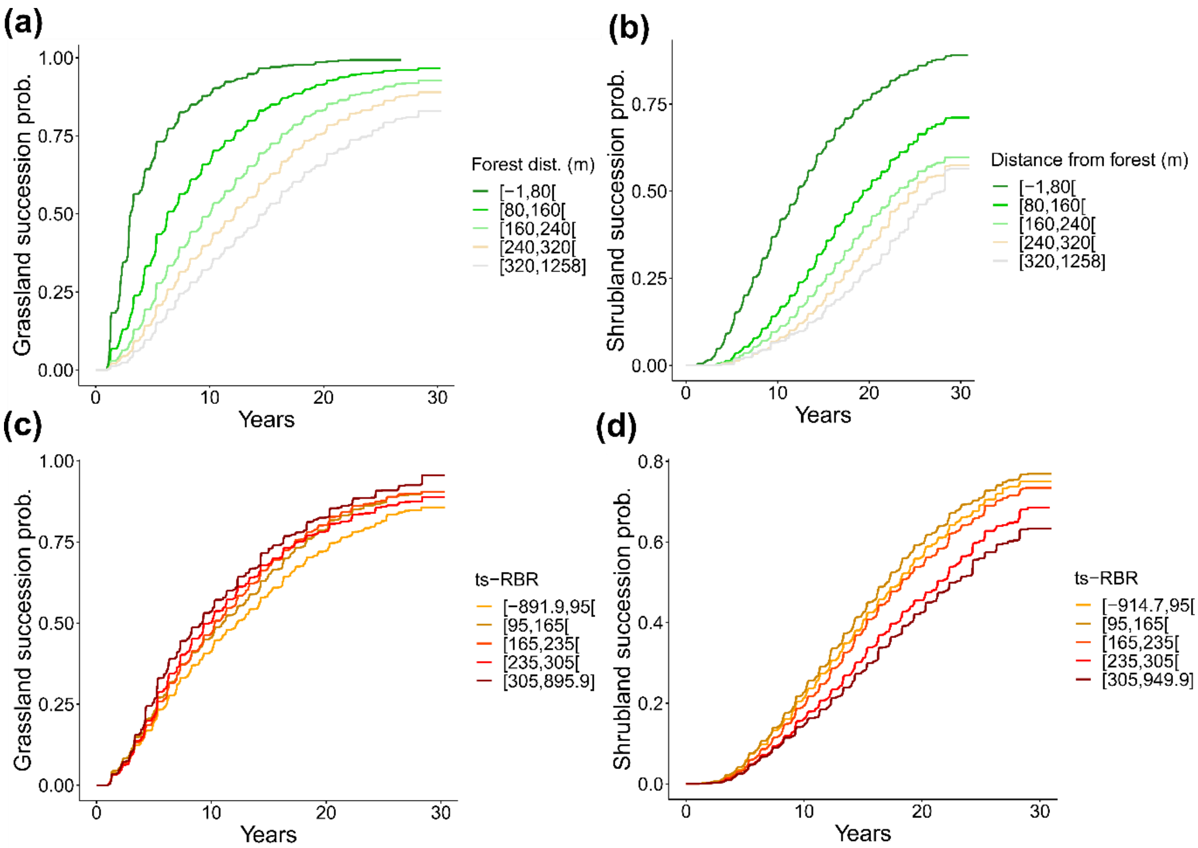

Supp. Figure B.5: Kaplan-Meier survival curves built from a dataset stratified by distance to the nearest forest patch (a and b) or by burn severity (c and d). Panels (a) and (c) represent burnt grassland to shrubland succession probability over time, while panels (b) and (d) represent burnt shrubland to forest succession probability over time.

Appendix C: Supplemental Information for Chapter 5

C.1 Effects of point density on repeated LiDAR data

Context

This section describes the sensitivity analysis where we tested how the point densities of the LiDAR datasets might affect DTM, CHM, and DSM construction. Previous studies have identified the point density as an important metric that affects the quality of LiDAR-derived products, with datasets of higher point densities being able to more accurately reconstruct the 3D structure of background topographies and forest canopies (Aguilar et al., 2010; Balsa-Barreiro & Lerma, 2014; M. E. Hodgson & Bresnahan, 2004). In our study the three LiDAR surveys had notably different point densities (5.3 points/m^2 in 2010, 5.9 points/m^2 in 2017, and 54.5 points/m^2 in 2020). The purpose of this exercise is to investigate whether thinning or resampling is necessary to ensure that the three DSMs are comparable.

Analyses

The analysis was carried out in the 10.8 km^2 Mau Ping region of Hong Kong, which includes vegetation ranging from short shrublands to mature secondary forests. The 2020 LiDAR dataset, which has the highest point density amongst the three datasets, was repeatedly thinned using the *lasthin* function in *LAStools*. More specifically, we lowered the point densities (pd) to 50, 30, 10, 7, 3, 2, 1, 0.5, and 0.25 points per m^2. We then constructed DTMs, CHMs, and DSMs using the same functions described in the main text.

As a first step, we used the DTM, CHM, and DSM constructed from pd = 50m^2 point cloud as a benchmark and measured how heights changed when the pd was lowered. The results are presented in **Supp. Figure C.1**. Overall, the lower the point density, the smaller the chance for some of the points to hit the ground layer, so the DTM gets overestimated (**Supp. Figure C.1**). In contrast, a sparser point cloud makes it difficult to capture the tops of trees, so DSMs tend to be underestimated (**Supp. Figure C.1**). CHM suffers from the largest drop in height as point density drops, as it is sensitive to both the overestimation of the ground layer and the underestimation of top of canopy height (**Supp. Figure C.1**). The results support our use of the DSM in estimating height changes as it was more robust to variations in point density.

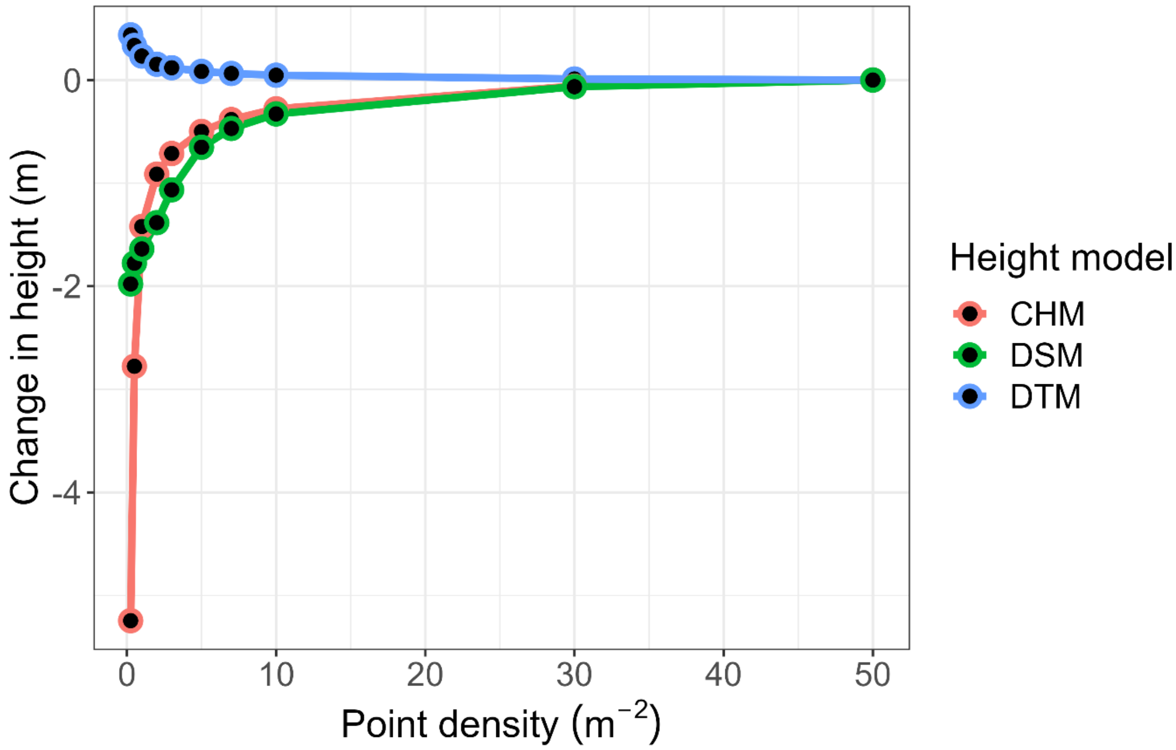

Supp. Figure C.1: Changes in heights of the canopy height model (CHM), digital surface model (DSM), and digital terrain model (DTM) across different point densities of the LiDAR dataset. We used the CHM, DSM, and DTM estimated from the pd = 50 dataset as the benchmark to calculate changes in height as we lowered the point density.

Secondly, we tested whether the strength of point density effects correlated with forest height. As expected, given the same point density, the heights of taller forests tend to be underestimated more. The magnitude of this point density effect was, however, manageable as long as point densities do not fall too low. For all height classes, the errors were <1m when pd = 2 and <0.5m when pd = 3.

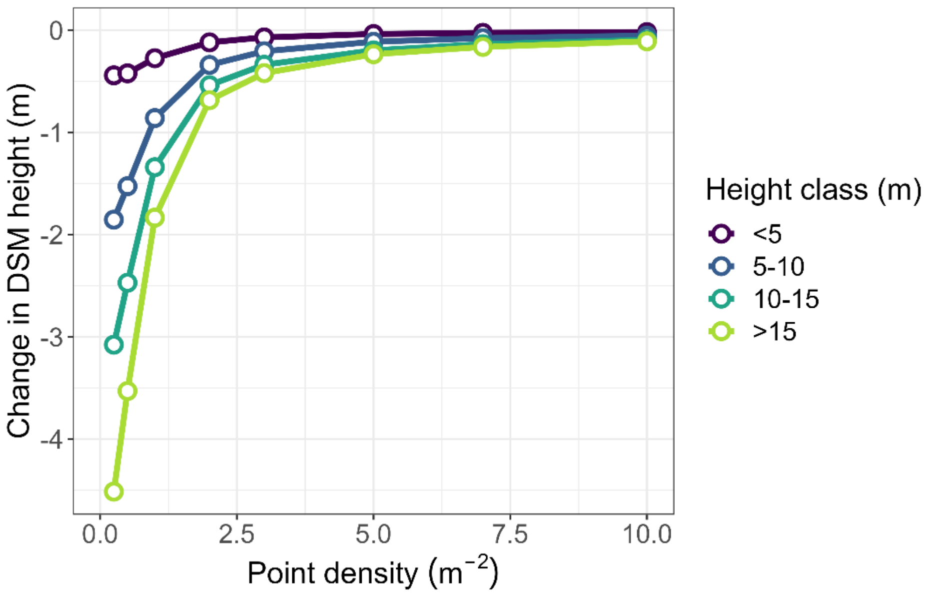

Supp. Figure C.2: The effects of lowering LiDAR point density on DSM heights. The DSM generated from the pd = 50 m-2 point cloud was used as the benchmark to calculated height differences. The four lines represent pixels of different canopy heights.

Part of these errors could be mitigated by lowering the resolution of the DSMs. The results from **Supp. Figure C.2** represent the errors of the original DSM with 1 m ground resolution. If the DSMs were resampled to a larger pixel size by taking the maximum, there might be a better chance of capturing the tops of trees. **Supp. Figure C.3** demonstrates how increasing the ground resolution from 1 m to 2-5 m could reduce the effects of low point densities on DSM height estimates.

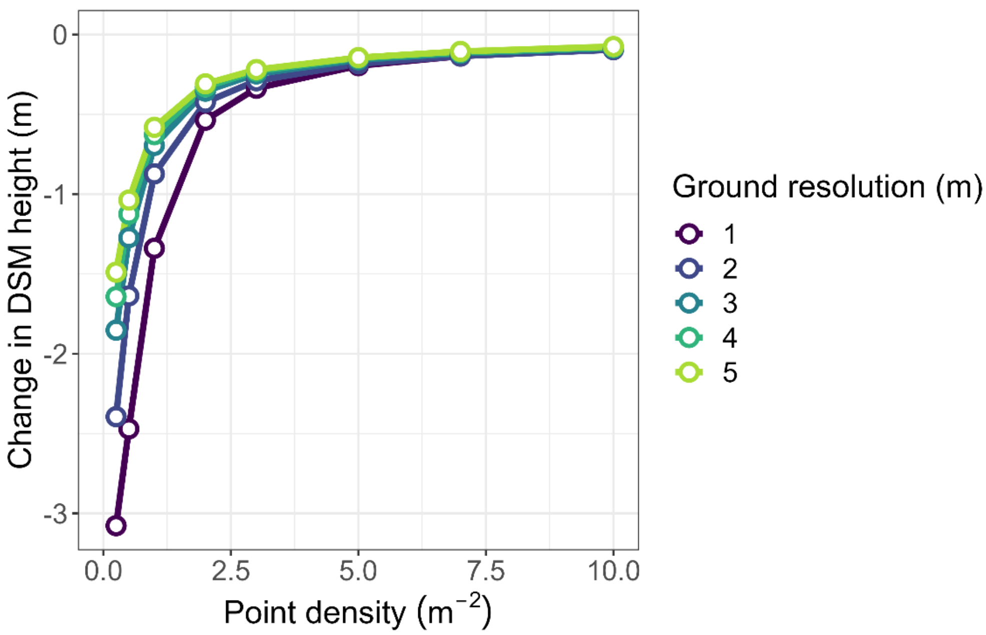

Supp. Figure C.3: Lowering the ground resolution of the DSMs by maximum resampling mitigates the drop in DSM due to lower LiDAR point densities. This graph represents trees in the 10-15 m height class. The DSM created from the pd = 50 m2 was used as a benchmark.

In light of the results from the sensitivity analysis, we adjusted our methodology in estimating changes in canopy height. Firstly, we differenced the DSMs instead of the CHMs as DSMs were less sensitive to changes in point density. Secondly, we lowered the point density of the 2020 dataset to 5.4 m^{-2} to match that of the two other datasets. Thirdly, when relevant, we excluded regions that had point densities <1.5 m^{-2} from the 2017 dataset, which should control the errors of the DSM to <1 m. Fourthly, to further mitigate these errors, we resampled the DSMs to 2 m ground resolution before differencing DSMs to estimate canopy height change. Lastly, it is important to note that errors in **Supp. Figure C.1-3** were calculated by comparing the DSMs with another DSM created from the pd = 50 m^{-2} point cloud. In our actual analysis, we were differencing DSMs created from similar point densities (i.e. all datasets would have been slightly underestimating height). After differencing, these errors would have partially been cancelled out. Hence, in the 2010-2017-2020 height change dataset, the actual errors attributable to differences in point density would be substantially smaller than that presented in **Supp. Figure C.1-3**.

C.2 Multiple regression model of 2017 – 2020 height change

Context

In the main text we described a multiple regression model that use different variables to predict canopy height change between 2017 and 2020 (damage by Typhoon Mangkhut). Here we (1) provide additional information on the variable selection process and (2) detail the results of the model.

Analyses

A number of environmental variables relevant to typhoon damage were measured or estimated in the study, namely 2017 canopy height, aspect, cosine aspect, elevation, mean wind speed, maximum Mangkhut wind speed, normalised maximum Mangkhut wind speed, Saga wetness index (SWI), topographical position index (TPI), and slope. Amongst these variables, elevation and aspect were used to build the wind models. Aspect additionally had a cyclical effect on forests and its linearised form (cosine aspect) would have complicated correlations with the wind variables. Hence, we excluded elevation, aspect, and cosine aspect from the model. We then generated a correlation matrix with the remaining variables (**Supp. Figure C.4**). We observed that long-term mean wind speed had a strong correlation with maximum wind speed during Typhoon Mangkhut (**Supp. Figure C.4**). Hence, instead of using both variables in the model, we predicted maximum wind speed from the long-term mean wind speed, then subtracted these predicted values from the maximum Mangkhut wind speed to create a normalised variable (norm. max). The new variable was more orthogonal to long-term mean wind speed. The three remaining topographical variables (SWI, TPI, and slope) were also somewhat correlated with each other (**Supp. Figure C.4**). We built the models with different permutations of these topographical variables and found that TPI had relatively small effect sizes on its own but significantly affected the coefficients of the other two variables. Hence, we built the final model without TPI. The resulting coefficients and the variance inflation factors (VIFs) for all variables in the final model could be found in **Supp. Table C.1**.

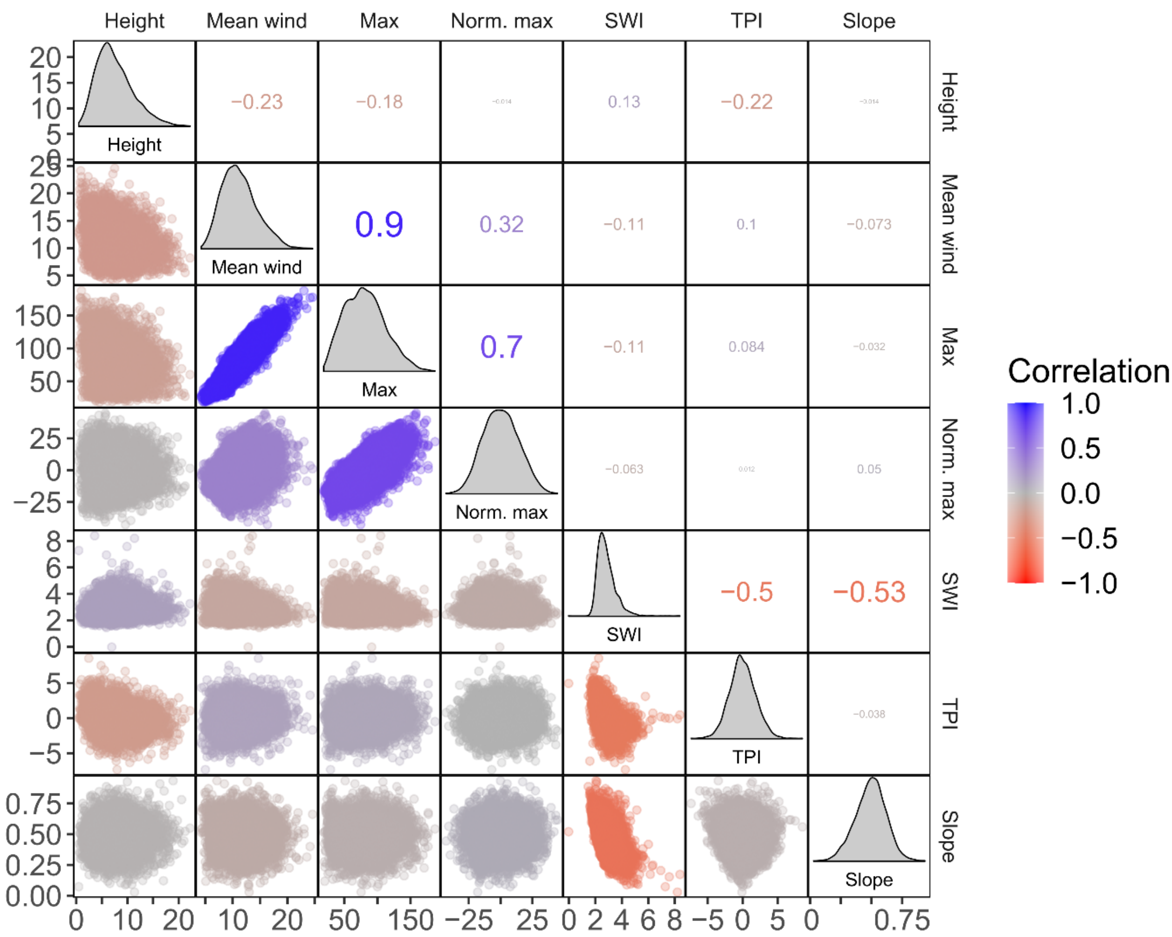

Supp. Figure C.4: Correlation matrix between various environmental variables

Supp. Table C.1: Summary statistics from the multiple regression model on 2017 – 2020 canopy height change. The sample size was 191704 pixels, each 30 m by 30 m in size. VIF = Variance Inflation Factor.

Variable	Estimate	Std. error	*t* value	*p*-value	VIF
(Intercept)	-0.091	0.0016	-57.8	<0.0001	N/A
2017 canopy height	-0.212	0.0015	-138.5	<0.0001	1.10
Mean wind	0.033	0.0016	20.5	<0.0001	1.25
Norm. max wind	-0.054	0.0016	-34.7	<0.0001	1.17
Height : Mean wind	0.035	0.0016	22.6	<0.0001	1.18
Height : Norm. max wind	-0.020	0.0016	-12.5	<0.0001	1.18
Mean : Norm. max wind	0.020	0.0016	12.3	<0.0001	1.07
SWI	-0.036	0.0018	-20.6	<0.0001	1.48
Slope	0.056	0.0018	31.7	<0.0001	1.45

C.3 Long-term wind acclimation increases forest typhoon resistance

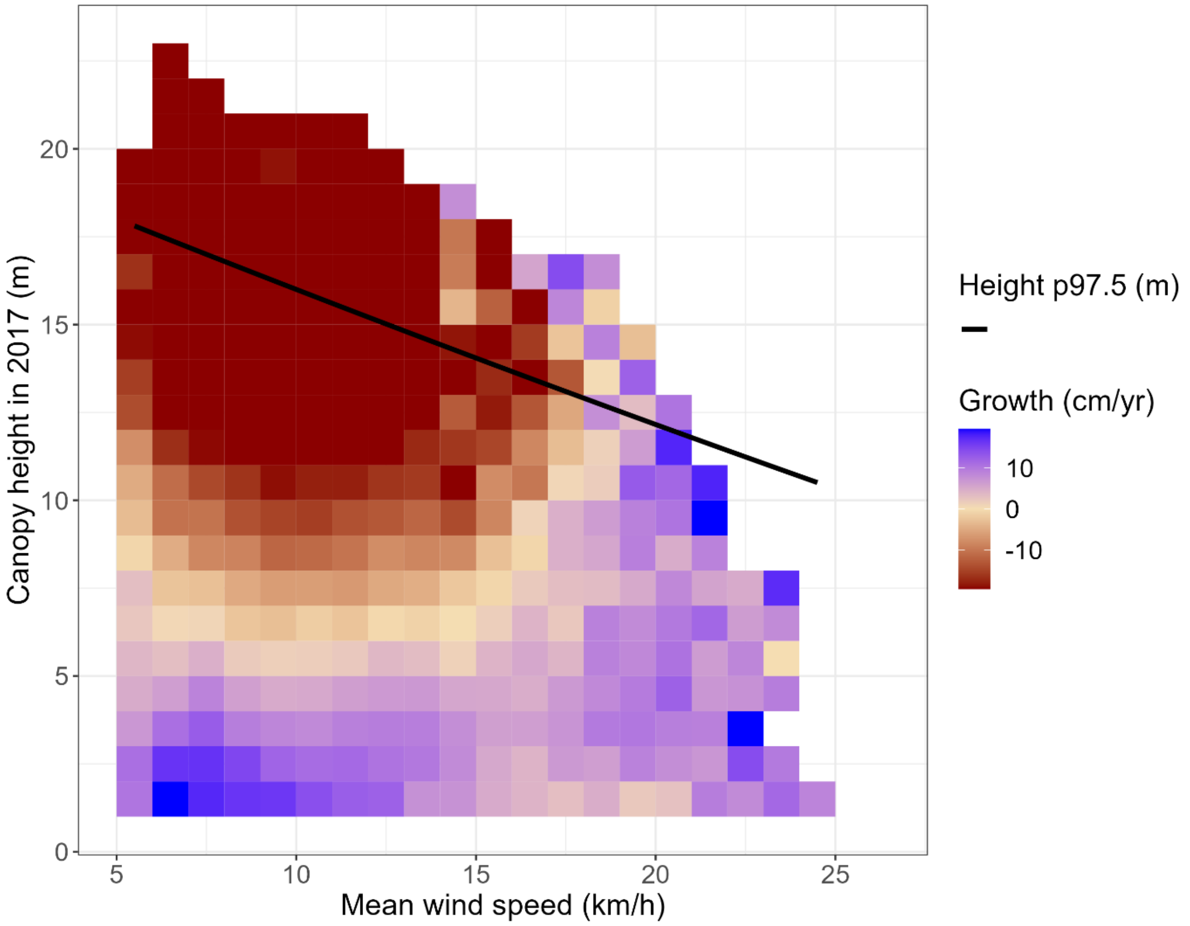

Supp. Figure C.5: The change in canopy height between 2017-2020 (n = 191744) against long-term mean wind speed and canopy height in 2017. The black line represents the maximum canopy height (97.5th percentile) estimated by second-order quantile regression. This is an alternative version of Figure 5a in the main text, but with long-term mean wind speed instead of maximum typhoon wind speed on the x-axis.

C.4 Quantile regression with 2020 canopy heights

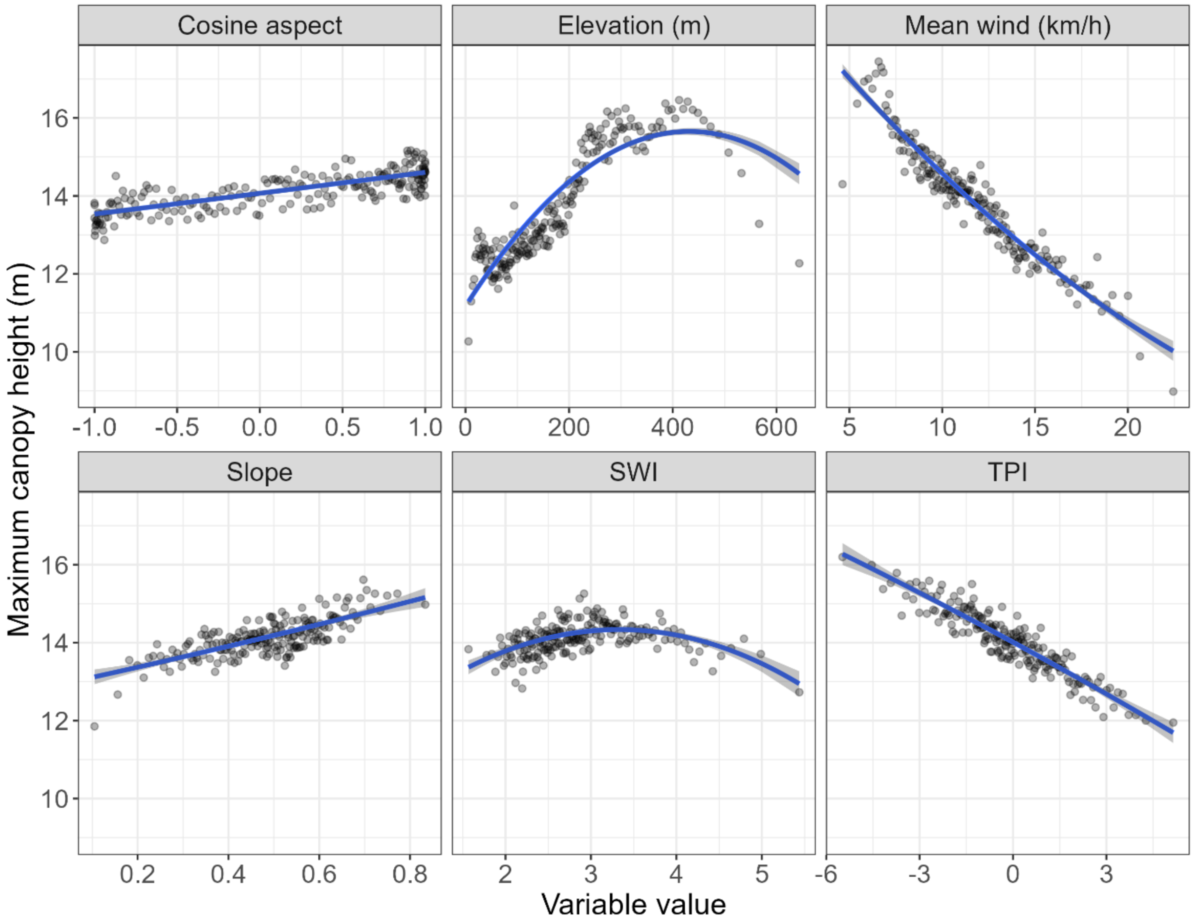

Supp. Figure C.6: Quantile regression on maximum canopy heights (97.5th percentile) in 2020. The patterns were very similar to that produced from 2010 canopy heights (Figure 5.6). Each point represents the maximum average canopy height (97.5thpercentile) amongst 2000 pixels. The blue lines were second order 97.5th quantile regression lines through the entire dataset. SWI = SAGA wetness index; TPI = topographical position index.

References

Abatzoglou, J. T., Battisti, D. S., Williams, A. P., Hansen, W. D., Harvey, B. J., & Kolden, C. A. (2021). Projected increases in western US forest fire despite growing fuel constraints. *Communications Earth & Environment 2021 2:1*, *2*(1), 1–8. https://doi.org/10.1038/s43247-021-00299-0

Abatzoglou, J. T., Williams, A. P., & Barbero, R. (2019). Global Emergence of Anthropogenic Climate Change in Fire Weather Indices. *Geophysical Research Letters*, *46*(1), 326–336. https://doi.org/10.1029/2018GL080959

Abbas, S., Nichol, J. E., & Fischer, G. A. (2016). A 70-year perspective on tropical forest regeneration. *Science of the Total Environment*, *544*, 544–552. https://doi.org/10.1016/j.scitotenv.2015.11.171

Abbas, S., Nichol, J. E., & Fischer, G. A. (2017). Mapping and assessment of impacts of cold and frost on secondary forest in the marginally tropical landscape of Hong Kong. *Agricultural and Forest Meteorology*, *232*, 543–549. https://doi.org/10.1016/J.AGRFORMET.2016.10.008

Abbas, S., Nichol, J. E., Fischer, G. A., Wong, M. S., & Irteza, S. M. (2020). Impact assessment of a super-typhoon on Hong Kong's secondary vegetation and recommendations for restoration of resilience in the forest succession. *Agricultural and Forest Meteorology*, *280*. https://doi.org/10.1016/j.agrformet.2019.107784

Abhilash, P. C. (2021). Restoring the Unrestored: Strategies for Restoring Global Land during the UN Decade on Ecosystem Restoration (UN-DER). *Land 2021, Vol. 10, Page 201*, *10*(2), 201. https://doi.org/10.3390/LAND10020201

Agee, J. K., & Skinner, C. N. (2005). Basic principles of forest fuel reduction treatments. *Forest Ecology and Management*, *211*(1–2), 83–96. https://doi.org/10.1016/J.FORECO.2005.01.034

Aguilar, F. J., Mills, J. P., Delgado, J., Aguilar, M. A., Negreiros, J. G., & Pérez, J. L. (2010). Modelling vertical error in LiDAR-derived digital elevation models. *ISPRS Journal of Photogrammetry and Remote Sensing*, *65*(1), 103–110. https://doi.org/10.1016/J.ISPRSJPRS.2009.09.003

Albrecht, A. T., Jung, C., & Schindler, D. (2019). Improving empirical storm damage models by coupling with high-resolution gust speed data. *Agricultural and Forest Meteorology*, *268*, 23–31. https://doi.org/10.1016/j.agrformet.2018.12.017

Alencar, A. A. C., Arruda, V. L. S., da Silva, W. V., Conciani, D. E., Costa, D. P., Crusco, N., Duverger, S. G., Ferreira, N. C., Franca-Rocha, W., Hasenack, H., Martenexen, L. F. M., Piontekowski, V. J., Ribeiro, N. V., Rosa, E. R., Rosa, M. R., Dos Santos, S. M. B., Shimbo, J. Z., & Vélez-Martin, E. (2022). Long-Term Landsat-Based Monthly Burned Area Dataset for the Brazilian Biomes Using Deep Learning. *Remote Sensing*, *14*(11), 2510. https://doi.org/10.3390/RS14112510/S1

Alencar, A., Asner, G. P., Knapp, D., & Zarin, D. (2011). Temporal variability of forest fires in eastern Amazonia. *Ecological Applications*, *21*(7), 2397–2412. https://doi.org/10.1890/10-1168.1

Aragão, L. E. O. C., Anderson, L. O., Fonseca, M. G., Rosan, T. M., Vedovato, L. B., Wagner, F. H., Silva, C. V. J., Silva Junior, C. H. L., Arai, E., Aguiar, A. P., Barlow, J., Berenguer, E., Deeter, M. N., Domingues, L. G., Gatti, L., Gloor, M., Malhi, Y., Marengo, J. A., Miller, J. B., … Saatchi, S. (2018). 21st Century drought-related fires counteract the decline of Amazon deforestation carbon emissions. *Nature Communications*, *9*(1), 1–12. https://doi.org/10.1038/s41467-017-02771-y

Araújo, F. D. C., Tng, D. Y. P., Apgaua, D. M. G., Coelho, P. A., Pereira, D. G. S., & Santos, R. M. (2017). Post-fire plant regeneration across a closed forest-savanna vegetation transition. *Forest Ecology and Management*, *400*, 77–84. https://doi.org/10.1016/J.FORECO.2017.05.058

Archibald, S., Scholes, R. J., Roy, D. P., Roberts, G., & Boschetti, L. (2010). Southern African fire regimes as revealed by remote sensing. *International Journal of Wildland Fire*, *19*(7), 861–878. https://doi.org/10.1071/WF10008

Ashworth, J. M., Corlett, R. T., Dudgeon, D., Melville, D. S., & Tang, W. S. M. (1993). Hong Kong flora and fauna: computing conservation. *World Wide Fund for Nature*.

Asner, G. P. (2001). Cloud cover in Landsat observations of the Brazilian Amazon. *International Journal of Remote Sensing*, *22*(18), 3855–3862.

Au, A. Y. Y., Corlett, R. T., & Hau, B. C. H. (2006). Seed rain into upland plant communities in Hong Kong, China. *Plant Ecology*, *186*(1), 13–22. https://doi.org/10.1007/s11258-006-9108-5

Axel, A. C. (2018). Burned Area Mapping of an Escaped Fire into Tropical Dry Forest in Western Madagascar Using Multi-Season Landsat OLI Data. *Remote Sensing 2018, Vol. 10, Page 371*, *10*(3), 371. https://doi.org/10.3390/RS10030371

Balsa-Barreiro, J., & Lerma, J. L. (2014). Empirical study of variation in lidar point density over different land covers. *Http://Dx.Doi.Org/10.1080/01431161.2014.903355*, *35*(9), 3372–3383. https://doi.org/10.1080/01431161.2014.903355

Barnosky, A. D., Matzke, N., Tomiya, S., Wogan, G. O. U., Swartz, B., Quental, T. B., Marshall, C., McGuire, J. L., Lindsey, E. L., Maguire, K. C., Mersey, B., & Ferrer, E. A. (2011). Has the Earth's sixth mass extinction already arrived? In *Nature* (Vol. 471, Issue 7336, pp. 51–57). Nature Publishing Group. https://doi.org/10.1038/nature09678

Barros, A. M. G., & Pereira, J. M. C. (2014). Wildfire Selectivity for Land Cover Type: Does Size Matter? *PLOS ONE*, *9*(1), e84760. https://doi.org/10.1371/JOURNAL.PONE.0084760

Bartels, S. F., Chen, H. Y. H., Wulder, M. A., & White, J. C. (2016). Trends in post-disturbance recovery rates of Canada's forests following wildfire and harvest. In *Forest Ecology and Management* (Vol. 361, pp. 194–207). Elsevier. https://doi.org/10.1016/j.foreco.2015.11.015

Bastarrika, A., Chuvieco, E., & Martín, M. P. (2011). Mapping burned areas from landsat TM/ETM+ data with a two-phase algorithm: Balancing omission and commission errors. *Remote Sensing of Environment*, *115*(4), 1003–1012. https://doi.org/10.1016/j.rse.2010.12.005

Bastin, J. F., Finegold, Y., Garcia, C., Mollicone, D., Rezende, M., Routh, D., Zohner, C. M., & Crowther, T. W. (2019). The global tree restoration potential. *Science*, *364*(6448), 76–79. https://doi.org/10.1126/science.aax0848

Beadle, N. C. W. (1940). Soil Temperatures During Forest Fires and Their Effect on the Survival of Vegetation. *The Journal of Ecology*, *28*(1), 180. https://doi.org/10.2307/2256168

Belcher, S. E., Harman, I. N., & Finnigan, J. J. (2011). The Wind in the Willows: Flows in Forest Canopies in Complex Terrain. *Https://Doi.Org/10.1146/Annurev-Fluid-120710-101036*, *44*, 479–504. https://doi.org/10.1146/ANNUREV-FLUID-120710-101036

Bell, R. H. V. (1984). Notes on elephant-woodland interactions. *Status and Conservation of Africa's Elephants and Rhinos*, 98–103.

Bellingham, P. J. (1991). Landforms Influence Patterns of Hurricane Damage: Evidence From Jamaican Montane Forests. *Biotropica*, *23*(4), 427. https://doi.org/10.2307/2388262

Berge, E., Gravdahl, A. R., Schelling, J., Tallhaug, L., & Undheim, O. (2006). Wind in complex terrain. A comparison of WAsP and two CFD-models. *Proceedings from EWEC*, *27*.

Bhagwat, S. A., Willis, K. J., Birks, H. J. B., & Whittaker, R. J. (2008). Agroforestry: a refuge for tropical biodiversity? *Trends in Ecology & Evolution*, *23*(5), 261–267. https://doi.org/10.1016/J.TREE.2008.01.005

Bohlin, J., Wallerman, J., & Fransson, J. E. S. (2012). Forest variable estimation using photogrammetric matching of digital aerial images in combination with a high-resolution DEM. *Scandinavian Journal of Forest Research*, *27*(7), 692–699. https://doi.org/10.1080/02827581.2012.686625

Bohn, F. J., & Huth, A. (2016). The importance of forest structure to biodiversity–productivity relationships. *Royal Society Open Science*, *4*(1). https://doi.org/10.1098/RSOS.160521

Böhner, J., & Selige, T. (2006). Spatial prediction of soil attributes using terrain analysis and climate regionalisation. *Gottinger Geographische Abhandlungen*, *115*, 13–28.

Bonnesoeur, V., Constant, T., Moulia, B., & Fournier, M. (2016). Forest trees filter chronic wind-signals to acclimate to high winds. *New Phytologist*, *210*(3), 850–860.

https://doi.org/10.1111/NPH.13836

Boschetti, L, Roy, D. P., & Justice, C. O. (2009). International global burned area satellite product validation protocol part I--production and standardization of validation reference data. *Committee on Earth Observation Satellites: Maryland, MD, USA*, 1–11.

Boschetti, Luigi, Roy, D. P., Giglio, L., Huang, H., Zubkova, M., & Humber, M. L. (2019). Global validation of the collection 6 MODIS burned area product. *Remote Sensing of Environment*, *235*, 111490. https://doi.org/10.1016/J.RSE.2019.111490

Boschetti, Luigi, Stehman, S. V., & Roy, D. P. (2016). A stratified random sampling design in space and time for regional to global scale burned area product validation. *Remote Sensing of Environment*, *186*, 465–478. https://doi.org/10.1016/J.RSE.2016.09.016

Boucher, D. H. (1990). Growing back after hurricanesCatastrophes may be critical to rain forest dynamics. *BioScience*, *40*(3), 163–166. https://doi.org/10.2307/1311359

Bowman, D. M. J. S., Zhang, Y., Walsh, A., & Williams, R. J. (2003). Experimental comparison of four remote sensing techniques to map tropical savanna fire-scars using Landsat-TM imagery. *International Journal of Wildland Fire*, *12*(4), 341–348. https://doi.org/10.1071/WF03030

Brancalion, P. H. S., & Holl, K. D. (2020). Guidance for successful tree planting initiatives. *Journal of Applied Ecology*, *57*(12), 2349–2361. https://doi.org/10.1111/1365-2664.13725

Brando, P. M., Paolucci, L., Ummenhofer, C. C., Ordway, E. M., Hartmann, H., Cattau, M. E., Rattis, L., Medjibe, V., Coe, M. T., & Balch, J. (2019). Droughts, Wildfires, and Forest Carbon Cycling: A Pantropical Synthesis. *Annual Review of Earth and Planetary Sciences*, *47*(1), 555–581. https://doi.org/10.1146/annurev-earth-082517-010235

Breiman, L., Cutler, A., Liaw, A., & Wiener, M. (2018). Package 'randomforest.' *University of California, Berkeley: Berkeley, CA, USA*. https://peerj.com/articles/9945/Supplemental_Data_S11.pdf

Bright, B. C., Hudak, A. T., Kennedy, R. E., Braaten, J. D., & Henareh Khalyani, A. (2019). Examining post-fire vegetation recovery with Landsat time series analysis in three western North American forest types. *Fire Ecology*, *15*(1), 1–14. https://doi.org/10.1186/S42408-018-0021-9/TABLES/7

Brun, P., Zimmermann, N. E., Hari, C., Pellissier, L., & Karger, D. N. (2022). Global climate-related predictors at kilometre resolution for the past and future. *Earth System Science Data Discussions*, *2022*, 1–44. https://doi.org/10.5194/essd-2022-212

Budiharta, S., Meijaard, E., Erskine, P. D., Rondinini, C., Pacifici, M., & Wilson, K. A. (2014). Restoring degraded tropical forests for carbon and biodiversity. *Environmental Research Letters*, *9*(11), 114020. https://doi.org/10.1088/1748-9326/9/11/114020

Busby, S. U., Moffett, K. B., & Holz, A. (2020). High-severity and short-interval wildfires limit forest recovery in the Central Cascade Range. *Ecosphere*, *11*(9), e03247. https://doi.org/10.1002/ECS2.3247

Cabral, A. I. R., Silva, S., Silva, P. C., Vanneschi, L., & Vasconcelos, M. J. (2018). Burned area estimations derived from Landsat ETM+ and OLI data: Comparing Genetic Programming with Maximum Likelihood and Classification and Regression Trees. *ISPRS Journal of Photogrammetry and Remote Sensing*, *142*, 94–105. https://doi.org/10.1016/J.ISPRSJPRS.2018.05.007

Cade, B. S., & Noon, B. R. (2003). A gentle introduction to quantile regression for ecologists. *Frontiers in Ecology and the Environment*, *1*(8), 412–420. https://doi.org/10.1890/1540-9295(2003)001

Cade, B. S., Terrell, J. W., & Schroeder, R. L. (1999). Estimating Effects of Limiting Factors with Regression Quantiles. *Ecology*, *80*(1), 311. https://doi.org/10.2307/176999

Cannas, M., & Arpino, B. (2019). A comparison of machine learning algorithms and covariate balance measures for propensity score matching and weighting. *Biometrical Journal*, *61*(4), 1049–1072. https://doi.org/10.1002/BIMJ.201800132

Carmo, M., Moreira, F., Casimiro, P., & Vaz, P. (2011). Land use and topography influences on wildfire occurrence in northern Portugal. *Landscape and Urban Planning*, *100*(1–2), 169–176. https://doi.org/10.1016/J.LANDURBPLAN.2010.11.017

Carreiras, J. M. B., Quegan, S., Tansey, K., & Page, S. (2020). Sentinel-1 observation frequency significantly increases burnt area detectability in tropical SE Asia. *Environmental Research Letters*, *15*(5), 054008. https://doi.org/10.1088/1748-9326/AB7765

Chan, A. H. Y., Barnes, C., Swinfield, T., & Coomes, D. A. (2021). Monitoring ash dieback (Hymenoscyphus fraxineus) in British forests using hyperspectral remote sensing. *Remote Sensing in Ecology and Conservation*, *7*(2), 306–320. https://doi.org/10.1002/RSE2.190

Chan, A. H. Y., Guizar-Coutiño, A., Kalamandeen, M., & Coomes, D. A. (2023). Reconstructing 34 Years of Fire History in the Wet, Subtropical Vegetation of Hong Kong Using Landsat. *Remote Sensing 2023, Vol. 15, Page 1489*, *15*(6), 1489. https://doi.org/10.3390/RS15061489

Chan, W.-W. E. (2005). *A feasibility study of hillfire management in Hong Kong Country Parks using GIS analysis*. University of Hong Kong.

Chand, S. S., Walsh, K. J. E., Camargo, S. J., Kossin, J. P., Tory, K. J., Wehner, M. F., Chan, J. C. L., Klotzbach, P. J., Dowdy, A. J., Bell, S. S., Ramsay, H. A., & Murakami, H. (2022). Declining tropical cyclone frequency under global warming. *Nature Climate Change 2022 12:7*, *12*(7), 655–661. https://doi.org/10.1038/s41558-022-01388-4

Chau, H. W. (2003). 漁獵採集 - 香港浴海定居的史前先民生活模式 [Hunter-gathering: The subsistence mode of the prehistoric coastal population in Hong Kong]. *South China Research Resources Station Newsletter 華南研究資料中心通訊*, *30*, 15–22.

Chau, K. C., & Marafa, L. M. (1999). Vegetation chronosequence in Hong Kong: Soil properties and successional development. *Singapore Journal of Tropical Geography*, *20*(1), 24–35. https://doi.org/10.1111/1467-9493.00041

Chau, K. L. (1994). *The ecology of fire in Hong Kong* [The University of Hong Kong]. https://doi.org/10.5353/th_b3123348

Cheung, C., Schwarcz, H., & Chisholm, B. (2022). Examining prehistoric diet at Tung Wan Tsai, Ma Wan Island, Hong Kong through stable isotope analysis. *The Journal of Island and Coastal Archaeology*. https://doi.org/10.1080/15564894.2022.2029629

Chi, C. H., McEwan, R. W., Chang, C. Te, Zheng, C., Yang, Z., Chiang, J. M., & Lin, T. C. (2015). Typhoon Disturbance Mediates Elevational Patterns of Forest Structure, but not Species Diversity, in Humid Monsoon Asia. *Ecosystems*, *18*(8), 1410–1423. https://doi.org/10.1007/S10021-015-9908-3/FIGURES/4

Chu, T., & Guo, X. (2013). Remote Sensing Techniques in Monitoring Post-Fire Effects and Patterns of Forest Recovery in Boreal Forest Regions: A Review. *Remote Sensing 2014, Vol. 6, Pages 470-520*, *6*(1), 470–520. https://doi.org/10.3390/RS6010470

Chuvieco, E., Aguado, I., Salas, J., García, M., Yebra, M., & Oliva, P. (2020). Satellite Remote Sensing Contributions to Wildland Fire Science and Management. *Current Forestry Reports*, *6*(2), 81–96. https://doi.org/10.1007/S40725-020-00116-5/TABLES/1

Chuvieco, E., Mouillot, F., van der Werf, G. R., San Miguel, J., Tanasse, M., Koutsias, N., García, M., Yebra, M., Padilla, M., Gitas, I., Heil, A., Hawbaker, T. J., & Giglio, L. (2019). Historical background and current developments for mapping burned area from satellite Earth observation. *Remote Sensing of Environment*, *225*, 45–64. https://doi.org/10.1016/J.RSE.2019.02.013

Clarke, H., Nolan, R. H., De Dios, V. R., Bradstock, R., Griebel, A., Khanal, S., & Boer, M. M. (2022). Forest fire threatens global carbon sinks and population centres under rising atmospheric water demand. *Nature Communications 2022 13:1*, *13*(1), 1–10. https://doi.org/10.1038/s41467-022-34966-3

Cleary, D. F. R., Boyle, T. J. B., Setyawati, T., & Menken, S. B. J. (2005). The impact of logging on the abundance, species richness and community composition of butterfly guilds in Borneo. *Journal of Applied Entomology*, *129*(1), 52–59. https://doi.org/10.1111/J.1439-0418.2005.00916.X

Clifton, A., Barber, S., Stökl, A., Frank, H., & Karlsson, T. (2022). Research challenges and needs for the deployment of wind energy in hilly and mountainous regions. *Wind Energy Science*, *7*(6), 2231–2254. https://doi.org/10.5194/WES-7-2231-2022

Cochrane, M. A., Moran, C. J., Wimberly, M. C., Baer, A. D., Finney, M. A., Beckendorf, K. L., Eidenshink, J., Zhu, Z., Cochrane, M. A., Moran, C. J., Wimberly, M. C., Baer, A. D., Finney, M. A., Beckendorf, K. L., Eidenshink, J., & Zhu, Z. (2012). Estimation of wildfire size and risk changes due to fuels treatments. *International Journal of Wildland Fire*, *21*(4), 357–367. https://doi.org/10.1071/WF11079

Cochrane, Mark A. (2003). Fire science for rainforests. In *Nature* (Vol. 421, Issue 6926, pp. 913–919). Nature Publishing Group. https://doi.org/10.1038/nature01437

Cocke, A. E., Fulé, P. Z., & Crouse, J. E. (2005). Comparison of burn severity assessments using Differenced Normalized Burn Ratio and ground data. *International Journal of Wildland Fire*, *14*, 189–198. https://doi.org/10.1071/WF04010

Coomes, D. A., & Allen, R. B. (2007). Effects of size, competition and altitude on tree growth. *Journal of Ecology*, *95*(5), 1084–1097. https://doi.org/10.1111/j.1365-2745.2007.01280.x

Coomes, D. A., Dalponte, M., Jucker, T., Asner, G. P., Banin, L. F., Burslem, D. F. R. P., Lewis, S. L., Nilus, R., Phillips, O. L., Phua, M.-H., & Qie, L. (2017). Area-based vs tree-centric approaches to mapping forest carbon in Southeast Asian forests from airborne laser scanning data. *Remote Sensing of Environment*, *194*, 77–88. https://doi.org/10.1016/J.RSE.2017.03.017

Coomes, D. A., Šafka, D., Shepherd, J., Dalponte, M., & Holdaway, R. (2018). Airborne laser scanning of natural forests in New Zealand reveals the influences of wind on forest carbon. *Forest Ecosystems*, *5*(1), 1–14. https://doi.org/10.1186/s40663-017-0119-6

Corbin, J. D., & Holl, K. D. (2012). Applied nucleation as a forest restoration strategy. *Forest Ecology and Management*, *265*, 37–46. https://doi.org/10.1016/J.FORECO.2011.10.013

Corlett, R. T. (1992). The Naturalized Flora of Hong Kong: A Comparison with Singapore. *Journal of Biogeography*, *19*(4), 421. https://doi.org/10.2307/2845570

Corlett, R. T. (1997). Human impact on the flora of Hong Kong Island. *The Changing Face of East Asia during the Tertiary and Quaternary*, 400–412.

Corlett, R. T. (1999). Environmental forestry in Hong Kong: 1871–1997. *Forest Ecology and*

Management, *116*(1–3), 93–105. https://doi.org/10.1016/S0378-1127(98)00443-5

Crausbay, S. D., & Martin, P. H. (2016). Natural disturbance, vegetation patterns and ecological dynamics in tropical montane forests. *Journal of Tropical Ecology*, *32*(5), 384–403. https://doi.org/10.1017/S0266467416000328

Cremer, K. W., Borough, C. J., McKinnell, F. H., & Carter, P. R. (1982). Effects of stocking and thinning on wind damage in plantations. *New Zealand Journal of Forestry Science*, *12*(2), 244–268.

Crockett, J. L., & Hurteau, M. D. (2022). Post-fire early successional vegetation buffers surface microclimate and increases survival of planted conifer seedlings in the southwestern United States. *Canadian Journal of Forest Research*, *52*(3), 416–425. https://doi.org/10.1139/CJFR-2021-0221/SUPPL_FILE/CJFR-2021-0221SUPPLA.DOCX

Curran, T. J., Perry, G. L. W., Wyse, S. V., & Alam, M. A. (2017). Managing Fire and Biodiversity in the Wildland-Urban Interface: A Role for Green Firebreaks. *Fire*, *1*(1), 3. https://doi.org/10.3390/FIRE1010003

Dai, F. C., Lee, C. F., Li, J., & Xu, Z. W. (2001). Assessment of landslide susceptibility on the natural terrain of Lantau Island, Hong Kong. *Environmental Geology*, *40*(3), 381–391. https://doi.org/10.1007/S002540000163/METRICS

Daldegan, G. A., Roberts, D. A., & Ribeiro, F. de F. (2019). Spectral mixture analysis in Google Earth Engine to model and delineate fire scars over a large extent and a long time-series in a rainforest-savanna transition zone. *Remote Sensing of Environment*, *232*, 111340. https://doi.org/10.1016/J.RSE.2019.111340

Daley, P. A. (1965). *Forestry and its place in natural resource conservation in Hong Kong: a recommendation for revised policy*.

Dalling, J. W., & Tanner, E. V. J. (1995). An Experimental Study of Regeneration on Landslides in Montane Rain Forest in Jamaica. *The Journal of Ecology*, *83*(1), 55. https://doi.org/10.2307/2261150

Davies, G. M., Pollard, L., & Mwenda, M. D. (2010). Perceptions of land-degradation, forest restoration and fire management: A case study from Malawi. *Land Degradation & Development*, *21*(6), 546–556. https://doi.org/10.1002/LDR.995

De Gouvenain, R. C., & Silander, J. A. (2003). Do Tropical Storm Regimes Influence the Structure of Tropical Lowland Rain Forests? *Biotropica*, *35*(2), 166–180. https://doi.org/10.1111/J.1744-7429.2003.TB00276.X

De Moraes, M. G., De Carvalho, M. A. M., Franco, A. C., Pollock, C. J., & Figueiredo-Ribeiro, R. D. C. L. (2016). Fire and Drought: Soluble Carbohydrate Storage and Survival Mechanisms in Herbaceous Plants from the Cerrado. *BioScience*, *66*(2), 107–117. https://doi.org/10.1093/BIOSCI/BIV178

Dechesne, C., Mallet, C., Le Bris, A., & Gouet-Brunet, V. (2017). Semantic segmentation of forest stands of pure species combining airborne lidar data and very high resolution multispectral imagery. *ISPRS Journal of Photogrammetry and Remote Sensing*, *126*, 129–145. https://doi.org/10.1016/J.ISPRSJPRS.2017.02.011

Derose, R. J., & Long, J. N. (2014). Resistance and Resilience: A Conceptual Framework for Silviculture. *Forest Science*, *60*(6), 1205–1212. https://doi.org/10.5849/FORSCI.13-507

Di Gregorio, A. (2005). *Land cover classification system: classification concepts and user manual: LCCS* (Vol. 2). Food \& Agriculture Org.

Dobrowski, S. Z. (2011). A climatic basis for microrefugia: the influence of terrain on climate. *Global Change Biology*, *17*(2), 1022–1035. https://doi.org/10.1111/J.1365-2486.2010.02263.X

Dubayah, R., Blair, J. B., Goetz, S., Fatoyinbo, L., Hansen, M., Healey, S., Hofton, M., Hurtt, G., Kellner, J., Luthcke, S., Armston, J., Tang, H., Duncanson, L., Hancock, S., Jantz, P., Marselis, S., Patterson, P. L., Qi, W., & Silva, C. (2020). The Global Ecosystem Dynamics Investigation: High-resolution laser ranging of the Earth's forests and topography. *Science of Remote Sensing*, *1*, 100002. https://doi.org/10.1016/j.srs.2020.100002

Dudgeon, D., & Corlett, R. (2004). *The ecology and biodiversity of Hong Kong*. Friends of the Country parks Hong Kong.

Dunn, S. T. (1906). *Forestry, Hong Kong Government Gazette, 15 June 1906*.

Dunnavan, G. M., & Diercks, J. W. (1980). An analysis of super typhoon Tip (October 1979). *Monthly Weather Review*, *108*(11), 1915–1923.

Dupont, S., Pivato, D., & Brunet, Y. (2015). Wind damage propagation in forests. *Agricultural and Forest Meteorology*, *214–215*, 243–251. https://doi.org/10.1016/j.agrformet.2015.07.010

Dwomoh, F. K., Wimberly, M. C., Cochrane, M. A., & Numata, I. (2019). Forest degradation promotes fire during drought in moist tropical forests of Ghana. *Forest Ecology and Management*, *440*, 158–168. https://doi.org/10.1016/J.FORECO.2019.03.014

Escuin, S., Navarro, R., & Fernández, P. (2007). Fire severity assessment by using NBR (Normalized Burn Ratio) and NDVI (Normalized Difference Vegetation Index) derived from LANDSAT TM/ETM images. *Http://Dx.Doi.Org/10.1080/01431160701281072*, *29*(4), 1053–1073.

https://doi.org/10.1080/01431160701281072

Everham, E. M., & Brokaw, N. V. L. (1996). Forest Damage and Recovery from Catastrophic Wind. *Botanical Review*, *62*(2), 113–185. https://doi.org/10.1007/BF02857920/METRICS

FAO. (2018). *Global Forest Resources Assessment 2020: Terms and Definitions*. https://www.fao.org/3/I8661EN/i8661en.pdf

Fernandes, K., Baethgen, W., Bernardes, S., DeFries, R., DeWitt, D. G., Goddard, L., Lavado, W., Lee, D. E., Padoch, C., Pinedo-Vasquez, M., & Uriarte, M. (2011). North Tropical Atlantic influence on western Amazon fire season variability. *Geophysical Research Letters*, *38*(12), 12701. https://doi.org/10.1029/2011GL047392

Fernández-de-Uña, L., Martínez-Vilalta, J., Poyatos, R., Mencuccini, M., & McDowell, N. G. (2023). The role of height-driven constraints and compensations on tree vulnerability to drought. *New Phytologist*. https://doi.org/10.1111/NPH.19130

Fernández-García, V., Quintano, C., Taboada, A., Marcos, E., Calvo, L., & Fernández-Manso, A. (2018). Remote Sensing Applied to the Study of Fire Regime Attributes and Their Influence on Post-Fire Greenness Recovery in Pine Ecosystems. *Remote Sensing 2018, Vol. 10, Page 733*, *10*(5), 733. https://doi.org/10.3390/RS10050733

Finnigan, J., Ayotte, K., Harman, I., Katul, G., Oldroyd, H., Patton, E., Poggi, D., Ross, A., & Taylor, P. (2020). Boundary-Layer Flow Over Complex Topography. *Boundary-Layer Meteorology*, *177*(2–3), 247–313. https://doi.org/10.1007/S10546-020-00564-3/FIGURES/13

Fire Services Department. (2021). *Year 2021 Statistic Report*. https://www.hkfsd.gov.hk/eng/source/statistics_2021eng_20220330_145624.pdf

Fletcher, C. J. N. (1997). The geology of Hong Kong. *Journal of the Geological Society*, *154*(6), 999–1000. https://doi.org/10.1144/GSJGS.154.6.0999

Florens, F. B. V. (2013). Conservation in Mauritius and Rodrigues: Challenges and Achievements from Two Ecologically Devastated Oceanic Islands. *Conservation Biology: Voices from the Tropics*, 40–50. https://doi.org/10.1002/9781118679838.CH6

Flores, B. M., Fagoaga, R., Nelson, B. W., & Holmgren, M. (2016). Repeated fires trap Amazonian blackwater floodplains in an open vegetation state. *Journal of Applied Ecology*, *53*(5), 1597–1603. https://doi.org/10.1111/1365-2664.12687

Flores, B. M., & Holmgren, M. (2021). Why forest fails to recover after repeated wildfires in Amazonian floodplains? Experimental evidence on tree recruitment limitation. *Journal of Ecology*, *109*(10), 3473–3486. https://doi.org/10.1111/1365-2745.13769

Forthofer, J., Butler, B., McHugh, C., Finney, M., Bradshaw, L., Stratton, R., Shannon, K., & Wagenbrenner, N. (2014). A comparison of three approaches for simulating fine-scale surface winds in support of wildland fire management. Part II. An exploratory study of the impact of simulated winds on fire growth simulations. *International Journal of Wildland Fire*, *23*(7), 969–981. https://doi.org/10.1071/wf12089

Fox, J. F. (1979). Intermediate-disturbance hypothesis. *Science*, *204*(4399), 1344–1345.

Franklin, J. (2013). Mapping Vegetation from Landscape to Regional Scales. *Vegetation Ecology*, 486–508. https://doi.org/10.1002/9781118452592.ch16

Franquesa, M., Lizundia-Loiola, J., Stehman, S. V., & Chuvieco, E. (2022). Using long temporal reference units to assess the spatial accuracy of global satellite-derived burned area products. *Remote Sensing of Environment*, *269*, 112823. https://doi.org/10.1016/J.RSE.2021.112823

Franquesa, M., Vanderhoof, M. K., Stavrakoudis, D., Gitas, I. Z., Roteta, E., Padilla, M., & Chuvieco, E. (2020). Development of a standard database of reference sites for validating global burned area products. *Earth System Science Data*, *12*(4), 3229–3246. https://doi.org/10.5194/ESSD-12-3229-2020

Frazier, R. J., Coops, N. C., Wulder, M. A., Hermosilla, T., & White, J. C. (2018). Analyzing spatial and temporal variability in short-term rates of post-fire vegetation return from Landsat time series. *Remote Sensing of Environment*, *205*, 32–45. https://doi.org/10.1016/J.RSE.2017.11.007

Frolking, S., Palace, M. W., Clark, D. B., Chambers, J. Q., Shugart, H. H., & Hurtt, G. C. (2009). Forest disturbance and recovery: A general review in the context of spaceborne remote sensing of impacts on aboveground biomass and canopy structure. *Journal of Geophysical Research: Biogeosciences*, *114*(G00E02). https://doi.org/10.1029/2008JG000911

Fung, T., & Jim, C. Y. (1993). Application of remote sensing/GIS in the analysis of hill fire impact on vegetation resources in Hong Kong. *Proceedings of IGARSS'93-IEEE International Geoscience and Remote Sensing Symposium*, 2073–2075.

Gandhi, K. J. K., & Herms, D. A. (2010). Direct and indirect effects of alien insect herbivores on ecological processes and interactions in forests of eastern North America. *Biological Invasions*, *12*(2), 389–405. https://doi.org/10.1007/S10530-009-9627-9/FIGURES/3

Gardiner, B. (2021). Wind damage to forests and trees: a review with an emphasis on planted and managed forests. *Https://Doi.Org/10.1080/13416979.2021.1940665*, *26*(4), 248–266. https://doi.org/10.1080/13416979.2021.1940665

Gardiner, B., Marshall, B., Achim, A., Belcher, R., & Wood, C. (2005). The stability of different silvicultural systems: a wind-tunnel investigation. *Forestry: An International Journal of Forest Research*, *78*(5), 471–484. https://doi.org/10.1093/FORESTRY/CPI053

Gaveau, D. L. A., Descals, A., Salim, M. A., Sheil, D., & Sloan, S. (2021). Refined burned-area mapping protocol using Sentinel-2 data increases estimate of 2019 Indonesian burning. *Earth System Science Data*, *13*(11), 5353–5368. https://doi.org/10.5194/ESSD-13-5353-2021

Gibson, R., Danaher, T., Hehir, W., & Collins, L. (2020). A remote sensing approach to mapping fire severity in south-eastern Australia using sentinel 2 and random forest. *Remote Sensing of Environment*, *240*, 111702. https://doi.org/10.1016/j.rse.2020.111702

Giglio, L., Boschetti, L., Roy, D. P., Humber, M. L., & Justice, C. O. (2018). The Collection 6 MODIS burned area mapping algorithm and product. *Remote Sensing of Environment*, *217*, 72–85. https://doi.org/10.1016/J.RSE.2018.08.005

Goldammer, J. G., & Seibert, B. (1989). Natural rain forest fires in Eastern Borneo during the Pleistocene and Holocene. *The Science of Nature 1989 76:11*, *76*(11), 518–520. https://doi.org/10.1007/BF00374124

Goldammer, Johann Georg. (1990). *Fire in the Tropical Biota* (Johann Georg Goldammer (ed.); Vol. 84). Springer Berlin Heidelberg. https://doi.org/10.1007/978-3-642-75395-4

Gonzalez-Dugo, V., Hernandez, P., Solis, I., Zarco-Tejada, P., Gonzalez-Dugo, V., Hernandez, P., Solis, I., & Zarco-Tejada, P. J. (2015). Using High-Resolution Hyperspectral and Thermal Airborne Imagery to Assess Physiological Condition in the Context of Wheat Phenotyping. *Remote Sensing*, *7*(10), 13586–13605. https://doi.org/10.3390/rs71013586

Goodwin, N. R., & Collett, L. J. (2014). Development of an automated method for mapping fire history captured in Landsat TM and ETM + time series across Queensland, Australia. *Remote Sensing of Environment*, *148*, 206–221. https://doi.org/10.1016/J.RSE.2014.03.021

Goosem, M., Paz, C., Fensham, R., Preece, N., Goosem, S., & Laurance, S. G. W. (2016). Forest age and isolation affect the rate of recovery of plant species diversity and community composition in secondary rain forests in tropical Australia. *Journal of Vegetation Science*, *27*(3), 504–514. https://doi.org/10.1111/JVS.12376

Gorelick, N., Hancher, M., Dixon, M., Ilyushchenko, S., Thau, D., & Moore, R. (2017). Google Earth Engine: Planetary-scale geospatial analysis for everyone. *Remote Sensing of Environment*. https://doi.org/10.1016/j.rse.2017.06.031

Gorgens, Eric B., Nunes, M. H., Jackson, T., Coomes, D., Keller, M., Reis, C. R., Valbuena, R., Rosette, J., de Almeida, D. R. A., Gimenez, B., Cantinho, R., Motta, A. Z., Assis, M., de Souza Pereira, F.

R., Spanner, G., Higuchi, N., & Ometto, J. P. (2021). Resource availability and disturbance shape maximum tree height across the Amazon. *Global Change Biology*, *27*(1), 177–189. https://doi.org/10.1111/GCB.15423

Gorgens, Eric Bastos, Motta, A. Z., Assis, M., Nunes, M. H., Jackson, T., Coomes, D., Rosette, J., Aragão, L. E. O. e. C., & Ometto, J. P. (2019). The giant trees of the Amazon basin. *Frontiers in Ecology and the Environment*, *17*(7), 373–374. https://doi.org/10.1002/FEE.2085

Gouveia, C., DaCamara, C. C., & Trigo, R. M. (2010). Post-fire vegetation recovery in Portugal based on spot/vegetation data. *Natural Hazards and Earth System Science*, *10*(4), 673–684. https://doi.org/10.5194/nhess-10-673-2010

Gower, S. T., McMurtrie, R. E., & Murty, D. (1996). Aboveground net primary production decline with stand age: Potential causes. *Trends in Ecology and Evolution*, *11*(9), 378–382. https://doi.org/10.1016/0169-5347(96)10042-2

Greifer, N. (2019). *Package 'WeightIt.'* CRAN.

Greifer, N. (2020). Covariate balance tables and plots: a guide to the cobalt package. *Accessed March*, *10*, 2020.

Grime, J. P. (1973). Competitive Exclusion in Herbaceous Vegetation. *Nature 1973 242:5396*, *242*(5396), 344–347. https://doi.org/10.1038/242344a0

Guariguata, M. R. (1990). Landslide Disturbance and Forest Regeneration in the Upper Luquillo Mountains of Puerto Rico. *The Journal of Ecology*, *78*(3), 814. https://doi.org/10.2307/2260901

Haberle, S. G., Rule, S., Roberts, P., Heijnis, H., Jacobsen, G., Turney, C., Cosgrove, R., Ferrier, A., Moss, P., Mooney, S., & others. (2010). Paleofire in the wet tropics of northeast Queensland, Australia. *Pages News*, *18*(2), 78–80.

Hagmann, R. K., Hessburg, P. F., Prichard, S. J., Povak, N. A., Brown, P. M., Fulé, P. Z., Keane, R. E., Knapp, E. E., Lydersen, J. M., Metlen, K. L., Reilly, M. J., Sánchez Meador, A. J., Stephens, S. L., Stevens, J. T., Taylor, A. H., Yocom, L. L., Battaglia, M. A., Churchill, D. J., Daniels, L. D., … Waltz, A. E. M. (2021). Evidence for widespread changes in the structure, composition, and fire regimes of western North American forests. *Ecological Applications*, *31*(8), e02431. https://doi.org/10.1002/EAP.2431

Halder, N. K., Merchant, A., Misbahuzzaman, K., Wagner, S., & Mukul, S. A. (2021). Why some trees are more vulnerable during catastrophic cyclone events in the Sundarbans mangrove forest of Bangladesh? *Forest Ecology and Management*, *490*, 119117. https://doi.org/10.1016/J.FORECO.2021.119117

Hall, J., Muscarella, R., Quebbeman, A., Arellano, G., Thompson, J., Zimmerman, J. K., & Uriarte, M. (2020). Hurricane-Induced Rainfall is a Stronger Predictor of Tropical Forest Damage in Puerto Rico Than Maximum Wind Speeds. *Scientific Reports 2020 10:1*, *10*(1), 1–10. https://doi.org/10.1038/s41598-020-61164-2

Hall, R. J., Castilla, G., White, J. C., Cooke, B. J., & Skakun, R. S. (2016). Remote sensing of forest pest damage: a review and lessons learned from a Canadian perspective. *The Canadian Entomologist*, *148*(S1), S296–S356. https://doi.org/10.4039/tce.2016.11

Hantson, S., Arneth, A., Harrison, S. P., Kelley, D. I., Colin Prentice, I., Rabin, S. S., Archibald, S., Mouillot, F., Arnold, S. R., Artaxo, P., Bachelet, D., Ciais, P., Forrest, M., Friedlingstein, P., Hickler, T., Kaplan, J. O., Kloster, S., Knorr, W., Lasslop, G., … Yue, C. (2016). The status and challenge of global fire modelling. *Biogeosciences*, *13*(11), 3359–3375. https://doi.org/10.5194/BG-13-3359-2016

Hantson, S., Pueyo, S., Chuvieco, E., Hantson, S., Pueyo, S., & Chuvieco, E. (2016). Global fire size distribution: from power law to log-normal. *International Journal of Wildland Fire*, *25*(4), 403–412. https://doi.org/10.1071/WF15108

Hau, B. C. H., & Corlett, R. T. (2002). A survey of trees and shrubs on degraded hillsides in Hong Kong. *Memoirs of the Hong Kong Natural History Society*.

Hau, B. C. H., & Corlett, R. T. (2003). Factors Affecting the Early Survival and Growth of Native Tree Seedlings Planted on a Degraded Hillside Grassland in Hong Kong, China. *Restoration Ecology*, *11*(4), 483–488. https://doi.org/10.1046/J.1526-100X.2003.REC0279.X

Hau, B. C. H., Dudgeon, D., Corlett, R. T., Sodhi, N. S., Koh, L. P., Brook, B. W., & Ng, P. K. L. (2005). Beyond Singapore: Hong Kong and Asian biodiversity. *Trends in Ecology & Evolution*, *20*(6), 281–282. https://doi.org/10.1016/J.TREE.2005.04.002

Hawbaker, T. J., Vanderhoof, M. K., Beal, Y. J., Takacs, J. D., Schmidt, G. L., Falgout, J. T., Williams, B., Fairaux, N. M., Caldwell, M. K., Picotte, J. J., Howard, S. M., Stitt, S., & Dwyer, J. L. (2017). Mapping burned areas using dense time-series of Landsat data. *Remote Sensing of Environment*, *198*, 504–522. https://doi.org/10.1016/J.RSE.2017.06.027

Héon, J., Arseneault, D., & Parisien, M. A. (2014). Resistance of the boreal forest to high burn rates. *Proceedings of the National Academy of Sciences of the United States of America*, *111*(38), 13888–13893. https://doi.org/10.1073/PNAS.1409316111/SUPPL_FILE/PNAS.1409316111.SD01.XLS

Hernandez, J. O., Maldia, L. S. J., & Park, B. B. (2020). Research Trends and Methodological Approaches of the Impacts of Windstorms on Forests in Tropical, Subtropical, and Temperate

Zones: Where Are We Now and How Should Research Move Forward? *Plants 2020, Vol. 9, Page 1709*, *9*(12), 1709. https://doi.org/10.3390/PLANTS9121709

Herrmann, J. D., Carlo, T. A., Brudvig, L. A., Damschen, E. I., Haddad, N. M., Levey, D. J., Orrock, J. L., & Tewksbury, J. J. (2016). Connectivity from a different perspective: comparing seed dispersal kernels in connected vs. unfragmented landscapes. *Ecology*, *97*(5), 1274–1282. https://doi.org/10.1890/15-0734.1

HK Lands Department. (2019). *HK Lands Department, 2019*. https://www.landsd.gov.hk/en/about/welcome.htm

HK Lands Department. (2020). *Hong Kong Map Service 2.0*. https://www.hkmapservice.gov.hk/OneStopSystem/home

Ho, K., Lau, T., & Lau, J. (2009). Forensic landslide investigations in Hong Kong. *Proceedings of the Institution of Civil Engineers - Civil Engineering*, *162*(5), 44–51. https://doi.org/10.1680/cien.2009.162.5.44

Hodgson, D., McDonald, J. L., & Hosken, D. J. (2015). What do you mean, 'resilient'? *Trends in Ecology & Evolution*, *30*(9), 503–506. https://doi.org/10.1016/J.TREE.2015.06.010

Hodgson, M. E., & Bresnahan, P. (2004). Accuracy of airborne lidar-derived elevation: Empirical assessment and error budget. *Photogrammetric Engineering and Remote Sensing*, *70*(3), 331–339. https://doi.org/10.14358/PERS.70.3.331

Hoffmann, W. A., Geiger, E. L., Gotsch, S. G., Rossatto, D. R., Silva, L. C. R., Lau, O. L., Haridasan, M., & Franco, A. C. (2012). Ecological thresholds at the savanna-forest boundary: How plant traits, resources and fire govern the distribution of tropical biomes. *Ecology Letters*, *15*(7), 759–768. https://doi.org/10.1111/J.1461-0248.2012.01789.X

Hoffmann, W. A., Jaconis, S. Y., Mckinley, K. L., Geiger, E. L., Gotsch, S. G., & Franco, A. C. (2012). Fuels or microclimate? Understanding the drivers of fire feedbacks at savanna–forest boundaries. *Austral Ecology*, *37*(6), 634–643. https://doi.org/10.1111/J.1442-9993.2011.02324.X

Hoffmann, W. A., Schroeder, W., & Jackson, R. B. (2003). Regional feedbacks among fire, climate, and tropical deforestation. *Journal of Geophysical Research: Atmospheres*, *108*(D23), 4721. https://doi.org/10.1029/2003JD003494

Holling, C. S. (1973). Resilience and stability of ecological systems. *Annual Review of Ecology and Systematics*, *4*(1), 1–23.

Holmgren, M., Scheffer, M., Ezcurra, E., Gutiérrez, J. R., & Mohren, G. M. J. (2001). El Niño effects on the dynamics of terrestrial ecosystems. *Trends in Ecology & Evolution*, *16*(2), 89–94.

https://doi.org/10.1016/S0169-5347(00)02052-8

Hong Kong Herbarium. (2012). *Check list of Hong Kong plants 2012*. Agriculture, Fisheries and Conservation Department.

Hong Kong Observatory. (2023). *Hong Kong Observatory*. https://www.hko.gov.hk/contente.htm

Huang, C., Goward, S. N., Masek, J. G., Gao, F., Vermote, E. F., Thomas, N., Schleeweis, K., Kennedy, R. E., Zhu, Z., Eidenshink, J. C., & Townshend, J. R. G. (2009). Development of time series stacks of Landsat images for reconstructing forest disturbance history. *International Journal of Digital Earth*, *2*(3), 195–218. https://doi.org/10.1080/17538940902801614

Huang, C., Goward, S. N., Masek, J. G., Thomas, N., Zhu, Z., & Vogelmann, J. E. (2010). An automated approach for reconstructing recent forest disturbance history using dense Landsat time series stacks. *Remote Sensing of Environment*, *114*(1), 183–198. https://doi.org/10.1016/j.rse.2009.08.017

Huang, F., & Pei, A. (2001). Pollen and Phytolith assemblage and archaeological implications in the Hochung site, Hongkong. *Acta Micropalaeontologica Sinica*, *18*(4), 398–405.

Hudak, A. T., & Brockett, B. H. (2010). Mapping fire scars in a southern African savannah using Landsat imagery. *Http://Dx.Doi.Org/10.1080/01431160310001632666*, *25*(16), 3231–3243. https://doi.org/10.1080/01431160310001632666

Humber, M. L., Boschetti, L., Giglio, L., & Justice, C. O. (2019). Spatial and temporal intercomparison of four global burned area products. *International Journal of Digital Earth*, *12*(4), 460–484. https://doi.org/10.1080/17538947.2018.1433727/SUPPL_FILE/TJDE_A_1433727_SM0303.ZIP

Ibanez, T., Keppel, G., Menkes, C., Gillespie, T. W., Lengaigne, M., Mangeas, M., Rivas-Torres, G., & Birnbaum, P. (2019). Globally consistent impact of tropical cyclones on the structure of tropical and subtropical forests. *Journal of Ecology*, *107*(1), 279–292. https://doi.org/10.1111/1365-2745.13039

Idris, M. H., Kuraji, K., & Suzuki, M. (2004). Evaluating vegetation recovery following large-scale forest fires in Borneo and northeastern China using multi-temporal NOAA/AVHRR images. *Journal of Forest Research*, *10*(2), 101–111. https://doi.org/10.1007/S10310-004-0106-Y

Ireland, G., & Petropoulos, G. P. (2015). Exploring the relationships between post-fire vegetation regeneration dynamics, topography and burn severity: A case study from the Montane Cordillera Ecozones of Western Canada. *Applied Geography*, *56*, 232–248. https://doi.org/10.1016/J.APGEOG.2014.11.016

Isenburg, M. (2020). *LAStools - efficient tools for LiDAR processing (version 200509, academic)*. http://rapidlasso.com/LAStools

Ishwaran, H., Kogalur, U. B., Blackstone, E. H., & Lauer, M. S. (2008). *Random survival forests*.

Ishwaran, H., Kogalur, U. B., & Kogalur, M. U. B. (2023). Package 'randomForestSRC.' *Breast*, *6*(1).

Iván, B., Juan, P., Luciana, A., Morales, J. M., & Thomas, K. (2023). Microclimate and species composition shape the contribution of fuel moisture to positive fire-vegetation feedbacks. *Agricultural and Forest Meteorology*, *330*, 109289. https://doi.org/10.1016/J.AGRFORMET.2022.109289

Jackson, T., Shenkin, A., Kalyan, B., Zionts, J., Calders, K., Origo, N., Disney, M., Burt, A., Raumonen, P., & Malhi, Y. (2019). A New Architectural Perspective on Wind Damage in a Natural Forest. *Frontiers in Forests and Global Change*, *1*, 417831. https://doi.org/10.3389/FFGC.2018.00013/BIBTEX

Jactel, H., Bauhus, J., Boberg, J., Bonal, D., Castagneyrol, B., Gardiner, B., Gonzalez-Olabarria, J. R., Koricheva, J., Meurisse, N., & Brockerhoff, E. G. (2017). Tree Diversity Drives Forest Stand Resistance to Natural Disturbances. *Current Forestry Reports*, *3*(3), 223–243. https://doi.org/10.1007/S40725-017-0064-1/FIGURES/3

Jasak, H. (2009). OpenFOAM: Open source CFD in research and industry. *International Journal of Naval Architecture and Ocean Engineering*, *1*(2), 89–94. https://doi.org/10.2478/IJNAOE-2013-0011

Jim, C. Y. (2003). Conservation of soils in culturally protected woodlands in rural Hong Kong. *Forest Ecology and Management*, *175*(1–3), 339–353. https://doi.org/10.1016/S0378-1127(02)00181-0

Johnstone, J. F., Hollingsworth, T. N., Chapin, F. S., & Mack, M. C. (2010). Changes in fire regime break the legacy lock on successional trajectories in Alaskan boreal forest. *Global Change Biology*, *16*(4), 1281–1295. https://doi.org/10.1111/j.1365-2486.2009.02051.x

Jucker, T., Bouriaud, O., Avacaritei, D., & Coomes, D. A. (2014). Stabilizing effects of diversity on aboveground wood production in forest ecosystems: linking patterns and processes. *Ecology Letters*, *17*(12), 1560–1569. https://doi.org/10.1111/ELE.12382

Jucker, T., Caspersen, J., Chave, J., Antin, C., Barbier, N., Bongers, F., Dalponte, M., van Ewijk, K. Y., Forrester, D. I., Haeni, M., Higgins, S. I., Holdaway, R. J., Iida, Y., Lorimer, C., Marshall, P. L., Momo, S., Moncrieff, G. R., Ploton, P., Poorter, L., … Coomes, D. A. (2017). Allometric equations for integrating remote sensing imagery into forest monitoring programmes. *Global Change Biology*, *23*(1), 177–190. https://doi.org/10.1111/gcb.13388

Jucker, T., Hardwick, S. R., Both, S., Elias, D. M. O., Ewers, R. M., Milodowski, D. T., Swinfield, T., & Coomes, D. A. (2018). Canopy structure and topography jointly constrain the microclimate of human-modified tropical landscapes. *Global Change Biology*, *24*(11), 5243–5258. https://doi.org/10.1111/GCB.14415

Kaimal, J. C., & Finnigan, J. J. (1994). Atmospheric Boundary Layer Flows: Their Structure and Measurement. *Atmospheric Boundary Layer Flows*. https://doi.org/10.1093/OSO/9780195062397.001.0001

Kamimura, K., Gardiner, B., Dupont, S., & Finnigan, J. (2019). Agent-based modelling of wind damage processes and patterns in forests. *Agricultural and Forest Meteorology*, *268*, 279–288. https://doi.org/10.1016/J.AGRFORMET.2019.01.020

Kelly, R., Chipman, M. L., Higuera, P. E., Stefanova, I., Brubaker, L. B., & Hu, F. S. (2013). Recent burning of boreal forests exceeds fire regime limits of the past 10,000 years. *Proceedings of the National Academy of Sciences of the United States of America*, *110*(32), 13055–13060. https://doi.org/10.1073/PNAS.1305069110/SUPPL_FILE/ST01.DOC

Kemp, K. B., Higuera, P. E., & Morgan, P. (2016). Fire legacies impact conifer regeneration across environmental gradients in the U.S. northern Rockies. *Landscape Ecology*, *31*(3), 619–636. https://doi.org/10.1007/s10980-015-0268-3

Kennedy, R. E., Yang, Z., & Cohen, W. B. (2010). Detecting trends in forest disturbance and recovery using yearly Landsat time series: 1. LandTrendr - Temporal segmentation algorithms. *Remote Sensing of Environment*, *114*(12), 2897–2910. https://doi.org/10.1016/j.rse.2010.07.008

Kennedy, R. E., Yang, Z., Cohen, W. B., Pfaff, E., Braaten, J., & Nelson, P. (2012). Spatial and temporal patterns of forest disturbance and regrowth within the area of the Northwest Forest Plan. *Remote Sensing of Environment*, *122*, 117–133. https://doi.org/10.1016/j.rse.2011.09.024

Keshav, S. (2012). *Mathematical foundations of computer networking*. Addison-Wesley.

Key, C. H., & Benson, N. C. (2006). Landscape assessment (LA). *In: Lutes, Duncan C.; Keane, Robert E.; Caratti, John F.; Key, Carl H.; Benson, Nathan C.; Sutherland, Steve; Gangi, Larry J. 2006. FIREMON: Fire Effects Monitoring and Inventory System. Gen. Tech. Rep. RMRS-GTR-164-CD. Fort Collins, CO: US Department Of , 164*.

Khoshgoftaar, T. M., Golawala, M., & Van Hulse, J. (2007). An empirical study of learning from imbalanced data using random forest. *Proceedings - International Conference on Tools with Artificial Intelligence, ICTAI*, *2*, 310–317. https://doi.org/10.1109/ICTAI.2007.46

Khosravipour, A., Skidmore, A. K., & Isenburg, M. (2016). Generating spike-free digital surface models using LiDAR raw point clouds: A new approach for forestry applications. *International Journal of Applied Earth Observation and Geoinformation*, *52*, 104–114. https://doi.org/10.1016/J.JAG.2016.06.005

Khosravipour, A., Skidmore, A. K., Isenburg, M., Wang, T., & Hussin, Y. A. (2014). Generating pit-free canopy height models from airborne lidar. *Photogrammetric Engineering \& Remote Sensing*, *80*(9), 863–872.

Kibler, C. L., Parkinson, A.-M. L., Peterson, S. H., Roberts, D. A., D'Antonio, C. M., Meerdink, S. K., & Sweeney, S. H. (2019). Monitoring Post-Fire Recovery of Chaparral and Conifer Species Using Field Surveys and Landsat Time Series. *Remote Sensing 2019, Vol. 11, Page 2963*, *11*(24), 2963. https://doi.org/10.3390/RS11242963

Kishi, Y., & others. (1995). *Pine wood nematode and the Japanese pine sawyer*. Thomas Company Limited.

Knutson, T. R., McBride, J. L., Chan, J., Emanuel, K., Holland, G., Landsea, C., Held, I., Kossin, J. P., Srivastava, A. K., & Sugi, M. (2010). Tropical cyclones and climate change. In *Nature Geoscience* (Vol. 3, Issue 3, pp. 157–163). Nature Publishing Group. https://doi.org/10.1038/ngeo779

Ko, F. W. Y., & Lo, F. L. C. (2018). From landslide susceptibility to landslide frequency: A territory-wide study in Hong Kong. *Engineering Geology*, *242*, 12–22. https://doi.org/10.1016/J.ENGGEO.2018.05.001

Koch, A., & Kaplan, J. O. (2022). Tropical forest restoration under future climate change. *Nature Climate Change 2022 12:3*, *12*(3), 279–283. https://doi.org/10.1038/s41558-022-01289-6

Kossin, J. P., Knapp, K. R., Olander, T. L., & Velden, C. S. (2020). Global increase in major tropical cyclone exceedance probability over the past four decades. *Proceedings of the National Academy of Sciences of the United States of America*, *117*(22), 11975. https://doi.org/10.1073/PNAS.1920849117/-/DCSUPPLEMENTAL

Kuenzer, C., Dech, S., & Wagner, W. (2015). Remote sensing time series. *Remote Sensing and Digital Image Processing*, *22*, 225–245.

Kurbanov, E., Vorobev, O., Lezhnin, S., Sha, J., Wang, J., Li, X., Cole, J., Dergunov, D., & Wang, Y. (2022). Remote Sensing of Forest Burnt Area, Burn Severity, and Post-Fire Recovery: A Review. *Remote Sensing*, *14*(19), 4714. https://doi.org/10.3390/RS14194714/S1

Kuussaari, M., Bommarco, R., Heikkinen, R. K., Helm, A., Krauss, J., Lindborg, R., Öckinger, E., Pärtel, M., Pino, J., Rodà, F., Stefanescu, C., Teder, T., Zobel, M., & Steffan-Dewenter, I. (2009). Extinction debt: a challenge for biodiversity conservation. *Trends in Ecology & Evolution*, *24*(10), 564–571. https://doi.org/10.1016/J.TREE.2009.04.011

Kwong, I. H. Y., Wong, F. K. K., Fung, T., Liu, E. K. Y., Lee, R. H., & Ng, T. P. T. (2022). A multi-stage approach combining very high-resolution satellite image, gis database and post-classification modification rules for habitat mapping in Hong Kong. *Remote Sensing*, *14*(1), 67. https://doi.org/10.3390/RS14010067/S1

Lamb, D., Erskine, P. D., & Parrotta, J. A. (2005). Restoration of degraded tropical forest landscapes. *Science*, *310*(5754), 1628–1632. https://doi.org/10.1126/SCIENCE.1111773/SUPPL_FILE/LAMB.SOM.PDF

Lange, B., & Højstrup, J. (2001). Evaluation of the wind-resource estimation program WAsP for offshore applications. *Journal of Wind Engineering and Industrial Aerodynamics*, *89*(3–4), 271–291. https://doi.org/10.1016/S0167-6105(00)00082-9

Law, Y. K., Lee, C. K. F., Pang, C. C., Hau, B. C. H., & Wu, J. (2023). Vegetation regeneration on natural terrain landslides in Hong Kong: Direct seeding of native species as a restoration tool. *Land Degradation & Development*, *34*(3), 751–762. https://doi.org/10.1002/LDR.4492

Lee, C. F., Li, J., Xu, Z. W., & Dai, F. C. (2001). Assessment of landslide susceptibility on the natural terrain of Lantau Island, Hong Kong. *Environmental Geology*, *40*(3), 381–391. https://doi.org/10.1007/s002540000163

Leigh, E. G. (1999). *Tropical forest ecology: a view from Barro Colorado Island*. Oxford University Press, USA.

Lemelin, D. R., Surry, D., & Davenport, A. G. (1988). Simple approximations for wind speed-up over hills. *Journal of Wind Engineering and Industrial Aerodynamics*, *28*(1–3), 117–127. https://doi.org/10.1016/0167-6105(88)90108-0

Leutner, B., Horning, N., Schwalb-Willmann, J., & Hijmans, R. J. (2019). Rstoolbox. R package version 0.2.6. *Online: Https://Github.Com/Bleutner/RStoolbox*.

Levine, J. M., & Murrell, D. J. (2003). The Community-Level Consequences of Seed Dispersal Patterns. *Https://Doi.Org/10.1146/Annurev.Ecolsys.34.011802.132400*, *34*, 549–574. https://doi.org/10.1146/ANNUREV.ECOLSYS.34.011802.132400

Lewis, S. L., Wheeler, C. E., Mitchard, E. T. A., & Koch, A. (2019). Restoring natural forests is the best way to remove atmospheric carbon. *Nature*, *568*(7750), 25–28.

Lin, T. C., Hogan, J. A., & Chang, C. Te. (2020). Tropical Cyclone Ecology: A Scale-Link Perspective. *Trends in Ecology & Evolution*, *35*(7), 594–604. https://doi.org/10.1016/J.TREE.2020.02.012

Liu, J., Heiskanen, J., Maeda, E. E., & Pellikka, P. K. E. (2018). Burned area detection based on Landsat time series in savannas of southern Burkina Faso. *International Journal of Applied Earth Observation and Geoinformation*, *64*, 210–220. https://doi.org/10.1016/J.JAG.2017.09.011

Liu, N., Ren, H., Yuan, S., Guo, Q., & Yang, L. (2013). Testing the stress-gradient hypothesis during the restoration of tropical degraded land using the shrub rhodomyrtus tomentosa as a nurse plant. *Restoration Ecology*, *21*(5), 578–584. https://doi.org/10.1111/J.1526-100X.2012.00937.X

Liu, Z., Barlow, J. F., Chan, P. W., Fung, J. C. H., Li, Y., Ren, C., Mak, H. W. L., & Ng, E. (2019). A Review of Progress and Applications of Pulsed Doppler Wind LiDARs. *Remote Sensing 2019, Vol. 11, Page 2522*, *11*(21), 2522. https://doi.org/10.3390/RS11212522

Lizundia-Loiola, J., Otón, G., Ramo, R., & Chuvieco, E. (2020). A spatio-temporal active-fire clustering approach for global burned area mapping at 250 m from MODIS data. *Remote Sensing of Environment*, *236*, 111493. https://doi.org/10.1016/J.RSE.2019.111493

Lizundia-Loiola, J., Pettinari, M. L., & Chuvieco, E. (2020). Temporal Anomalies in Burned Area Trends: Satellite Estimations of the Amazonian 2019 Fire Crisis. *Remote Sensing 2020, Vol. 12, Page 151*, *12*(1), 151. https://doi.org/10.3390/RS12010151

Lohberger, S., Stängel, M., Atwood, E. C., & Siegert, F. (2018). Spatial evaluation of Indonesia's 2015 fire-affected area and estimated carbon emissions using Sentinel-1. *Global Change Biology*, *24*(2), 644–654. https://doi.org/10.1111/GCB.13841

Long, T., Zhang, Z., He, G., Jiao, W., Tang, C., Wu, B., Zhang, X., Wang, G., & Yin, R. (2019). 30m resolution global annual burned area mapping based on landsat images and Google Earth Engine. *Remote Sensing*, *11*(5), 489. https://doi.org/10.3390/rs11050489

Longpre, T. W., & Morris, D. M. (2012). Environmental Drivers of Succession in Jack Pine Stands of Boreal Ontario: An Application of Survival Analysis. *Northern Journal of Applied Forestry*, *29*(2), 81–92. https://doi.org/10.5849/njaf.11-016

Lu, X., Jiang, L., Ye, Y., Wang, L., Xu, L., Guo, Q., Yu, D., & others. (2019). Study on potential geographical distribution of Phauda flammans Walker in China based on the MaxEnt model. *Journal of Environmental Entomology*, *41*(6), 1268–1275.

Luo, Y., Zhang, H., Zhao, Q., & Wong, M. (2005). HONG KONG SOIL RESEARCHES I. AN OVERVIEW. *Acta Pedologica Sinica*, *42*(2), 314–322.

Mabry, C. M., Hamburg, S. P., Lin Teng-Chiu, Horng, F. W., King, H. B., & Hsia, Y. J. (1998). Typhoon disturbance and stand-level damage patterns at a subtropical forest in Taiwan. *Biotropica*, *30*(2), 238–250. https://doi.org/10.1111/J.1744-7429.1998.TB00058.X

Mahood, A. L., & Balch, J. K. (2019). Repeated fires reduce plant diversity in low-elevation Wyoming big sagebrush ecosystems (1984–2014). *Ecosphere*, *10*(2), e02591. https://doi.org/10.1002/ECS2.2591

Mallek, C., Safford, H., Viers, J., & Miller, J. (2013). Modern departures in fire severity and area vary by forest type, Sierra Nevada and southern Cascades, California, USA. *Ecosphere*, *4*(12), 1–28. https://doi.org/10.1890/ES13-00217.1

Mallinis, G., & Koutsias, N. (2012). Comparing ten classification methods for burned area mapping in a Mediterranean environment using Landsat TM satellite data. *Http://Dx.Doi.Org/10.1080/01431161.2011.648284*, *33*(14), 4408–4433. https://doi.org/10.1080/01431161.2011.648284

Man, M., Wild, J., Macek, M., & Kopecký, M. (2022). Can high-resolution topography and forest canopy structure substitute microclimate measurements? Bryophytes say no. *Science of The Total Environment*, *821*, 153377. https://doi.org/10.1016/J.SCITOTENV.2022.153377

Marafa, L. M., & Chau, K. C. (1999). Morphological and chemical properties of soils along a vegetation gradient affected by fire in Hong Kong. *Soil Science*, *164*(9), 683–691. https://doi.org/10.1097/00010694-199909000-00008

Markoulidakis, A., Taiyari, K., Holmans, P., Pallmann, P., Busse, M., Godley, M. D., & Griffin, B. A. (2022). A tutorial comparing different covariate balancing methods with an application evaluating the causal effects of substance use treatment programs for adolescents. *Health Services and Outcomes Research Methodology*, 1–34. https://doi.org/10.1007/S10742-022-00280-0/FIGURES/3

Marlon, J. R., Bartlein, P. J., Gavin, D. G., Long, C. J., Anderson, R. S., Briles, C. E., Brown, K. J., Colombaroli, D., Hallett, D. J., Power, M. J., Scharf, E. A., & Walsh, M. K. (2012). Long-term perspective on wildfires in the western USA. *Proceedings of the National Academy of Sciences*, *109*(9), E535–E543. https://doi.org/10.1073/PNAS.1112839109

Marsh, C. D., Crockett, J. L., Krofcheck, D., Keyser, A., Allen, C. D., Litvak, M., & Hurteau, M. D. (2022). Planted seedling survival in a post-wildfire landscape: From experimental planting to predictive probabilistic surfaces. *Forest Ecology and Management*, *525*, 120524. https://doi.org/10.1016/J.FORECO.2022.120524

Marsh, C. D., Krofcheck, D. J., & Hurteau, M. D. (2022). Identifying microclimate tree seedling refugia in post-wildfire landscapes. *Agricultural and Forest Meteorology*, *313*, 108741. https://doi.org/10.1016/J.AGRFORMET.2021.108741

Martin, T. J., & Ogden, J. (2006). Wind damage and response in New Zealand forests: a review. *New Zealand Journal of Ecology*, 295–310.

Martins, V. S., Roy, D. P., Huang, H., Boschetti, L., Zhang, H. K., & Yan, L. (2022). Deep learning high resolution burned area mapping by transfer learning from Landsat-8 to PlanetScope. *Remote Sensing of Environment*, *280*, 113203. https://doi.org/10.1016/J.RSE.2022.113203

Mata, S., Braga, J. M. A., Moser, P., Sartori, R. A., Sánchez-Tapia, A., & Sansevero, J. B. B. (2022). Forever young: arrested succession in communities subjected to recurrent fires in a lowland tropical forest. *Plant Ecology*, *223*(6), 659–670. https://doi.org/10.1007/S11258-022-01239-4/FIGURES/4

Matos, D. M. S., Santos, C. J. F., & Chevalier, D. de R. (2002). Fire and restoration of the largest urban forest of the world in Rio de Janeiro City, Brazil. *Urban Ecosystems 2002 6:3*, *6*(3), 151–161. https://doi.org/10.1023/A:1026164427792

Matricardi, E. A. T., Skole, D. L., Pedlowski, M. A., Chomentowski, W., & Fernandes, L. C. (2010). Assessment of tropical forest degradation by selective logging and fire using Landsat imagery. *Remote Sensing of Environment*, *114*(5), 1117–1129. https://doi.org/10.1016/J.RSE.2010.01.001

Matschinger, H., Heider, D., & König, H. H. (2020). A Comparison of Matching and Weighting Methods for Causal Inference Based on Routine Health Insurance Data, or: What to do If an RCT is Impossible. *Gesundheitswesen (Bundesverband Der Arzte Des Offentlichen Gesundheitsdienstes (Germany))*, *82*(S 02), S139–S150. https://doi.org/10.1055/A-1009-6634

Mattivi, P., Franci, F., Lambertini, A., & Bitelli, G. (2019). TWI computation: a comparison of different open source GISs. *Open Geospatial Data, Software and Standards 2019 4:1*, *4*(1), 1–12. https://doi.org/10.1186/S40965-019-0066-Y

McKelvey, K. S., Skinner, C. N., Chang, C., Erman, D. C., Husari, S. J., Parsons, D. J., van Wagtendonk, J. W., & Weatherspoon, C. P. (1996). An overview of fire in the Sierra Nevada. *Sierra Nevada Ecosystem Project: Final Report to Congress*, *2*, 1033–1040.

Melchiorre, A., & Boschetti, L. (2018). Global Analysis of Burned Area Persistence Time with MODIS Data. *Remote Sensing 2018, Vol. 10, Page 750*, *10*(5), 750. https://doi.org/10.3390/RS10050750

Mikkola, J., Sinclair, V. A., Bister, M., & Bianchi, F. (2023). Daytime along-valley winds in the Himalayas as simulated by the Weather Research and Forecasting (WRF) model. *Atmospheric Chemistry and Physics*, *23*(2), 821–842. https://doi.org/10.5194/ACP-23-821-2023

Miller, A. D., Thompson, J. R., Tepley, A. J., & Anderson-Teixeira, K. J. (2019). Alternative stable equilibria and critical thresholds created by fire regimes and plant responses in a fire-prone community. *Ecography*, *42*(1), 55–66. https://doi.org/10.1111/ecog.03491

Miller, C. A., & Davenport, A. G. (1998). Guidelines for the calculation of wind speed-ups in complex terrain. *Journal of Wind Engineering and Industrial Aerodynamics*, *74–76*, 189–197. https://doi.org/10.1016/S0167-6105(98)00016-6

Miller, J. D., & Safford, H. (2012). Trends in Wildfire Severity: 1984 to 2010 in the Sierra Nevada, Modoc Plateau, and Southern Cascades, California, USA. *Fire Ecology 2012 8:3*, *8*(3), 41–57. https://doi.org/10.4996/FIREECOLOGY.0803041

Miller, J. D., & Thode, A. E. (2007). Quantifying burn severity in a heterogeneous landscape with a relative version of the delta Normalized Burn Ratio (dNBR). *Remote Sensing of Environment*, *109*(1), 66–80. https://doi.org/10.1016/J.RSE.2006.12.006

Mitri, G. H., & Gitas, I. Z. (2004). A semi-automated object-oriented model for burned area mapping in the Mediterranean region using Landsat-TM imagery. *International Journal of Wildland Fire*, *13*(3), 367. https://doi.org/10.1071/WF03079

Miyamoto, K., Aiba, S. ichiro, Aoyagi, R., & Nilus, R. (2021). Effects of El Niño drought on tree mortality and growth across forest types at different elevations in Borneo. *Forest Ecology and Management*, *490*, 119096. https://doi.org/10.1016/J.FORECO.2021.119096

Moi, D. A., García-Ríos, R., Hong, Z., Daquila, B. V., & Mormul, R. P. (2020). Intermediate Disturbance Hypothesis in Ecology: A Literature Review. *Https://Doi.Org/10.5735/086.057.0108*, *57*(1–6), 67–78. https://doi.org/10.5735/086.057.0108

Mori, A. S. (2011). Ecosystem management based on natural disturbances: hierarchical context and non-equilibrium paradigm. *Journal of Applied Ecology*, *48*(2), 280–292. https://doi.org/10.1111/J.1365-2664.2010.01956.X

Morrison, D. A., Cary, G. J., Pengelly, S. M., Ross, D. G., Mullins, B. J., Thomas, C. R., & Anderson, T. S. (1995). Effects of fire frequency on plant species composition of sandstone communities in the Sydney region: Inter-fire interval and time-since-fire. *Australian Journal of Ecology*, *20*(2), 239–247. https://doi.org/10.1111/J.1442-9993.1995.TB00535.X

Mortensen, N. G., Landberg, L., Troen, I., & Petersen, E. L. (1993). *Wind Atlas Analysis and Application Program (WAsP)*.

Morton, D. C., DeFries, R. S., Nagol, J., Souza, C. M., Kasischke, E. S., Hurtt, G. C., & Dubayah, R. (2011). Mapping canopy damage from understory fires in Amazon forests using annual time series of Landsat and MODIS data. *Remote Sensing of Environment*, *115*(7), 1706–1720. https://doi.org/10.1016/J.RSE.2011.03.002

Muenchow, G. (1986). Ecological Use of Failure Time Analysis. *Ecology*, *67*(1), 246–250. https://doi.org/10.2307/1938524

Murakami, H., Delworth, T. L., Cooke, W. F., Zhao, M., Xiang, B., & Hsu, P. C. (2020). Detected climatic change in global distribution of tropical cyclones. *Proceedings of the National Academy of Sciences of the United States of America*, *117*(20), 10706–10714. https://doi.org/10.1073/PNAS.1922500117/SUPPL_FILE/PNAS.1922500117.SAPP.PDF

Negrón-Juárez, R., Chambers, J., Hurtt, G., Annane, B., Cocke, S., Powell, M., Stott, M., Goosem, S., Metcalfe, D., Saatchi, S., Negrón-Juárez, R. I., Chambers, J. Q., Hurtt, G. C., Annane, B., Cocke, S., Powell, M., Stott, M., Goosem, S., Metcalfe, D. J., & Saatchi, S. S. (2014). Remote Sensing Assessment of Forest Disturbance across Complex Mountainous Terrain: The Pattern and Severity of Impacts of Tropical Cyclone Yasi on Australian Rainforests. *Remote Sensing*, *6*(6), 5633–5649. https://doi.org/10.3390/rs6065633

Nelson, K. J., Connot, J., Peterson, B., & Martin, C. (2013). The LANDFIRE Refresh Strategy: Updating the National Dataset. *Fire Ecology*, *9*(2), 80–101. https://doi.org/10.4996/FIREECOLOGY.0902080

Ni, Y., Wang, T., Cao, H., Li, Y., Bin, Y., Zhang, R., Wang, Y., Lian, J., & Ye, W. (2021). An old-growth subtropical evergreen broadleaved forest suffered more damage from Typhoon Mangkhut than an adjacent secondary forest. *Forest Ecology and Management*, *496*, 119433. https://doi.org/10.1016/J.FORECO.2021.119433

Nolan, R. H., Collins, L., Leigh, A., Ooi, M. K. J., Curran, T. J., Fairman, T. A., Resco de Dios, V., & Bradstock, R. (2021). Limits to post-fire vegetation recovery under climate change. *Plant, Cell & Environment*, *44*(11), 3471–3489. https://doi.org/10.1111/PCE.14176

Numata, I., Cochrane, M. A., & Galvëo, L. S. (2011). Analyzing the Impacts of Frequency and Severity of Forest Fire on the Recovery of Disturbed Forest using Landsat Time Series and EO-1 Hyperion in the Southern Brazilian Amazon. *Earth Interactions*, *15*(13), 1–17. https://doi.org/10.1175/2010EI372.1

Nunes, M. H., Jucker, T., Riutta, T., Svátek, M., Kvasnica, J., Rejžek, M., Matula, R., Majalap, N., Ewers, R. M., Swinfield, T., Valbuena, R., Vaughn, N. R., Asner, G. P., & Coomes, D. A. (2021). Recovery of logged forest fragments in a human-modified tropical landscape during the 2015-16 El Niño. *Nature Communications 2021 12:1*, *12*(1), 1–11. https://doi.org/10.1038/s41467-020-20811-y

Oliveira, S., Moreira, F., Boca, R., San-Miguel-Ayanz, J., & Pereira, J. M. C. (2013). Assessment of fire selectivity in relation to land cover and topography: a comparison between Southern European countries. *International Journal of Wildland Fire*, *23*(5), 620–630. https://doi.org/10.1071/WF12053

Oliveira, S., Oehler, F., San-Miguel-Ayanz, J., Camia, A., & Pereira, J. M. C. (2012). Modeling spatial patterns of fire occurrence in Mediterranean Europe using Multiple Regression and Random Forest. *Forest Ecology and Management*, *275*, 117–129. https://doi.org/10.1016/J.FORECO.2012.03.003

OpenStreetMap contributors. (2022). *Planet dump retrieved from https://planet.osm.org*.

Ostertag, R., Silver, W. L., & Lugo, A. E. (2005). Factors Affecting Mortality and Resistance to Damage Following Hurricanes in a Rehabilitated Subtropical Moist Forest1. *Biotropica*, *37*(1), 16–24. https://doi.org/10.1111/j.1744-7429.2005.04052.x

Padilla, M., Stehman, S. V, Ramo, R., Corti, D., Hantson, S., Oliva, P., Alonso-Canas, I., Bradley, A. V, Tansey, K., Mota, B., & others. (2015). Comparing the accuracies of remote sensing global burned area products using stratified random sampling and estimation. *Remote Sensing of Environment*, *160*, 114–121.

Paek, S. W., Balasubramanian, S., Kim, S., & de Weck, O. (2020). Small-Satellite Synthetic Aperture Radar for Continuous Global Biospheric Monitoring: A Review. *Remote Sensing 2020, Vol. 12, Page 2546*, *12*(16), 2546. https://doi.org/10.3390/RS12162546

Pan, Y., Birdsey, R. A., Fang, J., Houghton, R., Kauppi, P. E., Kurz, W. A., Phillips, O. L., Shvidenko, A., Lewis, S. L., Canadell, J. G., Ciais, P., Jackson, R. B., Pacala, S. W., McGuire, A. D., Piao, S., Rautiainen, A., Sitch, S., & Hayes, D. (2011). A large and persistent carbon sink in the world's forests. *Science*, *333*(6045), 988–993. https://doi.org/10.1126/SCIENCE.1201609/SUPPL_FILE/PAPV2.PDF

Pang, C., Ma, X. K., Lo, J. P., Hung, T. T., & Hau, B. C. (2018). Vegetation succession on landslides in Hong Kong: Plant regeneration, survivorship and constraints to restoration. *Global Ecology and Conservation*, *15*, e00428. https://doi.org/10.1016/J.GECCO.2018.E00428

Parker, G., Maass, M., & Araiza, S. (2018a). Effects of hurricane disturbance on a tropical dry forest canopy in western Mexico. *Forest Ecology and Management*, *426*, 39–52. https://doi.org/10.1016/J.FORECO.2017.11.037

Parker, G., Maass, M., & Araiza, S. (2018b). Effects of hurricane disturbance on a tropical dry forest canopy in western Mexico. *Forest Ecology and Management*, *426*, 39–52. https://doi.org/10.1016/J.FORECO.2017.11.037

Parks, S. A., Dillon, G. K., & Miller, C. (2014). A New Metric for Quantifying Burn Severity: The Relativized Burn Ratio. *Remote Sensing*, *6*(3), 1827–1844. https://doi.org/10.3390/RS6031827

Parks, S. A., Holsinger, L. M., Voss, M. A., Loehman, R. A., & Robinson, N. P. (2018). Mean

Composite Fire Severity Metrics Computed with Google Earth Engine Offer Improved Accuracy and Expanded Mapping Potential. *Remote Sensing 2018, Vol. 10, Page 879*, *10*(6), 879. https://doi.org/10.3390/RS10060879

Patenaude, G., Milne, R., & Dawson, T. P. (2005). Synthesis of remote sensing approaches for forest carbon estimation: reporting to the Kyoto Protocol. *Environmental Science & Policy*, *8*(2), 161–178. https://doi.org/10.1016/J.ENVSCI.2004.12.010

Paula, S., Naulin, P. I., Arce, C., Galaz, C., & Pausas, J. G. (2016). Lignotubers in Mediterranean basin plants. *Plant Ecology*, *217*(6), 661–676. https://doi.org/10.1007/S11258-015-0538-9/TABLES/2

Pausas, J. G., & Vallejo, V. R. (1999). The role of fire in European Mediterranean ecosystems. *Remote Sensing of Large Wildfires*, 3–16. https://doi.org/10.1007/978-3-642-60164-4_2

Pearl, J. (1995). Causal Diagrams for Empirical Research. *Biometrika*, *82*(4), 669. https://doi.org/10.2307/2337329

Pearl, J. (2009). Causal inference in statistics: An overview. *Https://Doi.Org/10.1214/09-SS057*, *3*(none), 96–146. https://doi.org/10.1214/09-SS057

Pebesma, E. J. (2018). Simple features for R: standardized support for spatial vector data. *R J.*, *10*(1), 439.

Pellegrini, A. F. A., Hein, A. M., Cavender-Bares, J., Montgomery, R. A., Staver, A. C., Silla, F., Hobbie, S. E., & Reich, P. B. (2021). Disease and fire interact to influence transitions between savanna–forest ecosystems over a multi-decadal experiment. *Ecology Letters*, *24*(5), 1007–1017. https://doi.org/10.1111/ELE.13719

Penha, T. V., Körting, T. S., Fonseca, L. M. G., Silva Júnior, C. H. L., Pletsch, M. A. J. S., Anderson, L. O., & Morelli, F. (2020). Burned Area Detection in the Brazilian Amazon using Spectral Indices and GEOBIA. *Revista Brasileira de Cartografia*, *72*(2), 253–269. https://doi.org/10.14393/rbcv72n2-48726

Pereira, M. C., & Setzer, A. W. (1993). Spectral characteristics of fire scars in Landsat-5 TM images of Amazonia. *Http://Dx.Doi.Org/10.1080/01431169308954022*, *14*(11), 2061–2078. https://doi.org/10.1080/01431169308954022

Pérez-Cabello, F., Montorio, R., & Alves, D. B. (2021). Remote sensing techniques to assess post-fire vegetation recovery. *Current Opinion in Environmental Science & Health*, *21*, 100251. https://doi.org/10.1016/J.COESH.2021.100251

Planning Department. (2001). *Landscape Value Mapping of Hong Kong Technical Report Chapter 5: Analysis of the Hong Kong Landscape*.

https://www.pland.gov.hk/pland_en/p_study/prog_s/landscape/tech_report/ch5.htm

Plucinski, M. P., Anderson, W. R., Bradstock, R. A., Gill, A. M., Plucinski, M. P., Anderson, W. R., Bradstock, R. A., & Gill, A. M. (2010). The initiation of fire spread in shrubland fuels recreated in the laboratory. *International Journal of Wildland Fire*, *19*(4), 512–520. https://doi.org/10.1071/WF09038

Polychronaki, A., Gitas, I., Veraverbeke, S., & Debien, A. (2013). Evaluation of ALOS PALSAR Imagery for Burned Area Mapping in Greece Using Object-Based Classification. *Remote Sensing*, *5*(11), 5680–5701. https://doi.org/10.3390/rs5115680

Prasasti, I., Rahmi, K. I. N., Nugroho, J. T., Sitorus, J., Arief, R., Triyono, D., & Suwarsono. (2020). Detecting the burned area in southern Kalimantan by using the sentinel-1 polarimetric SAR and landsat-8 OLI optic. *Journal of Physics: Conference Series*, *1528*(1), 012048. https://doi.org/10.1088/1742-6596/1528/1/012048

Price, K., Lilles, E. B., & Banner, A. (2017). Long-term recovery of epiphytic communities in the Great Bear Rainforest of coastal British Columbia. *FOREST ECOLOGY AND MANAGEMENT*, *391*, 296–308. https://doi.org/10.1016/j.foreco.2017.02.023

Prior, L. D., Murphy, B. P., Williamson, G. J., Cochrane, M. A., Jolly, W. M., & Bowman, D. M. J. S. (2017). Does inherent flammability of grass and litter fuels contribute to continental patterns of landscape fire activity? *Journal of Biogeography*, *44*(6), 1225–1238. https://doi.org/10.1111/JBI.12889

QGIS Development Team. (2021). *QGIS Geographic Information System*. https://www.qgis.org

Qiu, J., Wang, H., Shen, W., Zhang, Y., Su, H., & Li, M. (2021). Quantifying Forest Fire and Post-Fire Vegetation Recovery in the Daxin'anling Area of Northeastern China Using Landsat Time-Series Data and Machine Learning. *Remote Sensing 2021, Vol. 13, Page 792*, *13*(4), 792. https://doi.org/10.3390/RS13040792

R core team. (2021). *R: A language and environment for statistical computing.* R Foundation for Statistical Computing. http://www.r-project.org/

Reed, W. J., Larsen, C. P. S., Johnson, E. A., Macdonald, G. M., Reed, W. J., & Macdonald, M. (1998). Estimation of Temporal Variations in Historical Fire Frequency from Time-Since-Fire Map Data. *Forest Science*, *44*(3), 465–475. https://doi.org/10.1093/FORESTSCIENCE/44.3.465

Restrepo, C., & Alvarez-Berríos, N. (2006). Landslides and Their Contribution to Land-cover Change in the Mountains of Mexico and Central America1. *Biotropica*, *38*, 446–457. https://doi.org/10.1111/j.1744-7429.2006.00178.x

Reynolds, G., Payne, J., Sinun, W., Mosigil, G., & Walsh, R. P. D. (2011). Changes in forest land use and management in Sabah, Malaysian Borneo, 1990–2010, with a focus on the Danum Valley region. *Philosophical Transactions of the Royal Society B: Biological Sciences*, *366*(1582), 3168–3176. https://doi.org/10.1098/RSTB.2011.0154

Ribera, J., Tang, A. M. C., Schubert, M., Lam, R. Y. C., Chu, L. M., Leung, M. W. K., Kwan, H. S., Bas, M. C., & Schwarze, F. (2016). In-vitro evaluation of antagonistic Trichoderma strains for eradicating Phellinus noxius in colonised wood. *Journal of Tropical Forest Science*, 457–468.

Rochimi, D., Aj, W., & Meador, S. (2021). Evaluating early post-fire tropical lower montane forest recovery in Indonesia. *Source: Journal of Tropical Forest Science*, *33*(2), 113–125. https://doi.org/10.2307/27007560

Rogers, H. S., Beckman, N. G., Hartig, F., Johnson, J. S., Pufal, G., Shea, K., Zurell, D., Bullock, J. M., Cantrell, R. S., Loiselle, B., Pejchar, L., Razafindratsima, O. H., Sandor, M. E., Schupp, E. W., Strickland, W. C., & Zambrano, J. (2019). The total dispersal kernel: a review and future directions. *AoB PLANTS*, *11*(5), 1–13. https://doi.org/10.1093/AOBPLA/PLZ042

Rossi, E., Rogan, J., & Schneider, L. (2013). Mapping forest damage in northern Nicaragua after Hurricane Felix (2007) using MODIS enhanced vegetation index data. *GIScience and Remote Sensing*, *50*(4), 395–399. https://doi.org/10.1080/15481603.2013.820066

Roteta, E., Bastarrika, A., Padilla, M., Storm, T., & Chuvieco, E. (2019). Development of a Sentinel-2 burned area algorithm: Generation of a small fire database for sub-Saharan Africa. *Remote Sensing of Environment*, *222*, 1–17. https://doi.org/10.1016/J.RSE.2018.12.011

Roteta, Ekhi, Bastarrika, A., Ibisate, A., & Chuvieco, E. (2021). A Preliminary Global Automatic Burned-Area Algorithm at Medium Resolution in Google Earth Engine. *Remote Sensing 2021, Vol. 13, Page 4298*, *13*(21), 4298. https://doi.org/10.3390/RS13214298

Rurangwa, M. L., Matthews, T. J., Niyigaba, P., Tobias, J. A., & Whittaker, R. J. (2021). Assessing tropical forest restoration after fire using birds as indicators: An afrotropical case study. *Forest Ecology and Management*, *483*, 118765. https://doi.org/10.1016/J.FORECO.2020.118765

Ryan, K. C., & Opperman, T. S. (2013). LANDFIRE - A national vegetation/fuels data base for use in fuels treatment, restoration, and suppression planning. *Forest Ecology and Management*, *294*, 208–216. https://doi.org/10.1016/j.foreco.2012.11.003

Ryan, M. G., & Yoder, B. J. (1997). Hydraulic Limits to Tree Height and Tree Growth. *BioScience*, *47*(4), 235–242. https://doi.org/10.2307/1313077

Sánchez Sánchez, O., & Islebe, G. A. (1999). Hurricane Gilbert and structural changes in a tropical forest in south-eastern Mexico. *Global Ecology and Biogeography*, *8*(1), 29–38. https://doi.org/10.1046/J.1365-2699.1999.00317.X

Saremi, H., Kumar, L., Turner, R., & Stone, C. (2014). Airborne LiDAR derived canopy height model reveals a significant difference in radiata pine (Pinus radiata D. Don) heights based on slope and aspect of sites. *Trees - Structure and Function*, *28*(3), 733–744. https://doi.org/10.1007/s00468-014-0985-2

Scatena, F. N., & Lugo, A. E. (1995). Geomorphology, disturbance, and the soil and vegetation of two subtropical wet steepland watersheds of Puerto Rico. *Geomorphology*, *13*(1–4), 199–213. https://doi.org/10.1016/0169-555X(95)00021-V

Scheper, A. C., Verweij, P. A., & van Kuijk, M. (2021). Post-fire forest restoration in the humid tropics: A synthesis of available strategies and knowledge gaps for effective restoration. *Science of the Total Environment*, *771*, 144647. https://doi.org/10.1016/j.scitotenv.2020.144647

Secretariat, C. B. D. (2010). The strategic plan for biodiversity 2011--2020 and the Aichi biodiversity targets. *Secretariat of the Convention on Biological Diversity, Nagoya, Japan. UNEP/CBD/COP/DEC/X/2*.

Seidl, R., Thom, D., Kautz, M., Martin-Benito, D., Peltoniemi, M., Vacchiano, G., Wild, J., Ascoli, D., Petr, M., Honkaniemi, J., Lexer, M. J., Trotsiuk, V., Mairota, P., Svoboda, M., Fabrika, M., Nagel, T. A., & Reyer, C. P. O. (2017). Forest disturbances under climate change. *Nature Climate Change 2017 7:6*, *7*(6), 395–402. https://doi.org/10.1038/nclimate3303

Sewell, R. J., Tang, D. L. K., Diarmad, S., Campbell, G., Sewell, R. J., Tang, D. L. K., & Campbell, S. D. G. (2012). Volcanic-plutonic connections in a tilted nested caldera complex in Hong Kong. *Geochemistry, Geophysics, Geosystems*, *13*(1), 1006. https://doi.org/10.1029/2011GC003865

Shah, M., Norris, S. E., Turner, R., & Flay, R. G. J. (2023). A review of computational fluid dynamics application to investigate tropical cyclone wind speeds. *Natural Hazards*, *117*(1), 897–915. https://doi.org/10.1007/S11069-023-05888-0/TABLES/2

Sheil, D., & Burslem, D. F. R. P. (2013). Defining and defending Connell's intermediate disturbance hypothesis: A response to Fox. *Trends in Ecology and Evolution*, *28*(10), 571–572. https://doi.org/10.1016/j.tree.2013.07.006

Shimabukuro, Y. E., Beuchle, R., Grecchi, R. C., & Achard, F. (2014). Assessment of forest degradation in Brazilian Amazon due to selective logging and fires using time series of fraction images derived from Landsat ETM+ images. *Http://Dx.Doi.Org/10.1080/2150704X.2014.967880*, *5*(9), 773–782. https://doi.org/10.1080/2150704X.2014.967880

Shimabukuro, Y. E., Miettinen, J., Beuchle, R., Grecchi, R. C., Simonetti, D., & Achard, F. (2015). Estimating Burned Area in Mato Grosso, Brazil, Using an Object-Based Classification Method on a Systematic Sample of Medium Resolution Satellite Images. *IEEE Journal of Selected Topics in Applied Earth Observations and Remote Sensing*, *8*(9), 4502–4508. https://doi.org/10.1109/JSTARS.2015.2464097

Shinneman, D. J., Germino, M. J., Pilliod, D. S., Aldridge, C. L., Vaillant, N. M., & Coates, P. S. (2019). The ecological uncertainty of wildfire fuel breaks: examples from the sagebrush steppe. *Frontiers in Ecology and the Environment*, *17*(5), 279–288. https://doi.org/10.1002/FEE.2045

Shrier, I., & Platt, R. W. (2008). Reducing bias through directed acyclic graphs. *BMC Medical Research Methodology*, *8*(1), 1–15. https://doi.org/10.1186/1471-2288-8-70/FIGURES/7

Silva, C. V. J., Aragão, L. E. O. C., Young, P. J., Espirito-Santo, F., Berenguer, E., Anderson, L. O., Brasil, I., Pontes-Lopes, A., Ferreira, J., Withey, K., França, F., Graça, P. M. L. A., Kirsten, L., Xaud, H., Salimon, C., Scaranello, M. A., Castro, B., Seixas, M., Farias, R., & Barlow, J. (2020). Estimating the multi-decadal carbon deficit of burned Amazonian forests. *Environmental Research Letters*, *15*(11), 114023. https://doi.org/10.1088/1748-9326/ABB62C

Simard, M., Pinto, N., Fisher, J. B., & Baccini, A. (2011). Mapping forest canopy height globally with spaceborne lidar. *Journal of Geophysical Research: Biogeosciences*, *116*(G4), 4021. https://doi.org/10.1029/2011JG001708

Simon, M., Plummer, S., Fierens, F., Hoelzemann, J. J., & Arino, O. (2004). Burnt area detection at global scale using ATSR-2: The GLOBSCAR products and their qualification. *Journal of Geophysical Research: Atmospheres*, *109*(D14). https://doi.org/10.1029/2003JD003622

Simpson, K. J., Ripley, B. S., Christin, P. A., Belcher, C. M., Lehmann, C. E. R., Thomas, G. H., & Osborne, C. P. (2016). Determinants of flammability in savanna grass species. *Journal of Ecology*, *104*(1), 138–148. https://doi.org/10.1111/1365-2745.12503

Sinha, S., Jeganathan, C., Sharma, L. K., & Nathawat, M. S. (2015). A review of radar remote sensing for biomass estimation. In *International Journal of Environmental Science and Technology* (Vol. 12, Issue 5, pp. 1779–1792). Center for Environmental and Energy Research and Studies. https://doi.org/10.1007/s13762-015-0750-0

Sofan, P., Bruce, D., Jones, E., & Marsden, J. (2019). Detection and Validation of Tropical Peatland Flaming and Smouldering Using Landsat-8 SWIR and TIRS Bands. *Remote Sensing 2019, Vol. 11, Page 465*, *11*(4), 465. https://doi.org/10.3390/RS11040465

Souza-Alonso, P., Saiz, G., García, R. A., Pauchard, A., Ferreira, A., & Merino, A. (2022). Post-fire ecological restoration in Latin American forest ecosystems: Insights and lessons from the last two decades. *Forest Ecology and Management*, *509*, 120083. https://doi.org/10.1016/J.FORECO.2022.120083

Soverel, N. O., Perrakis, D. D. B., & Coops, N. C. (2010). Estimating burn severity from Landsat dNBR and RdNBR indices across western Canada. *Remote Sensing of Environment*, *114*(9), 1896–1909. https://doi.org/10.1016/J.RSE.2010.03.013

Spake, R., O'Dea, R. E., Nakagawa, S., Doncaster, C. P., Ryo, M., Callaghan, C. T., & Bullock, J. M. (2022). Improving quantitative synthesis to achieve generality in ecology. *Nature Ecology & Evolution 2022 6:12*, *6*(12), 1818–1828. https://doi.org/10.1038/s41559-022-01891-z

Staal, A., van Nes, E. H., Hantson, S., Holmgren, M., Dekker, S. C., Pueyo, S., Xu, C., & Scheffer, M. (2018). Resilience of tropical tree cover: The roles of climate, fire, and herbivory. *Global Change Biology*, *24*(11), 5096–5109. https://doi.org/10.1111/GCB.14408

Stage, A. R. (1976). An expression for the effect of aspect, slope, and habitat type on tree growth. *Forest Science*, *22*(4), 457–460.

Stage, A. R., & Salas, C. (2007). *Interactions of Elevation, Aspect, and Slope in Models of Forest Species Composition and Productivity*.

Stas, S. M., Spracklen, B. D., Willetts, P. D., Le, T. C., Tran, H. D., Le, T. T., Ngo, D. T., Le, A. V., Le, H. T., Rutishauser, E., Schwendike, J., Marsham, J. H., Kuijk, M. van, Jew, E. K. K., Phillips, O. L., & Spracklen, D. V. (2023). Implications of tropical cyclones on damage and potential recovery and restoration of logged forests in Vietnam. *Philosophical Transactions of the Royal Society B*, *378*(1867). https://doi.org/10.1098/RSTB.2021.0081

Stephens, S. S., & Wagner, M. R. (2007). Forest Plantations and Biodiversity: A Fresh Perspective. *Journal of Forestry*, *105*(6), 307–313. https://doi.org/10.1093/JOF/105.6.307

Stokes, E. (1995). *Hong Kong's wild places: an environmental exploration*. Oxford University Press (OUP).

Stone, C., & Mohammed, C. (2017). Application of Remote Sensing Technologies for Assessing Planted Forests Damaged by Insect Pests and Fungal Pathogens: a Review. *Current Forestry Reports*, *3*(2), 75–92. https://doi.org/10.1007/s40725-017-0056-1

Sutherland, W. J., Pullin, A. S., Dolman, P. M., & Knight, T. M. (2004). The need for evidence-based conservation. *Trends in Ecology and Evolution*, *19*(6), 305–308. https://doi.org/10.1016/j.tree.2004.03.018

Suttorp, M. M., Siegerink, B., Jager, K. J., Zoccali, C., & Dekker, F. W. (2015). Graphical presentation of confounding in directed acyclic graphs. *Nephrology Dialysis Transplantation*, *30*(9), 1418–

1423. https://doi.org/10.1093/NDT/GFU325

Swinfield, T., Afriandi, R., Antoni, F., & Harrison, R. D. (2016). Accelerating tropical forest restoration through the selective removal of pioneer species. *Forest Ecology and Management*, *381*, 209–216. https://doi.org/10.1016/J.FORECO.2016.09.020

Szpakowski, D. M., & Jensen, J. L. R. (2019). A Review of the Applications of Remote Sensing in Fire Ecology. *Remote Sensing 2019, Vol. 11, Page 2638*, *11*(22), 2638. https://doi.org/10.3390/RS11222638

Tanase, M. A., Belenguer-Plomer, M. A., Roteta, E., Bastarrika, A., Wheeler, J., Fernández-Carrillo, Á., Tansey, K., Wiedemann, W., Navratil, P., Lohberger, S., Siegert, F., & Chuvieco, E. (2020). Burned Area Detection and Mapping: Intercomparison of Sentinel-1 and Sentinel-2 Based Algorithms over Tropical Africa. *Remote Sensing 2020, Vol. 12, Page 334*, *12*(2), 334. https://doi.org/10.3390/RS12020334

Tang, L., & Shao, G. (2015). Drone remote sensing for forestry research and practices. *Journal of Forestry Research*, *26*(4), 791–797. https://doi.org/10.1007/s11676-015-0088-y

Tanner, E. V. J., & Bellingham, P. J. (2006). Less Diverse Forest Is More Resistant to Hurricane Disturbance: Evidence from Montane Rain Forests in Jamaica. *Journal of Ecology*, *94*(5), 1003–1010. http://www.jstor.org/stable/3879592

Tanner, E. V. J., Kapos, V., & Healey, J. R. (1991). Hurricane Effects on Forest Ecosystems in the Caribbean. *Biotropica*, *23*(4), 513. https://doi.org/10.2307/2388274

Tansey, K., Beston, J., Hoscilo, A., Page, S. E., & Hernández, C. U. P. (2008). Relationship between MODIS fire hot spot count and burned area in a degraded tropical peat swamp forest in Central Kalimantan, Indonesia. *Journal of Geophysical Research: Atmospheres*, *113*(D23), 23112. https://doi.org/10.1029/2008JD010717

Tansey, Kevin, Grégoire, J. M., Defourny, P., Leigh, R., Pekel, J. F., van Bogaert, E., & Bartholomé, E. (2008). A new, global, multi-annual (2000–2007) burnt area product at 1 km resolution. *Geophysical Research Letters*, *35*(1). https://doi.org/10.1029/2007GL031567

Tariq, A., Shu, H., Siddiqui, S., Mousa, B. G., Munir, I., Nasri, A., Waqas, H., Lu, L., & Baqa, M. F. (2021). Forest fire monitoring using spatial-statistical and Geo-spatial analysis of factors determining forest fire in Margalla Hills, Islamabad, Pakistan. *Http://Www.Tandfonline.Com/Action/JournalInformation?Show=aimsScope&journalCode=tgnh20#.VsXodSCLRhE*, *12*(1), 1212–1233. https://doi.org/10.1080/19475705.2021.1920477

Teixeira, A. M. C., Curran, T. J., Jameson, P. E., Meurk, C. D., & Norton, D. A. (2020). Post-Fire

Resprouting in New Zealand Woody Vegetation: Implications for Restoration. *Forests 2020, Vol. 11, Page 269*, *11*(3), 269. https://doi.org/10.3390/F11030269

Telewski, F. W., & Jaffe, M. J. (1986). Thigmomorphogenesis: Field and laboratory studies of Abies fraseri in response to wind or mechanical perturbation. *Physiologia Plantarum*, *66*(2), 211–218. https://doi.org/10.1111/J.1399-3054.1986.TB02411.X

Tepley, A. J., Thomann, E., Veblen, T. T., Perry, G. L. W., Holz, A., Paritsis, J., Kitzberger, T., & Anderson-Teixeira, K. J. (2018). Influences of fire–vegetation feedbacks and post-fire recovery rates on forest landscape vulnerability to altered fire regimes. *Journal of Ecology*, *106*(5), 1925–1940. https://doi.org/10.1111/1365-2745.12950

Therneau, T. M. (2019). *A package for survival analysis in R*. New York, NY, USA.

Thomas, S. C., Martin, A. R., & Mycroft, E. E. (2015). Tropical trees in a wind-exposed island ecosystem: height-diameter allometry and size at onset of maturity. *Journal of Ecology*, *103*(3), 594–605. https://doi.org/10.1111/1365-2745.12378

Tien Bui, D., Le, K.-T., Nguyen, V., Le, H., & Revhaug, I. (2016). Tropical Forest Fire Susceptibility Mapping at the Cat Ba National Park Area, Hai Phong City, Vietnam, Using GIS-Based Kernel Logistic Regression. *Remote Sensing*, *8*(4), 347. https://doi.org/10.3390/rs8040347

Tilman, D., May, R. M., Lehman, C. L., & Nowak, M. A. (1994). Habitat destruction and the extinction debt. *Nature 1994 371:6492*, *371*(6492), 65–66. https://doi.org/10.1038/371065a0

Tilman, D., Reich, P. B., & Knops, J. M. H. (2006). Biodiversity and ecosystem stability in a decade-long grassland experiment. *Nature 2006 441:7093*, *441*(7093), 629–632. https://doi.org/10.1038/nature04742

Tomar, S. (2006). Converting video formats with FFmpeg. *Linux Journal*, *2006*(146), 10.

Tompoulidou, M., Stefanidou, A., Grigoriadis, D., Dragozi, E., Stavrakoudis, D., & Gitas, I. Z. (2016). The Greek National Observatory of Forest Fires (NOFFi). *Https://Doi.Org/10.1117/12.2240560*, *9688*, 199–207. https://doi.org/10.1117/12.2240560

Town Planning Board. (2020). *Town Planning Board, Hong Kong*. https://www.pland.gov.hk/pland_en/info_serv/digital_planning_data/download.htm

Trauernicht, C., Ticktin, T., Fraiola, H., Hastings, Z., & Tsuneyoshi, A. (2018). Active restoration enhances recovery of a Hawaiian mesic forest after fire. *Forest Ecology and Management*, *411*, 1–11. https://doi.org/10.1016/J.FORECO.2018.01.005

Tsang, S. (2003). *A modern history of Hong Kong: 1841-1997*. Bloomsbury Publishing.

Uhl, C., Kauffman, J. B., & Cummings, D. L. (1988). Fire in the Venezuelan Amazon 2: Environmental Conditions Necessary for Forest Fires in the Evergreen Rainforest of Venezuela. *Oikos*, *53*(2), 176. https://doi.org/10.2307/3566060

Urza, A. K., Weisberg, P. J., Chambers, J. C., & Sullivan, B. W. (2019). Shrub facilitation of tree establishment varies with ontogenetic stage across environmental gradients. *New Phytologist*, *223*(4), 1795–1808. https://doi.org/10.1111/NPH.15957

van Butsic, Kelly, M., & Moritz, M. A. (2015). Land Use and Wildfire: A Review of Local Interactions and Teleconnections. *Land 2015, Vol. 4, Pages 140-156*, *4*(1), 140–156. https://doi.org/10.3390/LAND4010140

Van Nes, E. H., Staal, A., Hantson, S., Holmgren, M., Pueyo, S., Bernardi, R. E., Flores, B. M., Xu, C., & Scheffer, M. (2018). Fire forbids fifty-fifty forest. *PLOS ONE*, *13*(1), e0191027. https://doi.org/10.1371/JOURNAL.PONE.0191027

Van Nieuwstadt, M. G. L., Sheil, D., & Kartawinata, K. (2001). The Ecological Consequences of Logging in the Burned Forests of East Kalimantan, Indonesia. *Conservation Biology*, *15*(4), 1183–1186.

Vanderhoof, M. K., Fairaux, N., Beal, Y. J. G., & Hawbaker, T. J. (2017). Validation of the USGS Landsat Burned Area Essential Climate Variable (BAECV) across the conterminous United States. *Remote Sensing of Environment*, *198*, 393–406. https://doi.org/10.1016/J.RSE.2017.06.025

Verdone, M., & Seidl, A. (2017). Time, space, place, and the Bonn Challenge global forest restoration target. *Restoration Ecology*, *25*(6), 903–911. https://doi.org/10.1111/rec.12512

Viegas, D. X., & Viegas, D. X. (2004). Slope and wind effects on fire propagation. *International Journal of Wildland Fire*, *13*(2), 143–156. https://doi.org/10.1071/WF03046

Wadsworth, R. M. (1959). An Optimum Wind Speed for Plant Growth. *Annals of Botany*, *23*(89), 195–199. http://www.jstor.org/stable/42907466

Wagenbrenner, N. S., Forthofer, J. M., Page, W. G., & Butler, B. W. (2019). Development and Evaluation of a Reynolds-Averaged Navier–Stokes Solver in WindNinja for Operational Wildland Fire Applications. *Atmosphere 2019, Vol. 10, Page 672*, *10*(11), 672. https://doi.org/10.3390/ATMOS10110672

Walker, L. R. (1994). Effects of fern thickets on woodland development on landslides in Puerto Rico. *Journal of Vegetation Science*, *5*(4), 525–532. https://doi.org/10.2307/3235979

Walker, L., & Shiels, A. (2013). *Landslide Ecology*. Cambridge University Press. https://digitalcommons.unl.edu/icwdm_usdanwrc/1644

Wallbank, T. (2008). WindSim validation study. *CFD Validation in Complex Terrain*.

Wang, Haojie, Zhang, L., Luo, H., He, J., & Cheung, R. W. M. (2021). AI-powered landslide susceptibility assessment in Hong Kong. *Engineering Geology*, *288*, 106103. https://doi.org/10.1016/J.ENGGEO.2021.106103

Wang, Haoyu, Hua, J., Kang, M., Wang, X., Fan, X. R., Fourcaud, T., & de Reffye, P. (2022). Stronger wind, smaller tree: Testing tree growth plasticity through a modeling approach. *Frontiers in Plant Science*, *13*. https://doi.org/10.3389/FPLS.2022.971690/FULL

Weaver, P. L. (1986). Hurricane damage and recovery in the montane forests of the Luquillo Mountains of Puerto Rico. *Caribbean Journal of Science*, *22*(1–2), 53–70.

Wheeler, C. E., Omeja, P. A., Chapman, C. A., Glipin, M., Tumwesigye, C., & Lewis, S. L. (2016). Carbon sequestration and biodiversity following 18 years of active tropical forest restoration. *Forest Ecology and Management*, *373*, 44–55. https://doi.org/10.1016/J.FORECO.2016.04.025

Wieringa, J. (1986). Roughness-dependent geographical interpolation of surface wind speed averages. *Quarterly Journal of the Royal Meteorological Society*, *112*(473), 867–889. https://doi.org/10.1002/QJ.49711247316

Wilson, J. D. (1984). Determining a topex score. *Scot For*, *38*, 251–256.

Wimberly, M. C., & Reilly, M. J. (2007). Assessment of fire severity and species diversity in the southern Appalachians using Landsat TM and ETM+ imagery. *Remote Sensing of Environment*, *108*(2), 189–197. https://doi.org/10.1016/J.RSE.2006.03.019

Wittenberg, L., Malkinson, D., Beeri, O., Halutzy, A., & Tesler, N. (2007). Spatial and temporal patterns of vegetation recovery following sequences of forest fires in a Mediterranean landscape, Mt. Carmel Israel. *CATENA*, *71*(1), 76–83. https://doi.org/10.1016/J.CATENA.2006.10.007

Wu, C. (2004). Normalized spectral mixture analysis for monitoring urban composition using ETM+ imagery. *Remote Sensing of Environment*, *93*(4), 480–492. https://doi.org/10.1016/J.RSE.2004.08.003

Wu, M. C., Chang, W. L., & Leung, W. M. (2004). Impacts of El Niño–Southern Oscillation Events on Tropical Cyclone Landfalling Activity in the Western North Pacific. *Journal of Climate*, *17*(6), 1419–1428. https://doi.org/10.1175/1520-0442(2004)017

Wulder, M. A., Loveland, T. R., Roy, D. P., Crawford, C. J., Masek, J. G., Woodcock, C. E., Allen, R. G., Anderson, M. C., Belward, A. S., Cohen, W. B., Dwyer, J., Erb, A., Gao, F., Griffiths, P., Helder, D., Hermosilla, T., Hipple, J. D., Hostert, P., Hughes, M. J., … Zhu, Z. (2019). Current status of Landsat program, science, and applications. *Remote Sensing of Environment*, *225*, 127–

147. https://doi.org/10.1016/J.RSE.2019.02.015

Xu, S., Zhu, X., Helmer, E. H., Tan, X., Tian, J., & Chen, X. (2021). The damage of urban vegetation from super typhoon is associated with landscape factors: Evidence from Sentinel-2 imagery. *International Journal of Applied Earth Observation and Geoinformation*, *104*, 102536. https://doi.org/10.1016/J.JAG.2021.102536

Yan, F. W. (2018). Five Global Mass Extinctions in The Geological History and Their Traces in the Hong Kong Region. *Geological Society of Hong Kong Bullentin*, *13*(1).

Yang, S., Zheng, Z., Tan, H., Zhang, Z., Wang, H., Li, J., & Laws, E. A. (2018). Environmental changes and human activity since the Neolithic: Evidence from pollen and phytoliths in Hochung, Sai Kung area, Hong Kong. *Review of Palaeobotany and Palynology*, *258*, 36–47. https://doi.org/10.1016/J.REVPALBO.2018.07.001

Zheng, B., Ciais, P., Chevallier, F., Chuvieco, E., Chen, Y., & Yang, H. (2021). Increasing forest fire emissions despite the decline in global burned area. *Science Advances*, *7*(39). https://doi.org/10.1126/SCIADV.ABH2646/SUPPL_FILE/SCIADV.ABH2646_SM.PDF

Zhou, J., Jia, L., Menenti, M., & Gorte, B. (2016). On the performance of remote sensing time series reconstruction methods – A spatial comparison. *Remote Sensing of Environment*, *187*, 367–384. https://doi.org/10.1016/J.RSE.2016.10.025

Zhou, W., Chen, W., & Wang, D. X. (2012). The implications of El Niño-Southern Oscillation signal for South China monsoon climate. *Aquatic Ecosystem Health & Management*, *15*(1), 14–19. https://doi.org/10.1080/14634988.2012.652050

Zhu, H., Zhang, J., Cheuk, M. L., Hau, B. C. H., Fischer, G. A., & Gale, S. W. (2023). Monoculture plantations impede forest recovery: Evidence from the regeneration of lowland subtropical forest in Hong Kong. *Frontiers in Forests and Global Change*, *6*, 1098666. https://doi.org/10.3389/FFGC.2023.1098666/BIBTEX

Zhuang, X. Y., & Corlett, R. T. (1997). Forest and forest succession in Hong Kong, China. *Journal of Tropical Ecology*, *13*(6), 857–866. https://doi.org/10.1017/S0266467400011032